UNIVERSITÀ DEGLI STUDI
DI MODENA E REGGIO EMILIA

Dottorato di Ricerca in Ingegneria Industriale e del Territorio

Ciclo XXXV

Synergic approach of advanced combustion modelling methods in CFD codes and in chemical kinetics solvers: from particulate emissions to laminar flame speed for carbon-neutral fuels in flamelet combustion models

Candidata: Valentina Pessina

Relatore (Tutor): Prof. Stefano Fontanesi, Ph.D.

Correlatore (Co-Tutor): Dr. Fabio Berni, Ph.D.

Coordinatore del Corso di Dottorato: Prof. Alberto Muscio, Ph.D.

Anno Accademico: 2021-2022

Author and PhD Candidate: Valentina Pessina
Doctoral Student
Università degli Studi di Modena e Reggio Emilia
valentina.pessina@unimore.it

Supervisors: Professor Stefano Fontanesi, Ph.D.
Università degli Studi di Modena e Reggio Emilia
Department of Engineering "Enzo Ferrari"

Researcher Fabio Berni, Ph.D.
Università degli Studi di Modena e Reggio Emilia
Department of Engineering "Enzo Ferrari"

Head of the PhD School: Professor Alberto Muscio, Ph.D.
Università degli Studi di Modena e Reggio Emilia
Department of Engineering "Enzo Ferrari"

Reviewers: Associate Professor Martin Davy, Ph.D.
University of Oxford
Department of Engineering Science

Associate Professor Corinna Netzer, Ph.D.
Norwegian University of Science and Technology
Department of Energy and Process Engineering

Acknowledgements

My fervent interest in techniques for computational fluid dynamics was sparked during the lectures held by Prof. Fontanesi, who introduced me to this fascinating field and its applications to engines. He believed in me and supported me during my master's thesis on syngas combustion, and then I had the chance to continue the research on emissions and combustion modelling under the supervision of the same professor who kept on challenging me with interesting topics.

I am also thankful for the chance I had to spend some quality time abroad as a visiting PhD student at the University of Bundeswehr in Munich, where I had the pleasure to improve my research skills and use CFD and other computational techniques to explore fascinating topics such as the reentry of a spacecraft in a planetary atmosphere. For this, I am thankful to the researchers that welcomed me, as well as, the University of Modena and Reggio Emilia and Prof. Fontanesi for supporting such initiative.

I am thankful to R&D CFD for supporting the experiments for the surrogates on the research engine with optical access carried out by the researchers of STEM-IM of Napoli, Dr Merola, Dr. Irimescu, and PhD student Giovanni Cecere. I want to express my gratitude also to Prof. Mehl and Prof. Stagni for the stimulating conversations, in which I had the chance to perfect my knowledge of chemical kinetics.

Part of the PhD path comprises lonely moments in which one should read, think, apply knowledge, and explore new ideas. However, the real treasures are the moments of confrontation and exchange of perspective on the research topics. Collaboration and sharing knowledge can improve the quality of the research output since one can learn and see things differently while sharpening communication and human skills. We are human beings before being students and researchers, hence the importance of collaboration in a research group. In this, I was lucky to find in my laboratory people like Dr. Berni and Dr. Iacovano that helped me grow, challenged me to give my best and never give up, without losing the warmth of their human side.

My deepest gratitude goes to my family for the endless support and all the people who believed in me while undertaking this journey as PhD student.

These three years were intense, yet I am going to remember all the best parts of this journey and bring with me the mindset and a resilient heart.

Contents

Nomenclature

Abbreviations

CFD	Computational Fluid Dynamics
CI	Compression-Ignition
CK	Chemical Kinetics
DME	Dimethyl Ether
DISI	Direct Injection Spark Ignition
DSMC	Direct Simulation Monte Carlo
ECFM	Enhanced Coherent Flamelet Model
ECFM-3Z	Enhanced Coherent Flamelet Model 3-Zones
E-TRF	Ethanol Toluene Reference Fuel
FI	Flame Index
GDI	Gasoline Direct Injection
GFI	GruMo Flame Index
GHG	Green House Gas
GT	Gas Turbine
GTF	GruMo Tracer for Fuel
HoV	Heat of Vaporization
HPOST-FI	GruMo Flame Index
ICE	Internal Combustion Engine
IPSDF	Integral Particle Size Distribution Function
KS	Knock Sensitivity
LHV	Lower Heating Value
LII	Laser Induces Incandescence
LIF	Laser Induced Fluorescence
LFS	Laminar Flame Speed
MABP	Mole-Averaged Boiling Point
MD	Molecular Dynamics

MTBE	Methyl Tertiary Butyl Ether
MON	Motor Research Number
MW	Molecular Weight
NOx	Nitrogen Oxides
OESI	Oxygen Extended Sooting Index
OX	Oxidation
PAHs	Polycyclic Aromatic Hydrocarbons
PIONA	Paraffin Iso-paraffin Olefin Naphthenes Aromatic
PDF	Probability Density Function
PFI	Port Fuel Injection
PM	Particle Matter
PN	Particle Number
PSDF	Particle Size Distribution Function
PRF	Primary Reference Fuel
RANS	Reynolds Averaged Navier Stokes
RON	Research Octane Number
RVB	Combustion progress variable for ECFM-3Z
S.G.	Surface Growth
SG	Specific Gravity
SM	Smoke Point
SOI	Start Of Injection
SSM	Soot Sectional Method (diffusive library)
TDC	Top Dead Center
TF	Tracer of the fuel of ECFM model
TFS	Turbulent Flame Speed
TRF	Toluene Reference Fuel
TSI	Threshold Sooting Index
YSI	Yield Sooting Index
UNIFAC	UNIQUAC Functional-group Activity Coefficients
UHC	Unburned Hydrocarbons

WABP	Weight-Averaged Boiling Point

Symbols - Latin letters

BGS	Integrated PSDF for oil and engine-wear-related soot
c	Combustion progress variable
$\tilde{c}$	Favre averaged combustion progress variable
$C^{*}_{\mathrm{soot,i}}$	Active site on the soot particle belonging to section i
$\mathrm{C}_{\mathrm{COAG}}$	Tune constant for coagulation
$\mathrm{C}_{\mathrm{COND}}$	Tune constant for condensation
C_{OX}	Tune constant for oxidation
C_{PI}	Tune constant for particle inception
c_{p}	Specific heat at constant pressure
C_{SG}	Tune constant for surface growth
c_{v}	Specific heat at constant volume
d_{i}	Particle diameter for section i
$\mathrm{d}_{\mathrm{i+1}}$	Particle diameter for section $\mathrm{i}+1$
d_{p}	Particle diameters for Knudsen number calculation
$\mathrm{f}_{\mathrm{COAG}}$	Function for coagulation related soot
$\mathrm{f}_{\mathrm{COND}}$	Function for condensation related soot
f_{OX}	Function for oxidation soot
f_{PI}	Function for particle inception soot
f_{SG}	Function for surface growth soot
$\mathrm{gradY}_{\mathrm{CO}}$	Gradient of CO mass fraction in FI definition
$\mathrm{gradY}_{\mathrm{F}}$	Gradient of fuel mass fraction in FI definition
$\mathrm{gradY}_{\mathrm{O}}$	Gradient of oxygen mass fraction in FI definition
$\mathrm{IPSDF}\ (\Phi_{\mathrm{i}})$	Integral of the PSDF for a specified value of Φ_{i}
$\mathrm{IPSDF}^{\mathrm{Norm}}\ (\Phi_{\mathrm{i}})$	Normalization of IPSDF(Φ_{i}) over the stoichiometric value
$\mathrm{HPOST}_{\mathrm{AI}}$	Heat released due to autoignition
$\mathrm{HPOST}_{\mathrm{PM}}$	Heat released due to premixed flame front

$\mathrm{HPOST}_{\mathrm{DF}}$	Heat released due to diffusive combustion
k	Turbulent kinetic energy
$\tilde{k}$	Average value of turbulent kinetic energy within k - ε model
Kn	Knudsen number
l_{F}	Laminar flame thickness
l_{G}	Gibson length scale
l_{K}	Kolmogorov length scale
l	Characteristic turbulent length scale
$\mathrm{m}_{\mathrm{i,soot}}$	Mass of soot particle in section i
$\mathrm{m}_{\mathrm{cell}}$	Mass of the computational cell
n_{k}	Soot number density in section k
n_{y}	Soot number density in section y
$p_{\mathrm{vi,s}}$	Partial pressure of each component at the liquid interface
$p^{0}_{\mathrm{vi,s}}$	saturation pressure of the ith component
p	pressure
$\mathrm{P}_{\mathrm{i}}(\mathrm{i}=1,6)$	Pre-calculated function from tables
rsOpt	Variable of soot model relating to the library selection
$\tilde{S}^{\mathrm{u}}_{\mathrm{f,u}}$	Source term of fuel due to evaporation in unburnt gas region
$\tilde{S}^{\mathrm{b}}_{\mathrm{f,u}}$	Source term of fuel due to evaporation in burnt gas region
$\mathrm{s}^{0}_{\mathrm{L}}$	Laminar velocity for unstretched flame
s_{L}	Laminar flame speed
$s_{\mathrm{L,ref}}$	Laminar flame speed, chemical kinetics simulation
$s_{\mathrm{L,fit}}$	Laminar flame speed, fitting
$\mathrm{Sc}_{\mathrm{soot}}$	Schmidt number for soot
$\mathrm{s}_{\mathrm{L,mix}}$	Laminar flame speed of the mixture
$\mathrm{s}_{\mathrm{L,i}}$	Laminar flame speed of component i
t	Time
$\tilde{T}$	Cell-wise value of temperature (RANS)
T_{a}	Thermal age for surface reactivity calculation
T_{b}	Burnt gas temperature

T_{boil}	Normal boiling temperature
T_{u}	Unburnt temperature
v'	Turbulent velocity fluctuation
$\mathrm{v}_{\mathrm{C_2H_2}}$	Acetylene volume
vf	Volume fraction distribution through sections factor
$v_{\mathbf{i}}$	volume fraction of component i
$\mathrm{v}_{\mathrm{PAH}}$	Volume of pyrene
$\mathrm{v}_{\mathrm{i,min}}$	Minimum volume of particles in section i
$\mathrm{v}_{\mathrm{i,\ max}}$	Maximum volume of particles in section i
$\mathrm{v}_{\mathrm{i,mean}}$	Mean volume of particles in section i
$x_{\mathrm{H_2}}$	Mole fraction of component hydrogen
$x_{\mathbf{i}}$	Mole fraction of component i
x_{j}	Special coordinate
y_{i}	Mass fraction of component i
$\widetilde{\mathrm{Y}}_{\mathrm{i,soot}}$	Soot mass fraction for section i
$\mathrm{Y}_{\mathrm{f,b}}$	Burnt fuel mass fraction
$\mathrm{Y}_{\mathrm{f,u}}^{\mathrm{u}}$	Unmixed unburnt fuel mass fraction
$\mathrm{Y}_{\mathrm{f,u}}^{\mathrm{b}}$	Unmixed fuel in the burnt gas region
$\mathrm{Y}_{\mathrm{ox,u}}^{\mathrm{u}}$	Unmixed unburnt oxidizer mass fraction
$\mathrm{Y}_{\mathrm{f,u}}^{\mathrm{m}}$	Mixed unburnt fuel mass fraction
$\mathrm{Y}_{\mathrm{ox,u}}^{\mathrm{m}}$	Mixed unburnt oxidizer mass fraction
$\mathrm{Y}_{\mathrm{f,b}}^{\mathrm{m}}$	Mixed burnt fuel mass fraction
$\mathrm{Y}_{\mathrm{ox,b}}^{\mathrm{m}}$	Mixed unburnt oxidizer mass fraction
Y_{P}	Mass fraction of products in the unburnt region
$\mathrm{Y}_{\mathrm{P,b}}$	Mass fraction of products in the burnt region
Y_{TF}	Mass fraction of fuel tracer
Z	Mixture fraction
Z_{st}	Stoichiometric value of mixture fraction
$\tilde{Z}''$	Mixture fraction variance

Symbols - Greek letters

α_{st}	Stoichiometric air-fuel ratio
$\beta_{\mathrm{k,y}}$	Collision frequency faction between particle of section k and y
$\beta_{\mathrm{k,k}}$	Collision frequency faction between particle of section k and k
β_{PI}	Collision frequency factor for particle inception
β_{COND}	Collision frequency factor for condensation
$\varepsilon_{\mathrm{i,j}}$	Size-collision factor for coagulation
ε	Dissipation rate for turbulent structures
$\tilde{\varepsilon}$	Average dissipation rate for turbulent structures
χ	Scalar dissipation rate
$\tilde{\chi}$	Average scalar dissipation rate
χ_{T}	Turbulent Scalar dissipation rate
Φ	Equivalence ratio of the mixture
γ	Ratio of specific heats
γ_{i}	Activity coefficient for UNIFAC model
λ	Air index or Φ^{-1}
λ_{gas}	Free molecular path of a molecule in the gas phase
μ	Laminar viscosity or generally the viscosity
μ_{t}	Turbulent diffusion coefficient
θ	Fractal parameter (2 for spherical shape)
ξ_{FI}	Normalized flame index with maximum reactant gradients
$\xi_{\mathrm{FI,n}}$	Normalized flame index - alternative formulation
$\xi_{\mathrm{FI,\ mod}}$	Normalized flame index with CO
ρ	Density
$\bar{\rho}$	Mean gas density in the cell
ρ_{soot}	Soot particle density
σ^2	Quadratic error for laminar flame speed mixing rules
τ_{chem}	Chemistry characteristic time scale
τ_{mix}	Mixing time scale

$\tau_{\text{soot-chemistry}}$	Soot chemistry characteristic timescale
τ_{turb}	Turbulence characteristic time scale
ω_{sg}	Surface growth source terms of other models
$\bar{\omega}_{\text{S}}$	Average combustion source term
$\bar{\omega}_{\text{f,u}}^{\text{u}}$	Unburnt fuel source oxidation rate for AI/PF
$\bar{\omega}_{\text{f,u}}^{\text{b}}$	Unburnt fuel source oxidation rate for DF
$\overline{\dot{\omega}}_{\text{f,u}}^{\text{u}\rightarrow\text{b}}$	Fuel mass exchange rate between unburnt and burnt gas region
$\Omega_{\text{i,Soot}}$	Total soot source term
$\Omega_{\text{i,PI}}$	Particle inception soot term
$\Omega_{\text{i,COND}}$	Condensation inception soot term
$\Omega_{\text{i,COAG}}$	Coagulation soot term
$\Omega_{\text{i,SG}}$	Surface growth soot term
$\Omega_{\text{i,OX}}$	Oxidation soot term

Abstract

Combustion is still widely employed in both energy and transportation sectors, which are the backbone of the global economy. Given the current policies and regulations, the scientific community is making endeavors to achieve carbon-neutral processes. Within this framework, further optimization of combustion device operation can be achieved either via experiments and/or by simulations. Computational Fluid Dynamics (CFD) and chemical kinetics simulations offer an advanced tools to the investigation of the combustion process. The object of this thesis is the use of these tools for advanced application for internal combustion engines focusing on two essential facets: emissions and the use of carbon-neutral fuels.

- In the first part, the necessity for chemical kinetics simulations and the use of surrogate fuels in 3D CFD engine simulations is discussed in terms of composition definition, Lagrangian phase modelling approaches for the fuel spray (lumped or multi-component) and its influence over the sooting tendency of the stratified charge, and finally flame propagation. For this last, a flexible approach based on mixing rules and flame propagation modelling based on correlations derived from chemical kinetics is presented for Toluene Reference Fuels.

- In the second part of the thesis, the synergy between chemical kinetics and engine simulations is discussed focusing on the sootmatter modelling. On one hand, this pollutant is damaging the environment and the health of living beings since nanoparticles can enter the respiratory system, on the other hand, it is one of the most complex types of emission to model. As a further improvement to the current Sectional Method, customization of source terms reaction rate constants via look-up tables is presented and achieved by chemical kinetics simulations. The qualitative efficacy in catching the sooting threshold is tested in 3D CFD simulations of a premixed engine fed with gasoline surrogates with and without oxygenated content, and the extreme case of pure ethanol. Then, the case of partially premixed combustion is investigated since it may potentially occur in case of sudden evaporation of liquid film deposits under specific operational conditions. The tabulation of chemical reaction rates is based on two factors that are decided a priori: the fuel composition, thus the importance of surrogate fuels previously discussed, and the type of rectors. The simulation framework employed in this study offers two possibilities for the table generation: a pure diffusive flamelet or a premixed constant pressure reactor. In case of partially premixed combustion the choice is not so straightforward. A modification on the Fortran-based source code is operated to switch between the two libraries accordingly to the results of a cell-wise test. For this purpose, different criteria are tested for assessing the predominant type of combustion for the cell-wise test, and a new one is proposed based on the employed combustion model. Premixed combustion is initially assumed, and if required, the input table is switched from the default premixed one to the diffusive one. Finally, the efficacy is checked for two test cases.

- In the third part chemical kinetics is employed for developing input correlations for modelling carbon-neutral fuel combustion in flamelet CFD codes. Chemical kinetic simulations are used to derive input correlations for flame propagation in case the of carbon-neutral fuels One-dimensional freely propagating flames are used to build an extensive database for several ammonia-hydrogen blend single correlation for laminar flame speed is derived with hydrogen content as an additional parameter.

Keywords: flamelet, soot, ammonia, hydrogen, surrogates

Sommario

Ad oggi la combustione è una delle tecnologie più ampiamente utilizzate nell'industria dei trasporti e dell'energia, entrambi settori cardine dell'economia. La ricerca e il progresso scientifico sono stimolati delle normative sempre più stringenti ad andare verso lo sviluppo di processi a basse emissioni, in particolar modo di anidride carbonica. Di vitale importanza è la continua ottimizzazione di questi dispositivi, la quale può essere perseguita tramite via sperimentale o mediante simulazioni. La fluidodinamica computazionale (CFD) e le simulazioni di cinetica chimica offrono strumenti avanzati per lo studio del processo di combustione. Lo scopo di questa tesi è l'impiego di queste tecniche computazionali applicate al caso dei motori a combustione interna per indagare alcune problematiche di interesse, quali le emissioni di particolato e il possibile uso di combustibili e/o vettori energetici privi di carbonio.

- In primis è proposto un excursus sull'uso di combustibili surrogati necessari per rappresentare i più complessi combustibili reali, come la benzina. Questi sono formulati con una composizione ad hoc per replicare le proprietà di interesse del combustibile di riferimento. A seguito della formulazione, si discute dell'uso dei surrogati nelle simulazioni 3D CFD motore, presentando l'impatto che l'approccio della modellazione della fase Lagrangiana ha sulla distribuzione spaziale della tendenza a produrre particolato per motori ad iniezione diretta. In fine, è proposta una metodologia per la modellazione della propagazione del fronte di fiamma per miscele di toluene, n-eptano ed isottano nel caso dei modelli di combustione appartenenti alla famiglia dei modelli "flamelet". La strategia presentata è flessibile in quanto basata su regole di miscela per il calcolo della velocità laminare di fiamma del surrogato finale, a partire dalle tre correlazioni ricavate da simulazioni di cinetica chimica per ciascun componente.

- Nella seconda parte si discute sulle potenzialità della sinergia tra cinetica chimica e simulazione CFD motore per la formazione di particolato, inquinante dannoso per l'ambiente e la salute, ma estremamente complesso da modellare. Nell'ambito del metodo delle sezioni, la cinetica chimica è impiegata per produrre tabulazioni delle costanti di reazione ricavate ad-hoc sulla composizione di surrogati di benzine, con e senza contenuto di ossigenati, e nel caso estremo di etanolo puro. L'efficacia qualitativa è stata testata in simulazioni CFD 3D di un motore premiscelato. Per quanto sofisticate, queste tabulazioni si basano su due fattori decisi a priori: la composizione del combustibile e il tipo di reattore impiegato nelle simulazioni di cinetica chimica. Il solutore 3D CFD usato in questo studio offre due possibili tipi di reattori per la tabulazione completamente: uno diffusivo e uno premiscelato. Nel caso di una combustione parzialmente premiscelata, la scelta per la tabulazione non è scontata. È proposta una modifica al codice sorgente per passare da una libreria all'altra in base ai risultati di una verifica eseguita in ciascuna cella dove è in atto l'ossidazione del combustibile. Tra i diversi criteri di verifica esaminati, ne viene proposto uno nuovo basato sul modello di combustione utilizzato. Una verifica preliminare è presentata per casi test.

- In fine, nella terza parte, la cinetica chimica è adoperata per la derivazione di correlazioni di input per la velocità laminare di fiamma per miscele di ammoniaca e idrogeno. Le simulazioni di cinetica chimica per fiamme monodimensionali a propagazione libera sono utilizzate per le procedure di fitting da cui si ottengono correlazioni ad-hoc per ciascuna miscela e infine è proposta un'unica correlazione parametrizzata rispetto anche al contenuto di idrogeno.

Parole chiave: flamelet, particolato, ammoniaca, idrogeno, surrogati

Introduction

1. Introduction

1.1 Research background: use of combustion in the energy and transportation sectors

The current needs of the two main sectors in which combustion is still extensively employed are presented in this paragraph. The main topic of interest for the scientific and technological fields are also presented to provide a big picture in which the present research was developed. Energy production and transportation sectors are the backbones of nowadays economy. These sectors are undergoing changes that are moving towards low-carbon emission processes, and more ambitiously towards carbon-neutral systems. The wide-spreading awareness of climate change and global warming is pushing policymakers and the scientific community to find alternative solutions to traditional power generation technologies, enhancing the efficiency of processes and the sustainability of sources. Nowadays, combustion is the main process used for power generation in road and marine transportation, in aviation, as well as energy production (e.g. power plants or stationary power generation). Because of its many technological advantages, it is expected to remain a major player for most of the 21st century [1]. Within this framework, the scientific community has been spending efforts to improve efficiency and limit the environmental impact resulting from it. Combustion is the process in which the thermal energy from the fuel oxidation can be, for example, transformed into mechanical energy to power machines, whose results are combustion products and heat released because of the overall exothermic reactions. This process is employed in several applications such as gas turbines in power plants, combustors in industrial and manufacturing processes, and internal combustion engines. These last are employed in a broad spectrum of applications: light-duty vehicles, such as passenger cars, to power small tools (e.g. cutting saws for gardening), in power generation (e.g. Diesel engines for power emergency power generation), or heavy-duty applications, both in road transportation and marine sector. Internal Combustion Engines (ICEs) have undergone intense progress to improve efficiency and for meeting the increasingly strict regulations on the emissions stemming from combustion.

1.2 Aim of this study

Combustion is widely employed in both the energy generation and transportation sectors. While the transition towards ideally *carbon-neutral* is an ongoing process, the current technology such as internal combustion engines can be still the object of improvement in two main areas: emissions and carbon-neutral fuel combustion. On one hand, engines fueled with more traditional fuels, such as gasoline, are prone to produce carbon-based pollutant species, such as carbon dioxide and monoxide, soot particles, nitrogen oxides, and unburnt hydrocarbons. Among these, soot particles are a hazard to health and to the environment, hence developing tools to predict and estimate the soot generation during combustion is a valuable advantage. On the other hand, the scientific community, governments, and industry are spending endeavours to implement carbon-neutral fuel combustion in current devices. Of particular interest for internal combustion engines are the ammonia-hydrogen blends.

In light of the "boundary conditions" provided by governments and regulators, climate changes, and current research trends, this thesis aims to provide ready-to-use methodology for emission modelling and carbon-neutral fuel combustion simulations:

- **surrogate fuel modelling focusing on** the spatial distribution of the **sooting tendency** and its link to the Lagrangian multiphase modelling for Direct Injection engines.

- correlations for describing the **laminar flame speeds** in CFD codes, necessary input to flamelet combustion models for modelling Spark Ignition combustion. Based on **chemical kinetic simulations**, **laminar burning velocities** are collected in a database, on which a data fitting procedure is applied to obtain a four-parameter correlation tailored to the chemical nature of the fuel. The state of art methodology of the research groups is applied to each hydrocarbon of Toluene Reference Fuels, and then it is extended to test for multi-component mixtures and mixing rules implemented within the 3D full engine cycle simulation.

- a methodology to describe ammonia-hydrogen blend combustion for turbulent flamelet combustion is proposed. First, an extensive database of laminar burning velocities for ammonia with an increased hydrogen content is employed to test if the current methodology, derived for hydrocarbons, is suitable for carbon-neutral fuels. Then, **a novel five-parameters correlation** is proposed in this study **with hydrogen mole fraction as an additional parameter**.

- a customized use of **sectional method for soot modelling** is **applied to premixed combustion** for gasoline, oxygenated gasoline, and pure ethanol to prove the efficacy of the tabulation of the rates for the soot source terms in the transport equation. The simulation results are compared to experimental data of a metal engine from the literature. Then, a novel approach is proposed, implemented in the source code, and tested on a metal engine for three different starts of injection time, since this parameter can have an impact on fuel evaporation, hence on secondary and local diffusion phenomena, which may influence the soot formation and evolution. Working **directly on the source code**, with the **implementation of a cell-wise test criterion for assessing the predominant combustion mode**, the tabulated reaction rates are retrieved from tables derived with premixed or diffusive combustion. These tables are customized on the fuel composition, comprise the engine operative conditions, and are based on a collection of chemical kinetics simulations that can be carried out either using a premixed or a diffusive reactor. The modification proposed in this thesis answers the need for modelling soot formation in partially premixed combustion, whereas the standard implementation requires an a-priori choice of one table derived with on combustion mode. The efficacy of the **dynamic cell-wise switch between tabulated source terms** is **tested on two levels**: the first level is for checking the code implementation, then the second level **compares the simulation results with and without the library switch with experimental data from a metal engine**.

All **these applications rely on the synergy between CFD and chemical kinetics** solvers. The **main advantage of the approaches provided** is that the chemical kinetics is solved *off-line* with respect to the CFD simulation, thus computational time can be saved. Moreover, **the accuracy of the chemical nature of the fuels is not lost**, both for burning velocity and soot formation, **thanks to tabulation** accessed by the model, **or the correlations** given as inputs to it.

1.3 Computational methods

Experimental measurements are crucial for improving combustion devices' operation, from the combustion efficiency to the emission levels measurements. Besides experiments, computational models have enhanced and proved their effectiveness when validated with laboratory measurements. Computational Fluid Dynamics (CFD) and Chemical Kinetics (CK) simulations positively contribute to improving and optimizing the operational parameters of combustion devices, including internal combustion engines. These applications have gained more importance in the last decades, as described in the report by NASA on the forecast of computational fluid dynamics up to 2030 [2]. Thanks to the increased computational power, the use of more sophisticated models and computational techniques is rapidly evolving.

The prominent family of computational techniques can be categorized based on the type of flow regime. This distinction is made based on the Knudsen number (Kn), in which the ratio of the free molecular path λ and the characteristic length of the problem L is employed to assess if the regime is continuum (Kn $\ll 0.01$), transition ($0.01 <$ Kn < 0.1), or molecular (Kn $\gg 0.1$). Based on the type of regime, a different computational technique can be required. For example, Molecular Dynamics (MD) or Direct Simulation Monte Carlo (DSMC) methods are suitable for rarefied gases in transition to molecular regimes, where the MD approach simulates every molecule, and the DSMC is based on a statistical representation of particles whose properties are described from a Lagrangian point of view. Then, for the continuum regime, the CFD techniques are based on the resolution Navier-Stokes equations in which the mass and momentum are conserved, and the total energy is balanced within a fluid domain, divided into small volumes (computational cells). Since the analytic solution to the Navier-Stokes set of equations is not possible, numerical methods are employed. Similarly, CFD codes can describe several flows from zero to three dimensions to model combustion with one step reaction or with detailed chemistry or model the turbulent structures. Depending on the type of turbulence treatment, several numerical approaches can be possible. Widely employed in research and industrial applications, a Favre average of the flow quantities can be adopted. Thus the flow structures are solved using Reynolds Average Navier Stokes (RANS) equations. Alternatively, Unsteady Reynolds Navier Stokes (URANS) equations and Detached Eddy Simulation (DES) are possible. Another approach in which bigger vortices are simulated and the smaller isotropic ones are modelled is known as Large Eddy Simulation (LES) approach. Finally, the most computationally expensive approach is Direct Numeric Simulation (DNS).

Another family of CFD-based solvers is the Chemical Kinetics (CK) ones, whose aim is to solve equations of mass, momentum, and energy balance over a reacting thermodynamic system and to provide the temporal/spatial evolution of the chemical species. Generally, these solvers require thermal and transport properties of the species and the reaction mechanism. In this last, the reactions are described using the Arrhenius constant for the reaction rates. When this type of simulation is carried out, the higher the number of species and reactions the more the computational cost. Hence, the use of reduced reaction mechanisms comprising the most influential reactions is sometimes employed. These simulations can be utilized to obtain customized tabulation of input data for CFD combustion and emission models, such as ignition delays, reaction rates for pollutant species, or laminar flame speed values at engine-relevant conditions deriving correlations to the flamelet model for a chemistry-based description of the turbulent combustion. In this thesis, the RANS-CFD and its integration with chemical kinetics solvers are investigated, some applications are proposed for soot modelling, and the use of chemistry-based correlations for the laminar flame speed in CFD codes are derived and applied to fuels characterized by different chemical natures from gasoline surrogates to carbon-neutral energy carriers and fuels, like ammonia-hydrogen blends.

1.4 Surrogate fuel modelling

One of the most important inputs to chemical kinetic solvers is fuel composition, which can be problematic in the case of gasoline. For this reason, the surrogate fuel formulation is the best way to address this issue. By mixing in a specific proportion of a few representative hydrocarbons and chemical compounds, a representative surrogate fuel can be formulated to target the properties of interest of the reference fuel. The fuel modeling is necessary for chemical kinetic solver for extracting the data, and for assembling tables containing for example ignition delays, and reaction rate constants, that can be employed by 3D CFD without solving directly and in detail the chemistry for engine cycle applications, which can be advantageous in terms of computational cost.

The role of surrogate fuels can be essential for two computational approaches: chemical kinetics simulations and engine simulations with CFD codes. More in detail, using chemical kinetics solvers is relevant to the characterization of several aspects of the fuel oxidation phenomenon. It can be employed for tabulations of inputs for CFD simulations. In this case, detailed chemistry results can be directly read from the tables without additional computation with the advantage of increasing accuracy without substantial impact on the computational costs. For instance, tabulation can be employed in ignition delay characterization, essential for both compression and spark ignition devices, or reaction rate tabulations for describing pollutant species chemical evolution from NOx to soot emissions. Alternatively, data from engine-relevant conditions can be employed for flame propagation characterization using input correlations extrapolated from chemical kinetics simulation results. As for engine simulations, combustion models belonging to the flamelet family require as an input a correlation for the laminar flame speed employed to reckon the turbulent combustion velocity. Experimental data are usually far from the high pressures and temperatures experienced in engines; therefore, the key role of chemical kinetics simulations is in creating an extensive database of flame speed values. Given the importance of these simulations for increasing the accuracy of emissions and flame propagation calculations, the role of the surrogates is hereafter outlined. The fuel composition is a mandatory input for any combustion simulation, and its definition can be a complex task in the case of petroleum-derived fuels, such as gasoline, gas oil, or aviation fuels. Although the outlined principles are valid for any carbon-based fuel, the applications presented in this thesis revolve around aspects concerning Direct Injection Spark Ignition (DISI) engine simulations. Hence, different types of gasoline are the fuels of interest. Gasoline is a mixture of several compounds that differ in their chemical nature, whose proportion and type can be determined by experimental analysis, such as gas-chromatography [3]. Although the determination of the gasoline components can be achieved by detailed gas-chromatography, its use in chemical kinetics solver is unfeasible, and even more, when dealing with CFD engine simulations. The reason is twofold: first, some compounds may lack the characterization of thermal and transport properties, as well as their reaction rate constants, and secondly, most of the chemical kinetic solvers are based on numerical methods that require matrix inversion techniques, and the higher the number of input species, the more extensive and harder to handle this matrix will be, as well as the solution achievement.

In this picture, surrogate fuels can be employed as a substitute for real gasoline: they comprise a limited number of chemical compounds (from 2 up to 6-7 generally) mixed in a specific proportion defined by the resolution of a set of constraints on the target properties of the reference fuels to be matched.

1.4.1 Aim of the surrogate formulation in this study

The surrogate formulation aims to target the main combustion-relevant properties and the sooting tendency. Three surrogates are formulated with similar knock sensitivity, stoichiometric equivalence ratio, and stark differences in Threshold Soot Index (TSI). Then, the application of the formulated surrogates is presented for two facets of DISI engine simulations: Lagrangian phase simulation for spray and laminar flame speed input to flamelet turbulent combustion models. Two approaches for the Lagrangian phase are compared: the first one is the multi-component mixture, and then the single-component mixture with user-defined lumped properties. The sooting tendency characterization of a surrogate is usually linked to the TSI value, based solely on the chemical nature of the fuel. In this chapter, a step further in sooting tendency characterization is achieved: its spatial distribution is provided, and the differences between the multi and single-component approaches are drawn. Finally, a methodology is proposed for the flame propagation characterization of the Toluene Reference Fuels (TRFs) as a multi-component mixture. A laminar flame speed correlation is derived for each component of the TRF for a wide range of operational conditions. Then, different mixing rules are compared to assess which one provides the highest accuracy compared to chemical kinetic simulations with the actual composition. This methodology provides a flexible approach for reckoning laminar flame speed for flamelet models, in which no ad-hoc correlation is required when the composition proportions change. Thus, it can be applied to all the possible compositions of the solution space of a TRF surrogate, and the user-defined framework is easy to implement via user subroutine or on source code for open-source codes.

1.5 Soot and fuel combustion

Soot is a carbonaceous solid product that stems from fuel-rich hydrocarbon combustion. The soot production, both in size and concentration, depends on the combustion mode (diffusive/premixed, the excess of fuel) and the fuel chemical nature (e.g. aromatic compounds are more prone to produce soot during combustion due to the presence of carbon rings [4]). Soot formation and evolution are complex processes, characterized by the interplay of physical and chemical phenomena. To shed light on sooting tendency related to fuel nature, studies can be carried out on laminar flame optical observation with several techniques such as Laser Induces Incandescence (LII) or Laser Induced Fluorescence (LIF), and concentration measurements, along with the characterization of indexes such as the TSI or Smoke Point. Experiments can be carried out to investigate and describe the genesis of the Polycyclic Aromatic Hydrocarbons (PAHs), as reported by Desgroux et al. [5], then by Liang et al. [6] using LII and LIF optical observations of laminar premixed flames of PRF and TRF mixtures, as well as pure components like isooctane and n-heptane with variable equivalence ratio and pressure. Interestingly, this study suggested that the sooting tendency is enhanced by higher backpressure of the partially premixed laminar flames as shown in Figure 1 [6]. Laminar diffusion flames are also objects of several studies aiming to describe the soot formation, for instance, Yan et al. proposed experimental measurements [7], Botero et al. [4], investigated the precursors and soot formation for several fuels, establishing also a hierarchy of sooting tendency between hydrocarbon classes. In conjunction with experimental investigations, computational chemistry is efficiently adopted to model this phenomenon with the purpose of predictive analysis with chemical kinetic simulations [8] [9]. Chemical kinetics simulations with simplified reactors provide reliable tools for a preliminary design of combustion devices (choice of geometry, operational parameters like pressure, temperature, amount, and type of fuel).

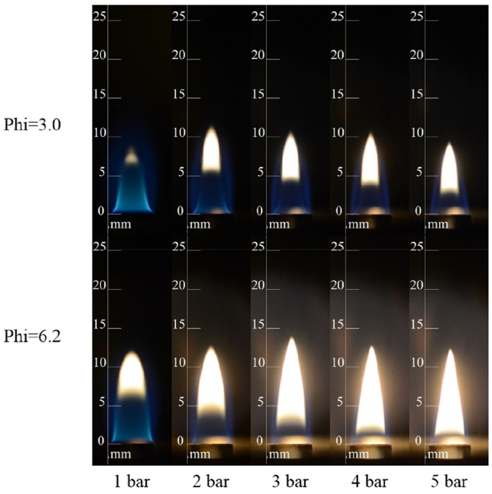

Figure 1: Experimental optics of laminar partially premixed flames of isooctane [6]: effect of the backpressure on the columns, the effect of the fuel enrichment of the flame (Φ) on the rows

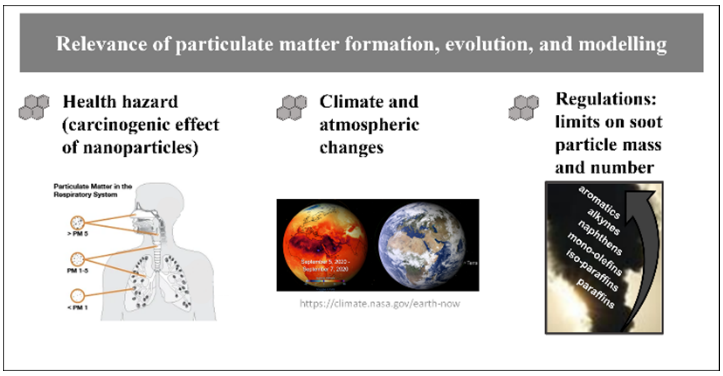

Figure 2: The reasons why the study of soot formation is important: health hazard, environmental impact, and emission limits imposed by governments.

Despite the potential ban of ICEs in Europe, the scientific community is still researching on the complexity of this phenomenon and the reason is threefold (Figure 2):

- from the environmental perspective and anthropocentric activity, this solid emission is of concern not only for ICEs of light-duty vehicles but also for the heavy-duty transportation sectors, like the marine one. This last has very few regulations, especially if compared to the road transportation sector. Naval engines are powered by heavy hydrocarbon mixtures, usually two-stroke or four-stroke Diesel engines with high power output and slow revving speed, or gas turbines with Brayton-Joule cycle internal combustion, or vapor turbines with external combustion Rankine cycle. Also, the aviation industry adopts carbon-based fuels, as well as most of the industrial processes involving furnaces.
- nanoparticle (especially if very small, such as 10 nm, $PM_{0.01}$) can be a threat to human and animal health causing respiratory and cardiovascular diseases. Smaller particles can enter the respiratory system, and the smallest combustion-based nanoparticles made of phenanthrene, pyrene, naphthalene, anthracene, can enter the blood circulation and deliver carcinogenic particles to other tissues and organs [10].
- as a result of the health and environmental impact of soot, binding regulations are pressing to curb emissions, starting from light-duty vehicles on road transportation.

1.5.1 Fuel sooting tendency for ICEs applications

Nowadays, internal combustion engines for light-duty applications are the center of attention for curbing carbon-based emissions in particular, whereas the marine transportation sector is moving towards carbon-neutral solutions (such as ammonia). Lastly, industrial and aviation sectors are trying alternative solutions, that will be implemented in a long term and depending on the geographic area. To meet the stringent regulations, internal combustion engines have been pushed to the improvement of fuel consumption, engine performance, and curbing emissions, including particulate matter in GDI engines, the use of oxygenated compounds is necessary [11]. These compounds can be added to improve the knocking resistance of gasoline and to enable the use of higher boosted pressures, and compression ratios, without risking the engine structural integrity [12], and increasing engine performances. Oxygenated compounds, such as ethanol (C_2H_5OH), MTBE (Methyl Tertiary Butyl Ether), DME (Dimethyl Ether), have also an impact on emissions [11] [13]. As for ICEs, they generally tend to reduce the soot formation [14][15]. However, the soot precursor production in oxygenate-doped flames should be carefully considered [16]. As reported by Desjardins et al. [16], the presence of oxygenated functional groups (moieties) can produce two effects: dilution and presence of oxygen-based functional groups can either replace the highly sooting components, or it can lead to the replacement of cleaner-molecules with more sooting and complex carbon-based molecules. However, the conclusion of this study, like many others [17] [13], is that increasing the oxygen presence via the OH-functional group of oxygenated compounds effectively curbs the soot precursors formation. As explained by the study of Liang et al. [7], higher oxygen concentration enhances the H-abstraction during fuel pyrolysis, and the CO formation is promoted instead of the rival reactions of ring-formation, from which the first aromatic-close-ring compounds stems from (such as benzene C_6H_6 or pyrene $C_{16}H_{10}$). The formation of precursors in the gas phase is very complex as well as the surface-gas-phase reactions for growth or oxidation of soot particles, and both are influenced by the thermodynamic conditions of the burning system. For example, the temperature has an exponential impact on the reaction rates as the modified Arrhenius equation suggests. Pressure also promotes the soot formation [7]: the higher the pressure, the higher the concentration of particles, hence the probability of successful collisions (Smoluchowski equation [18] [19]). Moreover, elevated pressure leads to a higher concentration of soot precursors first, and particles then. The increase of pressure and the consequent rise of soot concentration is reported in Figure 3 for a specific value of C/O ratio, the soot density, reckoned as both particles and PAHs, increases at higher pressures [20].

The fuel-rich mixtures are more prone to produce soot if compared to lean ones,

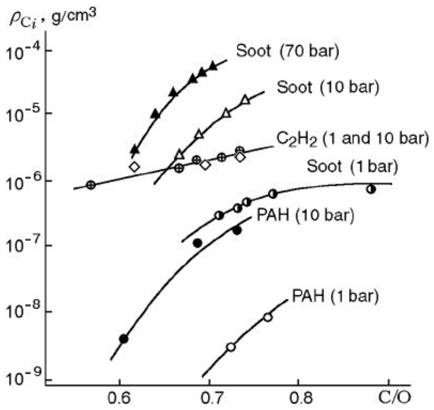

Figure 3: Carbon density of soot precursors and particles for specific pressures and for variable C/O ratios [21] for temperatures higher than 1700 K.

as reported by experimental studies [22]. Finally, the combustion mode has an impact on the soot formation related to ICEs. A key role in soot formation in ICEs is the mixing, thus the local value of the equivalence ratio. For an instance, in the case of direct injection, factors such as injection time or the degree of atomization of the fuel spray influence the soot exhaust emissions. In the case of early injection, for example, the fuel is guaranteed more time to evaporate and mix with the oxidizer, thus rich pocket or liquid film deposits should be effectively reduced with the right choice of SOI. In other words, the charge is more homogeneous in the case of early injection. This evidence is observed and reported both by experimental [23] [24] and numerical results [15]. During the oxidation of the fuel, soot formation can be mainly observed in the reaction zone where the C/O ratio reaches the threshold value, rather than in the post-flame zone [21] [25]. Moreover, in the post-flame zone, the concentration of H is generally too low to sustain the hydrogen abstraction and carbon addition mechanism [26], which are the fundamental mechanisms of soot formation and growth. In general, diffusive and premixed combustion are different types of combustion modes, thus they yield different physics, chemistry, and sooting tendency. For example, in diffusion flames, soot is formed on the fuel side, where the reactions leading to the closed-ring PAHs species are predominant on the oxidation. However, the flame temperature has an exponential effect on the kinetic rates. In particular, as reported by Sidebotham et al. [27] the C_4 reactions pathways leading to closed-ring benzene, may vary depending on the temperature, resulting in the promotion of some species reactions, such as butadienyl C_4H_5 and vinyl-radical C_4H_4 at lower temperatures, e.g. less than 1500 K, or other species such as butatrienyl radical C_4H_3 at higher temperatures, whereas in premixed flames the temperatures are usually higher enough to follow the second mechanism.

1.5.2 Soot formation and evolution

Soot formation is a complex phenomenon yet to be fully understood. However, given the impact on the environment, performance, and health, this topic has been profusely investigated by several fields (engineering, chemistry, computational science, medicine). Since this study focuses on modelling soot formation in CFD codes, the general phenomenology of soot production due to fuel pyrolysis and combustion is presented. This solid carbonaceous product stems from a tangled interplay of the physical and chemical phenomenon, that can be described as the occurrence of formation mechanisms rooted both in chemistry and in physical phenomena, such as the statistics of particle collision [18]. With a simplification of these complex phenomena, soot formation can be described with physics-based phenomena, such as particle inception, condensation, and coagulation, and then the chemistry-driven mechanisms, namely surface growth and oxidation.

Physical mechanisms of soot formation

The genesis of a soot particle is referred to as particle inception or nucleation. Carbonaceous particle origin is in the gas phase, in which closed-ring structures of carbon atoms starts to form from the hydrocarbon-based fuel undergoing the combustion process. At some point, soot precursor molecules, generally addressed as PAHs, collide and condense forming the primary particles of soot that evolve during the combustion process. Usually, computational models identify the soot precursors (Figure 4) as either the acetylene molecule C_2H_2, benzene C_6H_6, which is a 6 carbon-atom ring molecule bounded with 6 hydrogen atoms, or the pyrene $C_{16}H_{10}$. A remark should be done on the dependence of PAHs on the pressure: higher pressures yield an increment of collision probability; the same effect is addressed to the bigger size of the molecules [25] [28]. The effect of the oxygen present is relevant on the PAHs formation [28]. More specifically, the presence of oxygen enhances the hydrogen abstraction reactions in fuel pyrolysis and decomposition. Triggered by the presence of oxygen, the CO formation competes with the ring-formation reactions, which can effectively suppress the PAHs formation.

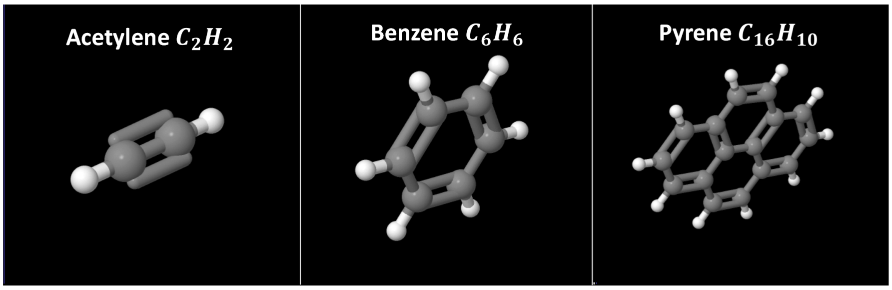

Figure 4: Main soot precursors considered in the main chemistry-based soot modelling approaches.

Once a particle is formed, it can either bond because of the Van der Waals forces with another solid particle, coagulation, or it can interact with a PAH molecule that will condense the primary particle, condensation. In this case, large polycyclic aromatic hydrocarbons are produced due to the condensation of PAHs (gas-phase) on the surface of the primary soot particles, produced by particle inception. As for coagulation, inter-particle collisions are dominated by statistics of molecular collisions, and they are independent of chemical reactions. The physics-based mechanisms of soot formation are regulated by the molecular collisions, which can be described by the Smolouchowski equation [18], and they can be regarded as phenomena occurring at the molecular regime. In the case of particle inception, the Smolouchowski equation can be expressed by eq.(1)

$$\dot{\mathrm{N}}_{\mathrm{i=2PAH,PI}} = \beta_{\mathrm{PAH,PAH}}\mathrm{N}_{\mathrm{PAH}}^{2} \tag{1}$$

where $\dot{\mathrm{N}}_{\mathrm{i=2PAH,PI}}$ is the collision rate between the two particles involved in the inception of the carbonaceous particle, for examples two PAHs (e.g. pyrene). The rate of collision depends quadratically on the particle number density ($\mathrm{N_{PAH}}$) and on the collision factor $\beta_{\mathrm{PAH,PAH}}$ between two PAHs. In eq.(1) the particle number density distribution should be evaluated for a size at a time, since $\beta_{\mathrm{PAH,PAH}}$ is a function of the particle radius. The general expression of $\beta^{\mathrm{m}}_{\mathrm{i,j}}$, the collision frequency between i-j pair in the molecular regime (eq.(2)) is a function of the temperature, the viscosity $\mu_{\mathrm{i,j}}$, and of the radii of the two molecules r_{i} and r_{j}.

$$\beta^{\mathrm{m}}_{\mathrm{i,j}} = \varepsilon_{\mathrm{i,j}} \sqrt{\frac{8\pi \mathrm{k_b} T}{\mu_{\mathrm{i,j}}}} \left(\mathrm{r_i} + \mathrm{r_j}\right)^2 \tag{2}$$

The attractive forces between particles are affected by the size of the pair involved in the collision, and this dependence on the molecular size is accounted for in $\varepsilon_{\mathrm{i,j}}$, the size-dependent coagulation enhancement factor. Although condensation, particle inception, and coagulation can be described with the same logic as Smolouchowski equation, the description of the collision frequency differs, due to the value of the Knudsen number (Figure 5) $\mathrm{Kn} = 2\,{}^{\lambda}/_{\mathrm{d_p}}$, where $\mathrm{d_p}$ is the particle diameter and λ is the free molecular path (the distance that a molecule in the gas phase should travel before it collides with another one).

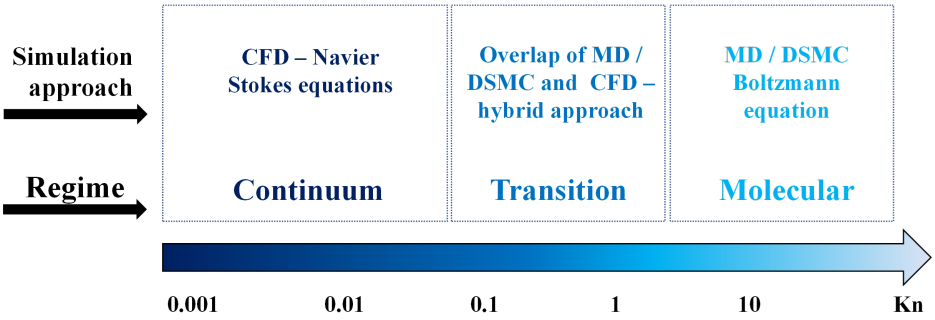

Figure 5: Flow regimes and the appropriate computational technique

For particle inception, the expression of $\beta^{\mathrm{m}}_{\mathrm{i,j}}$ can be derived from eq.(3) and eq.(4).

$$\beta^{\mathrm{m}}_{\mathrm{i,j}} = K_{\mathrm{m}} \left(i^{\frac{1}{3}} + j^{\frac{1}{3}}\right)^2 \left(\frac{1}{i} + \frac{1}{j}\right)^{\frac{1}{2}} \tag{3}$$

$$K_{\mathrm{m}} = \varepsilon_{\mathrm{i,j}} \left(\frac{3m_{1,m}}{4\pi\rho} \right)^{\frac{1}{6}} \left(\frac{6\mathrm{k_b}T}{\rho} \right)^{\frac{1}{2}} \tag{4}$$

For condensation, the frequency of collision factor $\beta_{\mathrm{i,PAH}}$ can be expressed by eq.(5), where $\mathrm{i_{PAH}}$ denotes the PAH particle size.

$$\beta_{\mathrm{i,PAH}} = K_{\mathrm{m}} 4\sqrt{2} \cdot \mathrm{i}_{\mathrm{PAH}}^{\frac{1}{6}} \tag{5}$$

For the molecular regime, the collision frequency can be described by eq.(3) and eq.(4) (for particle inception) or eq.(5) (for condensation), or for the continuum by eq.(6) and eq.(7), whereas for the transition regime, the empirical formula derived by Fuchs [29] should be employed.

$$\beta^{\mathrm{c}}_{\mathrm{i,j}} = K_{\mathrm{c}} \left(\mathrm{i}^{\frac{1}{3}} + \mathrm{j}^{\frac{1}{3}} \right)^2 \left(\frac{\mathrm{C_i}}{\mathrm{i}^{\frac{1}{3}}} + \frac{\mathrm{C_j}}{\mathrm{j}^{\frac{1}{3}}} \right)^{\frac{1}{2}} \tag{6}$$

$$K_{\mathrm{c}} = \frac{2k_{\mathrm{b}}T}{3\eta}, \mathrm{C_i} = 1 + 1.257 \cdot \mathrm{Kn_i} \tag{7}$$

In eq.ns (4),(5),(6), and (7) the subscripts “c” and “m” stands for “continuum” and “molecular” regime respectively, K_{c} and K_{m} are factors depending on temperature, density, and Boltzmann constant, k_b is the Boltzmann constant, $\mathrm{C_i}$ and $\mathrm{C_j}$ are slip correction factor for the accommodation factor (Cunningham slip factor [30]) relating to specific Kn_i and Kn_j, η and ρ are the gas viscosity and density respectively, $m_{1\mathrm{m}}$ is the one size unit of the colliding particles (for particle inception or condensation it can be typically assumed equal to $\mathrm{C_2}$, two carbon atoms).

Chemistry-driven mechanisms

Soot precursors collide and dimerize (formation of a molecule originating from two others) to form PAHs clusters, which further combine and grow leading to the formation of soot solid particles. The solid particle evolution is influenced by the surface reaction processes, which can either “erode” the particle, or “increase” its size. These mechanisms are known as oxidation and surface growth respectively. A key concept is the surface reactivity, which represents how prone is the soot particle surface to react with other species such as H_2, H_2O, H, C_2H_2, O_2 in the gas-phase. Their interaction with the active sites comprises specific chemical reactions taking place on the soot agglomerates surface and they are described by the Hydrogen-Abstraction Carbon-Addition Ring-Closure (HACARC) mechanism [31] [32]. T he active sites ($C^*_{\mathrm{soot}\ ,i}$) can be found on the soot particle surface, and they can react with either O_2, resulting in a C-atom removal (oxidation), or C_2H_2, leading to surface growth respectively (Figure 6).

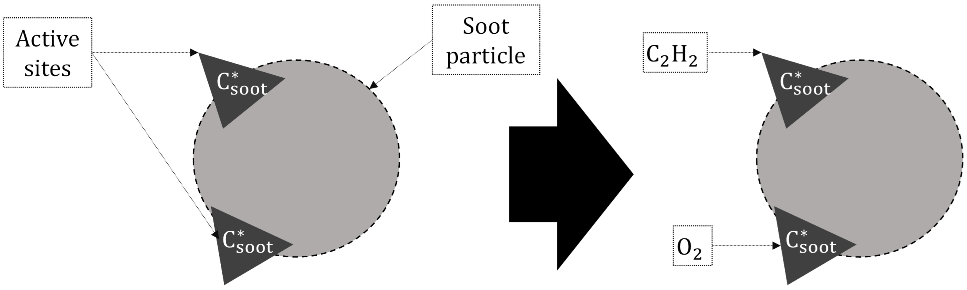

Figure 6: Active sites on a soot particle schematic (left), examples of molecules involved in the surface growth (C_2H_2) and in oxidation (O_2).

Besides temperature and residence time, the reactivity of soot particles depends on the number of active sites available for reaction with stable gas species (e.g., C_2H_2 and O_2). This number of active sites per unit surface area is correlated to the concentration of C-H sites, and as soot ages as residence time passes, the concentration of C-H decreases [33]. The phenomenon of the change in surface reactivity with residence time is known as particle ageing: C/H ratio increases with residence time, and as a result, the C-H sites decrease. As in all reactions and gas kinetics, the role of temperature is also significant: the higher the temperature, the more the collisions, hence the higher the probability of effective collisions. The concentration of the active sites $[C_{\mathrm{soot,i}}]$ can be described as (eq.(8)) a function of the number of sites per unit area χ_{soot}, the area S_i, N_i the number of soot particles of size "i", and the Avogadro number N_A, all proportional to a parameter α that accounts for the fraction of the possible active sites actually present.

$$[\mathrm{C}_{\mathrm{soot}\ ,\mathrm{i}}] = \alpha \frac{\chi_{\mathrm{soot}}}{\mathrm{N_A}} \mathrm{S_i N_i} \tag{8}$$

This last parameter is to be estimated, and within the context of the CFD model that is investigated in this study, the parameter α is assumed to be constant. In reality, it is influenced by temperature and particle ageing (residence time), as reported in the expression proposed by [33] in their experimental investigation. In their study, a thermal-age dependent expression of α was proposed after experimental data involving nine flames representative of methane/air, ethylene/air, and ethylene/diluted flames, with successful implementation in the CFD code "Co-Flame" validated with a 2D grid of an axisymmetric burner with a mesh refinement in the reaction zone [33]. Their argument is that α cannot be effectively described by a constant of a function of the thermodynamic temperature of the system T, but a more articulate expression is required. Authors of this study [33] proposed $\alpha\,(T_{\mathrm{a}})$, a function of the thermal age T_{a}, which is calculated as the integral of the T over the residence time. This way, the same thermal age can be reached by a particle at lower temperatures in a longer residence time or by a particle at higher temperatures in a shorter time. However, within this study framework, α is considered as a constant, for avoiding excessive complexity to the already articulate model that is employed. The active sites can undergo two types of processes: oxidation and surface growth. Surface growth is the size increase of a solid carbonaceous particle via surface addition. The process is chemistry-dominated by the mechanisms known ad Hydrogen Abstraction Carbon Addition Ring Closure (HACARC) proposed by Frenklach and Harris [34] [35], and implemented in one of the most advanced computational models for soot formation, the Sectional Method [36][31]. Hydrogen atoms bound to the carbon ring are extracted and unsaturated sites are formed, thus promoting the addition of carbon atoms or closed-ring of carbon atoms. This way larger soot structures are formed. On the other hand, oxidation is the chemistry-driven mechanism of soot particle size reduction. It is described by the HACARC mechanism formation [35][31][36]. In this study framework, the HACARC mechanism presented is the one actually implemented in the Sectional Model, which was proposed by [31], and it is described in Table 4. This set of chemical reactions describes the main interactions between $C^*_{\mathrm{soot,i}}$, the active site on the surface of the particle and the gas-phase molecules, such as (molecular and atomic) hydrogen, hydroxyl radical (OH), molecular oxygen (O_2), and acetylene C_2H_2. In Table 4 the active sites have an additional subscript "i" to describe the bin to whom the particle belongs depending on its size. To further elaborate on this concept, an analogy with the experimental measurements for engines can be provided. Usually, the output of a measurement can be the description of the particle diameter distribution, expressed as log-distribution of the Particle Size Distribution Function (PSDF): the measuring device count the aerosol particles, then group those characterized by a similar size in the same group (the bin). In the same fashion, the Sectional Method groups particles in different bins, called sections, depending on their size, thus providing a similar PSDF as the one achieved experimentally. Thus, due to surface reactivity, a particle belonging to section (bin) "i" can move to the next section "i+1" if the particle undergoes surface growth, or it can be counted in the previous section "i-1" in case it reacts with OH or O_2.

Table 4: HACARC mechanism actually implemented in the CFD code for the Sectional Method for soot modelling.

R1.a	$\mathrm{C_{soot,i}H + H \xleftrightarrow{k_{1a}} C^*_{soot,i} + H_2}$
R1.b	$\mathrm{C_{soot,i}H + OH}\ \overset{\mathrm{k_{1\ b}}}{longleftrightarrow}\ \mathrm{C^*_{soot,i} + H_2O}$
R2	$\mathrm{C^*_{soot\ ,i} + H \xrightarrow{k_{1a}} C_{soot\ ,i}H}$
R3.a	$\mathrm{C^*_{soot\ ,i} + C_2H_2 \xleftrightarrow{k_{3a}} C^*_{soot\ ,i}C_2H_2}$
R3.b	$\mathrm{C^*_{soot\ ,i}C_2H_2 \xrightarrow{k_{3}}}$$_b$ $\mathrm{C_{soot\ ,i+1}H + H}$
R4.a	$\mathrm{C^*_{soot,i} + O_2 \overset{k_{4}{\mathit{a}}}{\to} C^*_{soot,i-1} + 2CO}$
R4.b	$\mathrm{C^*_{soot\ ,i}C_2H_2 + O_2 \xrightarrow{k_{4\ b}} C^*_{soot\ ,i} + 2CHO}$
R5	$\mathrm{C_{soot\ ,i}H + OH \overset{K_5}{\to} C^*_{soot\ ,i-1}}$

The active site $C_{\mathrm{soot,i}}$ can react with either an H atom or with the OH radical, thus resulting in the hydrogen abstraction and radial site formation on the active site $C_{\mathrm{soot,i}}{}^*$ (R1.a and R1.b), both reversible reactions. The addition of C_2H_2 on the radical site $C_{\mathrm{soot,i}}{}^*$ occurs with R3.a (reversible) and R3.b, which is the ring opening or fragmentation reaction. The oxidation is described by R4.a, R4.b, and R5.

1.6 Carbon-neutral fuels and energy carriers

Another factor that pushed the internal combustion engines towards an evolutionary turning point is the traditional petrol-fed engine pending ban promised by regulators. For this reason, engine manufacturers and the automotive industry have been developing tools for emissions predictions, and now they are reacting with the development of engines fed by carbon-neutral fuels, such as ammonia and hydrogen. The ammonia-hydrogen blends show a promising perspective, especially for marine and heavy-duty applications: these can be the perfect substitute for the currently employed naphtha, which comprise heavy hydrocarbons characterized by strong sooting tendency. Hydrogen is a good candidate for being an effective energy carrier, to whom one can assign different labels (blue, green, grey)[37] depending on the type of resource employed for its production. However, safety, storage, handling, and emissions are to be discussed for this fuel type, and the scientific community and the industry are trying to address them.

Moreover, marine transportation, which is responsible for 90% of the goods logistics around the globe, still needs to be regulated as strictly as road transport, especially in the case of passenger car engines. It is undeniable that the demand for fewer polluting devices is leading the Darwinian evolution of engines, and the progress of other technologies, such as electric motors, should be supported and critically analyzed, as also recent events shed light on the importance of the energy supply demand. Billions of light-duty electric vehicles will require a power grid to satisfy consistent energy demand, hopefully with clean energy sources. Additionally, the comparison between light-duty vehicles should be carried out on the entire life cycle, not only the road emissions, for a fairer comparison. In this context, during the evolutionary process of the energy and transportation sectors, internal combustion engines still have a role to play. The scientific community is spending efforts developing efficient combustion devices fed by hydrogen-ammonia blends. Internal combustion engines fueled with ammonia-hydrogen blends are an option to be investigated both experimentally and numerically. Besides DNS simulations for hydrogen instabilities, the practical issue of ammonia and hydrogen combustion in ICEs is still open. The turbulent combustion regime of ICEs can be modelled using flamelet models, such as the Level Set (or G-equation) or the Enhanced Coherent Flamelet Model (ECFM), whose main input to the flame propagation model is the laminar flame speed correlation. This last depends on mixture quality and thermodynamic parameters and, above all, on the nature of the fuel. The profusely investigated laminar flame speed correlations tailored on hydrocarbon-based fuels are not suitable for ammonia or hydrogen, which are very different in nature from the traditional ones. For this reason, laminar flame speed correlations are derived for ammonia blended with increasing hydrogen content in this thesis. Finally, a single correlation is presented with a parametrization that also includes the hydrogen content.

1.6.1 Ammonia and hydrogen blends

Energy storage and distribution are key to human life, progress, and the economy. Nowadays, the major energy storage technologies are based on chemical (fuel cells), mechanical, electrical (batteries), and thermal (fuel combustion) energy. Batteries are becoming prominent among the solutions discussed by the scientific community. However, the current crises of raw materials and the demand for a large-scale application are suggesting alternatives. Several efforts are in place to promote the use of hydrogen H_2 [38], starting with the issues relating to its storage and employment in combustion systems (e.g. flame instability, high reactivity, high combustion adiabatic temperatures). For this reason, an energy carrier can help solve some of the issues related to hydrogen use. Among the candidates such as methane (CH_4) and ammonia (NH_3), the latter has recently gained its spotlight in the research effort. Several review studies [38] [39] [40] [41] [42] [43] highlighted these main points relating to the use of ammonia for energy generation purposes:

- source and production technologies: photocatalysis, electrocatalysis and plasma catalysis. Depending on the production process, ammonia can reduce CO_2 and GHG emissions, yet ammonia synthesis is still a high energy-intense process dependent on hydrocarbons [44]. Currently, China produces 28.5% of the globally produced amount (176 million of metric tons) [44].
- applications: 80% of worldwide produced ammonia is employed in agriculture (fertilizers), then other uses are related to plastics and fibers, pharmaceuticals, mining and metallurgy, pulp and paper, refrigeration, and explosives [44]. Recent applications are related to the transportation sector and energy generation: NOx emissions curb (DeNOx), the energy source for fuel cells, and finally, as a fuel and/or energy carrier.
- storage: at reasonable conditions (8 bar and 21 °C [45]), ammonia is conveniently stored as a liquid. In this form, energy density is approximately half that of gasoline and ten times more than batteries [38].
- it is an active part of the energy roadmap of several countries, such as Japan, New Zealand, Australia, United States, [38]. Although the production process needs to further detach from the dependency on fossil fuel sources, the research on the performance of ammonia used as an energy carrier should be pursued in the transportation industry since it can be advantageous for emission curbing on a Life Cycle Analysis basis [46].

1.6.2 Fields of application and current research trends

Besides production, storage, and distribution, the scientific community is investing efforts in research and clarification of the following facets of ammonia use related to combustion-based devices:

- flame behavior (quenching, flame thickness, flame instability onset) of pure ammonia and effect addition of hydrogen)
- emission of NOx depending on the type of combustion device (e.g., geometry of TG combustor) [47], and combustion parameters (e.g., pressure, unburnt temperature, dilution, hydrogen addition).

In the pursuit of decarbonization, combustion processes must convert to carbon-neutral fuel sources and energy carriers. In this context, hydrogen (H_2) and ammonia (NH_3) are regarded with interest, as they can be applied in internal combustion engines (ICEs), gas turbine burners [47], as well as furnaces [42] [43] [39], and their oxidation is characterized by the absence of carbon-based pollutants, such as CO, CO_2, and soot. Moreover, NH_3 has higher energy density when compared to liquid H_2, thus it is a suitable energy carrier for H_2 as reported by [43] [45]. However, their combustion process needs to be thoroughly controlled to mitigate the formation of other pollutant species, e.g., Nitrogen Oxides (NOx). Lee et al. [48] published an experimental and computational study regarding NH_3 blending in H_2/air spark-ignited spherical flames evaluating the effect of NH_3 addition on both emissions and flame behavior. For lean conditions, the addition of NH_3 increases the production of NOx compared to H_2/air flames, whereas for richer mixtures, the production of NOx is reduced [48]. A thorough review on NOx formation stemming from ammonia use in combustion devices is presented by [39]. The flame behavior and NOx production were also extensively studied by Karan [49], Hayakawa [50], and by Mashruk et al. [51]. The interplay of thermal decomposition, residence time, and heat losses in NOx formation was also investigated by Okafor [52] with highlights on combustor wall and flame interactions. Interestingly, NH_3 provides a potential suppression effect of preferential-diffusion and hydrodynamic instabilities which characterize ultra-lean and lean H_2/air mixtures. In this regard, NH_3 appears more effective than methane, the other valid H_2-carrier. Despite its stabilization effect on H_2/air lean flames, the use of NH_3 must be carefully investigated considering its potential high reactivity with the container materials and its toxicity [45]. NH_3 and H_2 blends for power generation have been extensively investigated by the scientific community, with studies ranging from experimental characterization to computational modelling, from gas turbine applications [47] to spark ignition engines [53]. Experiments are essential to characterize the combustion behavior of NH_3 mixtures: they provide information to derive and validate reaction mechanisms, which are employed in chemical kinetics simulations to calculate ignition delays, laminar flame speeds, and pollutant formation. The study presented by Shrestha et al. [54] includes both experimental and modelling approaches for the derivation of chemical kinetics models for the oxidation of NH_3/H_2 blends at high temperatures, as well those carried out by [49], and at conditions representative of commercial micro-turbines [55]. Chemical kinetics can be either directly integrated into CFD solvers via the solution of a transport equation for each reactant or product, or used off-line, to create libraries where ignition delays, laminar flame speeds, or species formation are stored as a function of thermodynamic parameters and mixture quality. Such libraries can be employed in association with specific models in the CFD solver to retain high fidelity in the chemical characterization of the mixture while reducing the overall computational cost of the simulations. Regardless of the approach, the integration of detailed chemical kinetics in the CFD process provides further insight into the combustion behavior within a specific device, and this is particularly true for unconventional fuels, such as NH_3. The use of NH_3 as an energy carrier was extensively discussed by [42] [43], [56]. Xiao et al. [47] applied CFD to a gas turbine burner fueled with NH_3/CH_4/air mixtures, whereas for internal combustion engines applications, NH_3 blends have already been the subject of experimental studies, as the one conducted by Lhuillier et al. [57], Verhelst et al. [58], and Chiong et al. [53] carried out a study regarding ammonia fueled engines. As for numerical modelling of premixed or partially premixed turbulent combustion in ICEs, which mostly falls in the wrinkled-flamelet regime [59] [60], the accurate description of flame propagation is based on the proper characterization of the laminar burning velocity of the mixture and on a correct representation of turbulent acceleration of the laminar-like flame via correlations [61]. The CFD solver employs as input the laminar flame speed correlations to compute the turbulent flame propagation, treating the turbulent combustion as a laminar flame with an increased flame surface area. For this reason, reliable laminar flame speed correlations are essential to achieve the correct modelling of turbulent combustion, which is predominant in industrial applications. Laminar flame speed correlation for ammonia-hydrogen blends

1.6.3 Laminar burning velocity modelling: state of the art

The laminar burning velocity of a mixture is the result of its composition, as well as its temperature and pressure, and summarizes into a single value the effects of chemical kinetics, thermodynamics, and diffusion [62]. The stark differences in the combustion behavior between H_2, NH_3, and hydrocarbons (e.g., alkanes, such as CH_4) require dedicated modelling of the flame propagation, thus a laminar flame speed description tailored on specific fuel composition is essential to achieve sufficient accuracy when modelling the combustion process. Traditionally, laminar flame speed correlations are derived using a fitting procedure of available experiments [63] [64] [65]. While high accuracy can be achieved at conditions close to the experiments, their correct extrapolation outside that range is not guaranteed. Experimental studies are available [54] [66] [67] [[68] [69] [70] at several conditions, however still far from the targeted ICE ones (i.e., for pressures ranging from 40 bar to 130 bar). Alternatively, chemical kinetics simulations can be done to cover engine-like conditions to provide a dataset of virtual experiments to formulate correlations suitable for full-load engine conditions. Several reaction mechanisms for chemical kinetics applications are available in the literature: an NH_3/H_2/air reaction mechanism (26 species and 119 reactions) was proposed by Gotama et al. [71] by working on the optimization of the mechanism presented by Han et al. [72] and perfecting the lean and rich conditions; a study that comprises of CH_4/NH_3 mixtures was presented by Okafor et al. [73], whereas an alternative reaction mechanism was proposed by Otomo et al. [74] on chemical kinetics of NH_3/H_2/air mixtures with a focus on laminar flame speed. Finally, a chemical kinetics reaction mechanism was proposed by Stagni et al. [75] [76]. As for the laminar flame speed correlations, extensive studies focused on hydrocarbon-based fuels [77] and gasoline surrogates [78] [79]. In the wake of the current focus on decarbonization, new studies on carbon-neutral and unconventional fuels, such as NH_3 and H_2, have emerged. Verhelst et al. [80] [81] proposed an extensive study on H_2 laminar flame speed, where correlations for H_2/air mixtures at engine relevant conditions (pressures up to 45 bar) were presented. Another correlation based on chemical kinetics simulations for pure H_2 was proposed by D'Errico et al. [82]. This last covers pressures up to 16 bar, and it was tested in one-dimensional thermo-fluid dynamic simulations of a S.I. engine. Goldmann et al. [83] successfully obtained laminar flame speed correlations for mixtures of NH_3 (0–100 mol%)-H_2 (0–60mol%)-air, for $1 \text{ bar} \leq \text{p} \leq 250 \text{ bar}$, $0.5 \leq \lambda \leq 1.7$, $300 \text{ K} \leq T_\text{u} \leq 1000 \text{ K}$ (where the air index λ is equal to the inverse of the equivalence ratio Φ, $\lambda = (\Phi)^{-1}$). Despite these previous works, the existing literature lacks of alternatives for typical ICE full-load conditions. This work aims to fill this gap of the availability of correlations for NH_3/air mixtures with increasing H_2 content, at typical full-load engine conditions ($40 \text{ bar} \leq p \leq 130 \text{ bar}$) and from ultra-lean to rich mixtures ($0.4 \leq \Phi \leq 1.5$). In particular, laminar flame speed correlations are derived for NH_3/air mixtures with an increasing H_2 percentage (0-20-40-60-80-90-100 mol%) using a fitting procedure on an extensive dataset of chemical kinetics simulations. Finally, a single laminar flame speed correlation accounting for H_2 mole fraction as an additional independent parameter is presented for lean-to-rich conditions ($0.7 \leq \Phi \leq 1.5$) for NH_3/air mixtures with high H_2 contents (60-80-90 mol%), and its effectiveness is compared to the results obtained with blend-specific correlations from dedicated fitting procedures.

2. Methodology

2.1 Surrogate formulation

2.1.1 General methodology for surrogate formulation

A surrogate fuel is a blend of a limited number of chemical compounds mixed in a specific proportion to match the properties of interest of a specific reference fuel. The possible properties that can be matched when formulating a surrogate are described in Figure 7.

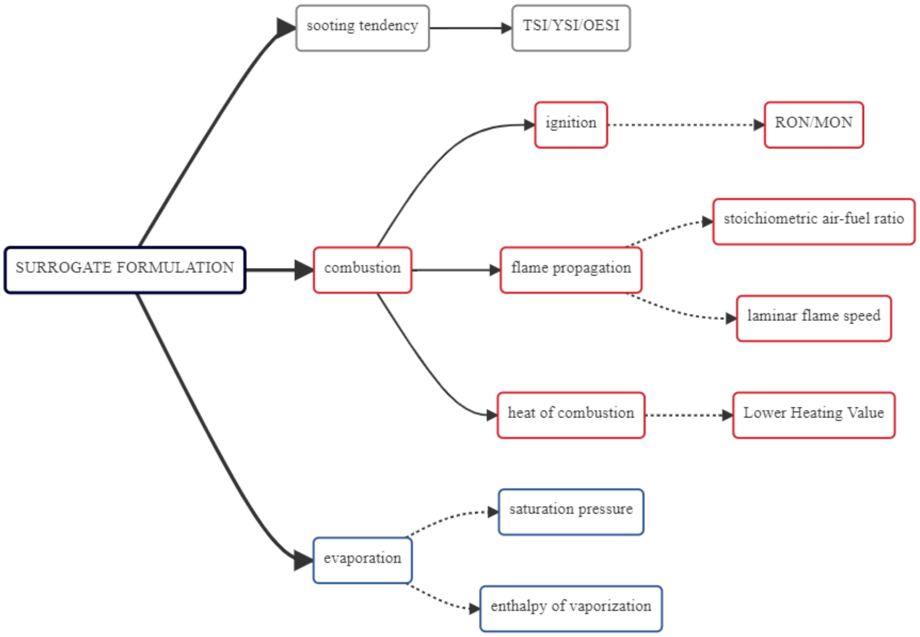

Figure 7: Possible choices of fuel properties for the surrogate formulation process.

The higher the number of properties to match, the more the components should be used in the mixing for a better match of the target values. The reason is that the surrogate fuel composition can be obtained by solving a system of equations that corresponds to a specific set of conditions on the mixture properties that are to be met. More specifically, the target properties of the mixture can be reckoned by using mixing rules: for each component, the value of the property is weight on, for example, the mole fraction within the mixing rule. Then, the set of actively target properties is solved with a numerical technique, and finally, the final surrogate composition is defined. The numerical technique can be based either on the method of least squares or on the minimization of an objective function. In this section, each property is investigated, and a mixing rule is proposed. Finally, the selected target properties are chosen, and the final compositions are discussed in the next paragraph. The general method for surrogate properties calculation is based on mixing rules weighting each component property based on its specific proportion. For the majority of the properties [84] [85] [86] [3] [87] a linear mixing rule, historically developed by Kay and widely adopted for hydrocarbon mixtures [88], is exploited: $F_{\text{mix}} = \sum_i (\theta_{\text{i}} F_{\text{i}})$ where F_{i} is the generic property, θ_{i} is the mole/mass/volume fraction of the component, the subscript "i" and "mix" stand for ith component and mixture respectively. Next, an overview of the possible target properties is provided, whereas the surrogate formulation for this specific work is discussed in the next paragraphs.

Mixture averaged molecular weight

The averaged molecular weight MW_{ave} of the surrogate can be reckoned as the linear average based on the equivalent number of carbon, hydrogen, and oxygen atoms eventually using eq.9.

$$\text{MW}_{\text{ave}} = \text{MW}_{\text{C}} \cdot n_{\text{C}} + \text{MW}_{\text{H}} \cdot n_{\text{H}} + \text{MW}_{\text{O}} \cdot n_{\text{O}} \tag{9}$$

Ignition and flame propagation properties

The Research Octane Number (RON) and the Motor Research Number (MON) are the most relevant properties for the characterization of the mixture ignition. For the formulated surrogate, these properties can be calculated either by linear mixing rules [84] [78] [3] [87] or by more elaborated correlations based on, for example, the functional groups [89] [90] [91]. However, as reported by Pera et al.[84], the linear by mole mixing rule is providing realistic predictions with the advantage to be mathematically easier to handle when multiple properties are constrained. Other properties of interest are the ones relating to flame propagation, which are linked to the chemical nature of the surrogate. For example the laminar flame speed, which depends also on the stoichiometric air/fuel ratio, can be target [78]. However, in this work, a novel approach is proposed: the laminar flame speed is derived for each component based on chemical kinetics simulations and expressed as a correlation of several parameters, then the laminar flame speed of the surrogate is calculated based on the cell-wise effective proportions of the component of the mixture. The advantage of this approach is the flexibility of the composition and the accuracy of the multi-component mixture flame propagation in the CFD code.

Normal boiling temperature

The evaporation curve and the normal boiling temperature are two characteristics of relevance, in case the surrogate has to match evaporation of the reference fuel. The normal boiling temperature T_b is the temperature at which the liquid phase turns completely into vapor, at a given pressure. The information regarding the normal boiling point derived from real distillation is not always available, and above all, a method to calculate the evaporation of the formulated surrogate should be defined as well. When a fluid is a mixture of hydrocarbons, the Average Boiling Point (ABP) can be calculated by using a mole, mass, or volume fraction law. The possible mixing rules are summarized in Figure 8: the mole and mass fraction based are mathematically easy to implement in optimization tools for surrogate formulation, however the mole fraction based is biased against the lightest component, whereas the mass fraction is for the heaviest one. Alternatively, empirical models developed for applications relating to chemical engineering, can be employed for hydrocarbon mixtures. One of the relationships that could be employed to compute the mixture boiling point in the Riazi-Daubert correlation [88],

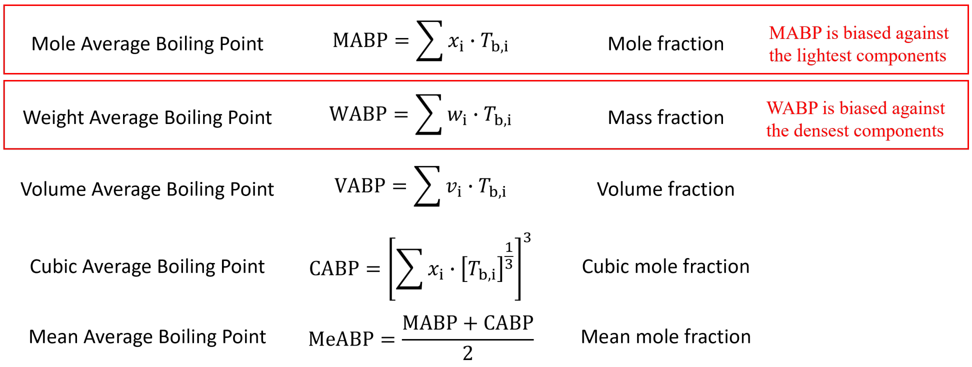

Mole Average Boiling Point	$\mathrm{MABP} = \sum x_\mathrm{i} \cdot T_\mathrm{b,i}$	Mole fraction	MABP is biased against the lightest components
Weight Average Boiling Point	$\mathrm{WABP} = \sum w_\mathrm{i} \cdot T_\mathrm{b,i}$	Mass fraction	WABP is biased against the densest components
Volume Average Boiling Point	$\mathrm{VABP} = \sum v_\mathrm{i} \cdot T_\mathrm{b,i}$	Volume fraction	
Cubic Average Boiling Point	$\mathrm{CABP} = \left[\sum x_\mathrm{i} \cdot [T_\mathrm{b,i}]^{\frac{1}{3}}\right]^3$	Cubic mole fraction	
Mean Average Boiling Point	$\mathrm{MeABP} = \dfrac{\mathrm{MABP} + \mathrm{CABP}}{2}$	Mean mole fraction	

Figure 8: Summary of possible mixing rules for the surrogate normal boiling temperature calculation.

as shown in eq.(10) for mixtures with molecular weight (MW) between 70 and 300 $\mathrm{g\,mol^{-1}}$. This empirical law uses as input parameters the molecular weight and specific gravity or relative density (SG), which is a dimensionless quantity defined as the ratio of the densities of specific substance and water (at 4 °C, $1000\,\mathrm{kg\,m^{-3}}$).

$$T_\mathrm{b} = 3.76587 \cdot e^{\mathrm{A_{exp}}} \cdot \mathrm{MW}^{\mathrm{b_{MW}}} \tag{10}$$

$$\mathrm{A_{exp}} = (3.7741 \times 10^{-3} \cdot \mathrm{MW} + 2.98404 \cdot \mathrm{SG}4.252\,88 \times 10^{-3} \cdot \mathrm{MW} \cdot \mathrm{SG}) \tag{10a}$$

$$\mathrm{b_{MW}} = (0.40167 \cdot \mathrm{SG} - 1.58262) \tag{10b}$$

As for the surrogate evaporation characterization, a simple computational method based on a mixing rule can be employed. In this context, the variation of the liquid volume fraction of the surrogate with the increase of temperature at constant pressure is referred to as evaporation curve and a method to derive it is presented. To account for the evaporation characteristics of the fuel liquid phase it is important to match the mixture Average Density (AD) and the mixture Average Molecular Weight (AMW). As reported by [3] [86] [85], by selecting pure hydrocarbons that has a low standard deviation from the reference fuel AMW (Average Molecular Weight), it is possible to target MW and density and check the T_b by using the Riazi-Daubert's correlation [88] and compare it to the one of the reference fuel. In addition, it is possible to account for the vapor pressure via a linear by mole average mixing rule [85].

Sooting tendency

The sooting tendency of a fuel depends on the types of hydrocarbon classes present in the mixture. For example, the presence of aromatics [4] leads to a more consistent soot formation since the first ring closure mechanism can be skipped given its presence in the aromatic hydrocarbon. Moreover, the formation of the first ring can be regarded as the limiting rate of the PAHs production onset. For this reason, the presence of aromatics in gasoline is usually limited to less than 34% [3]. Broadly speaking, gasoline consists of branched paraffins (iso- alkanes), cycloparaffins (cycloalkanes), and aromatics (benzene, mostly toluene), and the carbon numbers typically range from C_4 to C_{12}. As for the ignition quality of the mixture, the sooting tendency can be described by an index, and several approaches were proposed in literature. Each surrogate component can be characterized in terms of sooting tendency by experimental measurements of the Smoke Point (SP) [92] [93]. In this type of test, which is historically employed for aircraft engine fuel characterization, the SP is measured as the maximum height of a diffusion flame that can be reached before the flame exhibits a smoking behavior (in which the characteristic sooting wings can be observed [92]). The SP is dependent on the type of test, thus the Threshold Soot Index (TSI) is a better option for the surrogate tendency to produce soot [94] [14]: the sooting tendency is measured on a scale between 0 and 100, whose extremal values are set with reference fuels [94]. An alternative index measured by a more diluted fuel concentration ($\sim$1000 ppm) is the Yield Sooting Index (YSI) [95] [96]. Finally, for oxygenated fuels, the alternative Oxygen Extended Sooting Index (OESI) can be an option [97]. Alternatively, extensive experimental testing was conducted by Aikawa et al. at Honda [98], from which the Honda Particulate Matter Index (PMI) was calculated to provide a correlation between the sooting tendency of the gasoline and the double-bond equivalent between atoms, the weight fraction and the vapor pressure. In this work, the TSI is selected because of several data for the fuel of interest.

2.1.2 Gasoline surrogate for TSI and combustion properties

For gasoline, the target properties are related to the characterization of ignition and combustion (e.g. stoichiometric air-fuel ratio, H/C ratio, octane number) or, in case of a DISI engine, to the evaporation behavior in order to gain insight on the potential formation of liquid film deposits that impact emissions [99]. Several studies effectively attempted the combustion characterization by employing simple surrogates such as Primary Reference Fuels (PRF) or Toluene Reference Fuels (TRF). Since TRFs and PRFs comprise iso-octane, n-heptane, and toluene (this last is absent in PRFs), their mixtures are characterized by a relatively low normal-boiling temperature ($\sim 110\,^{\circ}\mathrm{C}$), thus they cannot match properly the evaporation behavior of a real gasoline [3] [99] in all engine conditions. However, in this study, the aim is to formulate simple mixtures that can be easily replicated in real experiments.

These mixtures should have an identical RON number and very stark differences in the TSI, and this is achieved by varying the aromatic content, without neglecting the miscibility (similar polarity of the components) and easy access to these solvents for the real experiments. The target $\mathrm{TSI}_{\mathrm{target}}$ values (6.50, 17.5, and 28.5) are set to achieve stark differences (~10 points) for keeping the possibility open for the extension of this first combustion investigation to the emission modelling. The surrogates, whose properties are summarized in Table 5, were formulated solving a system of equations with constraints over the toluene content to obtain different TSI values (eq.11), target RON of 95 for typical European gasoline [3] (eq.12), and the knock sensitivity (KS) ranging from 0 to 10 (eq.13).

Table 5: Properties of the three gasoline surrogates employed in this study.

Property	**PRF95**	**TRF30**	**TRF60**
α_{st}	15.05	14.61	14.14
LHV, $\mathrm{MJ\,kg^{-1}}$	40.764	41.984	43.391
RON	95	95	95
MON	95	90	85
KS	0	5	10
TSI	6.50	17.56	28.62
C_7H_8 mol%	0	30.30	60.61
C_7H_{16} mol%	5	11.06	17.12
C_8H_{18} mol%	95	58.64	22.27
ρ, $\mathrm{kg\,m^{-3}}$	689.70	728.50	779.04
T_{b}, K	372.3	375.5	379.1

The constraints over the surrogate properties are derived from linear by mole mixing rules, similarly to well established previous works [84] [78] [14].

$$\mathrm{TSI}_{\text{target}} = x_{\text{Tol.}} \cdot \mathrm{TSI}_{\text{Tol.}} + x_{\text{N-hept.}} \cdot \mathrm{TSI}_{\text{N-hept.}} + x_{\text{Iso-oct.}} \cdot \mathrm{TSI}_{\text{Iso-oct.}} \tag{11}$$

$$\mathrm{RON}_{\text{target}} = x_{\text{Tol.}} \cdot \mathrm{RON}_{\text{Tol.}} + x_{\text{N-hept.}} \cdot \mathrm{RON}_{\text{N-hept.}} + x_{\text{Iso-oct.}} \cdot \mathrm{RON}_{\text{Iso-oct.}} \tag{12}$$

$$\mathrm{MON}_{\text{target}} = x_{\text{Tol.}} \cdot \mathrm{MON}_{\text{Tol.}} + x_{\text{N-hept.}} \cdot \mathrm{MON}_{\text{N-hept.}} + x_{\text{Iso-oct.}} \cdot \mathrm{MON}_{\text{Iso-oct.}} \tag{13}$$

These three equations are the constraints for the determination of the proportions of each component of the TRF mixture, expressed as the mole fraction of each component ($x_{\text{Tol.}}$, $x_{\text{N-hept.}}$, $x_{\text{Iso}-\text{oct.}}$). The target KS is achieved by fixing $\mathrm{RON}_{\text{target}}$ and varying the $\mathrm{MON}_{\text{target}}$. Since RON and TSI are the main target properties, the matching of the evaporation of real gasoline is neglected since it cannot be represented properly by the use of TRF surrogates, since the normal boiling temperature is $\sim 100\,^{\circ}\mathrm{C}$, whereas the presence of heavier compounds in several types of commercial gasoline results in higher boiling points [3].

2.2 Multiphase surrogate modelling in CFD codes

In these paragraphs, a numerical comparison between two approaches for modelling TRF surrogates in CFD engine simulation is discussed. More specifically, the multi-component and the lumped approaches are compared: the former models the surrogate fuel as a mixture of three components, and all the mixing rules and evaporation are demanded by the solver; the latter models it as a single-component mixture with equivalent properties. When the soot formation in GDI engine is investigated, it can be computationally expensive, especially when particle mass, number, and size distribution are to be forecasted with the use of articulated models. An alternative to qualitatively predict which surrogate fuel or operational parameters are yielding a more accentuated soot formation can be the use of the spatial distribution of TSI before the spark. Soot formation heavily depends on the chemical and physical characteristics of the fuel, and based on the cell-wise value of TSI, the sooting tendency can be further characterized in engine simulations. More specifically, the a priori investigation of the factors influencing particulate onset in GDI engines can be explored by the spatial distribution of the TSI employing a gasoline representative surrogate. The use of surrogate fuels is a practical approach to cope with the complex chemical nature of gasoline both in CFD and chemical kinetics simulations. Although they poorly mimic the evaporation properties of a real gasoline, TRFs are broadly adopted to match combustion-relevant properties of real fuels. In this study, the TSI spatial distribution in the fluid domain is investigated for three surrogates characterized by an increased content of toluene (0 mol%, 30 mol%, 60 mo%). Sooting tendency is linked to charge stratification (local air/fuel ratio) and to the TSI values calculated with a linear by mole mixing rule. The aim is to evaluate the pre-spark values of these quantities to gauge the potential sooting tendency, and the three formulated surrogates with increasing TSI values are employed for testing. TSI spatial distribution is linked to charge stratification, which in turn may be susceptible to the Lagrangian multi-phase modelling, and to the SOI (early injection timing can yield a more homogeneous charge). This last can be described with two approaches: a multi-component approach and a single-component one, this last driven by a high-fidelity lumped modelling of the surrogate properties for both liquid and vapor phases.

2.2.1 Lagrangian multiphase approaches: lumped and multi-component

Of particular interest is the effect of the Lagrangian multiphase approach on fuel evaporation, which depends on the equilibrium at the liquid-vapor interface. The phase change equilibrium can be characterized by using either a simple Raoult's law or a more sophisticated description, as the one provided by the UNIQUAC Functional-group Activity Coefficients approach (UNIFAC) [100]. The latter relies on the use of activity coefficients γ_i to characterize the partial pressure of each component i at the liquid-vapor interface, and the properties of each fuel molecule are calculated as the sum of each functional group contribution. The activity coefficients γ_i are determined based on two types of contributions which are influenced by the size of the molecule and by the molecular interactions. The partial pressure of each component at the liquid-vapor interface $p_\mathrm{vi,s}$ is reckoned with eq.(14) for Raoult's law, and with eq.(15) for the UNIFAC model: x_i is the mole fraction, $p^0_\mathrm{vi,s}$ is the saturation pressure of the ith component in the liquid mixture.

$$p_\mathrm{vi,s} = x_\mathrm{i} \cdot p^0_\mathrm{vi,s} \tag{14}$$

$$p_\mathrm{vi,s} = \gamma_\mathrm{i} \cdot x_\mathrm{i} \cdot p^0_\mathrm{vi,s} \tag{15}$$

Since UNIFAC model accounts for the molecular interaction, it provides a more reliable description than the Raoult's law, especially if the surrogate components are very different in nature, like the case of oxygenated compounds and hydrocarbons. However, in the case of TRF, stark differences should not be present for evaporation. As an alternative to the multi-component approach, lumping all the fuel components into a single representative one can be an option. The properties are calculated from those of each hydrocarbon using mixing rules, from viscosity to heat of vaporization, for both liquid and vapor phases. To test the efficacy of the lumped-single-component strategy from the perspective of evaporation, charge stratification, TSI spatial distribution, high-fidelity properties are derived for each blend to provide a complete description of both liquid and vapor phase properties as a temperature-dependent description reckoned with mixing rules summarized in Figure 9.

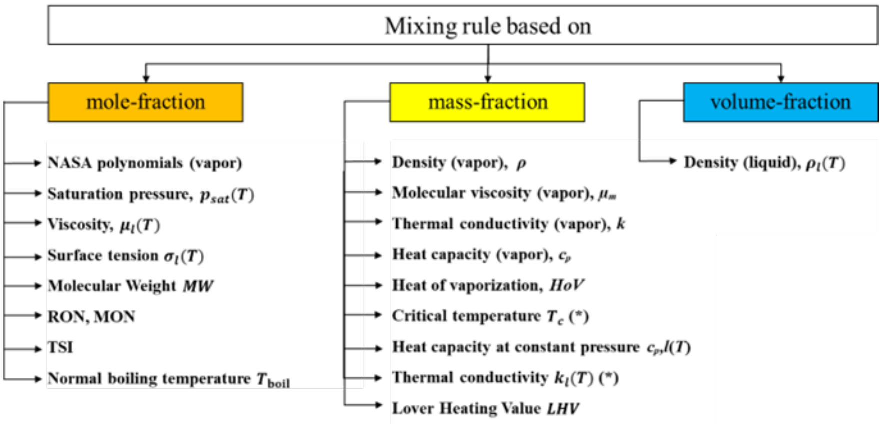

Figure 9: Schematic representation of the mixing rules adopted to calculate surrogate properties. Linear or not by mole, mass, or volume fraction mixing rules for each of the gas and liquid phase

As for the gaseous phase, the NASA polynomials (eq.(16)-(17)-(18)) of the TRFs are calculated using a mole-fraction linear mixing rule and the results (Figure 10 and Figure 11) provide a description of the thermal properties of the vapor phase.

$$\frac{c_p}{\mathrm{R}} = \mathrm{a}_0 + \mathrm{a}_1 \cdot T + \mathrm{a}_2 \cdot T^2 + \mathrm{a}_3 \cdot T^3 + \mathrm{a}_4 \cdot T^4 \tag{16}$$

$$\frac{h}{\mathrm{R}T} = \mathrm{a}_0 + \mathrm{a}_1 \cdot \frac{T}{2} + \mathrm{a}_2 \cdot \frac{T^2}{3} + \mathrm{a}_3 \cdot \frac{T^3}{4} + \mathrm{a}_4 \cdot \frac{T^4}{5} + \frac{\mathrm{a}_5}{T} \tag{17}$$

$$\frac{s}{\mathrm{R}} = \mathrm{a}_0 \cdot \ln T + \mathrm{a}_1 \cdot \frac{T}{2} + \mathrm{a}_2 \cdot \frac{T^2}{3} + \mathrm{a}_3 \cdot \frac{T^3}{4} + \mathrm{a}_4 \cdot \frac{T^4}{5} + \mathrm{a}_6 \tag{18}$$

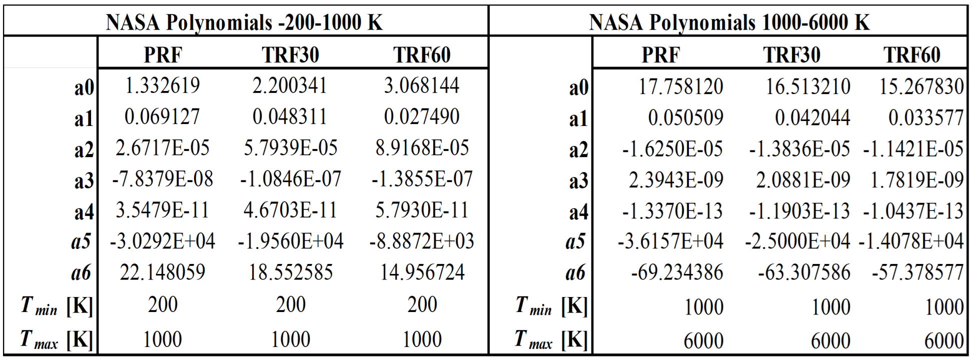

	NASA Polynomials -200-1000 K				NASA Polynomials 1000-6000 K		
	PRF	TRF30	TRF60		PRF	TRF30	TRF60
a0	1.332619	2.200341	3.068144	a0	17.758120	16.513210	15.267830
a1	0.069127	0.048311	0.027490	a1	0.050509	0.042044	0.033577
a2	2.6717E-05	5.7939E-05	8.9168E-05	a2	-1.6250E-05	-1.3836E-05	-1.1421E-05
a3	-7.8379E-08	-1.0846E-07	-1.3855E-07	a3	2.3943E-09	2.0881E-09	1.7819E-09
a4	3.5479E-11	4.6703E-11	5.7930E-11	a4	-1.3370E-13	-1.1903E-13	-1.0437E-13
a5	-3.0292E+04	-1.9560E+04	-8.8872E+03	*a5*	-3.6157E+04	-2.5000E+04	-1.4078E+04
a6	22.148059	18.552585	14.956724	*a6*	-69.234386	-63.307586	-57.378577
T_{min} [K]	200	200	200	T_{min} [K]	1000	1000	1000
T_{max} [K]	1000	1000	1000	T_{max} [K]	6000	6000	6000

Figure 10: NASA polynomial coefficients for the surrogates.

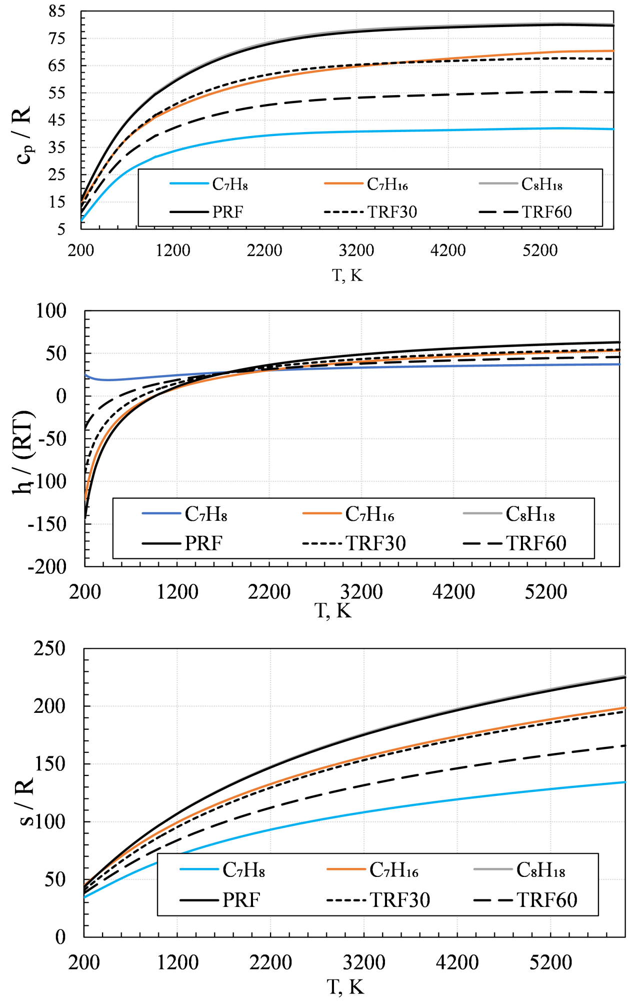

Figure 11: Plot of the results of NASA polynomials: normalized values of specific heat (top), enthalpy (center), and entropy (bottom).

The liquid phase properties $F_{\mathrm{j,mix}}$ are derived as monotone functions of temperature in the form of $F_{\mathrm{j,mix}} = \sum_{j=1}^{m} (\mathrm{a_j} T^{\mathrm{j}})$, where a_{j} are the fitting coefficients (Figure 12) derived in this work. These properties are given as input to the CFD code via Fortran user subroutines. The properties of each component are retrieved from the NIST database [101] and the final surrogate properties are all derived using a linear mixing rule (Figure 9), exceptions made for the liquid viscosity μ_{l}. As reported by [88] [86], the estimation of viscosity for liquid hydrocarbon mixtures can yield inaccurate results, if a linear mixing rule is employed. Another option can be the relation used by [86], which successfully employed the Grunberg-Nissan equation (eq.(19)), whereas in this study the method proposed by [88] is adopted: a nonlinear by mole mixing rule provided in eq.(20). The pure component viscosity is reckoned in the first place as a function of temperature as in eq.(20), where A, B, C, D, E are tabulated constants [88].

$$\mu_{\mathrm{l,mix}} = \left(\sum_{i=1}^{N} x_{\mathrm{i}} \cdot \mu_{\mathrm{l,i}}^{(1/3)} \right)^{3} \tag{19}$$

$$\mu_{\mathrm{l}} = 1000 \cdot \exp \mathrm{A} + \frac{\mathrm{B}}{T} + \mathrm{C} \ln T + D \cdot T^{\mathrm{E}} \tag{20}$$

The saturation pressure is another key property for phase transition and in this study, it is reckoned by a linear by mole mixing rule [86]. Each component saturation pressure is derived as a temperature-dependent function from NIST database [101]. The final saturation pressure for the TRFs is fitted to describe the vapor pressure with the Antoine's Equation eq.(21).

$$\log_{10} p_{\mathrm{sat}}(T) = \mathrm{A} - \frac{\mathrm{B}}{\mathrm{C} + T} \tag{21}$$

The final coefficients, parameters, and the temperature-dependent up to the critical temperature (from eq.(22) to (27)).

$$\mu_{\mathrm{l}}(T) = \mathrm{a_0} + \mathrm{a_1} \cdot T + \mathrm{a_2} \cdot T^2 + \mathrm{a_3} \cdot T^3 + \mathrm{a_4} \cdot T^4 + \mathrm{a_5} \cdot T^5 + \mathrm{a_6} \cdot T^6 \tag{22}$$

$$\sigma(T) = \mathrm{a}_0 + \mathrm{a}_1 \cdot T + \mathrm{a}_2 \cdot T^2 + \mathrm{a}_3 \cdot T^3 \tag{23}$$

$$\rho_\mathrm{l}(T) = \mathrm{a}_0 + \mathrm{a}_1 \cdot T + \mathrm{a}_2 \cdot T^2 \tag{24}$$

$$HoV(T) = \mathrm{a}_0 + \mathrm{a}_1 \cdot T + \mathrm{a}_2 \cdot T^2 \tag{25}$$

$$c_{p,\mathrm{l}}(T) = \mathrm{a}_0 + \mathrm{a}_1 \cdot T + \mathrm{a}_2 \cdot T^2 \tag{26}$$

$$k_\mathrm{l}(T) = \mathrm{a}_0 + \mathrm{a}_1 \cdot T \tag{27}$$

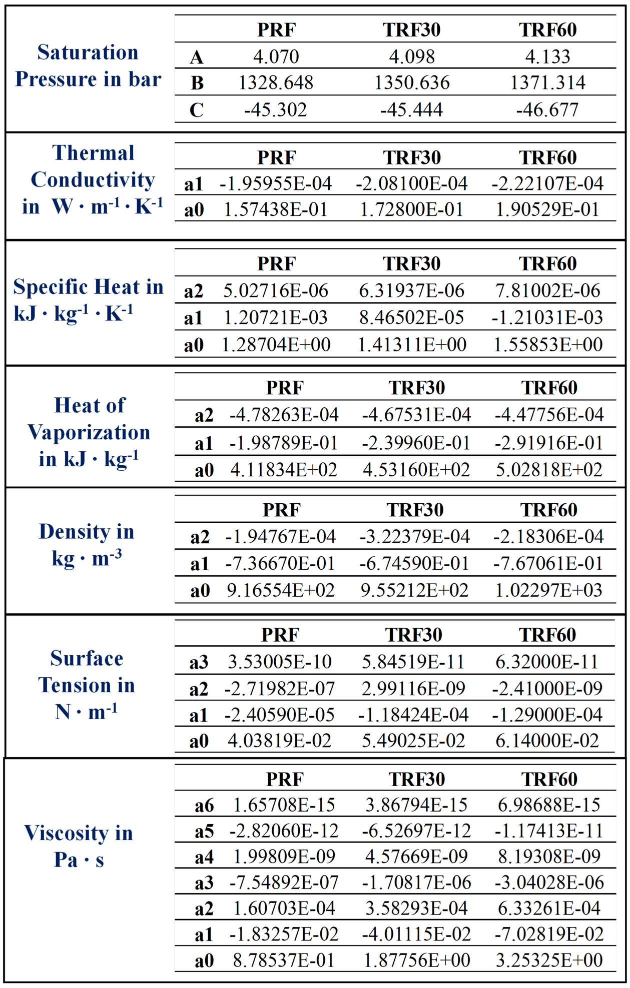

Saturation Pressure in bar

	PRF	TRF30	TRF60
A	4.070	4.098	4.133
B	1328.648	1350.636	1371.314
C	-45.302	-45.444	-46.677

Thermal Conductivity in W · m^{-1} · K^{-1}

	PRF	TRF30	TRF60
a1	-1.95955E-04	-2.08100E-04	-2.22107E-04
a0	1.57438E-01	1.72800E-01	1.90529E-01

Specific Heat in kJ · kg^{-1} · K^{-1}

	PRF	TRF30	TRF60
a2	5.02716E-06	6.31937E-06	7.81002E-06
a1	1.20721E-03	8.46502E-05	-1.21031E-03
a0	1.28704E+00	1.41311E+00	1.55853E+00

Heat of Vaporization in kJ · kg^{-1}

	PRF	TRF30	TRF60
a2	-4.78263E-04	-4.67531E-04	-4.47756E-04
a1	-1.98789E-01	-2.39960E-01	-2.91916E-01
a0	4.11834E+02	4.53160E+02	5.02818E+02

Density in kg · m^{-3}

	PRF	TRF30	TRF60
a2	-1.94767E-04	-3.22379E-04	-2.18306E-04
a1	-7.36670E-01	-6.74590E-01	-7.67061E-01
a0	9.16554E+02	9.55212E+02	1.02297E+03

Surface Tension in N · m^{-1}

	PRF	TRF30	TRF60
a3	3.53005E-10	5.84519E-11	6.32000E-11
a2	-2.71982E-07	2.99116E-09	-2.41000E-09
a1	-2.40590E-05	-1.18424E-04	-1.29000E-04
a0	4.03819E-02	5.49025E-02	6.14000E-02

Viscosity in Pa · s

	PRF	TRF30	TRF60
a6	1.65708E-15	3.86794E-15	6.98688E-15
a5	-2.82060E-12	-6.52697E-12	-1.17413E-11
a4	1.99809E-09	4.57669E-09	8.19308E-09
a3	-7.54892E-07	-1.70817E-06	-3.04028E-06
a2	1.60703E-04	3.58293E-04	6.33261E-04
a1	-1.83257E-02	-4.01115E-02	-7.02819E-02
a0	8.78537E-01	1.87756E+00	3.25325E+00

Figure 12: The A, B, C coefficients of Antoine's equation and $\mathrm{a_j}$ coefficients of the other liquid phase properties equations for the three surrogates.

2.3 Flame propagation and laminar burning velocity

In this section, the methodology to derive ready-to-use correlation is proposed as the state of the art along with extensions and a novel approach for the ammonia-hydrogen blends. The proposed correlations are meant to be used in CFD flamelet combustion model, and they can be easily implemented with a user-defined routine. When used in the CFD code, they are employed to reckon the laminar flame speed, and then the turbulent one from it, whereas the data employed for the fitting are stemming from chemical kinetic simulations in which the laminar burning velocity is calculated. The correlations represent, in fact, the *laminar burning velocity*, since they are a function of pressure, unburnt temperature, dilution, and equivalence ratio since they are calculated in a quiescent reactor (gas velocity is zero), *whereas* the *laminar flame speed* comprises the contribution of the laminar burning velocity and the gas flow velocity. However, sometimes text, the expression laminar flame speed is used for the correlations since they are still representing the laminar burning velocity, but the code is employing them as laminar flame speed [102][103].

2.3.1 Combustion regimes and flamelet models

Before describing the methodology and its extension to provide a correlations to model the flame propagation in CFD codes, the background of the state of art for CFD combustion models for engine application for flamelet regime is provided to explain how the flamelet combustion model can use these correlations derived from data fitting over an extensive database of laminar burning velocities. First, the combustion regimes are described, including the flamelet regime and its importance in this framework, and how the proposed methodology fits as a ready-to-use tool for modelling flame propagation for any time of fuel. As for turbulent flames, the definition of the combustion regime can be done using the Borghi-Peters diagram [60]. The most famous version of this diagram is for turbulent premixed flames, however, there is a version for diffusive flames as well.

Since this study focuses on predominantly premixed flames simulated with RANS approach for turbulence, the combustion regimes are presented referring to the classical diagram (Figure 13), where a 2-D chart with the non-dimensional velocity on the y-axis (represented as the ratio of the turbulent velocity fluctuation v' and the laminar flame speed s_L) and the turbulent length scale l and laminar flame thickness l_F ratio on the x-axis.

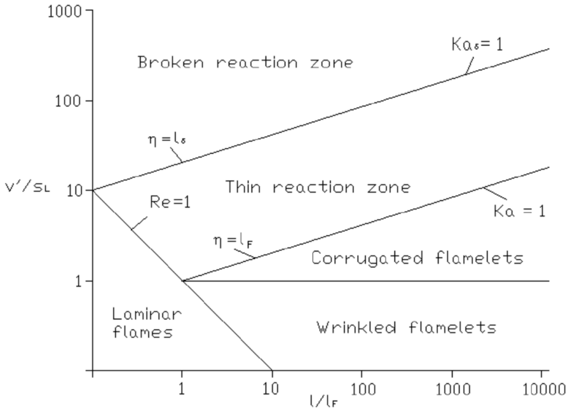

Figure 13: Turbulent premixed combustion regimes [60].

This diagram identifies five combustion regimes, one for laminar and four for turbulent:

- *laminar combustion* (bottom-left corner)
- turbulent combustion:
    - *Corrugated flames*: even the smallest turbulent length scale does not enter the reaction zone, and the only way turbulence interacts with the flame is by producing a corrugation of the reaction zone. The corrugated flame structures have an increased surface area. This area of the reaction is increased, resulting in faster combustion than the one that can be achieved by the flat laminar flame front. In this case, a purely kinematic interaction is established between the turbulent eddies and the advancing flame front (a limited region where the reactions take place). The turnover velocity of the large eddies exceeds the laminar

flame speed s_{L}, and these eddies will produce a corrugation of the flame front.

- *Wrinkled flames*: the interaction between the turbulent eddies and the flame front is also purely kinematic, in the same fashion of the corrugated flames. The borderline between wrinkled and corrugated flame regime can be drawn using the Gibson length scale $l_{\mathrm{G}} = {}^{(s_{\mathrm{L}})^3}/_{\varepsilon}$, where s_{L} is the laminar flame speed, and ε is the turbulent dissipation rate. The Gibson length scale is the lower cutoff scale of the scalar spectrum function in the corrugated flamelet regime, and this limit occurs if the eddy turnover velocity is equal to the laminar burning velocity. Thus, the wrinkled flamelet interacts only with eddies characterized by turnover velocity lower than the laminar flame speed.
- *Thin reaction zone*: in this case, the eddies belonging to the Kolmogorov length scale l_{K}, are smaller than the flame thickness l_{F} thus they can enter the reactive-diffusive flame structure
- *Broken or distributed reaction zone*: in this case, the Damköhler Number Da is equal or bigger than unity. As a matter of fact, the Kolmogorov-length scale is smaller than the inner layer thickness of the flame front, thus the smallest eddies can enter the reaction zone. As a consequence, an enhanced heat loss to the preheat zone leads to a temperature drop and the decrease of radical species concentrations, thus the chemistry breaks down locally. If this phenomenon is intense enough, the flame may be extinguished.

As for the SI engines, the partially or fully premixed turbulent combustion falls into the flamelet regime, which is characterized by corrugated/wrinkled flame structures. Turbulence induces random fluctuations in the flame structure, and the ensemble average reaction zone area (A_{flamelet}) is the “turbulent flame brush” (Figure 14), thus the turbulent flame description depends both on the thermochemical status and on the local flow structure, unlike the laminar burning velocity, which is affected only by the first set of factors. Several turbulent flame speed s_T models propose a description base on the simplified assumption that s_T can be expressed as function of s_L, starting from the observation that ${}^{s_\mathrm{T}}/_{s_\mathrm{L}} = {}^{A_\mathrm{flamelet}}/_{\bar{A}}$.

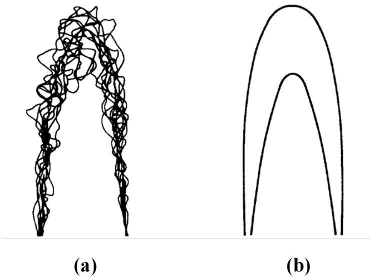

Figure 14: For RANS simulations: superposition of the instantaneous reaction fronts for different times (a); time-averaged view of the same flame front (turbulent flame "brush") (b) [60].

The most relevant parameters for the correlations dervied in the next paragraphs are:

- unburnt temperature T_u
- pressure p
- local equivalence ratio Φ or AFR α
- dilution (e.g. EGR% or its mass fraction y_EGR)

In light of these considerations, it is possible to use chemical kinetics simulations to derive values of laminar burning velocity for several variations of these four parameters (p, T_u, Φ, and EGR%), and then proceed with a fitting procedure to extract a correlation that can be generally implemented in several codes by user subroutine. This procedure is tested and extended to TRF surrogates, then it is applied to carbon-neutral ammonia-hydrogen blends, and a novel approach is proposed in this with a five-parameters correlation instead.

2.3.2 Correlation for hydrocarbon-based fuels: TRF surrogates

2.3.2.1 Hydrocarbon specific correlation The aim is to derive a correlation of the laminar flame speed for each surrogate component (toluene, n-heptane, and iso-octane) and to employ them in mixing rules to predict the value of the final surrogate. By virtu of the mixing rule, the correlations derived in this thesis apply to all the possible arrangements of the TRF surrogate components. Thus, the advantage is that the ∼1420 chemical kinetic simulations of 1D flamelet can be carried out only once for each component, and the results can be employed for any possible change in the component proportion without repeating the process of ad-hoc chemical kinetics simulations. Moreover, this type of surrogate is particularly suitable for mixing rules since the molecular weights are very similar. Consequently, linear by mass/volume/mole fraction rules will yield similar results as discussed. The goal is to have a vast database of laminar flame speed values covering the possible engine conditions for part-to -medium loads.

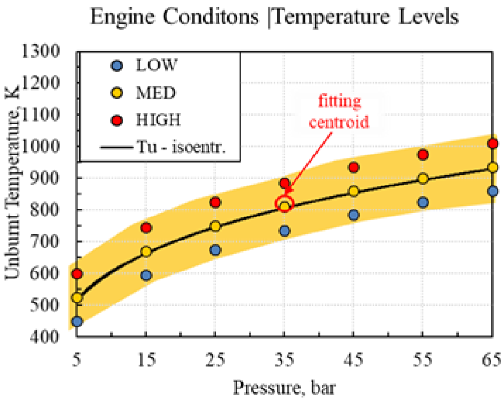

Figure 15: Temperature levels on pressure-unburnt temperature chart for the engine conditions of interest.

The operational conditions of interest are the in-cylinder values of pressure and unburnt temperatures: the former is taken from experimental data as described in the corresponding results section. The unburnt temperature is reckoned from the pressure by using an isentropic thermodynamic process after spark time to reckon the next value of unburnt temperature as $T_{\mathrm{u,i}} = T_{\mathrm{u,i-1}} \cdot ({}^{p_\mathrm{i}}/_{p_{\mathrm{i}-1}})^{\gamma\,-\,{}^{1}/_{\gamma}}$ where

γ is the ratio of specific heats $\gamma = {c_\mathrm{p}}/{c_\mathrm{v}}$ and it is set equal to 1.3, given this engine conditions. The resulting engine conditions are depicted in Figure 15: the yellow area is the validity range of the derived correlations, and it is defined for equivalence ratio values $0.4 \leq \Phi \leq 2.0$ and for dilution of the mixture expressed in EGR (Exhaust Recirculation Gas) from 0% to 30%. The fitting technique was improved for better accuracy for the lean and rich branches by Del Pecchia et al. [104] and it is applied in this work to get a correlation valid for a wide range of equivalence ratios. This technique consists of splitting the fitting into three equations: one for the central branch (eq.(28)), one for the lean (eq.(29)) and one for the rich (eq.(30)) side.

$$s_\mathrm{L}(\Phi) = \sum_{i=0}^{5} \left(\mathrm{a_i} \cdot (\ln(\Phi))^\mathrm{i} \cdot \left(\frac{T_\mathrm{u}}{T_0}\right)^{\sum_{i=0}^{5} \mathrm{b_i} \cdot (\ln(\Phi))^\mathrm{i}} \cdot \left(\frac{p_\mathrm{u}}{p_0}\right)^{\sum_{i=0}^{5} \mathrm{c_i} \cdot (\ln(\Phi))^\mathrm{i}} \right) \tag{28}$$

$$s_\mathrm{L}^\mathrm{lean}\,(\Phi) = s_\mathrm{L}^\mathrm{ref}\,(\Phi|_{0.7}) \cdot \frac{\left(\mathrm{w_T}\ \mathrm{TSF}^{\ \mathrm{lean}}\,(\Phi) + \mathrm{w_P}\,\mathrm{PSF}^\mathrm{lean}\,(\Phi)\right.}{\mathrm{w_T} + \mathrm{w_p}} \tag{29}$$

$$s_\mathrm{L}^\mathrm{rich}(\Phi) = s_\mathrm{L}^\mathrm{ref}\,(\Phi|_{1.4}) \cdot \frac{\left(\mathrm{w_T}\mathrm{TSF}^\mathrm{rich}(\Phi) + \mathrm{w_P}\mathrm{PSF}^\mathrm{rich}\,(\Phi)\right)}{\mathrm{w_T} + \mathrm{w_p}} \tag{30}$$

The coefficients m and q for rich and lean sides are polynomial expressions of fitted values of laminar burning velocities in these branches expressed as fitting coefficients $\mathrm{q_i}$ and $\mathrm{m_i}$, as shown in eqs. (31), (32) for lean branch, and eqs. (33), (34) for the rich one.

$$\mathrm{m_j^{lean}}\,(\Phi) = \mathrm{m_{2,j}^{lean}} \cdot (\Phi)^2 + \mathrm{m_{1,j}^{lean}} \cdot (\Phi) + \mathrm{m_{0,j}^{lean}} \tag{31}$$

$$\mathrm{q_j^{lean}}\,(\Phi) = \mathrm{q_{2,j}^{lean}} \cdot (\Phi)^2 + \mathrm{ql_{1,j}^{lean}} \cdot (\Phi) + \mathrm{ql_{0,j}^{lean}} \tag{32}$$

$$\mathrm{m_j^{rich}}\,(\Phi) = \mathrm{ml_{4,j}^{rich}} \cdot (\Phi)^4 + \mathrm{ml_{3,j}^{rich}} \cdot (\Phi)^3 + \mathrm{ml_{2,j}^{rich}} \cdot (\Phi)^2 + \mathrm{ml_{1,j}^{rich}} \cdot (\Phi) + \mathrm{ml_{0,j}^{rich}} \tag{33}$$

$$\mathrm{q_j^{rich}}\,(\Phi) = \mathrm{ql_{4,j}^{rich}} \cdot (\Phi)^4 + \mathrm{ql_{3,j}^{rich}} \cdot (\Phi)^3 + \mathrm{ql_{2,j}^{rich}} \cdot (\Phi)^2 + \mathrm{ql_{1,j}^{rich}} \cdot (\Phi) + \mathrm{ql_{0,j}^{rich}} \tag{34}$$

For the lean and rich branches, the procedure requires also pressure and temperature scaling factors (PSF and TFS respectively). The former is calculated from the coefficients of the polynomial fit of the normalized values of the laminar burning velocities to account for the several pressure levels as shown in eq.n (35) and (36). The values of Φ_{min} and Φ_{max} are the limit values of the equivalence ratio for the central fitting (0.7 and 1.4 respectively), whereas $\Phi_{\mathrm{min,limit}}$ and $\Phi_{\mathrm{max,limit}}$ are relating to absolutes limits, of the lean side (0.4) and of the rich side (2.0) respectively.

$$\mathrm{PSF}^{\mathrm{lean}}\left(\Phi\right)=\frac{\mathrm{l}_3^{\mathrm{lean}}\ \left|\Phi-\Phi_{\mathrm{min}}\right|^3+\mathrm{l}_2^{\mathrm{lean}}\ \left|\Phi-\Phi_{\mathrm{min}}\right|^2+\mathrm{l}_1^{\mathrm{lean}}\ \left|\Phi-\Phi_{\mathrm{min}}\right|+\mathrm{l}_0^{\mathrm{lean}}}{l_0}$$
$$\left(\mathrm{m}''_{\mathrm{lean}}\cdot\frac{p-p_{\mathrm{ref,fit}}}{p_{\mathrm{ref,fit}}}\cdot\frac{\left|\Phi-\Phi_{\mathrm{min}}\right|}{\left|\Phi_{\mathrm{min,limit}}\ -\Phi_{\mathrm{min}}\right|}\right) \tag{35}$$

$$\mathrm{PSF}^{\mathrm{rich}}\left(\Phi\right)=\frac{\mathrm{l}_3^{\mathrm{rich}}\ \left|\Phi-\Phi_{\mathrm{max}}\right|^3+\mathrm{l}_2^{\mathrm{rich}}\ \left|\Phi-\Phi_{\mathrm{max}}\right|^2+\mathrm{l}_1^{\mathrm{rich}}\ \left|\Phi-\Phi_{\mathrm{max}}\right|+\mathrm{l}_0^{\mathrm{rich}}}{l_0}$$
$$\cdot\left(\mathrm{m}''_{\mathrm{rich}}\cdot\frac{p-p_{\mathrm{ref,fit}}}{p_{\mathrm{ref,fit}}}\cdot\frac{\left|\Phi-\Phi_{\mathrm{max}}\right|}{\left|\Phi_{\mathrm{max,limit}}\ -\Phi_{\mathrm{max}}\right|}\right) \tag{36}$$

Similarly, a fitting procedure is performed to extract the TFS, to account for the scaling of laminar burning velocity for each temperature level (low, medium, high) as shown in eq. (37) and (38).

$$\mathrm{TFS}_{\mathrm{j}}^{\mathrm{lean}}\ \left(\Phi,T_{\mathrm{u}}\right)=\mathrm{m}_{\mathrm{j}}^{\mathrm{lean}}\left(\Phi\right)\cdot\frac{T_{\mathrm{u}}}{T_{\mathrm{ref}}}+\mathrm{q}_{\mathrm{j}}^{\mathrm{lean}}\left(\Phi\right) \tag{37}$$

$$\mathrm{TFS}_{\mathrm{j}}^{\mathrm{rich}}\ \left(\Phi,T_{\mathrm{u}}\right)=\mathrm{m}_{\mathrm{j}}^{\mathrm{rich}}\left(\Phi\right)\cdot\frac{T_{\mathrm{u}}}{T_{\mathrm{ref}}}+\mathrm{q}_{\mathrm{j}}^{\mathrm{rich}}\left(\Phi\right) \tag{38}$$

The reference values of pressure $p_{\mathrm{ref,fit}}$ and temperature $T_{\mathrm{ref,fit}}$ are the reference values for the rich/lean sides of the fitting, hence different from the one relating to the central fit (p_0 , and T_0). Finally, the TFS and PSF are weighted through two coefficients $\mathrm{w_T}$ and $\mathrm{w_p}$, whose sum is indicated as $\mathrm{w_{tot}}$.

On a final note, in all the correlation expressions, S.I. units are used, but the predicted values of laminar flame speeds are in cm/s.

2.3.2.2 Mixing rules for multi-component mixtures Since a multi-component approach is employed, the characterization of the laminar flame speed for each component is modelled via a mixing rule implemented with user coding. One correlation is derived for each constituent via an extensive database of chemical kinetics simulations of one-dimensional freely propagating flame for the following conditions: $450\,\mathrm{K} \leq T_\mathrm{u} \leq 450\,\mathrm{K}$, $5\,\mathrm{bar} \leq p \leq 65\,\mathrm{bar}$, $0.4 \leq \Phi \leq 2.0$, and $0 \leq \mathrm{y}_\mathrm{EGR} \leq 0.3$. The employed chemical kinetics solver is DARSv4.30 licensed by Siemens PLM [105], and the reaction mechanism is the one for gasoline fuel surrogates developed by Creck Modelling Group [106]-[107]-[108].

A further step from the previous methodology [78]is taken in this study and it is suitable for any TRF: the multi-component mixture laminar flame speed $s_\mathrm{L,mix}$ is calculated using a mixing rule, unlike repeating chemical kinetics simulations and fitting procedure any time the TRF composition changes. This approach is advantageous since it enables the final $s_\mathrm{L,mix}$ to be calculated from the already derived correlation of each component without the need to repeat the process (chemical kinetics simulations and fitting procedure) every time the TRF is formulated differently. In general, a mixing rule can be biased towards lighter components (linear-by-mole mixing rules) or biased toward the heavier ones (linear-by-mass mixing rule) [109]. However, in this case, the components are characterized by similar values of molecular weights, thus no stark difference in results should be yielded by the use of different mixing rules. In this study, before the implementation, three types of mixing rules are compared with the respect of the actual values obtained from chemical kinetics simulations (15 bar and 670 K): Le Chatelier [110] mixing rule (eq.(39)), a linear by mole (eq.(40)) [88], and a linear by mass [88] (eq.(41)) mixing rule.

$$s_\mathrm{L,mix} = \sum_i \left(\frac{1}{\frac{x_i}{s_\mathrm{L,i}}} \right) \tag{39}$$

$$s_\mathrm{L,mix} = \sum_i \left(s_{\mathrm{L,i} \cdot x_i} \right) \tag{40}$$

$$s_{\mathrm{L,mix}} = \sum_i \left(s_{\mathrm{L,i}} \cdot y_i\right) \tag{41}$$

The error stemming from the use of each mixing rule with respect of the actual mixture laminar flame speed obtained from chemical kinetic simulation is evaluated in terms of the quadratic error (Figure 16) $\sigma^2 = \left[s_{\mathrm{L,\,data}} - s_{\mathrm{L,mix}}\right]^2$, and by the relative difference in laminar burning velocity (Figure 17) $\Delta s_{\mathrm{L}} = s_{\mathrm{L,\,data}} - s_{\mathrm{L,mix}}$, for which the magnitude of the maximum error is $\sim 0.15\,\mathrm{cm\,s^{-1}}$.

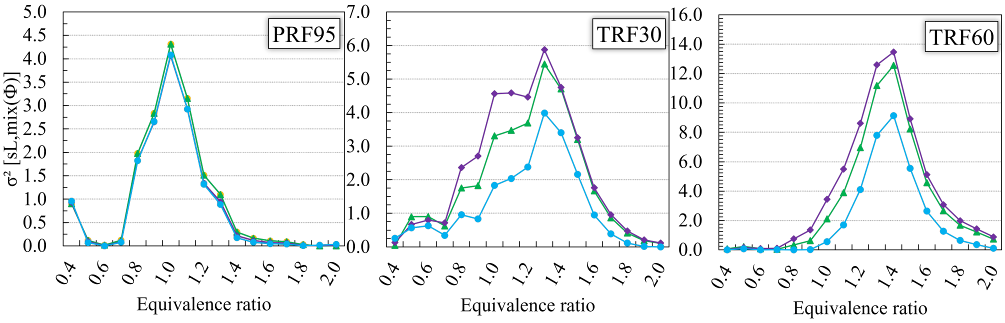

Figure 16: Quadratic error between mixing rule predictions and chemical kinetics results evaluated at a random point (15 bar, 670 K, and EGR 0%).

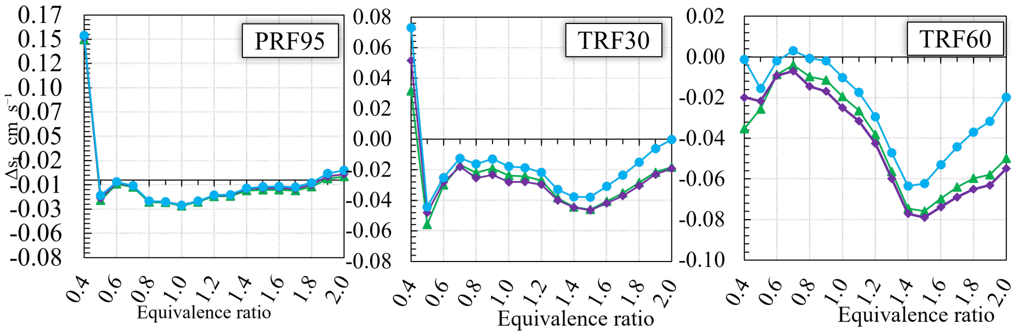

Figure 17: Relative difference of laminar flame speed values of the mixing rule predictions and the chemical kinetic results at a random sample point (15 bar, 670 K, and EGR 0%).

2.3.3 Correlation for carbon-neutral fuels: ammonia-hydrogen blends

2.3.3.1 Chemical kinetics simulations The laminar burning velocity prediction via fitting of chemical kinetics simulation data is achieved using the chemical kinetics solver DARS v4.30[105]. Freely propagating laminar flames are simulated in a one-dimensional reactor using reaction mechanisms, thermodynamics, and transport data derived by Stagni et al. [76].

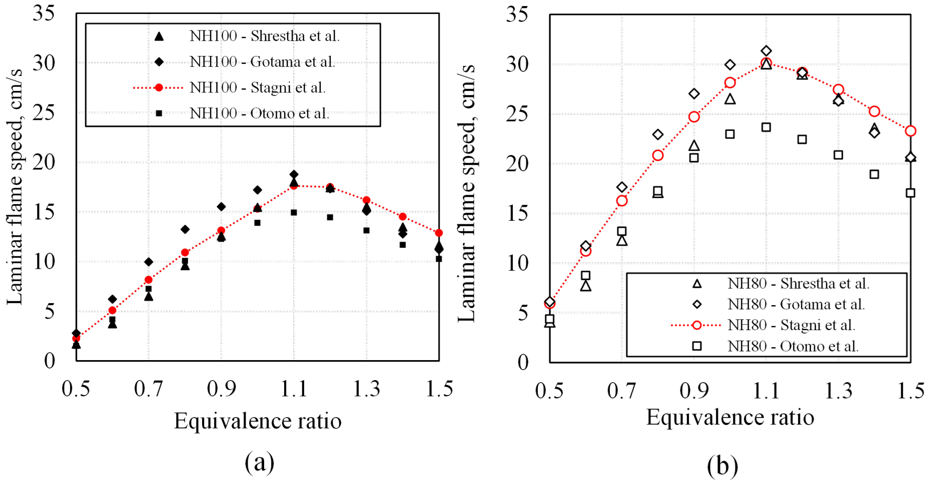

Figure 18: Results with different reaction mechanisms at 450 K and 1 bar for NH100 (a) and NH80 (b).

Although this reaction mechanism has already been validated, a brief comparison with reaction mechanisms proposed by Shrestha [54], Gotama [71], and Otomo [74] is presented for NH100 (100 mol% of NH_3) and NH80 (80 mol% of NH_3) in Figure 18(a) and Figure 18(b) respectively. Simulation results are reported for freely propagating laminar flames at 450 K and 1 bar, with no dilution. Given its fundamental role in the combustion reaction mechanisms of hydrocarbons, H_2 chemical kinetics has been extensively studied, whereas the combustion reactions of NH_3 is under scrutiny only recently. Since NH_3 mechanisms present higher uncertainties and variability, the comparison between reaction mechanisms is carried out for blends in which the NH_3 oxidation chemistry is predominant.

2.3.3.2 Blend-specific correlation with four parameters The fitting procedure adopted in this work was firstly proposed by Brusca et al. [111], further developed and successfully applied to hydrocarbon-based fuels [77] [78]. In the first part of this study, this procedure is applied to carbon-neutral fuels mixtures of H_2 and NH_3 for the derivation of dedicated laminar flame speed correlations by data fitting on an extensive database of laminar burning velocity values obtained from chemical kinetics simulations at engine-like conditions, (Table 6), for differentNH_3/air, H_2/air and NH_3/H_2/air mixtures (Table7).

Table 6: Engine conditions.

p (bar)	40	50	60	70	80	90	100	110	120	130
$T_{\mathrm{u,low}}$(K)	720	752	784	826	848	880	912	944	976	1008
$T_{\mathrm{u,med}}$ (K)	820	852	884	916	948	980	1012	1044	1076	1108
$T_{\mathrm{u,high}}$ (K)	920	952	984	1016	1048	1080	1112	1144	1176	1208

Table 7: Ammonia/hydrogen blends investigated in this study.

Blend	NH100	NH80	NH60	NH40	NH20	NH10	NH0
NH_3 mol%	100	80	60	40	20	10	0
H_2 mol%	0	20	40	60	80	90	100

The laminar flame speed is expressed as a function of pressure, unburnt temperature, and equivalence ratio: $s_{\mathrm{L}} = s_{\mathrm{L}}(p, T_{\mathrm{u}}, \Phi)$. The fitting procedure described in section 2.3.2 is applied to more than 2500 simulated laminar flame speed values (360 for each blend) and exploits two distinct functions depending on the equivalence ratio Φ range to minimize the fitting errors. A fitting procedure for lean to rich mixtures ($0.7 \leq \Phi \leq 1.5$) results in coefficients reported in Appendix B (4) for the calculation of the laminar burning velocity via eq.(28). This poly-logarithmic expression successfully represents the bell-shaped data trend from lean to rich conditions. However, the use of this procedure for an extended range of equivalence ratio values that comprises also ultra-lean conditions would result in increased prediction errors [77]. A different polynomial expression that operates a linear scaling on the pressure and temperature conditions can reduce the error in the ultra-lean range as extensively discussed in [77] [78]. Thus, ultra-lean conditions ($0.4 \leq \Phi < 0.7$) are treated using a dedicated fitting methodology: pressure and temperature scaling factors are derived and employed in the laminar flame speed calculation. Although the functions and the data-fitting techniques differ, the continuity of the polynomial expression is ensured by linking the laminar flame speed value of the lower limit ($\Phi = 0.7$) to the upper limit of the ultra-lean branch of the laminar burning velocity [77]. This scaling procedure is identical to the one described for hydrocarbons for TRF surrogates, In this case, the effectiveness at higher loads and different engine conditions and its reliability are tested in this study for NH_3 and H_2 fuels. The final value of the laminar burning velocity for ultra-lean mixtures is obtained by weighting pressure and temperature scaling factors (PSF and TSF respectively) as described in 2.3.2 and the coefficients are reported in Appendix B (4).

2.3.3.3 Generalized correlation with five parameters

NH_3 is characterized by slow laminar burning velocities, especially if compared to H_2. When blended with H_2, the laminar burning velocity of NH_3/air mixtures considerably increases. The acceleration of the laminar flame speed with the increase of H_2 is related to the H_2.-chemistry chain branching reaction $O_2 + H = OH + O$, which is the most sensitive reaction for NH_3 as well. This reaction sensitivity grows with the increment of H_2, thus the laminar burning velocity accelerates [45].

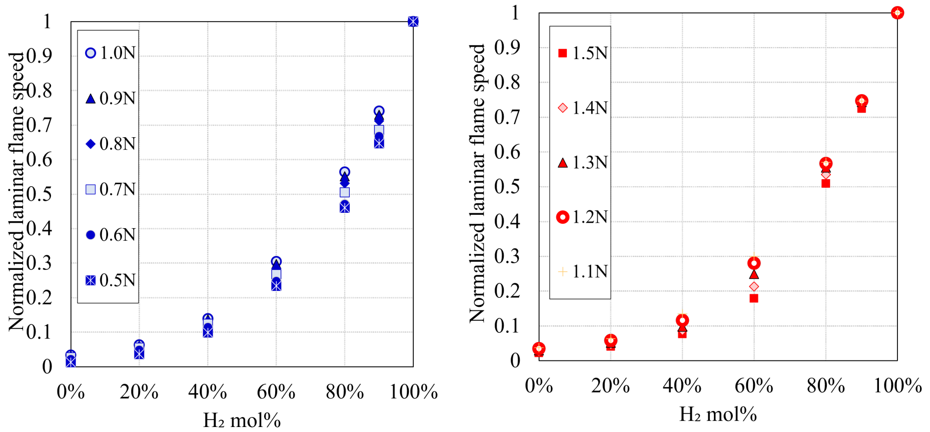

(a) **(b)**

Figure 19: Laminar flame speed values at 400 K and 1 bar for increasing H_2 content (from 0mol% to 100mol%), for ultra-lean to stoichiometric (a) and for rich (b) mixtures.

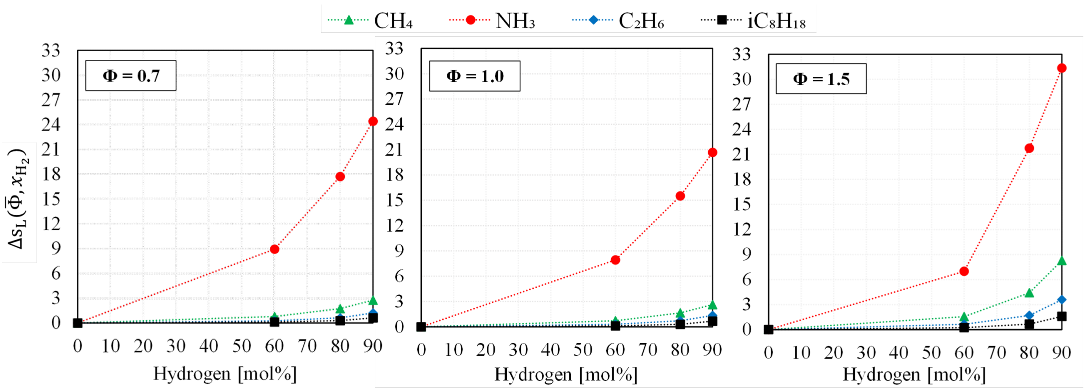

Figure 20: Relative increment of laminar flame speed with increasing H_2 content (chemical kinetics simulations at 400 K and 1 bar)

While blends with scaled levels of dilution (e.g. Exhaust Recirculation Gas EGR) show a linear blending behavior, relatively small amounts of NH_3 have a stronger-than-expected inhibiting effect on flame propagation. In detail, as visible in Figure 19 and 20, the trend of the laminar burning velocity increment with H_2 addition is exponential: the enhancement is limited for low H_2 content, while the growth rate becomes progressively steeper for higher concentrations, and this is partially due to the increased relevance of the H_2-chemistry chain branching reaction [45] and to its relatively high reactivity [66]. A similar behavior is reported y Di Sarli et al.[110] and by Mitu et al. [70] for H_2/CH_4/air mixtures. The impact of H_2 addition depends on the properties of the other component(s) of the fuel mixture. An example is depicted in Figure 20: for stoichiometric, lean, and rich mixtures the impact of increasing level of H_2. on laminar burning velocity is shown for fuels characterized by different molecular weights, such as iso-octane (114 g/mol), ethane (30 g/mol), methane (16 g/mol), and NH_3 (17 g/mol). The relative increment $\Delta s_{\mathrm{L}}(\bar{\Phi}, x_{\mathrm{H}_2})$ is the difference of the laminar flame speed values of blend $s_{\mathrm{L}}\left(\bar{\Phi}, x_{\mathrm{H}_2}\right)$ and the pure component $s_{\mathrm{L}}(\bar{\Phi}, x_{\mathrm{H}_2}|_{0\mathrm{mol}\%})$, normalized over the latter (eq.(42)):

$$\Delta s_{\mathrm{L}}\left(\bar{\Phi}, x_{\mathrm{H}_2}\right) = \left[s_{\mathrm{L}}\left(\bar{\Phi}, x_{\mathrm{H}_2}\right) - s_{\mathrm{L}}\left(\bar{\Phi}, x_{\mathrm{H}_2}|_{0\ \mathrm{mol}\%}\right)\right] / s_{\mathrm{L}}\left(\bar{\Phi}, x_{\mathrm{H}_2}|_{0\ \mathrm{mol}\%}\right) \tag{42}$$

Since iso-octane and methane are not available in the mechanism adopted in this study [76], the results presented in Figure 20 stem from chemical kinetics simulations using the reaction mechanism proposed by CRECK Modeling Group [112] [108] [113]. As shown in Figure 20, the increase of laminar flame speed due to H_2 addition is relevant at very high values of H_2 mole fraction x_{H_2}, especially for the heavier compounds, such as iso-octane: the heavier the hydrocarbon the lower the mass fraction of H_2 in the mixture, for a fixed value of the mole fraction. As a reference for Figure 20, values of the laminar flame speed for fuel without H_2 addition are listed for the stoichiometric combustion: 60 cm/s methane, 71 cm/s ethane, and 57 cm/s iso-octane, whereas 12 cm/s ammonia for a test point characterized by 400 K and 1 bar. This suggests that in case large discrepancies exist among the molecular weights of the individual components, the adoption of mole fraction-based mixing rules may be biased towards the lighter ones. This is confirmed by the analysis of C_8H_{18}/H_2 mixtures, where a marked speed-up of laminar flame speed can be spotted only for very high x_{H_2} (∼90-95%), corresponding to ∼10-15% mass fraction. Despite all fuels show consistent trends, a general correlation between laminar flame speed increase and molecular weight ratio cannot be established: interestingly, the increase in laminar burning velocity is more significant for NH_3, than for CH_4, despite their very similar molecular weights. In the light of the observations above, a generalized description of the laminar flame speed with H_2 content as an additional parameter $s_L = s_L(p,\ T_u,\ \Phi,\ x_{H_2})$ can be achieved using an exponential law, that increases the velocity with the increment of the H_2 mole fraction x_{H_2}. The correlation proposed in this study is valid for NH_3/air blends with an additional H_2 content ranging from 60 mol% to 90 mol% and for $(0.7 \leq \Phi \leq 1.5)$ and for thermodynamic conditions reported in Table 6. It is based on a scaling function parametrized on equivalence ratio and H_2 mole fraction (x_{H_2}), as reported in eq.(43), (44), (45).

$$\mathrm{s_{L\ mix}}\ (\Phi, x_{H_2}) = \mathrm{s_{LH_2}}(\Phi) \cdot \mathrm{A}(\Phi) \cdot \mathrm{e}^{\left[\mathrm{a}(\Phi)\cdot \mathrm{x_{H_2}}\right]} \tag{43}$$

$$\mathrm{a}(\Phi) = \mathrm{am} \cdot \Phi + \mathrm{aq} \tag{44}$$

$$\mathrm{A}(\Phi) = \mathrm{Am} \cdot \Phi + \mathrm{Aq} \tag{45}$$

Such function scales the pure H_2 laminar flame speed depending on the blend composition. The scaling factor $\mathrm{A}\left(\Phi\right)$ and the exponential factor $\mathrm{a}\left(\Phi\right)$ are computed using data related to NH40 (60mol% of H_2), NH20 (80mol% of H_2), and NH10 (90mol% of H_2) chemical kinetics simulations. Firstly, for a fixed equivalence ratio $\bar{\Phi}$, laminar flame speeds $s_{L,\mathrm{mix}}\left(\bar{\Phi}, x_{H_2}\right)$ are normalized considering the corresponding value $s_{L,\mathrm{mix}}\left(\bar{\Phi}, x_{H_2}\right)$ of the pure H_2/air mixture (NH0). Values of $\mathrm{A}\left(\Phi\right)$ and $\mathrm{a}\left(\Phi\right)$ for each fixed equivalence ratio value are derived from a fitting procedure using an exponential expression, as reported in eq.(43). The variation of $\mathrm{A}\left(\Phi\right)$ and $\mathrm{a}\left(\Phi\right)$ with the equivalence ratio is then analyzed: as visible in Figure 21, a quasi-linear trend can be observed, thus their value can be described as a linear polynomial expression as reported in eq.(43)(44)(45) respectively. It is important to point out that the value of the H_2 laminar flame speed in eq.(43) is calculated using the polynomial expression in eq.(28) and not from the chemical kinetics simulations results. Blend-specific correlations are derived for extra-lean

Table 8: Scaling and exponential factor values for the generalized correlation.

Am	Aq	am	aq
-0.019788	0.0404458	0.9534167	2.622453

to rich conditions for ammonia blended with increasing hydrogen content (from 10mol% to 100 mol%).

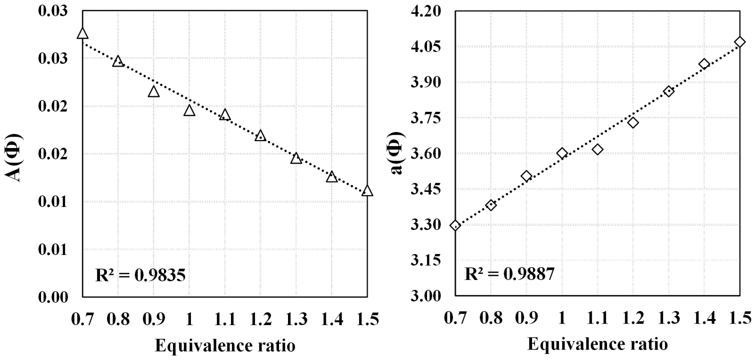

Figure 21: Linear trend of the scaling and exponential factor for lean to rich conditions.

2.4 Soot modelling in CFD codes

2.4.1 State of the art

Several computational models can be found in the literature for the description of soot aggregate formation and evolution, which exhibits fractal behavior. When soot formation is modelled or whenever a computational description of its evolution is to be laid down, the main mechanisms of soot formation are modelled as rates of formation/consumption, for example with the use of source term in s^{-1}. Usually, soot models exhibit a large sensitivity to the input variables, thus reliable experimental data for validation are required. Unlike other gaseous pollutant species such as nitrogen oxides (NOx) or unburned hydrocarbons (UHC), soot particulate matter (soot PM) is not a defined chemical species, nor it can be classified as belonging to a specific class (e.g. alkanes or paraffins); it is rather a mixture of small solid particles (nm or µm) or liquid droplets suspended in a gaseous phase, thus its modelling is a complex task. Soot formation modelling is of interest for aircraft engines, since non-volatile particle formation is triggered in the hottest part of the combustion, in the early stages of the turbine. Carbon-based deposits on the turbine have impact on the radiative heat, and emissions are the unwanted results of the hydrocarbon combustion in jet engines. A similar issue can be found in internal combustion engines for both light-duty vehicles and heavy-duty applications (e.g. marine sector). When soot is produced in combustion, an increase in the flame temperature can be observed due to its radiative heat. On one hand, radiative heat of soot particles can be exploited for optical techniques for experimental measurements (e.g. LII, LIF), on the other hand, it can be a problem for the longevity of some combustion systems, such as gas turbine [28], or internal combustion engines (carbonaceous deposits on the piston or on the exhaust valve part that faces the combustion chamber). For this reason, it is useful to rely also on computational models trading off between computational cost and high fidelity in both chemistry and physics-driven phenomena. As a starting point for every soot model, the key concept is that high temperatures and poor mixing resulting in fuel-rich pockets are the main triggers to soot formation in carbon-based fuel combustion. Moreover, soot depends heavily on the flame structure, unlike other pollutants such as NOx. The model presented by Lindstedt [114] and then improved by a PDF-based description with a transport equation [115] is suitable for nucleation, oxidation, and surface growth. The nucleation rate is proportional to the acetylene concentration ($[C_2H_2]$) and is influenced by the rate of the first ring formation since it is the rate-limiting phenomenon. Similarly, the surface growth rate is dependent on the C_2H_2 concentration, whereas the oxidation rate is linked to OH, only one of the possible options among the potential species involved in soot particle oxidation, such as H_2O, CO_2, O_2, O (although the most relevant are OH and O_2). In Lindstedt model, temperature and local value of air-fuel ratio (AFR or α) affect the rates related to the soot formation mechanisms. Alternatively, for surface growth Colket and Hall [116] proposed a model in which both concentration of hydrogen [H] and acetylene $[C_2H_2]$ are accounted in conjunction with a temperature function $\omega_{sg} = f\left(T\right)[\mathrm{H}]\left[\mathrm{C_2H_2}\right]$. A more articulated model for surface growth was proposed by Frenklach [35] [31] in which a mechanism of hydrogen-abstraction carbon-addition is described, including both H and C_2H_2 in this size increase due to chemistry-driven phenomenon on the particle surface. Finally, coagulation depends on the collision efficacy and frequency of the particles and thus is dominated by the Maxwell-Boltzmann theory of gas kinetics. Moving on to more sophisticated descriptions via computational models for advanced combustion applications, such as ICEs, two methods are well known: the method of moments and the Sectional Method. The Method of moments is based on a statistical description of the particle's population by the application of statistical moments. An instance of this method was proposed and applied by Mueller et al. [117], and successfully applied by Wu et al. [118]. Finally, the Sectional Method description is extensively provided in this chapter, since it is an object of modification on the source code. The sectional model is selected for this work investigation since it allows flexible customization of the source terms depending on the chemical nature of the fuel by reaction rate constants tabulation.

2.4.2 Sectional Method

The Sectional Method is described in this section along with the advanced customized tabulated approach that yields high-fidelity chemistry results. The Sectional Method is an advanced computational model that provides information on soot-related quantities, such as soot Particle Mass (PM), Particle Number (PN), and Particle Size Distribution Function (PSDF), as extensively discussed by [31]. Moreover, Sectional Method can be employed for advanced 3D-CFD simulations of GDI engines since it is compatible with the flamelet combustion models such as ECFM-3Z, suitable for partially premixed combustion. To account for the soot particles' different sizes, this model relies on a volume-based discretization of the particle population constituting the PSDF. The PSDF is discretized by dividing the PSDF itself into a finite number of sections (from a minimum of 20 up to a maximum of 50). Each section is populated by particles characterized by an equal representative mean volume $\mathrm{v_{i,m}}$, calculated as the arithmetic average of the lower and upper boundaries of the generic *ith* section, identified as in eq.(46) and eq.(47), where $\mathrm{v_{PAH}} = 4.00 \times 10^{-28}\,\mathrm{m}^3$ is the pyrene volume.

$$\mathrm{v_{i,min}} = 1.5 \cdot \mathrm{v_{PAH}} \cdot 2^{\mathrm{i}-1} \tag{46}$$

$$\mathrm{v_{i,max}} = 2 \cdot \mathrm{v_{i,min}} \tag{47}$$

The minimum volume throughout all the sections belongs to the smallest particles resulting from the nucleation due to the collision of two soot precursors in the gaseous phase, commonly named PAHs (Polycyclic Aromatic Hydrocarbons) and represented by pyrene in this model. This mathematical description of the soot formation accounts for all the main phenomena involved in soot formation: physics-based phenomena, such as nucleation, condensation, and coagulation, as well as the chemistry-based mechanisms that increase (surface growth) or decrease (oxidation) the size of the soot particles. This method is based on a set of assumptions:

- nucleation, the formation of the primary solid particle, stems from the collision of two molecules with four carbon rings, the pyrenes [35]. Pyrenes are the only PAHs considered for the determination of the smallest primary particles. Nucleation can occur only in the first section, which is characterized by particles with the smallest diameter ($\sim \mathrm{v}_{\mathrm{min},1} = 6.00 \times 10^{-28}\,\mathrm{m}^3$). In the other sections, the source term of nucleation $\widetilde{\Omega}_{i,PI}$ is null.

- the shape of the soot particle is spherical and soot is considered to consist only of carbon atoms and the presence of hydrogen is neglected. This hypothesis is not so far-fetched from reality: usually, $\sim 1\%$ by weight of soot particles comprises H_2.

- soot particles mass is homogeneously distributed in every particle, and a fixed density value $\rho_{\mathrm{soot}} = 1800\,\mathrm{kg\,m^{-3}}$ for the entire particle's population. As the experimental measurements suggest, soot particle density decreases as the dimension of the soot particle increases [119] and this assumption could lead to particle mass overestimation. However, this hypothesis is essential to keep the model mathematically lean.

As extensively reported by [31], for each of the finite number of sections, a transport equation (eq.(48)), is solved to compute the soot mass fraction $\widetilde{Y}_{\mathrm{soot,i}}$ in the *ith* section, which is related to the Q_{i} by the relation shown in eq.(49), where $\bar{\rho}$ is the gas-phase density, ρ_{soot} is the soot density, and μ_{t} is the turbulent diffusion coefficient.

$$\bar{\rho}\frac{\partial \widetilde{Y}_{\mathrm{i,\ soot}}}{\partial t} + \bar{\rho} u_j \frac{\partial \widetilde{Y}_{i,\ \mathrm{soot}}}{\partial x_j} = \frac{\partial}{\partial x_j}\left(\bar{\rho}\frac{\mu_t}{Sc_{\mathrm{soot}}}\frac{\partial \widetilde{Y}_{i,\ \mathrm{soot}}}{\partial x_j}\right) + \rho_{\mathrm{soot}}\,\widetilde{\Omega}_{\mathrm{i,\ soot}} \quad \text{for i} = 1 : \mathrm{i}_{\mathrm{max}} \tag{48}$$

$$Q_i = \frac{\bar{\rho}}{\rho_{\mathrm{soot}}} \cdot \tilde{Y}_{\mathrm{i,\ soot}} = \frac{\bar{\rho}}{\rho_{\mathrm{soot}}} \cdot \frac{m_{\mathrm{\ i,\ soot}}}{m_{\mathrm{cell}}} \tag{49}$$

The source term $\widetilde{\Omega}_{\mathrm{soot,i}}$ in eq.(50) regulates the soot mass fraction in each section by accounting for each one of the soot formation and evolution mechanisms: particle inception ($\widetilde{\Omega}_{\mathrm{i,PI}}$), condensation ($\widetilde{\Omega}_{\mathrm{i,COND}}$), coagulation ($\widetilde{\Omega}_{\mathrm{i,COAG}}$), oxidation ($\widetilde{\Omega}_{\mathrm{i,OX}}$), and surface growth ($\widetilde{\Omega}_{mathrmi,SG}$).

$$\begin{aligned} \tilde{\Omega}_{i,\text{ Soot }} &= \tilde{\Omega}_{\text{i, P I}} + \tilde{\Omega}_{\text{i, COND}} + \tilde{\Omega}_{\mathrm{i,COAG}} + \tilde{\Omega}_{\mathrm{i,OX}} + \tilde{\Omega}_{\mathrm{i,SG}} \\ \text{with } & \left.\widetilde{\Omega}_{\mathrm{i,PI}}\right|_{\mathrm{i}\neq 1} = 0 \end{aligned} \tag{50}$$

For each section, the evaluation of the terms in eq. 44 is carried out using five closure equations (eqs.(51)-(55)):

$$\widetilde{\Omega}_{\mathrm{i,PI}} = \mathrm{C}_{\mathrm{PI}}\mathrm{f}_{\mathrm{PI}}\left(\mathrm{P}_1, \mathrm{P}_2, \tilde{Y}^{\mathrm{imax}}_{\text{j=1, soot}}, \widetilde{T}\right); \quad \Omega_{\mathrm{i}\neq 1,\mathrm{PI}} = 0 \tag{51}$$

$$\tilde{\Omega}_{i,\text{ COND}} = \mathrm{C}_{\mathrm{COND}}\, \mathrm{f}_{\mathrm{COND}}\left(\mathrm{P}_1, \tilde{Y}_{\text{i, soot}}, \widetilde{T}\right) \tag{52}$$

$$\tilde{\Omega}_{\mathrm{i,SG}} = (\mathrm{P}_3 - \mathrm{P}_4)\, \mathrm{C}_{\mathrm{SG}}\mathrm{f}_{\mathrm{SG}}\left(\tilde{Y}_{\text{i}-1\text{, soot}}, \tilde{Y}_{\text{i, soot}}\right) \tag{53}$$

$$\tilde{\Omega}_{i,\mathrm{OX}} = (\mathrm{P}_5 + \mathrm{P}_6)\, \mathrm{C}_{\mathrm{OX}}\mathrm{f}_{\mathrm{OX}}\left(\tilde{Y}_{\mathrm{i,soot}}, \tilde{Y}_{\text{i+1, soot}}\right) \tag{54}$$

$$\tilde{\Omega}_{i,COAG} = \mathrm{f}_{\mathrm{COAG}}\left(\tilde{Y}^{\mathrm{imax}}_{\text{j=1, soot}}, \tilde{T}, p\right) \tag{55}$$

where $\widetilde{T}$ and p are the cell-wise temperature and pressure in the cell respectively, Pi (with i=1,6) are factors obtained from a pre-calculation of tabulated coefficients and these are highly dependent on the chemical reaction mechanism employed. These coefficients can be derived via dedicated chemical kinetics simulations accounting for the specific fuel composition (e.g. a surrogate). The coefficients C_{PI}, $\mathrm{C}_{\mathrm{COND}}$, C_{SG}, and C_{OX} are scaling factors that can be exploited to tune the functions computed from chemical tabulation to better match experimental results (default values are 1.5, 1.3, 1.0, 1.0 respectively). A more detailed expression for each of the contribution to the source term is reported hereafter. For particle inception occurring only in the first section, a steady-state assumption between the PAHs rate of formation ($\widetilde{\mathrm{RPAH}}$) and their rate of consumption by primary particle inception (or nucleation) or by condensation is assumed. Form this assumption, a more detailed expression of eq.(51) and (51) can be written:

$$\widetilde{\Omega}_{1,\mathrm{PI}} = \frac{2\mathrm{v}_{\mathrm{PAH}}\widetilde{\mathrm{RPAH}}^{2}}{\left[2\mathrm{C}_{\mathrm{PI}}\mathrm{A}\left(\widetilde{\mathrm{Y}}_{\mathrm{i,\ soot}}\right)^{2}\sqrt{\tilde{T}} + 2\widetilde{\mathrm{RPAH}} + 2\ \mathrm{A}\left(\widetilde{\mathrm{Y}}_{\mathrm{i,\ soot}}\right)\mathrm{C}_{\mathrm{PI}}\sqrt{\tilde{T}}\sqrt{\frac{2\widetilde{\mathrm{RPAH}}}{\mathrm{C}_{\mathrm{PI}}\sqrt{\tilde{T}}} + \mathrm{A}\left(\widetilde{\mathrm{Y}}_{\mathrm{i,\ soot}}\right)^{2}}\right]} \tag{56}$$

$$\tilde{\Omega}_{i,\ \mathrm{COND}} = \frac{\mathrm{v}_{\mathrm{PAH}}\mathrm{C}_{\mathrm{coND}}\mathrm{f}\left(\frac{\bar{\rho}\tilde{\mathrm{Y}}_{\mathrm{i},500t}}{\rho_{\mathrm{soot}}}\right)\widetilde{\mathrm{RPAH}}}{0.5\sum_{\mathrm{i=1}}^{\mathrm{i_{max}}}\mathrm{C}_{\mathrm{COND}}\ \mathrm{f}\left(\frac{\bar{\rho}\tilde{\mathrm{Y}}_{\mathrm{i,\ sooot}}}{\rho_{\mathrm{soot}}}\right) + \sqrt{\frac{2\mathrm{C}_{\mathrm{PI}}\widetilde{\mathrm{RPAH}}}{\sqrt{\tilde{T}}} + \left(0.5\sum_{\mathrm{i=1}}^{\mathrm{i_{max}}}\mathrm{C}_{\mathrm{coND}}\mathrm{f}\left(\frac{\bar{\rho}\tilde{\mathrm{Y}}_{\mathrm{i},500t}}{\rho_{\mathrm{soot}}}\right)\right)^{2}}} \tag{57}$$

and, given *imax* the maximum number of sections, the collision frequency factors for particle inception β_{PI} and for condensation β_{COND} are expressed as in eqs.(58)(59)

$$\beta_{\mathrm{PI}} = \mathrm{C}_{\mathrm{PI}}\left(\frac{3}{4\pi}\right)^{\frac{1}{6}}\sqrt{\frac{6\mathrm{k_b}}{\rho_{\mathrm{soot}}}}\sqrt{\frac{2}{\mathrm{v}_{\mathrm{PAH}}}}4\left(\mathrm{v}_{\mathrm{PAH}}\right)^{\frac{2}{3}}\sqrt{\tilde{T}} \tag{58}$$

$$\beta_{\mathrm{COND}} = \sum_{\mathrm{i=1}}^{\mathrm{i_{MAX}}} 1.3\left(\frac{3}{4\pi}\right)^{\frac{1}{6}}\sqrt{\frac{6\mathrm{k_b}}{\rho_{\mathrm{soot}}}}\sqrt{\frac{1}{\mathrm{v}_{\mathrm{i,\ mean}}} + \frac{1}{\mathrm{v}_{\mathrm{PAH}}}}\left(\mathrm{v}_{\mathrm{i,\ mean}}^{\frac{1}{3}} + \mathrm{v}_{\mathrm{PAH}}^{\frac{1}{3}}\right)^{2}\mathrm{f}\left(\frac{\bar{\rho}\widetilde{\mathrm{Y}}_{\mathrm{i,\ soot}}}{\rho_{\mathrm{soot}}}\right)\sqrt{\widetilde{T}} \tag{59}$$

where k_{b} the Boltzmann constant ($1.380\,649 \times 10^{-23}\,\mathrm{J\,K^{-1}}$), A is a function of tabulated rates [31]. For the increment or decrement of the carbonaceous solid particles, two chemistry-driven mechanisms are accounted in this model and the closure equations for each are eq.(60) for surface growth (increment) and eq.(61) for oxidation (reduction).

$$\begin{aligned}
\tilde{\Omega}_{i,SG} = {} & \alpha\left(\mathrm{v}_{\mathrm{C_2H_2}}\right)^{\frac{3-\theta}{\theta}}\left(\tilde{\mathrm{k}}_{\mathrm{d}} - \tilde{\mathrm{k}}_{\mathrm{rev}}\right) \\
& \cdot\left[2\left(\frac{3}{3+\theta}\mathrm{q}_{\mathrm{i-1}}\left(\mathrm{v}_{\mathrm{i-1,max}}\frac{3-\theta}{\theta} - \mathrm{v}_{\mathrm{i-1,min}}\frac{3-\theta}{\theta}\right)\right.\right. \\
& \left. + \frac{3}{\theta}q_{i-1}^{vf}\left(v_{i-1,\max}\frac{\theta}{3} - v_{i-1,\min}\frac{\theta}{3}\right)\right) - \left(\frac{3}{3+\theta}q_i\left(v_{i,\max}\frac{3-\theta}{\theta} - v_{i,\min}\frac{3-\theta}{\theta}\right)\right. \\
& \left.\left. + \frac{3}{\theta}q_{i}^{vf}\left(v_{i-1,\max}\frac{\theta}{3} - v_{i-1,\min}\frac{\theta}{3}\right)\right)\right]
\end{aligned} \tag{60}$$

$$\begin{aligned}
&\tilde{\Omega}_{i,\mathrm{OX}} = \alpha \left(\mathrm{v}_{\mathrm{C_2H_2}}\right)^{\frac{3-\theta}{\theta}} \left(\tilde{\mathrm{k}}_{\mathrm{O_2}} + \tilde{\mathrm{k}}_{\mathrm{OH}}\right) . \\
&\sum \left[\frac{3}{3+\theta} q_{i+1} \left(v_{i+1,\max} \frac{3-\theta}{\theta} - v_{i+1,\min} \frac{3-\theta}{\theta} \right) \right. \\
&+ \frac{3}{\theta} q_{i+1}^{vf} \left(v_{i+1,m_x}^{\frac{\theta}{3}} \right. \\
&\left. \left. - v_{i+1,\min} \frac{\theta}{3} \right) - 2 \left(\frac{3}{3+\theta} q_i \left(v_{l,\max}^{\frac{3-\theta}{\theta}} - v_{1,\min} \frac{3-\theta}{\theta} \right) + \frac{3}{\theta} q_i^{vf} \left(v_{l,\max}{}^{\frac{\theta}{3}} - v_{l,\min} \frac{\theta}{3} \right) \right) \right]
\end{aligned} \tag{61}$$

where $\mathrm{v}_{\mathrm{C_2H_2}}$is the acetylene volume (2.14×10^{-29} m^3), θ is the fractal factor, which is equal to 2 as a consequence of the spherical shape assumption [120] [31], q_{i} is the soot volume fraction of particles in section i, v_{f} and α are volume fraction related parameter discussed by Netzell [36], and $\widetilde{k}_{\mathrm{O_2}}$ and $\widetilde{k}_{\mathrm{OH}}$, $\widetilde{k}_{\mathrm{d}}$, $\widetilde{k}_{\mathrm{rev}}$ are the tabulated coefficients. Finally, the soot evolution related to coagulation, a process driven by effective collision probability and independent from the tabulated chemistry coefficients [18] [31] [36], is modelled with the $\widetilde{\Omega}_{\mathrm{i,COAG}}$ and its closure equation eq.(62).

$$\begin{aligned}
\widetilde{\Omega}_{\mathrm{i,COAG}} = \sum_{\mathrm{k=1}}^{\mathrm{j-1}} (\beta_{\mathrm{k,k}} \mathrm{n_k} n_{\mathrm{k}} 2 \mathrm{v}_{\mathrm{mean,k}}) - \beta_{\mathrm{j,j}} n_{\mathrm{j}} \mathrm{n_j} 2 \mathrm{v}_{\mathrm{mean,j}} \; + \sum_{\mathrm{k=1}}^{\mathrm{j-1}} \sum_{\mathrm{y=k+1}}^{\mathrm{j}} (\beta_{\mathrm{k,y}} \mathrm{n_k} \mathrm{n_y} 2 \mathrm{v}_{\mathrm{mean,k}}) \\
- \sum_{\mathrm{k=j+1}}^{\mathrm{i_{MAX}} \; -1} (\beta_{\mathrm{j,k}} \mathrm{n_j} \mathrm{n_k} 2 v_{\mathrm{meanj}})
\end{aligned} \tag{62}$$

As shown in eq.(62), a pair of two particles belonging to section k and section y is considered: $\mathrm{n_k}$ is soot number density for the section k, $\beta_{\mathrm{k,y}}$ the frequency collision factor between particles belonging to section k and y. The last quantities for the closure of this model are the coefficients for reaction rate describing the main chemistry-dominated mechanisms for soot formation. As previously discussed, primary particle inception is dominated by $\widetilde{RPAH}$, the rate of production of soot precursors (pyrenes in this model), as well as the condensation. As described by the HACARC process, once a solid carbonaceous particle is formed, it can undertake a process of oxidation, which leads to particle size reduction, described by $\widetilde{k}_{\mathrm{O_22}}$ and $\widetilde{k}_{\mathrm{OH}}$, or its size can be increase by the surface growth, ruled by $\widetilde{k}_{\mathrm{d}}$ and $\widetilde{k}_{\mathrm{rev}}$. The accuracy of soot prediction can be increased [15] thanks to the possibility of coupling the Sectional Method to the tabulation of these coefficients derived by chemical kinetics simulations tailored to the fuel composition. The framework of this approach is described in Figure 22.

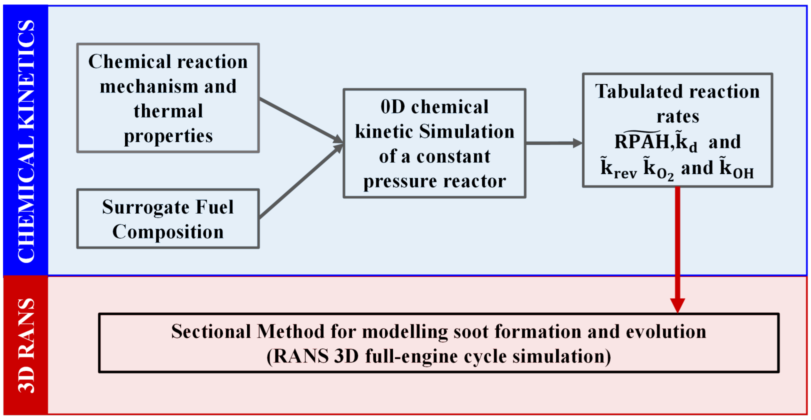

Figure 22: Framework of engine simulations for soot prediction with a customized tabulated approach for Sectional Method [121].

During the simulation, each element of the source term (eq.(50)) is computed for each section, using the five coefficients Table 9, exception made for the coagulation ($\widetilde{\Omega}_{\mathrm{i,COAG}}$). The values of the five coefficients are retrieved from the table and are assigned in each cell of the fluid domain depending on the thermodynamic conditions (p^*, $T_{\mathrm{u}}{}^*$), on the local mixture properties, thus the equivalence ratio ϕ^* and EGR* for premixed combustion and local value of the Z^* mixture fraction for diffusive combustion, and on the progress variable c^*. The meaning of the aforementioned coefficients and their relationship with the source terms in eq.(50) are summarized in Table 9.

With regards to the Sectional Method implemented in STAR CD v4.30 [102], it is important to clarify the nature of the interplay between the soot chemistry and the turbulent combustion model adopted, which is EFCM-3Z. The soot model and the combustion model are decoupled since the soot-chemistry timescale is assumed to be longer than the characteristic turbulence timescale, hence the Damköhler

Table 9: Influence of the chemistry-based coefficients and the soot source terms implemented in the Sectional Method.

Coefficient	**Description**	**Source term**
$\widetilde{\mathrm{RPAH}}$	Rate of formation of the soot precursors in the gaseous phase	$\widetilde{\Omega}_{\mathrm{PI,i}}$ $\widetilde{\Omega}_{\mathrm{COND,i}}$
$\tilde{\mathrm{k}}_{\mathrm{d}}$ and $\tilde{\mathrm{k}}_{\mathrm{rev}}$	Influence on the surface growth of the particles (forward and backward reaction rate constants in the HACARC mechanism [31])	$\widetilde{\Omega}_{\mathrm{SG,i}}$
$\tilde{\mathrm{k}}_{\mathrm{O_2}}$ and $\tilde{\mathrm{k}}_{\mathrm{OH}}$	Influence on the oxidation in the HACARC mechanism [31]	$\widetilde{\Omega}_{\mathrm{OX,i}}$

Number related to soot ($\mathrm{Da_{soot}} = {}^{\tau_{turb}}/_{\tau_{soot-chemistry}} < 1$) is much smaller than the combustion one ($\mathrm{Da_{comb}} = {}^{\tau_{turb}}/_{\tau_{soot-chemistry}} \gg 1$). Thus, in terms of chemistry (e.g., reaction rates) soot formation can be modelled separately from the combustion process, which occurs faster. On the other hand, combustion changes the thermodynamic parameters of the reacting system, like pressure and temperature that are fundamental inputs to access the tabulated reaction rates constants employed in the source term of the soot mass fraction transport equation. On a final note, the use of this modelling approach can be a valid option in the design of a large plethora of combustion devices, whose emissions are or will soon be subject to regulation. Soot modelling has been a prerogative of Diesel engines [122][31], especially for light duty application, such as automotive. In these engines, the production (mass and dimension) of particle is related to the atomization of the spray [123] due to regulations that were limiting the particle number, mass, and dimensions. Moreover, industrial applications of furnaces working with diffusive flame are subject to emission regulation. Another example are the aeronautic engines, like turbojets in which the soot produced by the combustor can affect the radiative heat of the whole engine, thus must be carefully evaluated [124]. The flamelet approach with one-step reaction was compared to the detailed chemistry in terms of computational costs [125] suggesting that soot prediction is better estimated with detailed chemistry due to its capability to model more precisely the acetylene and other PAH formation, but the computational cost would be too high for whole engine cycle simulations. For this reason, flamelet models in conjunction with the Sectional Method with tabulated approach tailored on the fuel-specific chemistry can be a winning strategy. So far, the Sectional Method can be coupled with tables produced using chemical kinetics simulations of either diffusive 1D-flame reactor or a premixed constant pressure reactor (CP), thus the soot formation in partially premixed combustion cannot be adequately modelled. To further improve this already advanced model, a switch condition and integration of the tables for the partially premixed combustion can be evaluated to better soot prediction in GDI engines, but also for aeronautic engine combustors.

2.4.3 Sectional method with customized tabulated approach

For a thorough understanding of the interaction of the customized libraries and the sectional method, it is essential to present the two types of reactor employed in the chemical kinetics simulations to tabulate the reaction rate constants.

The first option is a fully premixed constant pressure reactor whose combustion is simulated in several conditions in which the composition is kept constant, whereas temperature, pressure, AFR, and dilution is explored. The final output of these simulations is a table (a database) of several values of rate constants stored in a specific order so that during the 3D-CFD simulation the soot formation model can access the information needed for the soot source terms calculation (eq.(51) to (54)). This table is suitable for predominantly premixed combustion, whereas, for diffusive combustion, another table is recommended. In this case, the database of reaction rate constants is derived using chemical kinetics simulations based on a diffusive flamelet reactor. The results stemming from this tabulation procedure should be used in the case of predominantly diffusive combustion (e.g. Diesel engine combustion). On a final note, the independent parameters adopted for the tabulation spacing are presented and compared at best, since the two types of reactors require two slightly different inputs given their nature. A comparison of the output tabulated data is also carried out to spot eventual trends in these two approaches.

2.4.3.1 Library generation Two main types of combustion can occur: premixed or diffusive. In premixed combustion, the reactants are mixed before the combustion onset, the oxidation rate is the dominant time scale. In diffusive flames, reactants are separated, and they diffuse in a thin region, the reaction zone, where the combustion takes place if the local value of AFR is within the flammability limit. In this case, the diffusion time scale is slower than the oxidation rate, thus it is the leading phenomenon. Lastly, a combination of these two modes can occur when predominantly premixed combustion takes place, and at the same location, secondary diffusive oxidation phenomena take place simultaneously. This is known as partially premixed combustion, and it can be observed in modern combustion devices such as gas-turbine combustor, or some internal combustion engines with fuel injected directly into the combustion chamber. During the power stroke in ICEs, turbulent combustion takes place, and the combustion mode can be predominantly diffusive or premixed. The former is observed in Diesel engines: the fuel is injected, and it diffuses in the oxidizer (already present in the combustion chamber), thus the diffusive combustion is influenced by the diffusion of the reactants in each other's stream. In Spark Ignition (SI) engines, the combustion can be regarded as premixed. More specifically, the Port Fuel Injection (PFI) mode ensures the intake of premixed fresh charge in the engine, since the fuel is injected in the intake port, thus purely premixed combustion will take place in this case. In the case of Gasoline Direct Injection (GDI), the fuel is injected directly into the combustion chamber during the intake phase, then its evaporation within the air is favored by the increase of temperature due to the increase of the average in-cylinder temperature. Air and fuel vapor mixing is promoted by the flow field in the cylinder, and as a result, a stratified charge is formed. For several reasons (e.g. operative conditions, combustion chamber geometry, wall temperatures), the injected fuel may form a liquid film, which can evaporate before or after the combustion onset, thus partially premixed combustion may occur in this case.

It is possible to provide customized tables for the soot source term calculations for the Sectional Method. In this section, a new surrogate is formulated based on representative high-performance gasoline for GDI engines [121]. The comparison of the most combustion-relevant properties of the reference fuel and surrogate fuel is reported in Table 10.

Table 10: Surrogate properties compared to the ones of the reference gasoline [121].

	RON	MON	H/C	O/C	TSI
Ref.	98	88	1.895	0.037	-
Surr.	96.2	89.1	1.919	0.017	14.65

The surrogate composition is assessed by targeting the reference fuel properties using the formulation method described by Del Pecchia et al.[14][78]: ethanol 11.50 mol%, toluene 30.51 mol%, n-heptane 10.80 mol%, iso-octane 47.19 mol%. The surrogate fuel is employed as input for the fuel composition within the reaction rate constants tabulation process.

Two types of reactors can be employed for the tabulation, whose main features are shown in Figure fig:48:

- the diffusion flamelet, suitable for predominantly diffusive combustion (e.g. Diesel applications), This reactors is a 1-D domain in which the reactants diffuse into each other towards the reaction zone.
- the constant pressure reactor, suitable for a predominantly premixed combustion (e.g. SI engines). This is a 0-D reactor in which the reactants are already premixed (hence homogeneous composition) when the combustion occurs.

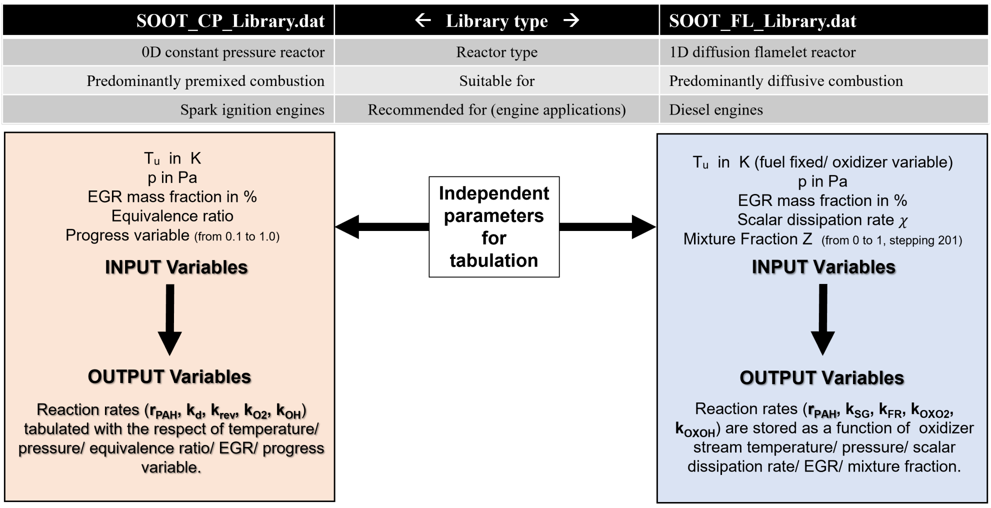

Figure 23: Schematic of the input parameters for each tabulation approach derived from the chemical kinetic simulations.

In the currently implemented version, the library to employ, thus the predominant combustion mode, must be specified before the 3D CFD engine simulation starts. For this reason, the accuracy of this method in case of partially premixed combustion can be called into question. To explore a possibility of a dynamic switch between libraries during the simulation, the nature of input/output parameters must be discussed.

Libraries inputs

The input parameter for the tabulation are presented first. Starting from the similarity between these two reactors, besides the fuel composition, another common input is the reaction mechanism, which should comprise both the main constituent of the surrogate fuel and the PAH formation pathways for the soot rate constant evaluation. Once again, the mechanism developed by Cai et al. [17] is the most appropriate choice for E-TRF surrogates (Ethanol Toluene Reference Fuel). Since the two employed reactors differ on the nature of the combustion, a slight difference in the input parameters between the two is expected. The constant pressure reactor (cp-reactor) employed in the chemical kinetic simulations is a 0-D reactor in which the premixed combustion is simulated for several values of equivalence ratio corresponding to those potentially available in the cells of the 3D engine simulation. The inputs for the cp-reactors are summarized in Table 11. The assigned values are derived from plausible low load and revving speed operational conditions for a GDI engine.

Table 11: Inputs to the library generation based on the cp-reactor chemical kinetic simulations.

Oxidizer composition	N_2 0.767 mol% - O_2 0.233 mol%
Fuel composition	C_2H_5OH 11.50 mol%, C_7H_8 30.51 mol%, C_7H_{16} 10.80 mol%, C_8H_{18} 47.19 mol%
Pressure (bar)	0.5, 1, 2, 2.5, 3, 3.5, 4, 4.5, 5, 5.5, 6, 8, 10, 12, 15
EGR (%) (N_2 100 mo%)	0, 5, 10, 15, 20, 25, 30, 40, 50
Mixture unburnt temperature (K)	450, 500, 550, 600, 650, 700, 750, 800, 850, 900, 1000
Equivalence ratio	0.4, 0.5, 0.6, 0.7, 0.8, 0.9, 1.0, 1.05, 1.1, 1.15, 1.2, 1.25, 1.3, 1.35, 1.4, 1.45, 1.5, 1.55, 1.6, 1.65, 1.7, 1.75, 1.8, 1.85, 1.9, 1.95, 2.0, 2.1, 2.2, 2.3, 2.4, 2.5
Combustion progress variable c	0:0.01:1.0

As for the flamelet reactor, the reactants are introduced by two separate streams, and they diffuse toward the reaction zone. The variation of the mixture fraction Z along the x-axis is described using the scalar dissipation rate χ ($c_\chi = 2$), which can be defined as eq.(63) for the laminar flamelet reactor within the chemical kinetic simulations, and as eq.(64) for the RANS 3D turbulent combustion simulations, where χ_T is the turbulent scalar dissipation rate, $\widetilde{\chi}$ the average dissipation rate, $\tilde{\varepsilon}/\tilde{k}$ is the ratio of the average values of eddy dissipation and turbulent kinetic energy within the k-epsilon turbulence model.

$$\chi = c_\chi \cdot \left(\frac{dZ}{dx}\right)^2 \tag{63}$$

$$\tilde{\chi} \cong \chi_{\mathrm{T}} = \mathrm{c}_{\chi} \cdot \frac{\tilde{\varepsilon}}{\tilde{k}} \cdot \tilde{Z}'' \tag{64}$$

Since the flamelet has two separate streams for the oxidizer and the fuel, their unburnt temperature is set separately, and whereas for the oxidizer a range can be set, the fuel unburnt temperature can assume only one value, which is set to 650 K accordingly to a plausible value of unburnt temperature in the combustion chamber before spark in a GDI engine. Further details on the inputs to the diffusive tabulation based on the diffusive reactor are summarised in Table 12.

Table 12: Inputs to the diffusive flamelet simulations for the tabulation of SSM library.

Oxidizer composition	N_2 0.767 mol% - O_2 0.233 mol%
Fuel composition	C_2H_5OH 11.50 mol%, C_7H_8 30.51 mol%, C_7H_{16} 10.80 mol%, C_8H_{18} 47.19 mol%
Pressure (bar)	0.5, 1, 2, 2.5, 3, 3.5, 4, 4.5, 5, 5.5, 6, 8, 10, 12, 15
EGR (%) (N_2 100 mol%)	0, 5, 10, 15, 20, 25, 30, 40, 50
Fuel unburnt temperature (K)	650
Oxidizer unburnt temperature (K)	450, 500, 550, 600, 650, 700, 750, 800, 850, 900, 1000
Scalar dissipation rate (χ)	0.001, 0.01, 0.05, 0.10, 0.25, 0.75, 1.00, 5.50, 10.00

Libraries oputputs The outputs of the libraries are the reaction rate constants, accessed by the simulation using the independent parameters (Table 11 and Table 12) summarised and compared in Figure 23 and Figure 24.

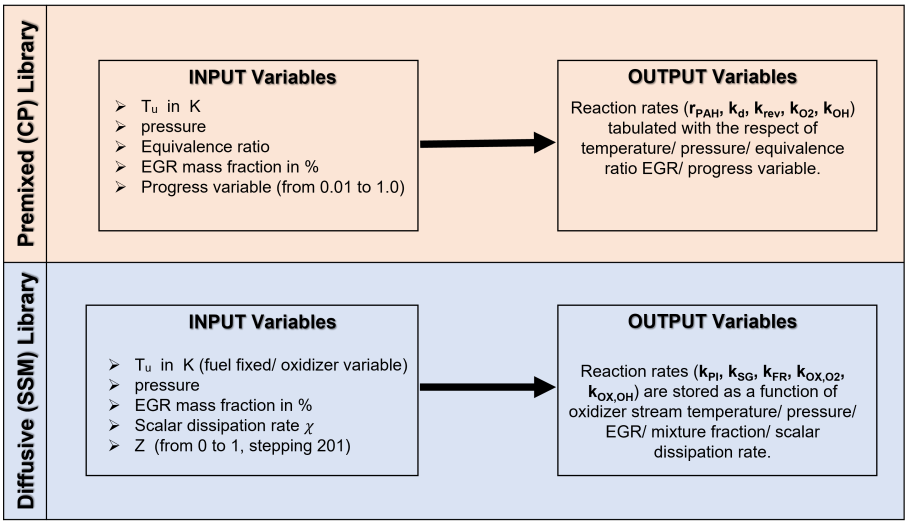

Figure 24: Comparison of the input and output of the two different possible library generation tools from chemical kinetic simulations.

2.4.4 Sectional method with a dynamic switch between libraries for partially premixed combustion

2.4.4.1 Motivation of the library switch Combustion in GDI engines is predominantly premixed since the spray and fuel evaporation occur sufficiently before the spark time to enable a proper mixture formation. The stratified charge in the combustion chamber burns by predominantly premixed combustion. However, a persistent liquid film near walls can be present unwillingly in some operating engine conditions. In this case, the complete evaporation of the liquid fuel may only occur after the main flame front reaches this region. In this case, if the main flame front has arrived in this region, the evaporation of the liquid film of fuel can be triggered when the main combustion is already in place. Thus, the fuel rapidly evaporates due to the heat released locally by the premixed combustion, and it starts to diffuse in the region where the oxidizer and the previously mixed fuel are present. It diffuses in a region where fuel and oxidizer are already burning, and here the fuel oxidation can be associated with a secondary combustion phenomenon characterized by a diffusive combustion mode rather than a premixed one. By definition, diffusive combustion is dominated by the diffusion of the reactants, both oxidizer, and fuel, in the reaction zone. Similarly, in the case of liquid film evaporation in the proximity of the reaction zone, the fuel evaporated from a fuel liquid pocket diffuses in a mixture of fuel and oxidizer. However, when consistent liquid pockets of fuel are generated, they can evaporate after the main flame front has reached that fluid domain zone. In this case, the combustion phenomenon can be considered partially premixed. A mainly premixed combustion mode characterizes partially premixed combustion, along with secondary diffusive burning modes, occurring in the same region. For the CFD simulation, this idea can be clarified by an example of the evolution of combustion-scalar quantities that a specific set of cells experiences. A cell near a wall region be considered (e.g., next to the piston head, cylinder wall, or valve surface). The hypothesis is that there is a liquid fuel pocket in this cell, and when the main combustion flame front (premixed) reaches this region, the heat released can trigger the fuel evaporation locally. In this cell and in its neighboring cells, the scalar representing the fuel diffuses in the zone where the main combustion is already burning the mixture. In this set of cells, one may assume that the soot formation occurs in a fashion that resembles the phenomena related more to a diffusive rather than premixed combustion. Thus, there may be more appropriate choices than the exclusive use of a library based on a premixed 0-D constant pressure reactor. The chosen library is essential since the coefficients to compute the source terms are retrieved from it, which is part of the soot mass fraction transport equation. At the same time, a purely diffusive library approach is an inaccurate choice for partially premixed combustion. A test in each cell to determine whether combustion has to be considered a locally premixed or locally diffusive phenomenon can be a viable option to switch from one library to another. The aim is to evaluate/propose a practical criterion to switch between the two libraries locally. The best candidates from the literature are described in the next paragraphs, as well as the novel alternatives presented in this work, which are more suitable to the combustion and soot models adopted in this study.

2.4.4.2 Features of ECFM combustion model employed for the switch condition In this paragraph the combustion model adopted for the RANS simulations of the partially premixed turbulent flame is presented with highlights on its main features relevant to the modification implemented in the soot model. In particular, the modification proposed is based on assessing the local predominant combustion mode via a test condition based on some cell-wise quantities, whose evolution is reckoned by the combustion model. Traditionally, RANS turbulent combustion models have been specifically developed for either premixed or non-premixed/diffusive combustion. Nowadays, this stark distinction between combustion modes does not apply to most of industrial combustion devices. In fact, usually up to three types of combustion mode can occur simultaneously in a single combustion device:

- premixed autoignition (AI): charge autoignites after a specific delay time determined by pressure, temperature, local value of AFR, and presence of dilution (e.g. EGR for ICEs). This phenomenon triggers the spontaneous charge ignition in Compression Ignition (CI) engines, or the phenomenon occurring locally under the spark plug of a Spark Ignition (SI) engine in the proximity of the electric arch between the spark plug electrodes, or the unwanted autoigntion of the charge known as knock.
- purely premixed combustion or premixed flame (PF): fuel and oxidizer are already mixed, and this flame propagates throughout the combustion chamber.
- diffusive flame (DF): fuel and oxidizer diffusive in a thin reaction zone that separates them and where the burnt gases are formed.

These three types of combustion can occur at the same time inside the combustion chamber. Thus, a more accurate turbulent combustion description requires a model that can represent them simultaneously. The Enhanced Coherent Flamelet

Model 3-Zones (ECFM3Z), pioneered by Kalmthout et al.[126] for DNS simulations, belongs to the family of models that are based on the surface density Σ concept. However, ECFM3Z presented by Colin et al. [103] is the version that accounts for all of three combustion modes (AI, PF, DF) at the same time. This work focuses on the implementation of a library switch between customized soot libraries for ICEs in the case of partially premixed turbulent combustion with RANS-CFD simulations. For this reason, the more sophisticated model ECFM3Z [60] [61] [127] is employed instead of any other combustion model. It is one of the most flexible and elaborated combustion models for 3D-CFD RANS implemented in the CFD framework adopted in this study [102]. This model is suitable for premixed, partially premixed, and diffusive turbulent combustion, and for its flexibility, it is selected as the combustion model over other candidates, such as the "Level set" model, also known as G-equation model, which in turn cannot handle diffusive combustion. ECFM for spark ignition engine combustion model [103] conceptually divides the cell into three zones: two unmixed zones, one with fuel and the other one with air and eventually diluent (e.g. EGR), and finally a mixing zone as shown in Figure 25-26-27. It is in this zone that combustion can occur.

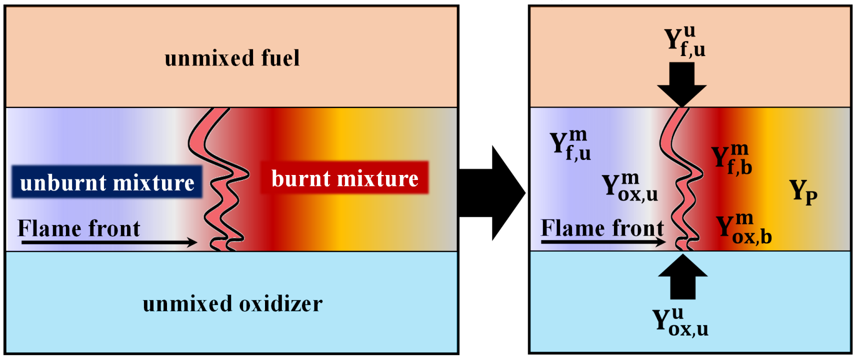

Figure 25: Schematic representation of the computational cell conceptually divided into zones for unmixed reactants and mixed reactants, burnt and unburnt gases.

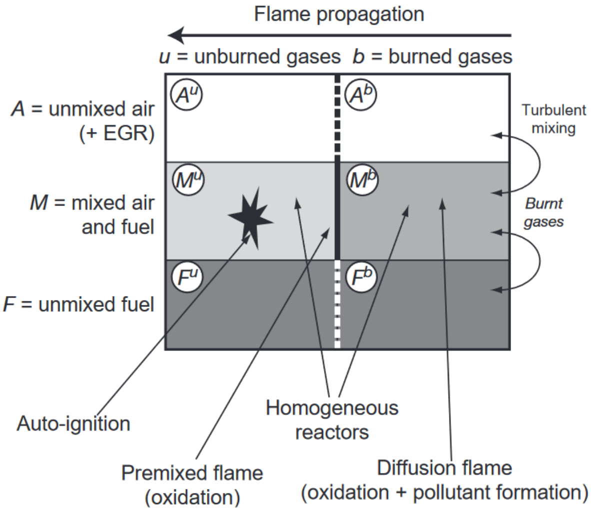

Figure 26: ECFM-3Z schematic representation of the computational cell[103].

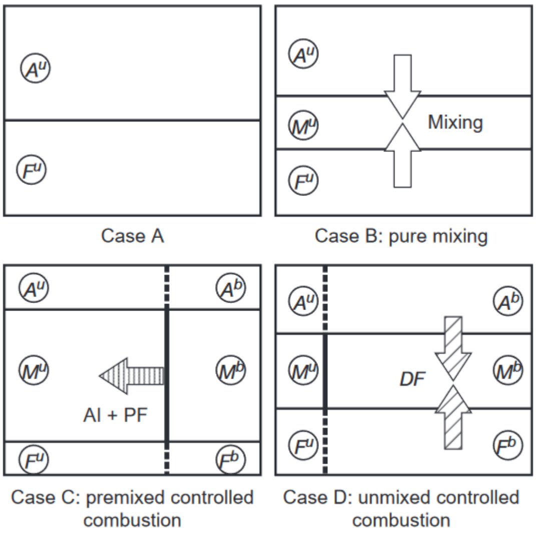

Figure 27: Evolution of the zones during the combustion within the ECFM3Z combustion model framework [102].

The ECFM3Z model belongs to the flamelet models, thus is grounded into the assumption that the flame front is a thin interface that separates the unburnt gases, that comprise the fuel ($Y_{\mathrm{f,u}}$) and the oxidizer ($Y_{\mathrm{ox,u}}$ air and eventually EGR) from the burnt ones ($Y_{\mathrm{f,b}}$, $Y_{\mathrm{ox,b}}$, $Y_{\mathrm{P,b}}$). The fresh mixture is burned in the mixing zone by consumption by autoignition and premixed combustion terms proportionally to its mass fraction. The conservation of the mass in the flame front ensures that the mean progress variable ($\widetilde{c}$) is locally proportional to the fraction of fuel mass burnt as described in eq.(65).

$$\tilde{c} = 1 - \frac{\overline{\mathrm{m}}^{\mathrm{u}}}{\overline{\mathrm{m}}} = 1 - \frac{\widetilde{\mathrm{Y}}^{\mathrm{u}}_{\mathrm{f,u}}}{\widetilde{\mathrm{Y}}_{\mathrm{TF}}} \tag{65}$$

$$c = \frac{T - T_{\mathrm{u}}}{T_{\mathrm{b}} - T_{\mathrm{u}}} \quad \text{or} \quad c = \frac{Y_{\mathrm{P}}}{Y_{\mathrm{P,b}}} \tag{66}$$

The fuel unmixed unburnt fuel $\widetilde{Y}^{\mathrm{u}}_{\mathrm{f,u}}$ and the unburnt fuel tracer $\widetilde{Y}_{\mathrm{TF}}$, a scalar transported quantity the is spatially constant in case of perfect mixing, otherwise it varies in space and time because of uneven charge due to imperfect mixing. When it comes to turbulent combustion and ECFM3Z, the mean progress variable ($\widetilde{c}$) is computed using the Favre Average and using eq.(65), and it is of paramount importance, along with the mixture fraction Z, for the gas mixture spatial description as a function of (Z, $\widetilde{c}$). More specifically, this model provides a description in time and space of the whole combustion process using this 2D space of parameters. The combustion progress variable $\widetilde{c}$ (the tilde stands for the averaged value in the RANS simulation) is not a new concept, as it was first introduced in the classical flamelet model for premixed combustion, the Bray-Moss-Libby model (BML) [60] c as a scalar quantity defined as a normalized temperature or as a normalized product mass fraction (eq.(66)). The progress variable is described by two delta function at $c = 0$ and at $c = 1$, and these two Probability Density Function (PDF) are representing the probability of having unburnt or burnt mixture, respectively at a given time and location. The PDF assumes that the combustion system is either in chemical equilibrium (or intermediate states are highly unlikely to occur).

In case of SI engine simulations, within the computational cell, the evolution of the (Z, $\widetilde{c}$) starts with only two zones (Figure 27, case A), each one filled with the oxidizer, and the other one is filled with evaporated amount of the liquid fuel injected in the combustion chamber before the start of combustion in case of GDI engines. Then, reactants progressively move in the mixture [103] (Figure 27, case B). After the combustion onset, only two states for the gas in the computational cell are possible: unburnt (reactants) or burnt (products) (Figure 27, case C/D). It is important to highlight that case D in Figure 27 is typical of CI engines, in which the amount of unmixed reactant can be relevant even after the combustion onset, and the unmixed gases proceed to move in the mixing zone. Here, the fraction of unburnt reactant $\widetilde{c}$ mixes with the species in the burnt region with a mixing time τ_{mix} that is defined as proportional to the ratio of turbulent kinetic energy (k) and turbulence dissipation rate (ε) for k-ε turbulence model, and it is usually much larger than the chemistry time scales τ_{chem}, that is related to combustion reactions. Thus, in this region the species diffusion and mixing are the controlling phenomena for the combustion mode (DF). The rest of the unmixed gases corresponding to $1-\widetilde{c}$ mixes with the unburnt gases in the unburnt region, and consequently consumed by a predominantly premixed combustion mechanism (AI and PF).

This is a schematic description of how the combustion process is modelled by ECFM3Z accounting for AI, PF, and DF simultaneously. All the mass fractions are computed using a transport equation solved for the Favre average mass densities of each species as reported in eq.(67) for the generic species "S".

$$\frac{\partial \bar{\rho}\widetilde{\mathrm{Y}}_{\mathrm{S}}}{\partial t}+\frac{\partial \bar{\rho}\tilde{u}_{\mathrm{i}}\widetilde{\mathrm{Y}}_{\mathrm{S}}}{\partial x_{\mathrm{i}}}=\frac{\partial}{\partial x_{\mathrm{i}}}\left(\left(\frac{\mu}{\mathrm{Sc}}+\frac{\mu_{\mathrm{t}}}{\mathrm{Sc}_{\mathrm{t}}}\right)\frac{\partial \widetilde{\mathrm{Y}}_{\mathrm{S}}}{\partial x_{\mathrm{i}}}\right)+\bar{\dot{\omega}}_{\mathrm{S}} \tag{67}$$

Where $\bar{\rho}$ is the mean gas density, μ and μ_{t} the laminar and turbulent viscosity, Sc and Sc_{t} are the laminar and turbulent Schmidt number, and finally $\bar{\dot{\omega}}_{\mathrm{S}}$ is the average combustion source term. Since three combustion modes are accounted for in this model, the fuel is split into two contributions, one for the unburnt ($\widetilde{Y}^{\mathrm{u}}_{\mathrm{f,u}}$) that is consumed by AI and PF, and one for the burnt gases ($\widetilde{Y}^{\mathrm{b}}_{\mathrm{f,u}}$) that is consumed by DF. Each fuel contribution has its own transport equation (eq.(68) for unburnt

$$\frac{\partial\bar{\rho}\widetilde{\mathrm{Y}}^{\mathrm{u}}_{\mathrm{f,u}}}{\partial t}+\frac{\partial\bar{\rho}\tilde{u}_{\mathrm{i}}\widetilde{\mathrm{Y}}^{\mathrm{u}}_{\mathrm{f,u}}}{\partial x_{\mathrm{i}}}=\frac{\partial}{\partial x_{\mathrm{i}}}\left(\left(\frac{\mu}{\mathrm{Sc}}+\frac{\mu_{\mathrm{t}}}{\mathrm{Sc}_{\mathrm{t}}}\right)\frac{\partial\widetilde{\mathrm{Y}}^{\mathrm{u}}_{\mathrm{f,u}}}{\partial x_{\mathrm{i}}}\right)+\bar{\rho}\tilde{S}^{\mathrm{u}}_{\mathrm{f,u}}+\bar{\omega}^{\mathrm{u}}_{\mathrm{f,u}}-\bar{\omega}^{\mathrm{u}\rightarrow\mathrm{b}}_{\mathrm{f,u}} \tag{68}$$

and eq.(69)) for burnt)

$$\frac{\partial\bar{\rho}\widetilde{\mathrm{Y}}^{\mathrm{b}}_{\mathrm{f,u}}}{\partial t}+\frac{\partial\bar{\rho}\tilde{u}_{\mathrm{i}}\widetilde{\mathrm{Y}}^{\mathrm{b}}_{\mathrm{f,u}}}{\partial x_{\mathrm{i}}}=\frac{\partial}{\partial x_{\mathrm{i}}}\left(\left(\frac{\mu}{\mathrm{Sc}}+\frac{\mu_{\mathrm{t}}}{\mathrm{Sc}}\right)\frac{\partial\widetilde{\mathrm{Y}}^{\mathrm{b}}_{\mathrm{f,u}}}{\partial x_{\mathrm{i}}}\right)+\bar{\rho}\tilde{S}^{\mathrm{b}}_{\mathrm{f,u}}+\overline{\dot{\omega}}^{\mathrm{b}}_{\mathrm{f,u}}-\overline{\dot{\omega}}^{\mathrm{u}\rightarrow\mathrm{b}}_{\mathrm{f,u}} \tag{69}$$

with source terms due to evaporation $\widetilde{\dot{\mathrm{S}}}^{\mathrm{u}}_{\mathrm{f,u}}$ and $\widetilde{\dot{\mathrm{S}}}^{\mathrm{b}}_{\mathrm{f,u}}$ that regulates the production of $\widetilde{Y}^{\mathrm{u}}_{\mathrm{f,u}}$ and $\widetilde{Y}^{\mathrm{b}}_{\mathrm{f,u}}$ respectively. The source term accounting for the evaporation splits the fuel addition to fresh and burnt gas proportionally to the combustion progress variable ($\widetilde{c}$) and its complement ($1-\widetilde{c}$) respectively. Moreover, the fuel mass transfer from unburned to burnt region is modelled by the sink term $\bar{\dot{\omega}}^{u\rightarrow b}_{\mathrm{f,u}}$, whereas the rates $\bar{\dot{\omega}}^{\mathrm{u}}_{\mathrm{f,u}}$ and $\bar{\dot{\omega}}^{\mathrm{b}}_{\mathrm{f,u}}$ are the oxidation rates associated with AI-PF and DF respectively.

Another important aspect of this model is the fuel tracer (TF). As described in eq.(65), the local combustion progress can be described as the local burned fuel mass fraction, which is proportional to the fraction of the oxidized fuel due to the mass conservation through the thin reaction zone. More specifically, $\widetilde{Y}_{\mathrm{TF}}$ is the mass fraction of fuel before the combustion onset (e.g., after a spark and ignition delay). The main feature of this pseudo-species $\widetilde{Y}_{\mathrm{TF}}$ is that it undergoes convection and diffusion like a real species, but it is not consumed during the combustion progress, and it can increase only because of the evaporation $\widetilde{\dot{S}}_{\mathrm{f}}$ (eq.(70)).

$$\frac{\partial\bar{\rho}\widetilde{\mathrm{Y}}_{\mathrm{TF}}}{\partial t}+\frac{\partial\bar{\rho}\tilde{u}_{\mathrm{i}}\widetilde{\mathrm{Y}}_{\mathrm{TF}}}{\partial x_{\mathrm{i}}}=\frac{\partial}{\partial x_{\mathrm{i}}}\left(\left(\frac{\mu}{\mathrm{Sc}}+\frac{\mu_{\mathrm{t}}}{\mathrm{Sc}_{\mathrm{t}}}\right)\frac{\partial\widetilde{\mathrm{Y}}_{\mathrm{TF}}}{\partial x_{\mathrm{i}}}\right)+\bar{\rho}\tilde{\mathrm{S}}_{f} \tag{70}$$

Analogously, tracers are defined also for other species: O_2, CO, NO, H_2, and soot.

2.4.4.3 Flame index and alternatives from the literature To switch between libraries, a test condition to assess the predominant combustion mode must be identified. The desired features of the switch should be:

- it should enable the test of the predominant combustion mode using the main quantities of the 3D-CFD combustion model
- the test condition should produce a switch from the premixed library to the one based on the diffusive reactor only in the specific cell in which the test set a positive logic value for the combustion mode switching to locally diffusive
- the switch inputs for testing should be from the combustion model quantities and from the transport equation of the main species (e.g. reactants), the output should be able to successfully communicate to the soot model when to switch from one to another library dynamically accordingly to the switch-test results.

As first step, the main examples available in literature are described. One of the classical conditions for assessing if the combustion is predominantly premixed or diffusive, is the Flame Index (FI) by Yamashita et al. [128]: in this case for a 2D computational domain, the test is carried out based on the sign of the reactant gradients, that identify if the streams of the fuel and of the oxidizer are diffusing in the same direction (positive value), or not (negative value). The study suggested by Yamashita et al. shown that the flame structure is an ensemble of instantaneous local premixed, diffusion, and partially premixed flames, thus they proposed a flame index based on the spatial gradient of fuel and oxidizer as an index to distinguish premixed flames from diffusion flames (Figure 28).

The same concept, but with the normalization of the FI, was proposed by Rosenberg et al. [129], this time accounting only for the maximum values of the gradients of the reactants mass fractions grad($Y_{\mathrm{F,max}}$) and grad($Y_{\mathrm{O,max}}$). Another example of flame index can be found in Domingo's study [130], in which DNS simulations of a weakly-turbulent lifted flame are carried out for both gaseous and liquid fuel spray. This time, the $\xi_{\mathrm{FI,n}}$ is normalized, and it ranges from 0 (fully premixed) to 1 (diffusive). This definition of flame index was also employed by Som et al. [131], $\xi_{\mathrm{FI,mod}}$ with only one alteration: CO, the product of incomplete

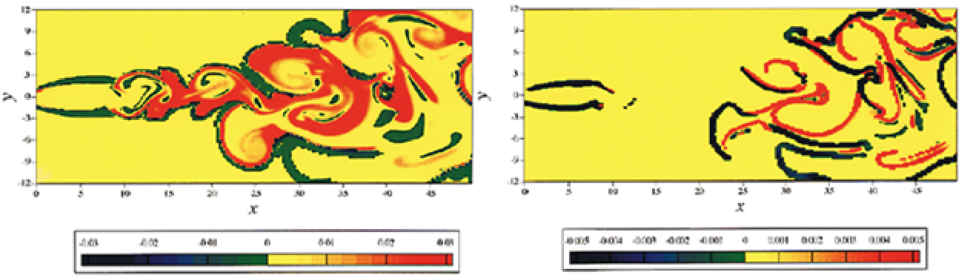

Figure 28: Mixedness (left) and flame index (right) for a diffusion flame by Yamashita et al.[128]

combustion, is used instead of the fuel to distinguish the rich-premixed region from the non-remixed ones. A summary of the formulation of FI in literature is depicted in Table 13. On a final note, a mention of works that distinguish between premixed and non-premixed combustion can be based on a *non-flame-index* definition, such as those conducted by Knudsen and Pitsch [132], Pierce et al. [133], and finally, Ihme [134]. These lasts are not explored, since they are not relevant to the flame-index idea selected in this work.

2.4.4.4 Proposed alternative index - HPOST-FI Within this framework, two alternatives to the FI defined by the literature were proposed after testing the index proposed by Yamashita [128] first, and Rosenberg [129] then. Prior to the description of the alternatives, the implementation of the classical definition of FI [128] and its results are briefly described for the test case. A one-degree GDI engine sector is employed for testing all the FI, with a liquid film initialization on the walls, to increase the chance of local diffusive combustion phenomena, since the local gradient of fuel will go from the wall towards the mixture and not just the oxidizer stream since the aim is to have the evaporation of as much fuel as possible in GDI engine. Two versions of the FI [128] are implemented and tested in the CFD case: the original version (Table 13) and the normalized version (eq.(71)). The test condition for the switch should be able to spot reliably the type of combustion that occurs in the cell and the test should be carried out every

Table 13: Summary of the flame index available in the literature.

Author	**CFD framework**	**Flame index definition**
[128]	Numerical study on flame stability at the transition point of jet diffusion flame. (2D time-dependent flow).	$\mathrm{FI} = \mathrm{grad}\, Y_{\mathrm{F}} \cdot \mathrm{grad}\, Y_{\mathrm{O}}$ $\mathrm{TFI} > 0 \rightarrow$ Premixed $\mathrm{TFI} < 0 \rightarrow$ Diffusive
[129]	Experimental measurements in a burner with LIF to evaluate reactants gradients and their statistical analysis.	$\xi_{\mathrm{FI}} = \left(\frac{\mathrm{grad}\, Y_{\mathrm{F,max}} \cdot \mathrm{grad}\, Y_{\mathrm{O,max}}}{\left\|\mathrm{grad}\, Y_{\mathrm{F,max}} \cdot \mathrm{grad}\, Y_{\mathrm{O,max}}\right\|} \right)$ $\xi_{\mathrm{FI}} = 0 \rightarrow$ Premixed $\xi_{\mathrm{FI}} = 1 \rightarrow$ Diffusive
[130]	DNS analysis of partially premixed combustion in spray and gaseous turbulent flame-bases stabilized in hot air.	$\xi_{\mathrm{FI,n}} = \frac{1}{2} \left(1 + \frac{\mathrm{grad}\, Y_{\mathrm{F}} \cdot \mathrm{grad}\, Y_{\mathrm{O}}}{\left\|\mathrm{grad}\, Y_{\mathrm{F}} \cdot \mathrm{grad}\, Y_{\mathrm{O}}\right\|}\right)$ $\xi_{\mathrm{Fl,n}} = 0 \rightarrow$ Premixed $\xi_{\mathrm{FI,n}} = 1 \rightarrow$ Diffusive
[131]	A modified flame index is employed to distinguish the flame structure, which indicates a dual combustion mode.	$\xi_{\mathrm{FI,mod}} = \frac{1}{2} \left(1 + \frac{\mathrm{grad}\, Y_{\mathrm{CO}} \cdot \mathrm{grad}\, Y_{\mathrm{O_2}}}{\left\|\mathrm{grad}\, Y_{\mathrm{CO}} \cdot \mathrm{grad}\, Y_{\mathrm{O_2}}\right\|}\right)$ $\xi_{\mathrm{FI,mod}} = 0 \rightarrow$ Rich Premixed $\xi_{\mathrm{FI,mod}} = 1 \rightarrow$ Non Premixed

time before spark time (for SI and GDI engines) until in all the computational domain, the combustion progress variable is such that the combustion is completed. The implemented versions of FI are not suitable for the employed combustion model and for this type of combustion, whereas they are suitable for jet diffusion flames. The test for the flame index is carried out on a one-degree engine sector, whose bore is 96 mm, which is the same grid employed for the first stage of the switch testing. As shown in Figure 30 and in Figure 31, the spatial gradients of the reactant oxygen and fuel are depicted. As for the dimensionless approach, the possible values range from -1 (diffusive) to +1 (premixed). In eq.(71), the denominator is purposely chosen so that, on the one hand, FI is equal to zero only when the sum of the products of partial derivatives is equal to zero, but at least two of them differ from zero. On the other hand, a denominator equal to zero means that all the gradients are null. In this case, the dimensionless FI is artificially set to -1.2 as an arbitrary choice for numerical reasons. For the FI implementation in conjunction with ECFM-3Z, for both the classical expression by [128] and the dimensionless one (eq.(71)) the following issues arise from the test case:

- Cell-wise values of FI must be calculated with active scalars (not with tracers). For example, with a stratified mixture, FI based on tracers would improperly yield diffusive combustion, although the latter is fully premixed. Again, with homogeneous mixtures, FI would be null, preventing the detection of the combustion mode. In Figure 60, the dimensionless FI, whose result is more intuitive since it ranges from -1 to +1, is depicted against the value of the combustion progress variable RVB.
- FI should be calculated only in the reaction zone otherwise null values should be expected in the burned region (thus preventing the detection of the combustion mode). In case the gradients in the burned region were not null, misleading values of FI may be encountered.

$$\mathrm{FI} = \frac{\nabla \mathrm{Y_F} \cdot \nabla \mathrm{Y_{O2}}}{\left|\frac{\partial \mathrm{Y_F}}{\partial x} \cdot \frac{\partial \mathrm{Y_{O2}}}{\partial x}\right| + \left|\frac{\partial \mathrm{Y_F}}{\partial y} \cdot \frac{\partial \mathrm{Y_{O2}}}{\partial y}\right| + \left|\frac{\partial \mathrm{Y_F}}{\partial z} \cdot \frac{\partial \mathrm{Y_{O2}}}{\partial z}\right|} \tag{71}$$

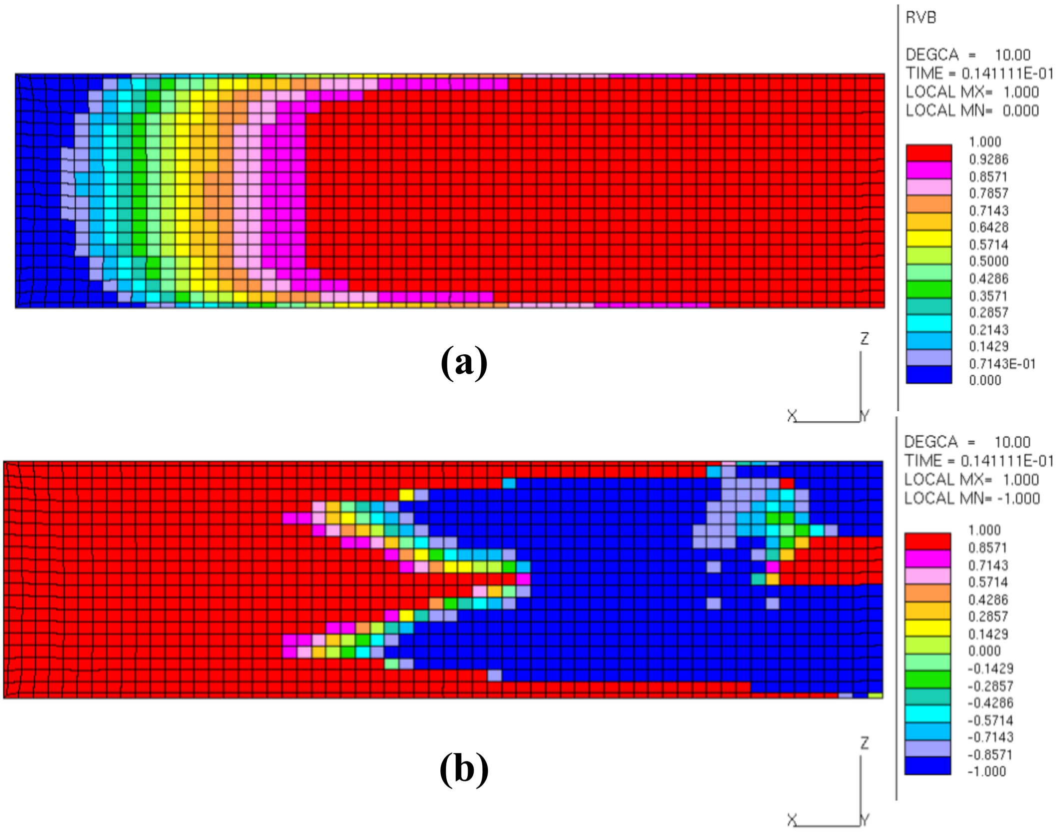

Figure 29: Comparison for the test case of RVB (1 for completely burnt mixture, 0 for completely unburnt mixture) and dimensionless FI (as per eq.(72), -1 fully diffusive, +1 fully premixed). RVB form ECFM-3Z model [102] and FI implemented via user subroutine. The engine sector length is $\sim$ 48 mm, which corresponds to half of the piston bore.

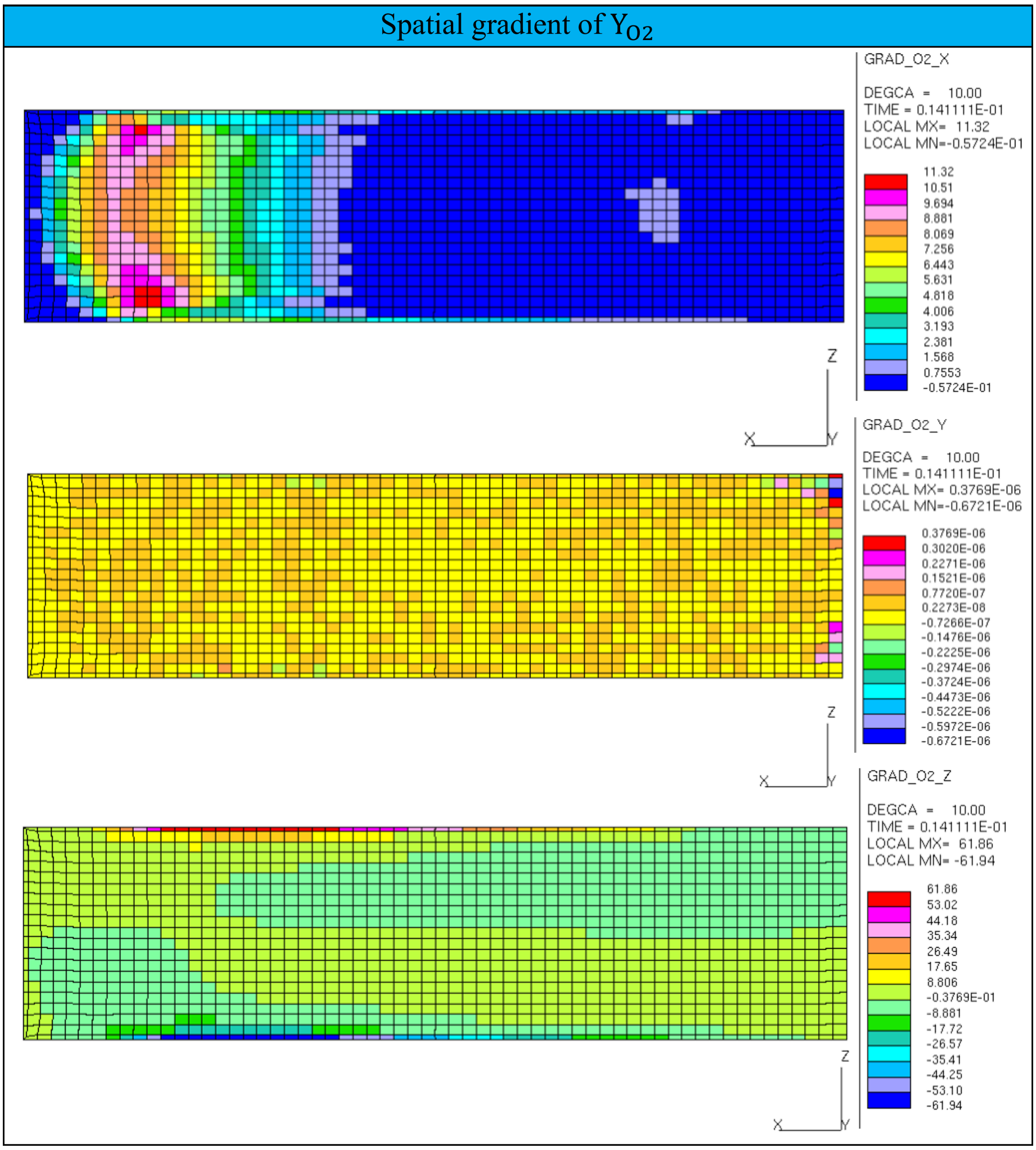

Figure 30: Cell-wise values of spatial gradients of the oxygen mass fraction in x, y, z directions.The engine sector length is ∼ 48 mm, which corresponds to half of the piston bore.

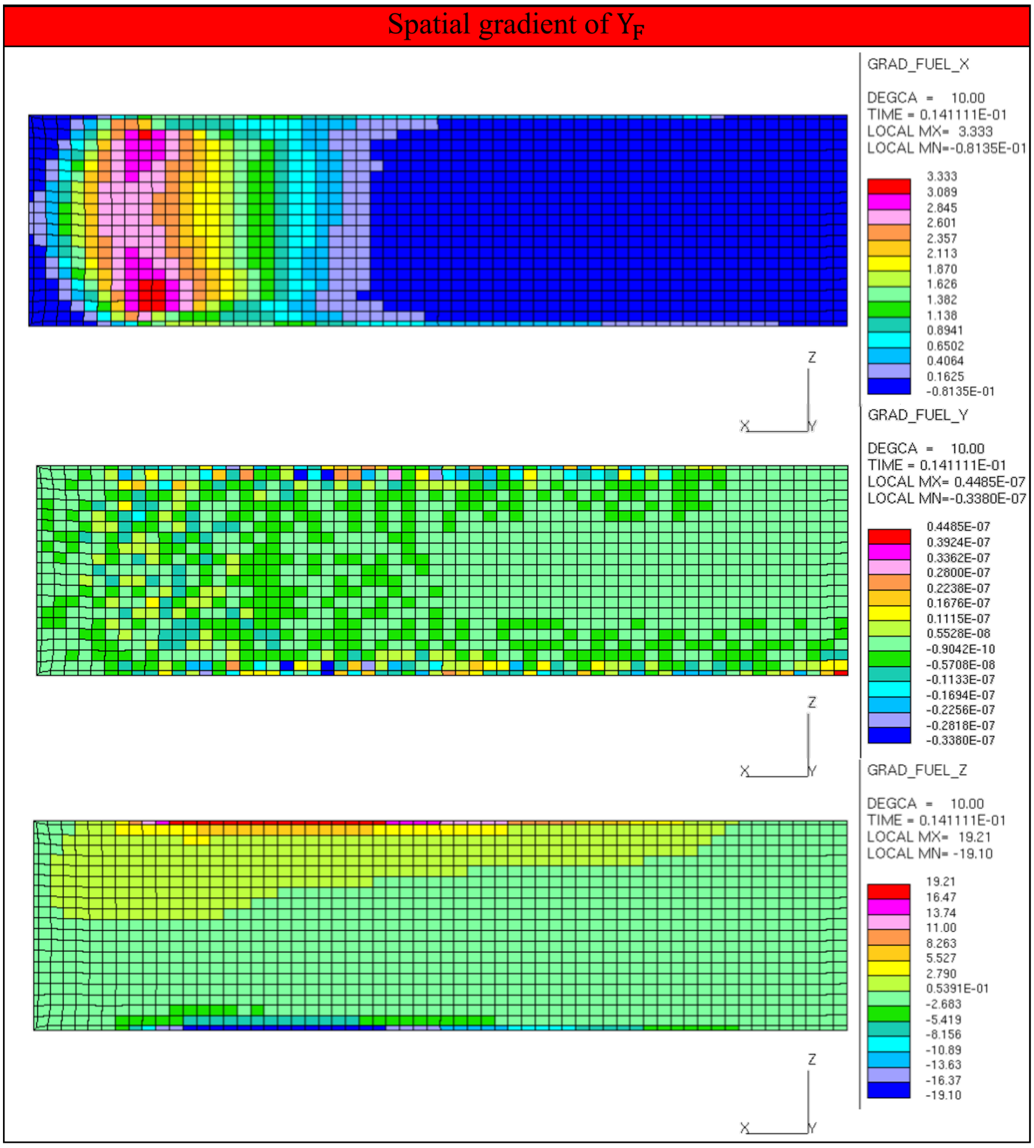

Figure 31: Cell-wise values of spatial gradients of the fuel mass fraction in x, y, z directions.The engine sector length is ∼ 48 mm, which corresponds to half of the piston bore.

$$\text{HPOST-FI} = \frac{\text{HPOST}_{\text{AI}} + \text{HPOST}_{\text{PM}}}{\text{HPOST}_{\text{AI}} + \text{HPOST}_{\text{PM}} + \text{HPOST}_{\text{DF}}} \tag{72}$$

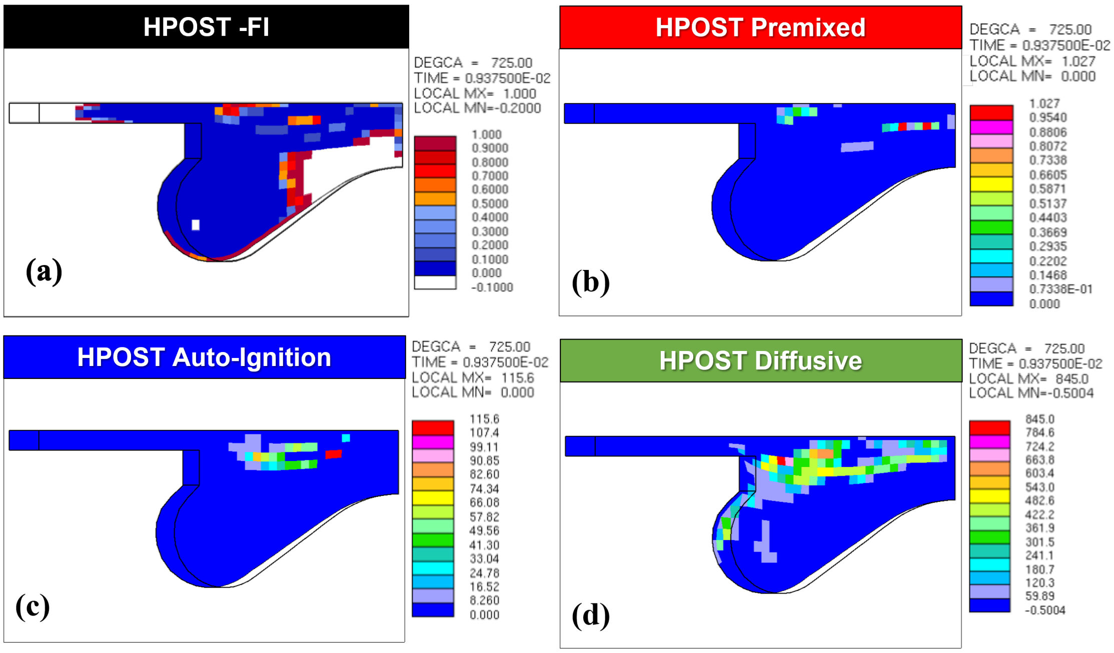

Figure 32: Cell-wise values of HPOST-FI for the CI engine sector test-case (a); distinct contributions of heat released due to each of the three combustion modes represented in ECFM-3Z, premixed (b), autoignition (c), and diffusive (d) five degrees after the TDC.

For these reasons, an alternative strategy is investigated. The first alternative index is based on the heat contribution calculated by the ECFM-3Z combustion model, which can account for three main distinct type of combustion modes: heat released by autoignition ($\mathrm{HPOST}_{\mathrm{AI}}$) (Figure 32 (c)), in this case due to spark, heat by the premixed main flame front ($\mathrm{HPOST}_{\mathrm{PM}}$)(Figure 32 (b)), and finally the diffusive secondary combustion phenomenon ($\mathrm{HPOST}_{\mathrm{DF}}$) (Figure 32 (cd)[102] [103]. The heat released from combustion is employed as a criterion to identify the predominant combustion mode in each cell of the computational domain with the HPOST Flame Index (HPOST-FI), described in eq.(72). If a fully premixed combustion occurs, HPOST-FI is equal to unity. Otherwise, a fully diffusive combustion leads to HPOST-FI equal to zero. If all the contributions are null (no reaction takes place) and HPOST-FI is set equal to -0.2. This index implementation is tested in a CI engine sector with a bowl-shaped piston, fueled with ($C_{12}H_{26}$) which is injected at 590 degrees. The fuel choice is led by the observation that $C_{12}H_{26}$ is characterized by a slower evaporation that better represents the gas oil for a Diesel engine rather than a TRF surrogate fuel. Since the formulation of a representative surrogate is not the focus of the task, $C_{12}H_{26}$ is used. The HPOST-FI results are plotted after five degrees from TDC, and the contribution of the diffusive combustion is expected to be predominant, whereas the autoignition is still present, yet not predominant, and finally the premixed is the less relevant compared to the other two (Figure 32 and 33). As for both FI and HPOST-FI, null values are expected in the burned region. However, to decide which soot library should be adopted, it is necessary to have index that is effective in the burned region as well. For these reasons, an alternative strategy is pursued.

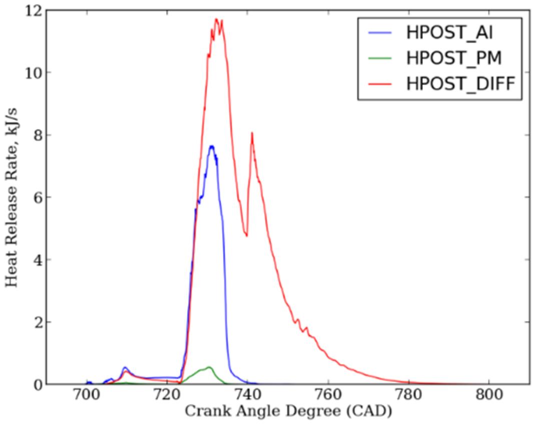

Figure 33: Heat release rate during engine cycle for the CI-engine sector.

2.4.4.5 GruMo Flame Index - GFI In this paragraph, the description of the chosen flame index for implementation is provided. The alternative approach is based on a dedicated passive scalar GTF (GruMo Tracer for Fuel) defined to trace the potential evaporation of the fuel in the burnt gases, thus in cells in which the combustion progress variable is greater than 0.01. This scalar definition is necessary since $Y_{\mathrm{f,b}}$ is consumed and it cannot be adopted to switch between the tables after the combustion ends. At spark time, GTF is initialized equal to Y_{TF}, also referred to as TF. Then, for every timestep and for each cell, if the combustion progress variable (RVB) of the ECFM-3Z model is bigger than the threshold value 0.01 in accordance with the starting value of the combustion progress variable c of the tabulated coefficients (RVB ≤ 0.01), GTF is kept equal to Y_{TF}. In other words, if RVB ≤ 0.01, Y_{TF} accounts for the eventual evaporation of fuel deposits before the combustion onset in the specific cell; conversely, if RVB ≥ 0.01, GTF is not reinitialized as Y_{TF}. For this reason, the difference between GTF and Y_{TF} (DIFFTF) in cells in which RVB ≥ 0.01 is a cell-wise measure of the fuel mass fraction evaporated or diffused because of the liquid deposit evaporation.

$$\mathrm{GFI} = \frac{|\mathrm{Y_{TF}} - \mathrm{GTF}|}{\mathrm{GTF}} \tag{73}$$

Therefore, GTF (eq.(73)) can be used to characterize the conditions that can trigger the secondary combustion mode. The value of the difference between GTF and Y_{TF} can be employed as a switch condition for assessing which is the predominant combustion mode in a specific cell, and consequent assessment of the library switched from the default one (premixed) to the diffusive library. More in detail, if the ratio of DIFFTF and GTF is greater than a specific threshold, the switch from premixed to the diffusive library is carried out, else the library choice stays as premixed.

The logic of the library-switch test is depicted in Figure 34: if the test condition is true, the input values for the reaction rate constants for the soot model are read from the diffusive library, thus switching the input library from the default one, the premixed, for the cells in which the condition is true; otherwise if the condition is false, no switch is carried out. The DIFFTF ratio measures how relevant the increase of fuel evaporated is after the combustion onset in that cell, compared with the previously evaporated fuel, GTF. Thus, a threshold value is arbitrarily set as 0.5, which means the following: in a cell in which the combustion onset has already occurred, the newly evaporated fuel stored in Y_{TF} is compared to the cell-wise value of Y_{TF} at the beginning of the oxidation process (GTF), and if more than 50% of fuel has evaporated, the combustion process is set as predominantly diffusive. Thus the library is switched from the default one to the diffusive one. A schematic representation of the computational fluid dynamic domain is shown in Figure 35: the flame front travels from left to right, where the blue cells are characterized by RVB ≤ 0.01 (no combustion is occurring), then two liquid fuel deposits are present in two cells, and in the one behind the flame front the evaporated fuel increases the value of Y_{TF} and the difference between GTF and Y_{TF} is compared to the threshold value to assess if the library switch should occur.

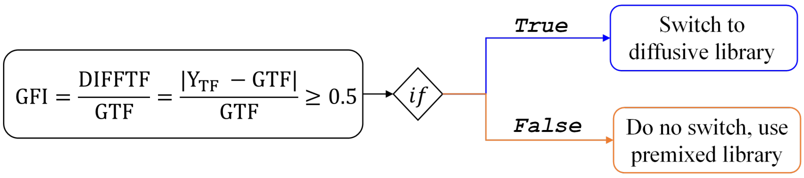

Figure 34: Schematic of switch-test logic for GFI implementation.

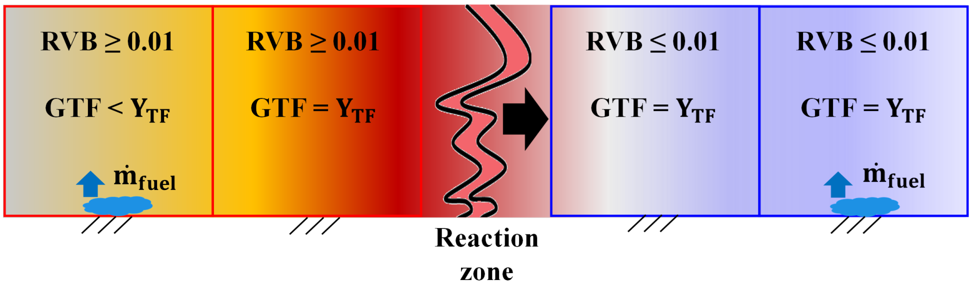

Figure 35: Schematics of the cell-wise evaluation of the implemented quantities for combustion mode definition. GTF, fuel tracer (Y_{TF}), and evaporated fuel mass in each cell with respect of the flame propagation (reaction zone is advancing from left to right).

2.4.4.6 GFI implementation in the code for dynamic library switch

After describing the selected flame index (paragraph 2.4.4.5) in this section, the implementation of the GFI within the combustion and soot model framework is presented. First, the main quantities employed in the test and in the soot reckoning are listed below and their interactions with the combustion model, the soot model, and the new implementation are further clarified in Table 14:

- Y_{TF}: fuel tracer from the combustion model (ECFM-3Z). The model computes it at each iteration via a dedicated transport equation. It is a passive scalar, thus the only "source term" in its transport equation is related to the evaporated fuel.
- GTF: this is a new passive scalar introduced in the source code. It has its own transport equation, and at each iteration it is re-initialized equal to Y_{TF} only if the combustion onset has not occurred yet in that specific computational cell.
- DIFFTF: it is the difference between Y_{TF} and GTF. It is employed in the switch condition.
- Switch condition: the ratio of DIFFTF and GTF is compared to the threshold value. The logic value of this test communicates to the soot model from which library the rate constants should be retrieved. In the case of a true value, the input library is switched from premixed to diffusive.
- The threshold value for the switch is arbitrarily set to 0.5, which means that the library switch occurs when the value of fuel vapor registered at the beginning of the combustion in that specific cell is increased by at least 50%. In cells in which the flame front has not arrived yet, the switch test is not carried out and the GTF is re-initialized as Y_{TF}, and only at the next iteration, the switch may be possible in that cell accordingly to the logic value of the switch test.

The switch test is implemented in the soot model source code. The CFD solver adopted in this work is STAR-CD v4.34 [102], written in Fortran. Out of the many subroutines available, the ones relating to the soot model and the combustion model are employed. In general, the selection of the library is fixed, and it cannot be changed once the simulation is running (no online or dynamic switch). In contrast, the modification aims to make this information dynamically changeable according to the logic value of the switch condition during the simulation.

Table 14: Quantities involved in the input-output of the switch condition.

Quantity	Input from	Output to
Y_{TF}	Combustion model (ECFM)	Switch test, combustion and soot models
GTF	New implementation (soot model)	Switch test, soot model
DIFFTF	New implementation (soot model)	Switch test, soot model

The information of the library is stored in the "EXTENDED DATA", a portion of the text file in which all the simulation setup is stored given the user's instructions. This information is stored in the variable "rsOpt" as an integer that can assume the value of:

- rsOpt = 4 for the diffusive library
- rsOpt = 5 for the premixed library

In the newly implemented modification, the rsOpt value is set as 5, stating that the expected default combustion mode is premixed. This information is initially read by the solver from the simulation setup file, and the initial value assigned to all the computational cells is 5 at the combustion onset. Then, after the combustion onset, the switch condition is cell-wise tested only if the cells where the combustion progress variable RVB is different than null. Accordingly to the logic value of the test, rsOpt is reassigned to each cell where the combustion is occurring and the input values for the soot source term calculation in eq.(50). As shown in Figure 36, after the spark advance (SA), the newly implemented modification computes the variables that will be employed for the test condition for the eventual switch (Table 14). The modification on the source code of the soot model subroutine is communicating with the novel implemented one and the subroutines for the ECFM-3Z model. The interplay between input/output parameters of the subroutines is shown in Figure 36.

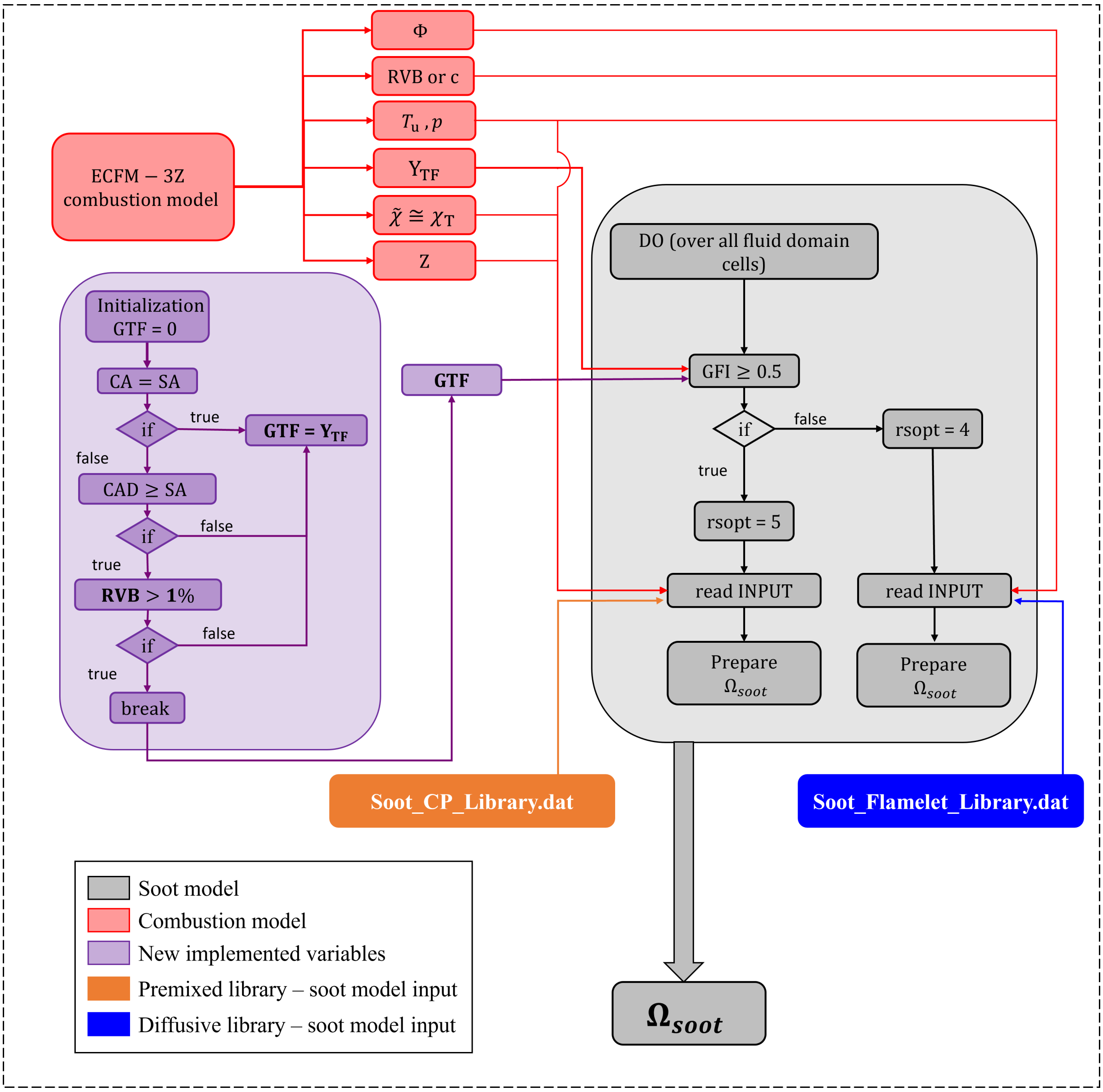

Figure 36: Source code modification: highlights on the combustion and soot model interaction with inputs and outputs, the selection of the tabulated coefficients stored.

Results and Discussion

3. Results and discussion

3.1 TSI spatial distribution for TRF surrogates with different Lagrangian approaches

3.1.1 Engine simulation setup

The surrogates are tested in a simplified model of single-cylinder naturally aspirated engine [15], operated at 2000 rpm at Wide Open Throttle (WOT). For this numerical-to-numerical analysis, the dynamic effects of the crevice volumes, which are considered in a second step of this chapter, are neglected. This approximation is acceptable since the simulation results are collected for the evaporation and right before the spark advance, and the blow-by through the crevice volumes is proportional to the pressure difference between the carter and combustion chamber, and it would be more critical during the expansion stroke. The engine runs with a compression ratio of 10:1 and at average stoichiometric conditions with a nominal injected mass of 28 mg. The Start of Injection is labeled as SOI 300, since the fuel is injected 300 degrees before Top Dead Center firing (bTDC) directly in the combustion chamber with a 6-hole injector, positioned on the symmetry plane. Given the geometric symmetry and the adopted RANS modelling approach for turbulence, saving computational cost can be achieved by using half of the combustion chamber as a fluid domain as shown in Figure 37. The mesh has a minimum number of cells of 112‘000 (at TDC, Figure 37) and a maximum number of cells of 290‘000 (at BDC). For turbulence modelling, a $k - \varepsilon$ RNG is adopted given the successful application in similar studies [15]. Droplets are initialized following the approach proposed in [135] [136] whereas the spray breakup is modelled with Reitz-Diwakar's [137] model and the droplet-wall interaction with Senda's model [138]. Heat transfer is modeled using a recently improved

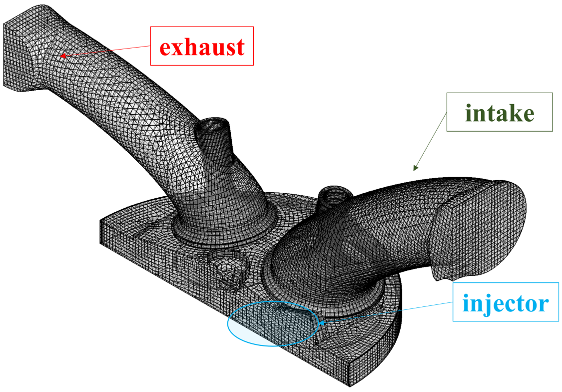

Figure 37: Schematic representation of the computational grid for the engine simulation.

version of the GruMo-Unimore heat transfer model [139] [140] which has proven to be successful in a wide range of engine applications [141]. The cyclic boundary conditions are derived from experimental data and from a 1D engine mode, as discussed for the combustion part in the next paragraphs. Further details on the boundary conditions relevant to this analysis, such as the wall temperatures, are summarised in Table 15

Table 15: Additional boundary conditions, relevant for the multi-phase modelling: wall temperatures set as boundary conditions on the whole engine for the 2000 rpm case. These temperatures stem from either the experimental measurements conducted on this engine, or from the 1D simulation of the whole engine.

Part	Piston Crown	Cylinder Walls	Comb. dome	Spark plug	Intake port	Exhaust port
T_{Wall}	400 K	430 K	450 K	1000 K	319 K	809 K

3.1.2 TSI spatial distribution

In this paragraph, the spatial distribution of cell-wise TSI values is investigated with the purpose to provide a picture of the mixture sooting tendency at spark time. The frozen values analysed are the ones that the flame front potentially will experience during its expansion towards the end-gas region. The relevance of this investigation lies in the use of TRF surrogates that are actually used to fed the real engine in the experimental data for extraction of the boundary conditions, and even further the effect of toluene increasing content can be taken into account.

The TSI spatial distribution is directly related to the local air-fuel ratio AFR α, which in turn depends on the evaporation and mixing in the GDI engine injection and compression phase when the fuel evaporation takes place forming the charge stratification. For this reason, an overview on the evaporation behavior of the TRFs is presented before the results for TSI spatial distribution reported at spark time, which occurs 15 degrees bTDC, as representative conditions experienced by the flame during the propagation in the case of one-step flamelet combustion model. In Table 17 a summary of the thermodynamic conditions at spark time is provided: some scatter in trapped fuel mass can be explained by slight changes of the flow field of the charge during the intake and the spray, whereas the differences between temperatures are a consequence of the limited differences in Heat of Vaporization. The temporal evolution of the spray evaporation is characterized as the percentage of evaporated fuel Evap.% (x-axis) at the corresponding crank angle degree (y-axis) as summarized in Figure 38.

Table 17: Summary of thermodynamic condition in the combustion chamber right before the spark time (15 deg bTDC) for multi-component (M) and lumped-single component (L).

Toluene mol%	**0 (M.)**	**0 (L.)**	**30 (M.)**	**30 (L.)**	**60 (M.)**	**60 (L.)**
Air Index λ	0.96	0.98	1.00	0.98	1.02	1.03
Fuel mass in mg	13.90	13.87	13.65	13.87	13.86	13.81
Air mass in mg	200.9	204.4	200.0	199.3	200.5	202.8
Temperature in K	667	663	674	677	679	678
Pressure in bar	15.58	15.68	15.68	15.69	15.86	15.98

The evaporation delay exhibited by the lumped approach can be addressed to the approximation on the Heat of Vaporization and the partial pressure obtained using Raoult's law. These differences in the global evaporation rate have an impact on the charge stratification at spark time, as indicated by both the equivalence ratio scalar field Figure 39 and the cell-wise occurrence frequency of equivalence ratio in Figure 40. In particular, as shown in Figure 39, there are differences between the lumped single-component and the multi-component approach.

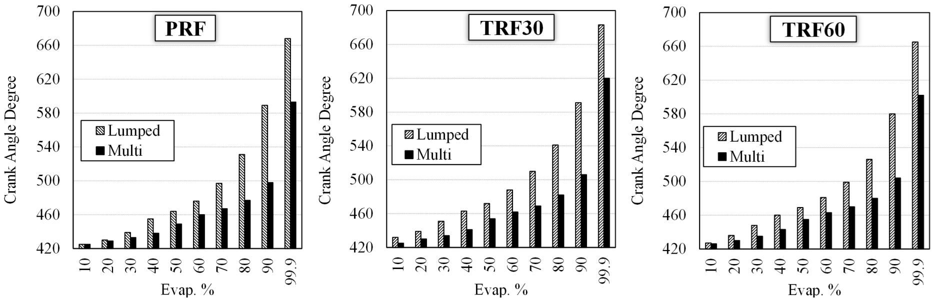

Figure 38: Evaporation description: multi-component (full) and lumped-single component (striped) evaporation percentages on the x-axis at the corresponding crank angle degree (CAD) on the y-axis.

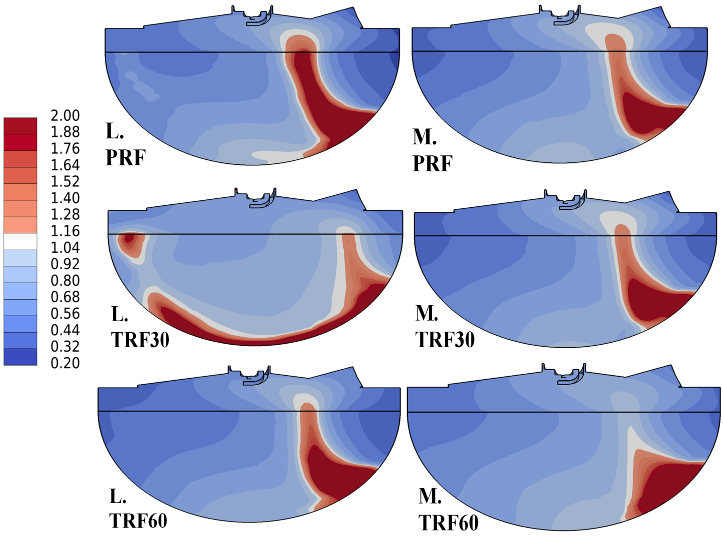

Figure 39: Equivalence ratio scalar field at spark time for lumped-single component (L.) and multi-component (M.) at spark time.

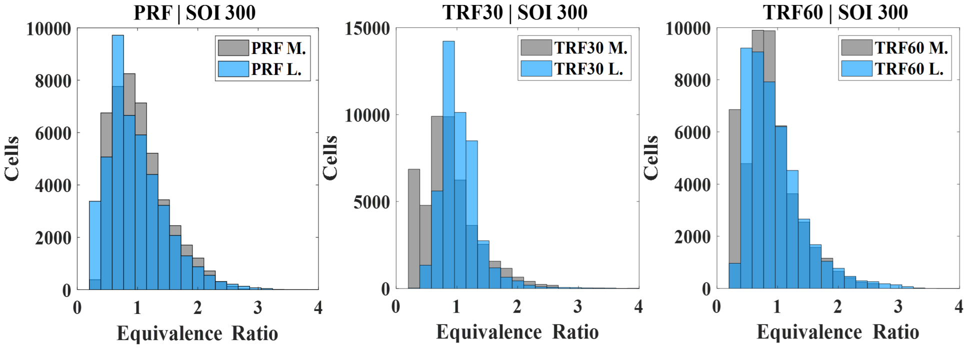

Figure 40: Histogram of cell-wise values of equivalence ratio for lumped-single component (L.) and multi-component (M.) at spark time.

A possible explanation of these different charge stratification, very evident for TRF30, can be the treatment of the Lagrangian phase transition between liquid to vapor state. More specifically, the multi-component approach employs the UNIFAC model that seems to be more effective in modelling the fuel evaporation, while keeping a coherent trend for the three surrogates with increasing toluene content. Conversely, the lumped approach yields a global trend coherent with the increasing toluene content if one account only for the evap% in Figure **??**, but it fails near wall ($T_{\text{wall,cyl}}$ and $T_{\text{wall,piston}}$ set to 400 K). Near the walls, the evaporation description can be more sensible to the temperature since both the heat of evaporation and saturation pressure are expressed as a function of temperature, hence the polynomial representation may be faulty. Since the PRF does not exhibit any critical difference with respect of the multi-component approach since it is mostly composed by one constituent, hence the differences in the evaporation behavior that may rise when using a simple Rault's law or the UNIFAC are less evident. Apparently, these differences are relevant for the TRF30 only case in which the mole fractions of the component have no stark difference. Althought the three surrogates are characterized by a similar T_{b}, the actual composition plays a role in the local evaporation pattern, once again highligting the importance of a multi-component approach for the cases in which there is no stark predominance of on of the three components.

Moving on to the sooting tendency, for the multi-component approach, the cell-wise TSI value is calculated by user coding and a linear-by-mole mixing rule $\sum_i (x_{\text{i}} \cdot \text{TSI}_{\text{i}})$ using the cell-wise values of the mole fractions of each component i and the TSI values [14]. As for the lumped approach, the mole fraction of the user defined fuel and the final surrogate value of TSI for the TRF blend are employed. The frequency of the occurrence of the TSI values in the domain is shown in Figure 41: the histograms of the multi-component and the one of the lumped approach are superimposed to highlight the eventual discrepancies, which as expected are very limited for the PRF, while they tend to increase for the TRF30 and TRF60 blends. Once again, the case of TRF30 is the one characterized by starker differences between the two approaches for the reasons discussed previously.

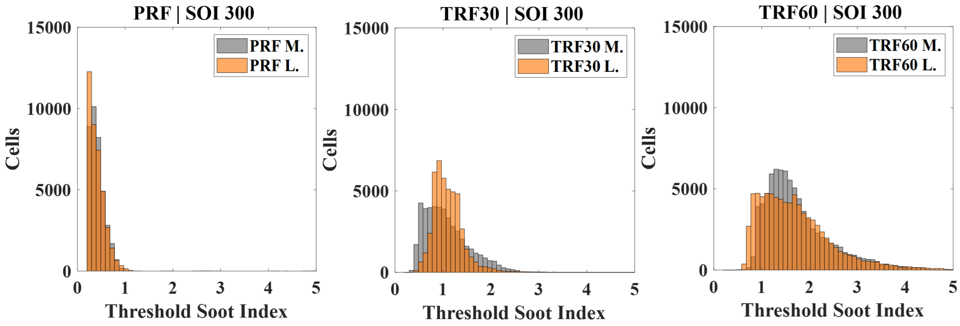

Figure 41: TSI cell-wise values histogram at spark time.

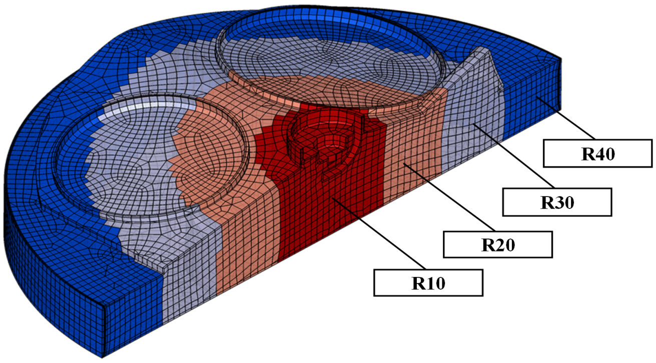

Figure 42: Schematic representation of the sectors of the fluid-dynamic domain.

Table 19: Sector TSI value: comparison between single-lumped (L) and multi-component (M) for each sector, both absolute values and the percentage error (err%) calculated as the difference between single-lumped and multi-component.

	Sector 1	**Sector 2**	**Sector 3**	**Sector 4**	**Tot. aver.**
R_i, mm	0	10	20	30	
R_i, mm	10	20	30	40	
ID	R10	R20	R30	R40	
PRF-M	0.342	0.371	0.409	0.409	0.397
PRF-L	0.315	0.360	0.394	0.420	0.393
TRF30-M	0.902	0.989	1.104	1.122	1.075
TRF30-L	0.871	0.959	1.059	1.238	1.106
TRF60-M	1.427	1.541	1.735	1.934	1.765
TRF60-L	1.346	1.548	1.758	1.828	1.719
err% PRF	8%	3%	4%	-3%	1%
err% TRF30	3%	3%	4%	-10%	-3%
err% TRF60	6%	0%	-1%	5%	3%

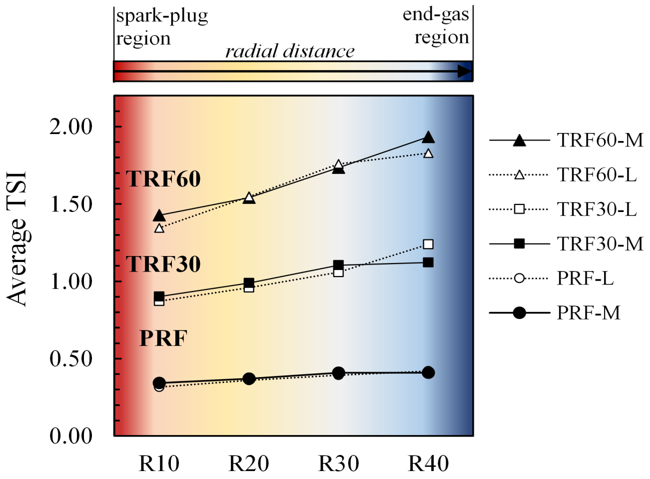

Figure 43: Cell-wise average TSI for each sector for multi-component (full dot) and lumped-single component (empty dot) at spark time.

To further characterize the TSI spatial distribution, a subdivision of the computational domain in coaxial cylindrical sectors is achieved by varying the radius of the sectors from 0 mm to 40 mm, with a 10 mm stepping. To each sector (Figure 42) an average value is reckoned as the algebraic average of all the TSI values in the cells belonging to that subsector. A satisfying agreement between the two Lagrangian phase modelling approaches is observed for the averaged TSI, as reported in Figure 43. The values reported in Figure 43 and Table 20 portrait the initial sooting tendency of the mixture that the flame front encounters during its propagation throughout the combustion chamber. However, local maxima of TSI also influence the soot formation, thus it is of use to spot cell-wise differences obtained with the two approaches. In Figure 44, the TSI cell-wise distributions of high-TSI thresholds are reported as a complementary information to their averaged counterparts.

A satisfying agreement for PRF is reached, whereas increasing variations of the TSI pattern can be spotted for the two TRFs. The numerical comparison between a single-component approach and a multi-component approach in DISI engine focuses on predicting sooting tendency of the stratified charge. Three surrogate

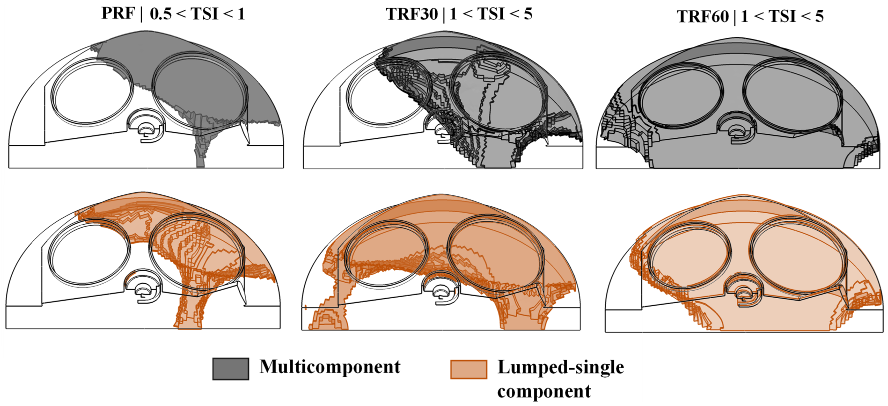

Figure 44: Local TSI distribution in the combustion chamber at spark time.

fuels, characterized by an increasing toluene content, are investigated. In addition, the methodology for deriving temperature-dependent vapor and liquid phase properties for the lumped approach is presented since it is necessary to examine to what extent the results provided by the lumped approach differ from the one stemming from the more detailed multi-component with UNIFAC modelling. The results highlighted that the lumped approach yields a slight evaporation delay for each surrogate compared to the multi-component one. This effect has a limited, yet observable, impact on the charge stratification for TRF30 and TRF60. For all the surrogate blends, a satisfying agreement of the radial TSI averaged value is achieved between the two approaches. The spatial distribution of TSI peaks is very similar for the PRF surrogate while increasing deviations between the single-component and the multi-component fuel representations are observed for the toluene-doped blends.

On a final remark, the lumping method presented works properly in mixtures comprising similar components. In the case of different compounds accounted for in the mixture of the PIONA (Paraffins, Iso-paraffins, Olefins, Naphthenes, Aromatics) surrogate, such as alcohols (e.g. ethanol), non-linear blending effects can be observed (e.g., azeotropic behavior). In his case, a linear mixing rule may yield some errors.

3.2 Laminar burning velocity correlations and flame speed for CFD codes

3.2.1 TRF surrogates fuels and mixing rule

Continuing with the characterization and modelling of the TRF surrogates in engine simulations, the next step is the flame propagation modelling. In this paragraph, the correlations derived using the procedure discussed in the methodology section are examined and applied to an engine simulation. As first thing, the values of laminar burning velocities predicted by the correlations are compared to the values calculated with chemical kinetics simulations to measure the prediction error due to the fitting. The values predicted by the use of the extended methodology previously discussed and the reference data from chemical kinetics $s_{\mathrm{L,ref}}$ are compared to evaluate the normalized prediction error calculated as the $\left(\left(s_{\mathrm{L,fit}} - s_{\mathrm{L,ref}}\right)/s_{\mathrm{L,ref}}\right) \cdot 100$. The majority of the results lie below 5%, with some exceptions at the extremal values of the independent variable (e.g. Φ 1.9) as shown in Figures 45-46-47. However, the values of interest for this study are characterized by peak pressures around 40 bar and equivalence ratios near stoichiometry. The coefficients relating to the fitting expressions are reported in Appendix A (4).

3.2.1.1 Engine simulation results for the mixing rule In this paragraph, the following subsections are presented:

- Experimental engine and tests
- Boundary conditions and 1D engine model
- 3D-CFD engine simulation setup

For testing the laminar flame speed and the Le Chatelier's mixing rule, an engine geometry is needed for generating the computational fluid domain, as well

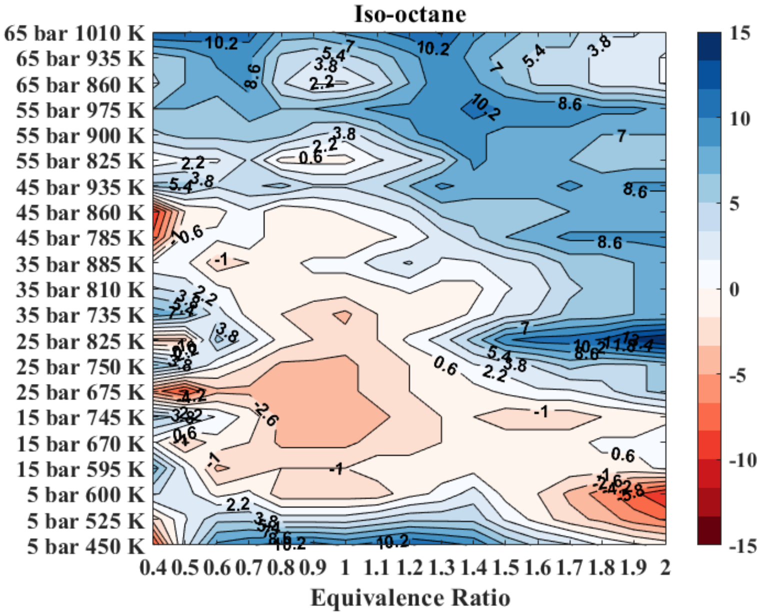

Figure 45: Prediction error between values of laminar flame speed predicted by the correlation and the actual values from chemical kinetics for iso-octane.

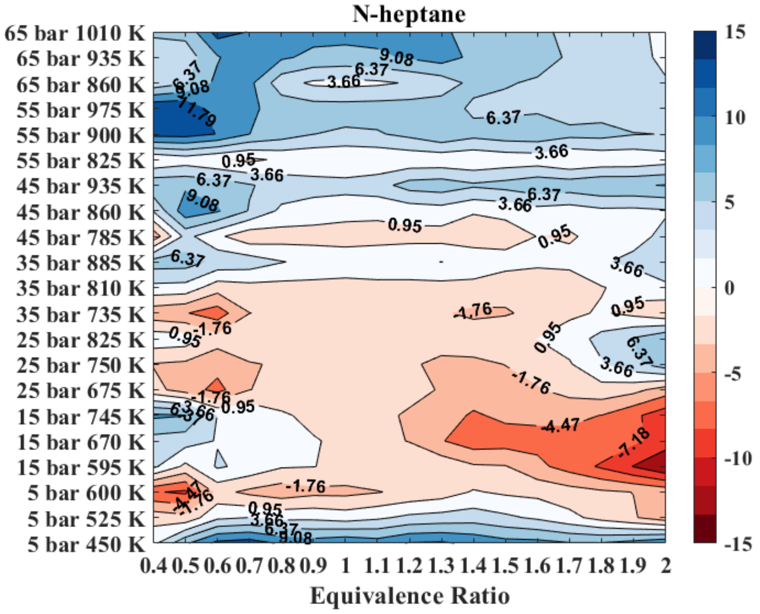

Figure 46: Prediction error between values of laminar flame speed predicted by the correlation and the actual values from chemical kinetics for n-heptane.

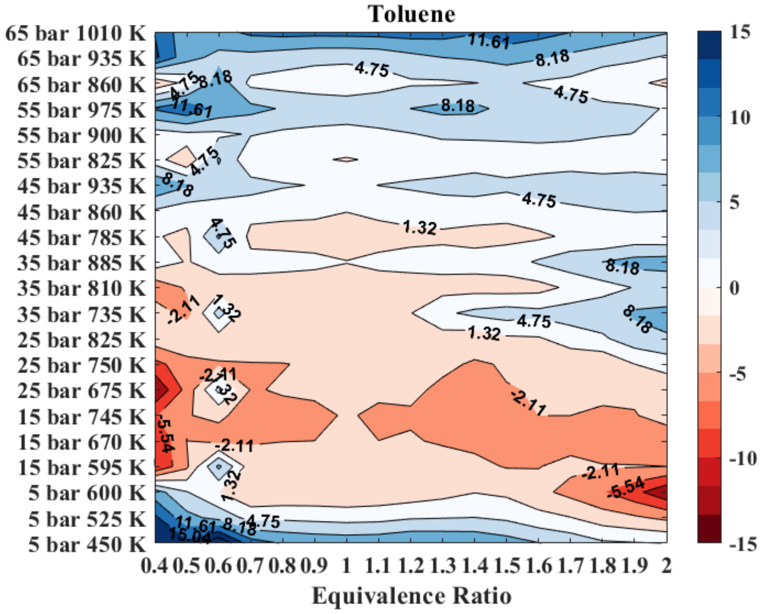

Figure 47: Prediction error between values of laminar flame speed predicted by the correlation and the actual values from chemical kinetics for toluene.

as boundary conditions. Data provided by an actual single-cylinder research engine with optical access are provided by the STEM-IM Centro Ricerca Nazionale (CNR) of Napoli, within collaboration with the research group Gruppo Motori (GruMo) of the University of Modena and Reggio Emilia. The experimental campaign was conducted using actual surrogate fuels, not just commercial gasoline. This last is necessary for the comparison of the pressure traces and the heat released for validating the surrogates. This way, it is possible to assess how close they are to the actual commercial gasoline. The tests are carried out for each of the fuels (PRF95, TRF30, TRF60) with three different Start of Injection (SOI) time to explore the impact of the fuel charge stratification in the GDI engine.

The average value of air index $\lambda \sim 1$ is measured with the lambda-probe at the exhaust, thus, having different α_{st} the injected mass for the three surrogate fuels is slightly varied to adjust to $\lambda \sim 1$. The in-cylinder pressure traces measured from the experiments of the three surrogates are very close to the original gasoline, with differences that are not remarkable as shown in Figure 48.

Table 21: Engine description.

Engine type	GDI - single cylinder
Engine revving speed	2000 rpm
Bore	79 mm
Rod length	81.3 mm
Squish height	5.6 mm
Compression ratio	∼10
Injection timing (SOI)	260, 300, 340 deg bTDC
Intake pressure	∼1 bar and naturally aspirated
Injected fuel	mass ∼28 mg
Spark Advance	705 deg (-15 bTDC)
Mean air index λ	1
Investigated fuels	PRF95, TRF30, TRF60, commercial gasoline

A summary of the engine geometric features and geometrical parameters is provided in Table 21. The optical access has implications for the engine geometry and operation: since the quartz window is needed for image acquisition, the lubrication of the upper part of the cylinder is not possible, instead low-friction Teflon piston rings are employed. Moreover, the thermal expansion of the piston is fast and after ∼200 cycles, the engine should be stopped to avoid piston gripping. This facet of the optically accessible engine requires specific care in the 1D model as well as the 3D-CFD one. Since the Teflon rings cannot provide optimal sealing, a small portion of the fresh mixture in the combustion chamber is filtered toward the carter during the compression stroke and vice versa during the expansion phase. This phenomenon is known as blow-by, and it is present in this type of research engines, as well as the old ones with consumed piston rings. The blow-by effect is a partial reduction of the peak pressure, and it is modelled by using an additional dead volume at the bottom of the piston, in the same fashion as what happens in the real case as shown in Figure 52. The crevice length is 46 mm, and the thickness is 0.5 mm, and at the bottom of it the mass flow boundary is set for the 3D model, and the equivalent is done in the 1D model. As first thing,

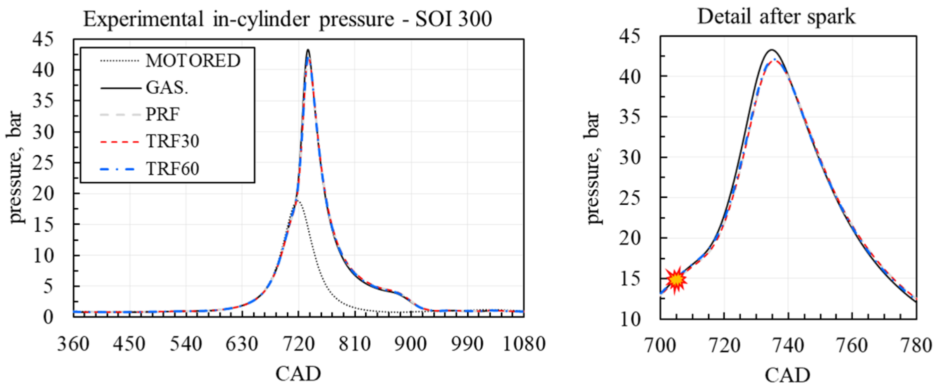

Figure 48: Experimental in-cylinder pressure traces of the real gasoline with the surrogates; detail of the active phase to the right. Results are reported for SOI 300.

the 1D model is set and simulated using GT-POWER [142]: the block scheme of the entire engine is simulated as shown in Figure 86 (enlarged scheme in the appendix, Figure **??** in 4).

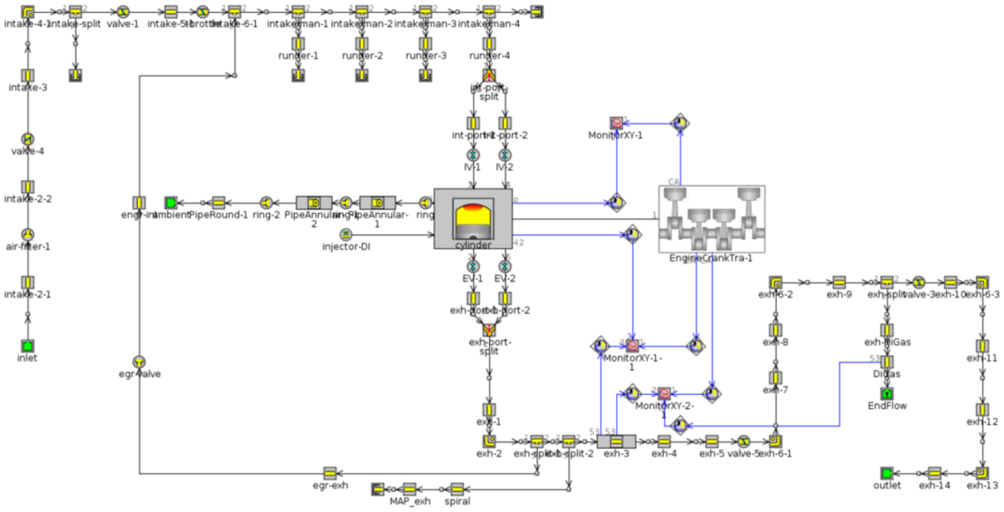

Figure 49: Block scheme of the whole engine 1D simulation.

In Figure 50 the 1D simulation results are in satisfying agreement with the experimental available data, pressure traces, and additional details are reported in Table 23.

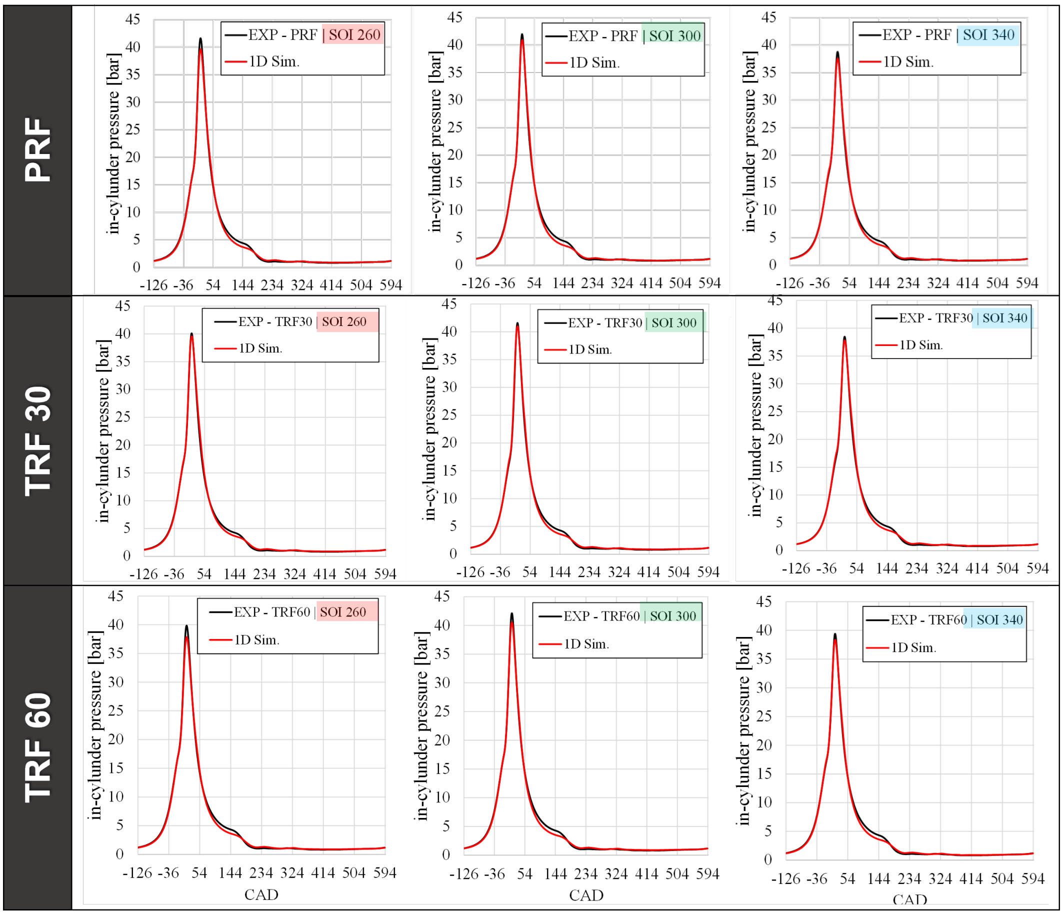

Figure 50: Experimental and 1D simulation results: comparison of the pressure traces for each surrogate at different SOIs.

The main aim of the 1D model is the extraction of cyclic boundary conditions for the 3D-CFD engine simulation on the base of the experimental results: the intake and exhaust pressure, in-cylinder pressure, and finally the blow-by mass flow rate. However, it is fundamental that these values are extracted from the 1D model at the corresponding point of the 3D-CFD geometry. Whereas for the crevice and the in-cylinder pressure no problem arises, the intake and the exhaust values must be probed at a specific length in the respective manifold as shown in Figure 51.

Once the cyclic boundary conditions for the 3D-CFD engine simulation are derived, the next step is to check the mass trapped in the cylinder: since no mass

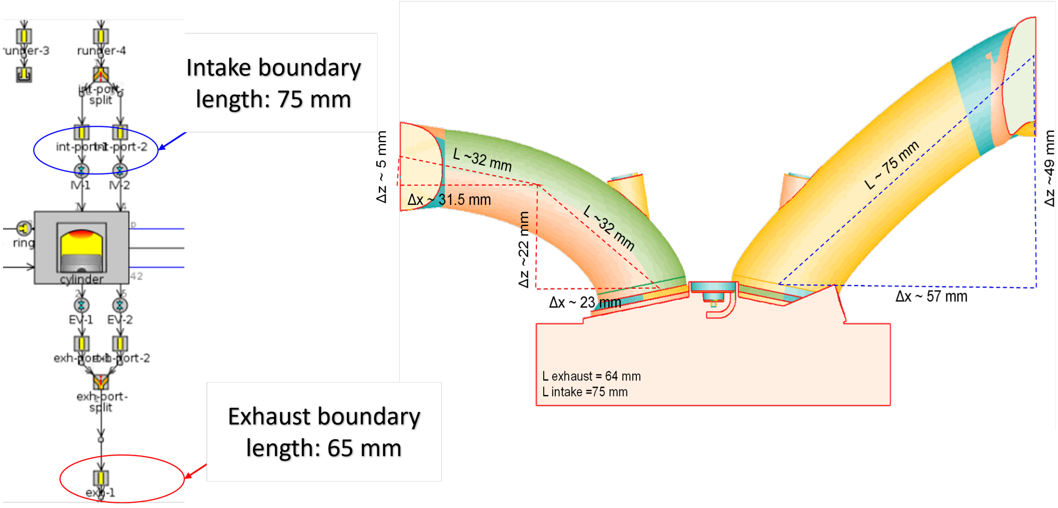

Figure 51: Probing distance in the intake and exhaust manifolds for the boundary conditions extraction.

Table 23: Summary of peak pressure and the corresponding crank angle. Experimental results are averaged over the measured 200 cycles.

		SOI260		SOI 300		SOI 340	
		bar	deg	bar	deg	bar	deg
PRF95	* EXP	41.6	15.0	42.0	15.6	38.6	16.6
	1D sim.	39.6	16.0	40.9	16.0	37.6	18.0
TRF30	* EXP	40.1	15.6	41.6	15.4	38.4	16.6
	1D sim.	39.6	16.0	41.0	16.0	37.8	18.0
TRF60	* EXP	39.8	15.8	42.1	15.6	39.4	16.6
	1D sim.	37.8	16.0	40.5	16.0	38.4	17.0

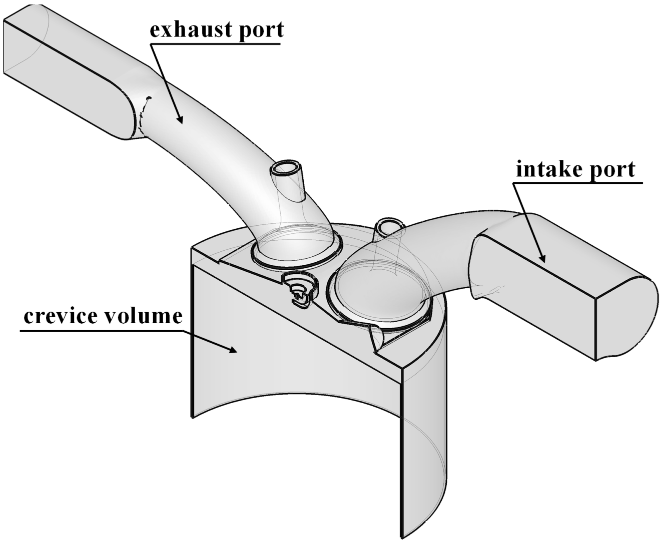

Figure 52: Fluid domain equivalent to the real engine; the crevice volume is highlighted.

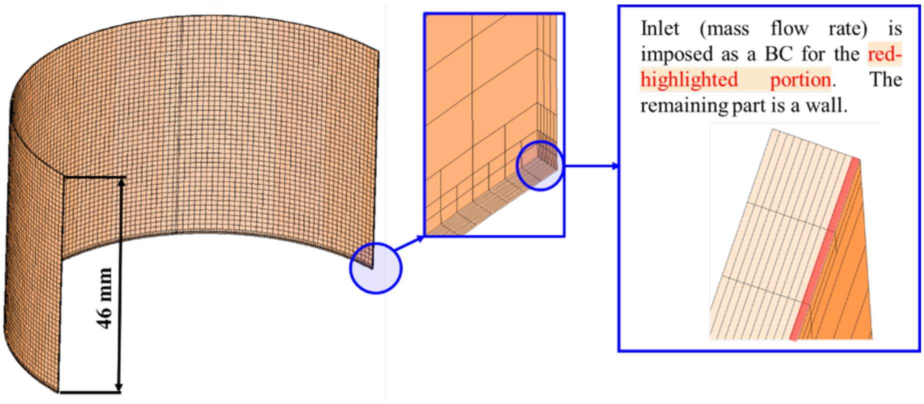

Inlet (mass flow rate) is imposed as a BC for the red-highlighted portion. The remaining part is a wall.

Figure 53: Details of the crevice volume of the 3D-CFD model. The mass flow boundary is a portion of the bottom surface of the crevice volume, and it is highlighted in red.

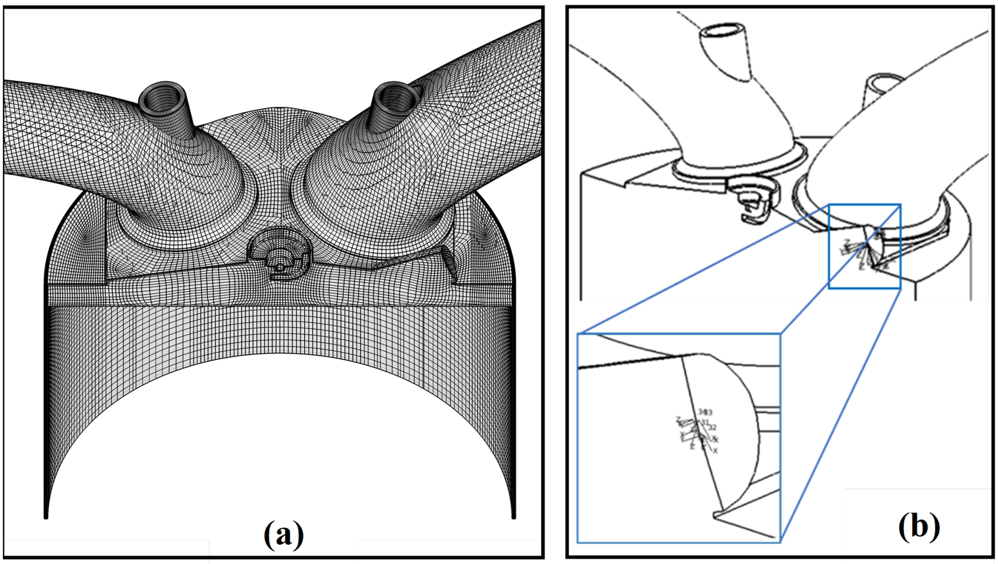

Figure 54: Details of the computational grid (a) and highlight of the injection coordinate systems corresponding to the 6-hole injector (b).

flow rate is measured, the 1D simulation is successfully compared to the 3D one (Figure 55).

To shed light on the flame propagation of the three surrogates, 3D Computational Fluid Dynamics (CFD) is employed to investigate the equivalence ratio Φ and the laminar flame speed at spark time. Turbulent combustion modelling is achieved using the flamelet models, which usually require laminar flame speed as an input, as the ones previously derived. The computational grid corresponds to half the real engine geometry, comprises of a moving mesh with a base size of 0.6 mm and the minimum is 0.15 mm near the spark plug, and it is obtained using the pre-processor es-ice and then simulations are run with STARCDv.2020.1.2 [102] solver, licensed by Siemens PLM. The maximum number of cells at BDC is ∼578600, whereas the minimum number at TDC is ∼265900 (Figure 54). The Heat transfer is modelled using the [139], which is widely validated for engine applications. The CFD RANS simulations are carried out using a multi-component approach to reproduce with high-fidelity the behavior of each of the surrogate fuels employed in the experiments for both combustion and injection. As for the injection, the

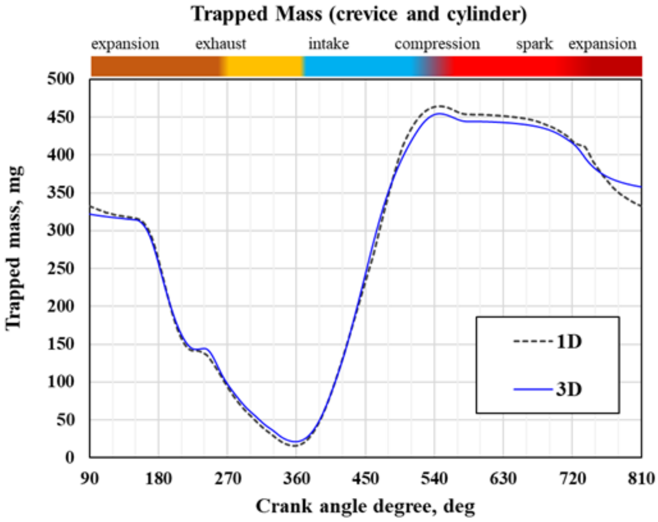

Figure 55: Trapped mass for the total cylinder and crevice volume during the engine cycle.

multi-component approach is adopted as previously described in the Lagrangian multiphase paragraph. This time, also the combustion is investigated and the main aim is to obtain the laminar flame speed values at spark time for each fuel to better highlight differences in flame propagation propensity at spark time. The combustion model employed is G-equation [102], also known as “Level set”. The laminar flame speed is provided as user-defined correlation for each component and then the mixing rule is responsible for the final value $s_{\mathrm{L,mix}}$. Then, the turbulent flame speed is computed with the conventional Peters correlation [60] for turbulent flame speed (eq.(74)), in which the turbulent flame speed s_{T} is a function of the turbulent Damköhler number $\mathrm{Da_t}$, and the fluctuation of turbulent flow velocity $u\prime$, and several parameters such as $\mathrm{b_1} = 2.5$, $\mathrm{b_3} = 1.25$, $\mathrm{a_4} = 0.97$ (default values are 2.0, 1.0, 0.78 respectively).

$$\frac{s_{\mathrm{T}} - s_{\mathrm{L}}}{u'} = \left[\left(\frac{\mathrm{a_4}\,(\,\mathrm{b_3})^2}{2\ \mathrm{b_1}} \cdot \mathrm{Da_t} \right)^2 + \mathrm{a_4}\,(\,\mathrm{b_3})^2 \cdot \mathrm{Da_t} \right] - \frac{\mathrm{a_4}\,(\,\mathrm{b_3})^2}{2\ \mathrm{b_1}} \cdot \mathrm{Da_t} \tag{74}$$

The results obtained using the default laminar flame speeds and the Damköhler correlation for reckoning s_{T} are compared to the one stemming from the user-defined setup. The "default laminar flame speeds " are the ones implemented in the software [102] stemming from the studies conducted by Metghalchi et al. [64]. As shown in Figure 56, numerical results with the default approach yield an overestimation of the pressure peak, whereas the proposed approach with user-defined combustion modelling is closer to the experimental results (as instance, results for SOI 300 and TRF30). The faster combustion obtained with the default correlations can be also observed by plotting, for example, the combustion regress variable (RVB) five degrees after TDC the RVB defined as shown in Figure 57.

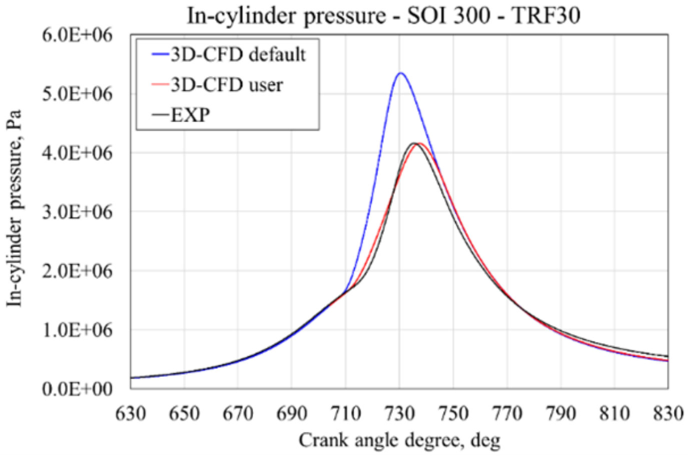

Figure 56: Detail of the pressure tracer for default and user-defined methods for computing the turbulent and laminar flame speed.

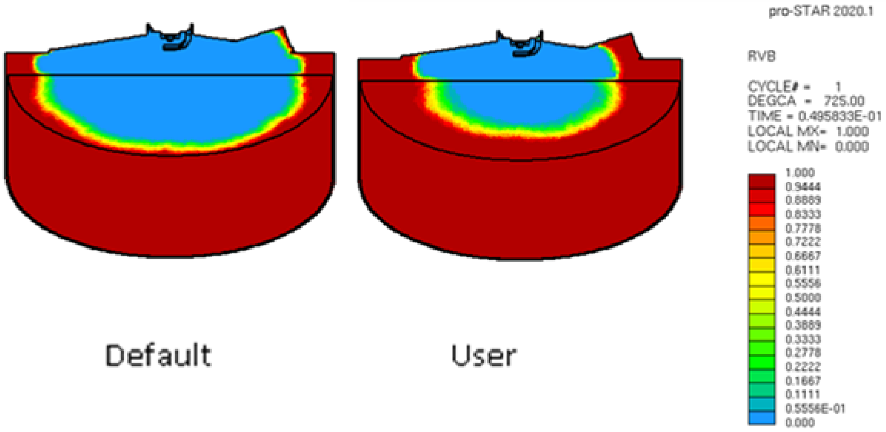

Figure 57: Combustion regress variable (RVB) after 5 deg after TDC: default versus user correlation for laminar and turbulent flame speed calculation.

3.2.1.2 Laminar flame speed values at spark time

In this section, the results from the use of the mixing rule for the TRF surrogate laminar burning velocity correlation are analysed. In particular, the CFD code takes as input the laminar burning velocity from the correlations and uses it as the laminar flame speed, as shown in the plots in the results. The code [102], in fact, accounts for the flow field influence and of the laminar burning velocity to reckon the output laminar flame speed.

The Le Chatelier mixing rule is implemented via user coding to obtain the scalar fields of laminar flame speed in the combustion chamber before spark time (-15 CAD bTDC). Since the equivalence ratio is an input to $s_{\mathrm{L,mix}}$, the stoichiometric air-fuel-ratio is computed cell-wise using the actual composition in the cell (mole fraction of the fuel components) and a mole-based mixing rule (eq.(75)), which is employed to compute α_{st} for the surrogate fuels.

$$\alpha_{\mathrm{st}} = \sum_{i} (\alpha_{\mathrm{i}} \cdot x_{\mathrm{i}}) \tag{75}$$

Since the average pressure and combustion temperature pre-spark are 15 bar and 650K, the $s_{\mathrm{L,mix}}$ values are clipped up to 80 cm/s for better representing gradients in the combustion chamber. Between SOIs, there are differences both in $s_{\mathrm{L,mix}}$ (Figure 58) and in charge stratification (Figure 59). However, the patterns of the $s_{\mathrm{L,mix}}$ observed for each SOI depict local differences in magnitude, thus suggesting the possibility of different flame propagation behavior. Although the surrogates are formulated targeting the same RON number of the reference gasoline, the differences in the type and composition of hydrocarbons for the surrogates play a role in the representation of the flame propagation.

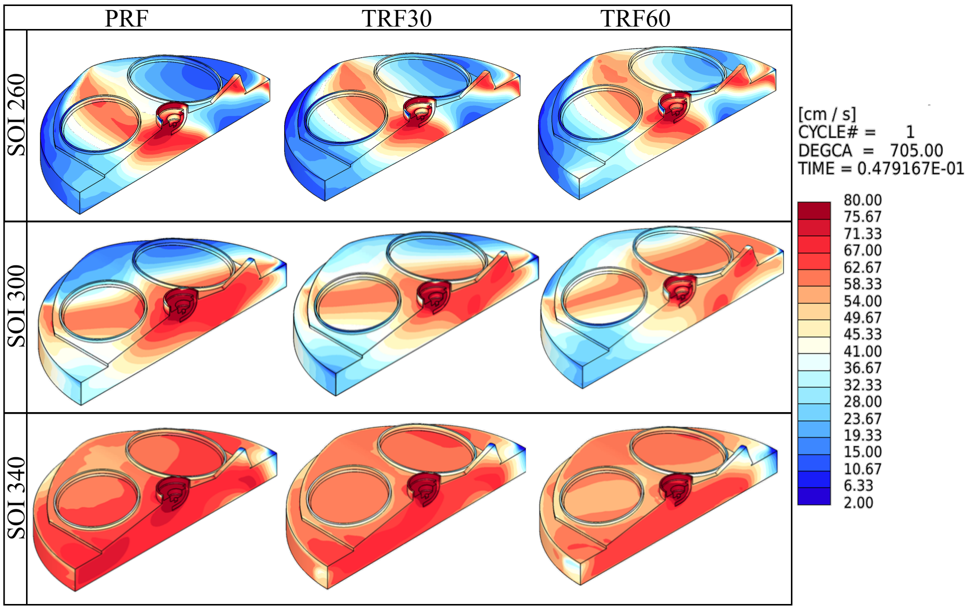

Figure 58: Laminar flame speed scalar fields for different SOI (rows) and different surrogate fuels (columns) evaluated at spark time (-15 CAD bTDC).

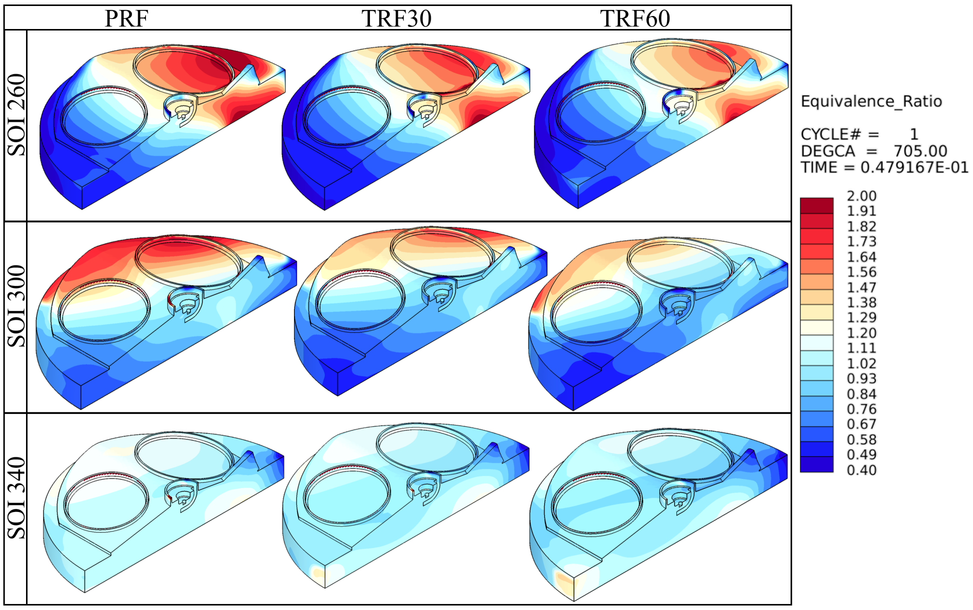

Figure 59: Charge stratification for different SOI (rows) and different surrogate fuels (columns) evaluated at spark time (-15 CAD bTDC).

Further insight on the cell-wise values of laminar flame speed for the different surrogates is provided by frequency histogram (Figure 60) for each SOI, to further highlight the different patterns of each blend. In particular, SOI 300 is characterized by the more consistent differences in the central band of laminar flame speed values (20 - 80 cm/s).

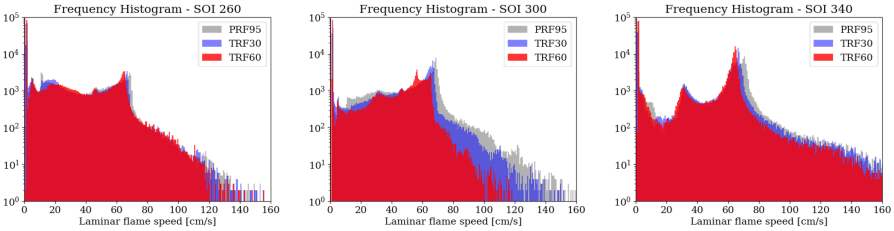

Figure 60: Frequency of cell-wise values of each surrogate for the three SOIs, evaluated at spark time (-15 CAD bTDC).

3.2.2 Ammonia-hydrogen blends

In the first part of this study, seven correlations are derived, one for each NH_3/NH_2 blend, including the options of pure NH_3 and pure NH_2. For each blend and physical/chemical state, a relative measure of the difference between the value predicted using the correlation $s_{\mathrm{L,fit}}$ and the one provided by chemical kinetics simulations $s_{\mathrm{L,data}}$ (i.e. a percentage error) is reckoned as $\mathrm{err}\% = (s_{\mathrm{L,fit}} - s_{\mathrm{L,data}})/s_{\mathrm{L,data}}$. Results are summarized in Figure 61-65 using error maps: despite a few isolated peaks are visible, the average err% is below ±2.5%, whereas the maximum err% lies between 10% (NH100) and 16% (NH10 and NH40), and it affects the higher values of pressure-temperature range of the fitting (130 bar and 1208 K).

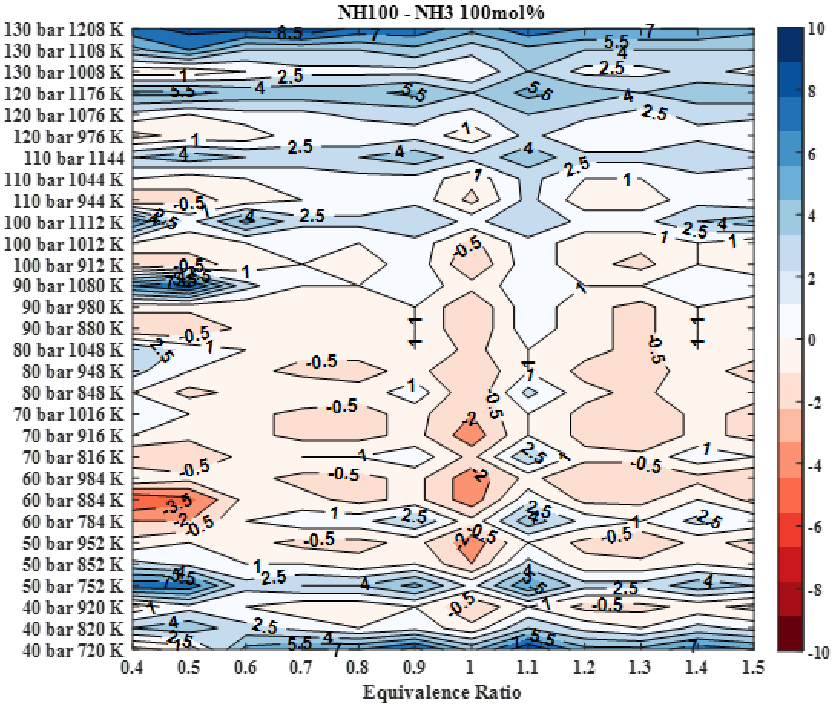

(a) Contour map of percentage error: NH100 with blend specific correlation

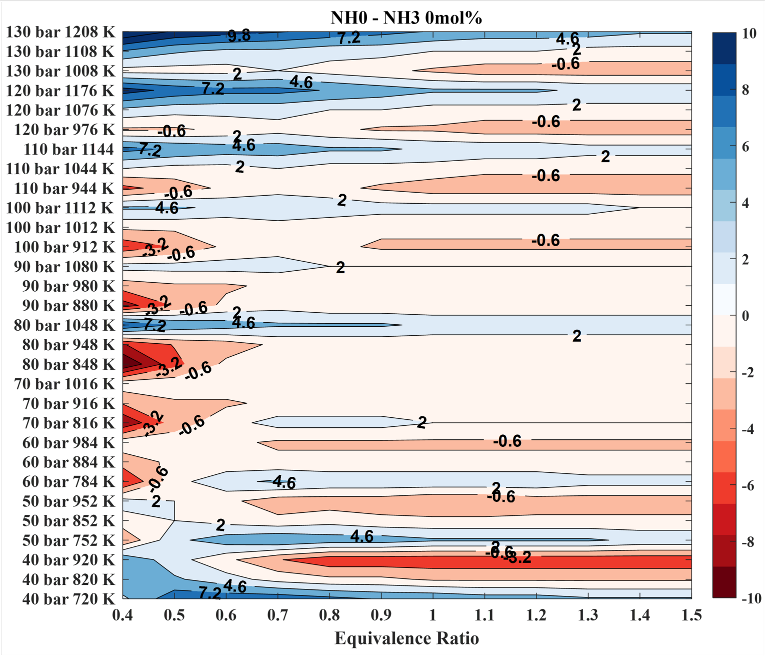

(b) Contour map of percentage error: NH0 with blend specific correlation

Figure 61: Contour map of percentage error

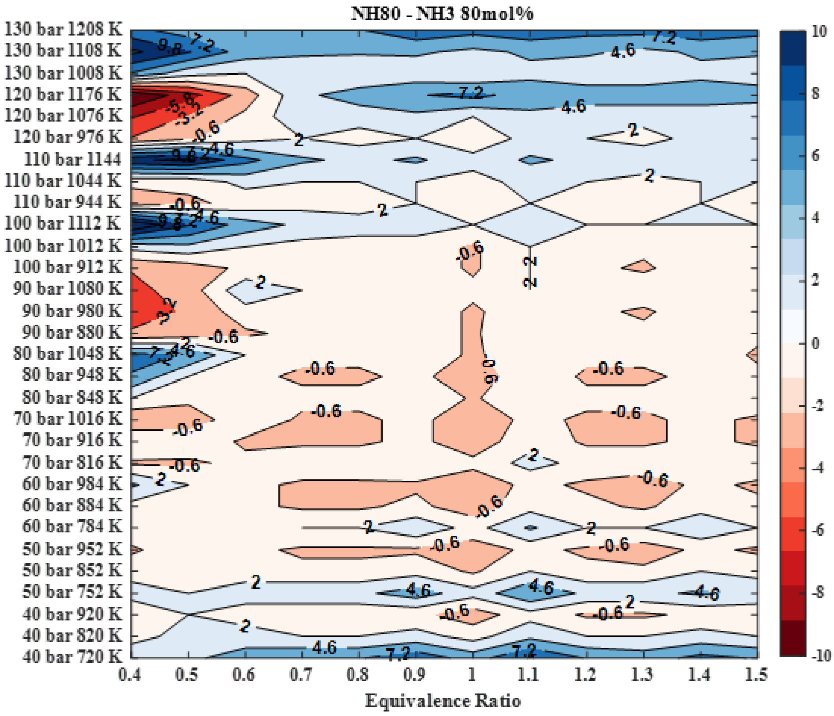

(a) Contour map of percentage error: NH80 with blend specific correlation

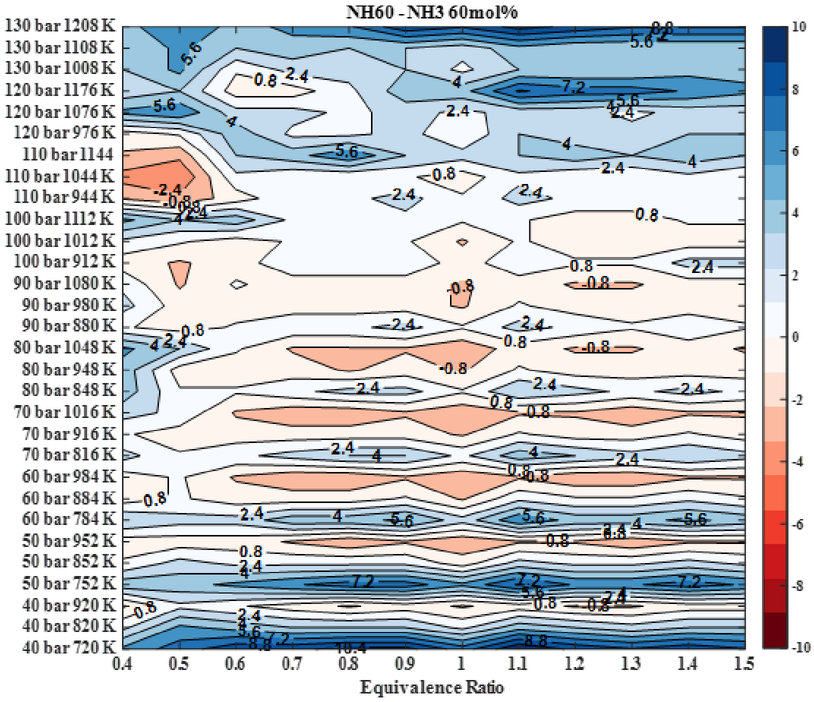

(b) Contour map of percentage error: NH60 with blend specific correlation

Figure 62: Contour map of percentage error

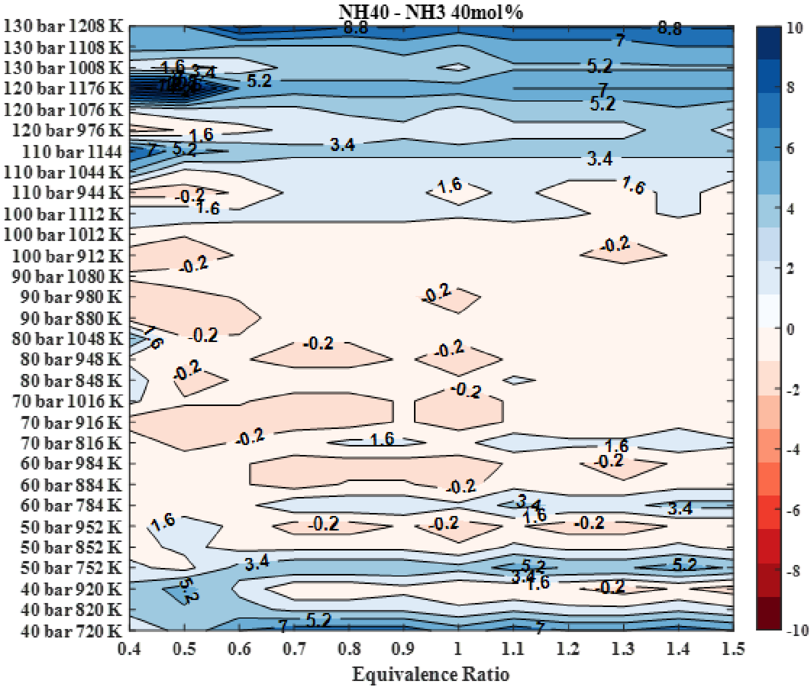

(a) NH40 with blend specific correlation

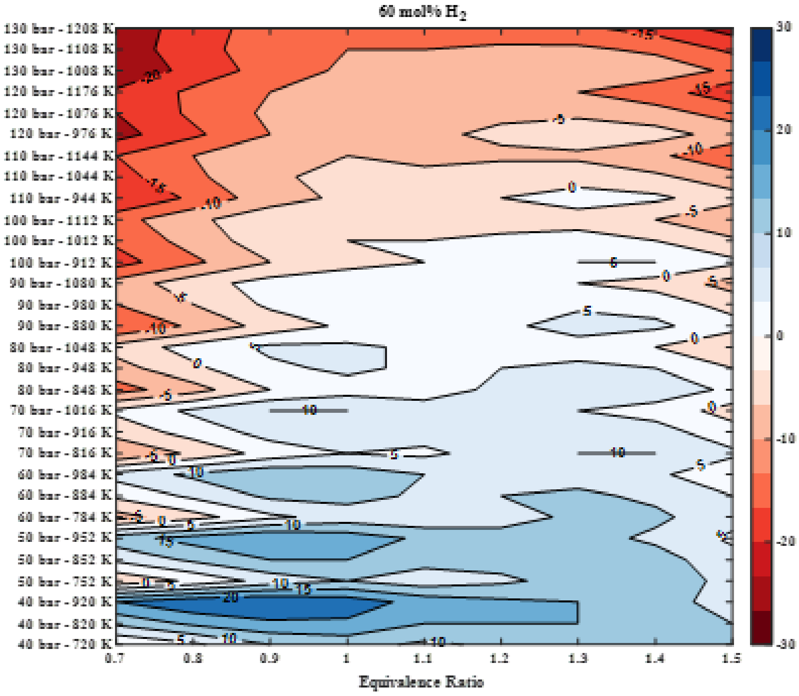

(b) NH40 with generalized correlation

Figure 63: Contour map of percentage error

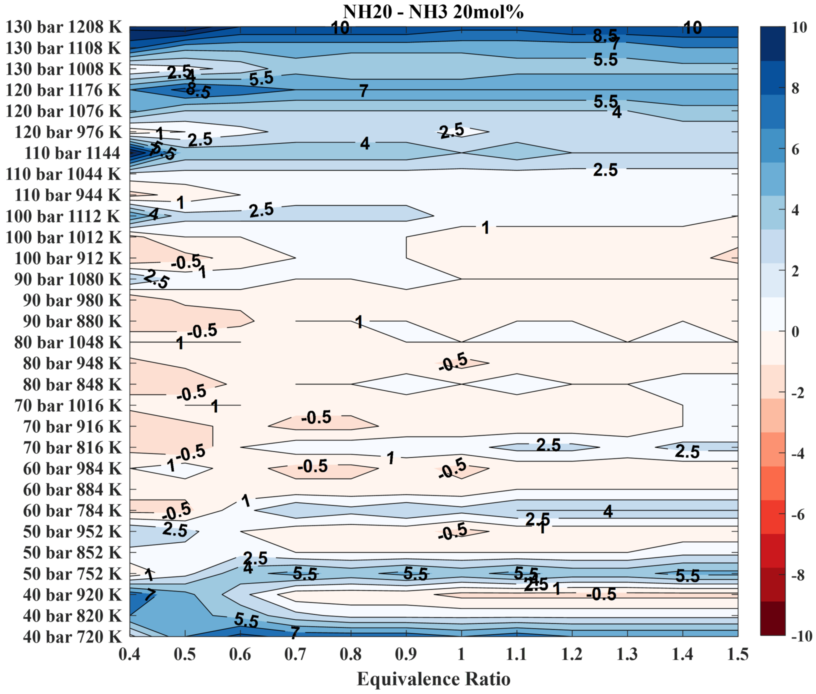

(a) NH20 with blend specific correlation

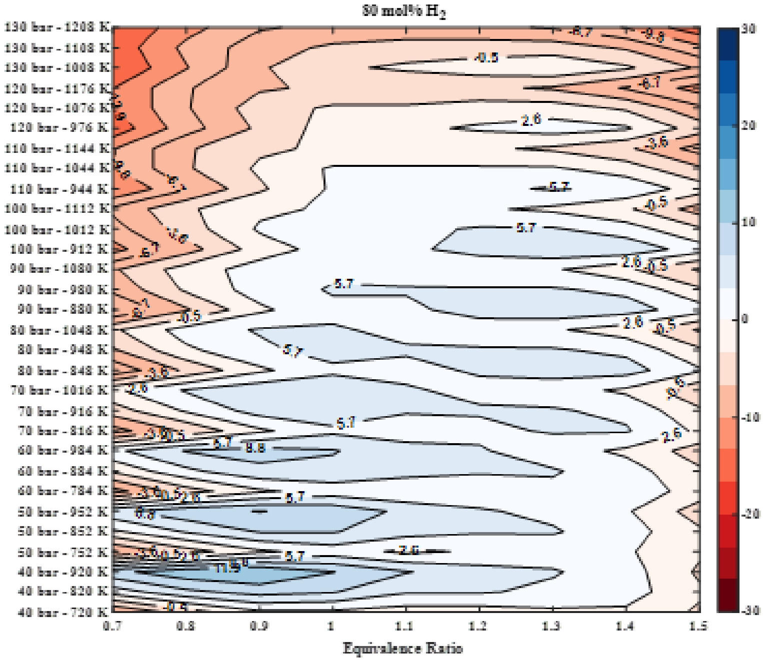

(b) NH20 with generalized correlation

Figure 64: Contour map of percentage error

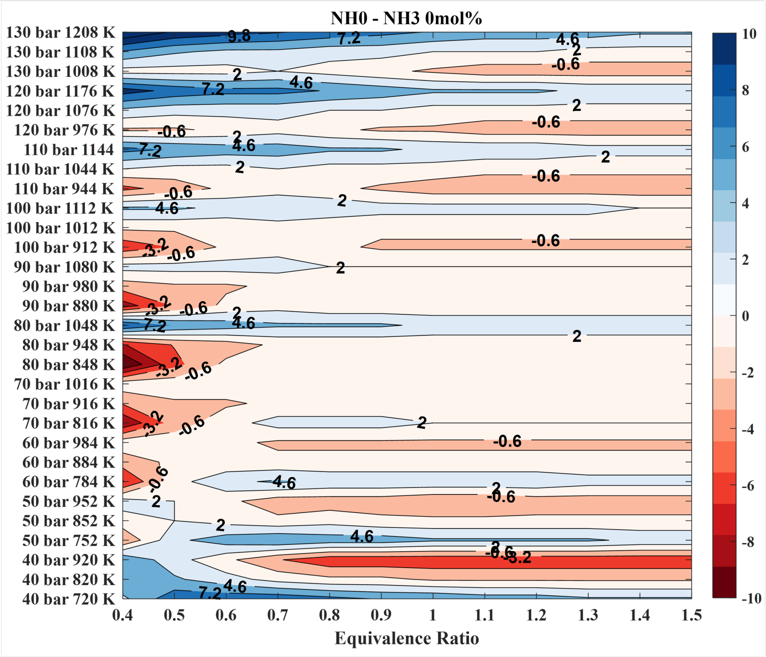

(a) NH0 with blend specific correlation

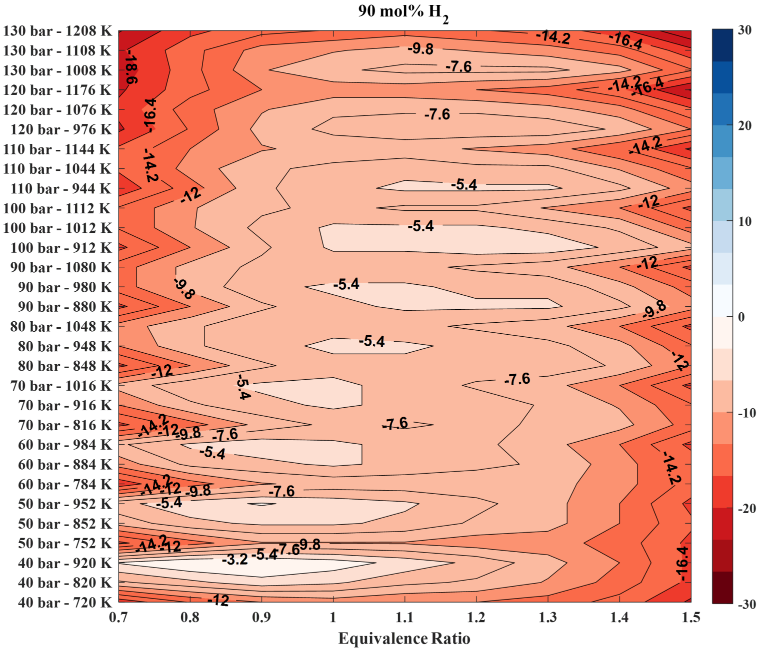

(b) NH0 with generalized correlation

Figure 65: Contour map of percentage error

A further assessment of the accuracy of the fitted correlations can be made by

Table 24: Statistics about the prediction accuracy compared to the chemical kinetics simulation database. The number of predicted values with a percentage error above 5% is the number of values over the 360 total values for each blend.

NH_3 mol%	100	80	60	40	20	10	0
Mean err%	1.7%	1.9%	2.3%	2.3%	2.5%	2.2%	1.5%
Number of err% above 5%	44	55	67	59	70	63	54
Maximum err%	10%	15%	12%	16%	13%	16%	15%
$s_{L,fit}$ in cm/s at maximum err%	52.7	19.5	170	89	157	135	194
$s_{L,data}$ in cm/s at maximum err%	58.5	22.9	194	105	181	161	227
$(s_{L,fit} - s_{L,data})$ in cm/s	5.8	3.4	24	16	24	26	33

comparing them with the chemical kinetics database via global quality estimators such as those reported in Table 24, for all the operating conditions examined for each one of the seven fuel mixtures (NH0, NH10, NH20, NH40, NH60, NH80, NH100). Details regarding the points characterized by the maximum prediction error (err%) are stored in Table 24: first the raw values of the laminar flame speed both predicted ($s_{\mathrm{L,fit}}$) and from simulations ($s_{\mathrm{L,data}}$) are reported along with the absolute error $s_{\mathrm{L,fit}} - s_{\mathrm{L,data}}$, all expressed in cm/s. The overall average err% is lower than 2.5% for the dedicated correlations.

As for the generalized correlation, the error increases slightly. Despite the lower accuracy, it is worth reminding that a generalized correlation can be useful in the conceptual design stage of the combustion system where the detailed characteristics of the fuel are yet to be determined and they can be used as a degree of freedom in the design space. In cases where a wide range of solutions and conditions must be tested, a reasonably accurate estimate of the effect of different H_2 content can be quickly provided relying on the sole availability of the laminar burning velocity of pure H_2. Moreover, since the generalized correlation is derived by scaling the H_2 correlation, in this case the estimated err% inherits the err% from the H_2 correlation (average mean err% equal to 1.51%). The reason for this strategy of evaluation of err% stems from the CFD combustion modelling workflow, in which correlations are provided as polynomial expressions.

An additional test to evaluate the proposed correlations is performed through the comparison against those available in literature, compared to Goldmann's [83] and to Verhelst's [81] respectively. For the sake of compactness, only the cases with NH100 and NH0 are considered. Since the correlations proposed by Verhelst [81] for H_2 is valid within a reduced pressure range, the evaluation of the laminar flame speed is firstly carried out within the validity range.

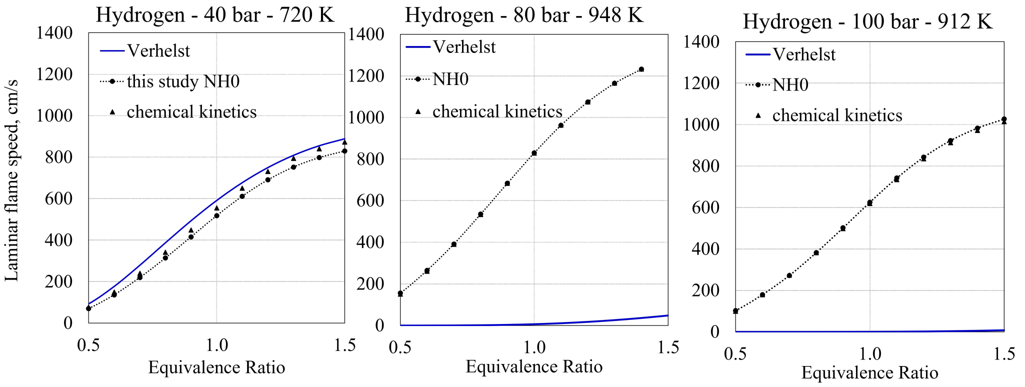

Figure 66: Laminar flame speed values for hydrogen: comparison between Verhelst and this study.

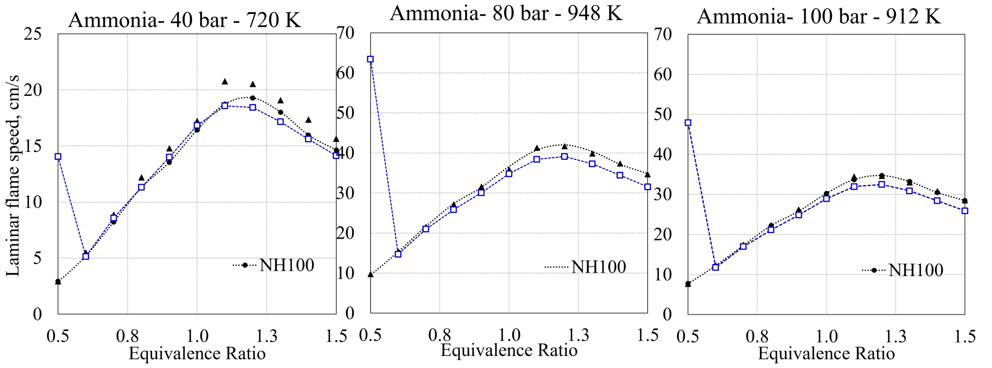

Figure 67: Laminar flame speed prediction at high pressures and temperatures for NH_3/air mixtures.

Nevertheless, since a need to apply the correlation for higher pressure may rise for typical ICE full-load conditions, the comparison is then extended beyond such range to help readers to understand the validity of the proposed method [81]. Figure 66 and 67 show that the results at low pressures and temperatures confirm the validity of the correlations in literature, but outside the validity range the correlations start to largely deviate from the chemical kinetics outcomes. In particular, Goldmann (Figure 67) provides unrealistic values for ultra-lean NH_3/air mixtures (values of $\Phi \leq 0.5$ out of the fitting range [83]), while Verhelst provides excessively low laminar flame speed values for very high pressures (beyond the validity range). For this reason, the use of those correlations [83] outside their validity range is questionable at full-load engine-like conditions, motivating the alternative choice provided in the present study.

Finally, values of laminar flame speed for the NH_3/H_2 mixtures obtained with the fitting procedure are depicted in Figure 68-69-70: the increment of laminar burning velocity is coherent with the addition of H_2 in the mixture, as expected. Moreover, a comparison with the laminar flame speeds for a gasoline surrogate E5 (with 5% of oxygenated compounds) from [78] is proposed in Figure 68-69-70 as an example of the potential differences between conventional gasoline and an alternative NH_3/H_2 blend in terms of laminar flame speed. The effect of the pressure and temperature is also evaluated for the NH_3/H_2 and the E5 surrogate: by fixing the temperature (948 K) first Figure 69, and secondly, stark differences occur only for H_2 content above 80 mol%. Coherent increase of laminar flame speed with the higher temperatures at fixed pressure (Figure 70), whereas a decrease of the laminar flame speed is spotted when the pressure is increased at fixed temperature since the flame front is expected to be thinner as the pressure increases.

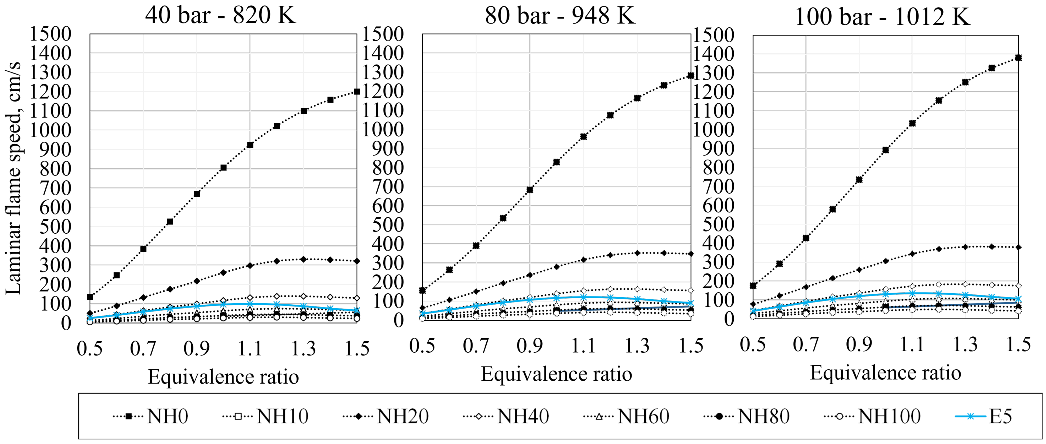

Figure 68: Laminar flame speed values for NH_3/H_2 blends and for a gasoline surrogate as an example of conventional fuels for spark ignition engines(E5)[78]

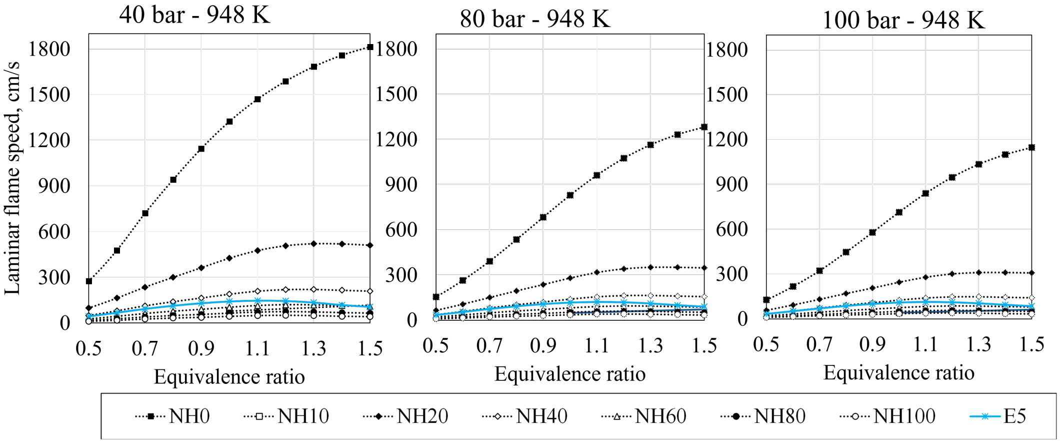

Figure 69: Effect of pressure variation on laminar flame speed for NH_3/H_2 blends and E5.

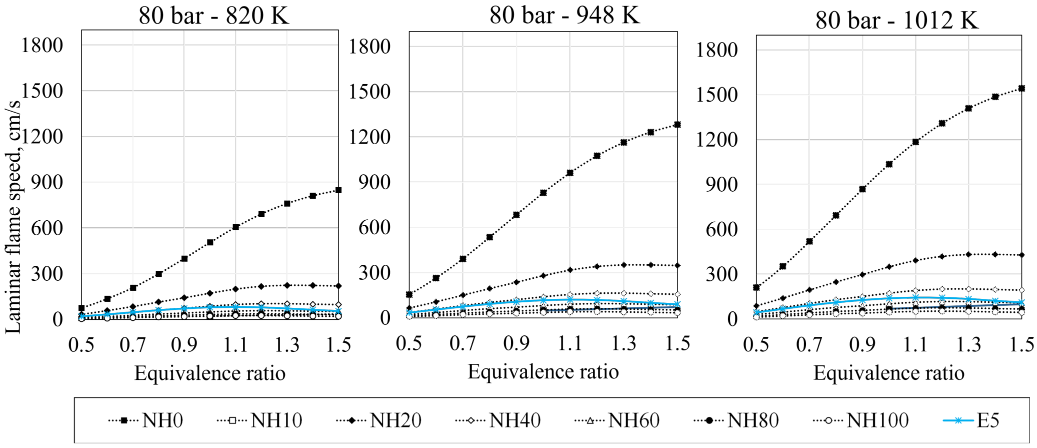

Figure 70: Effect of temperature variation on laminar flame speed for NH_3/H_2 blends and E5.

A further comparison for different x_{H2} is carried out between this study blend-specific correlations and the one provided by literature [83]. For a test point (800 K and 45 bar) the laminar flame speed increment with the increase of x_{H2} is caught in accordance with the values obtained with the correlation provided by Goldamann et al. with similar values (Figure 71).

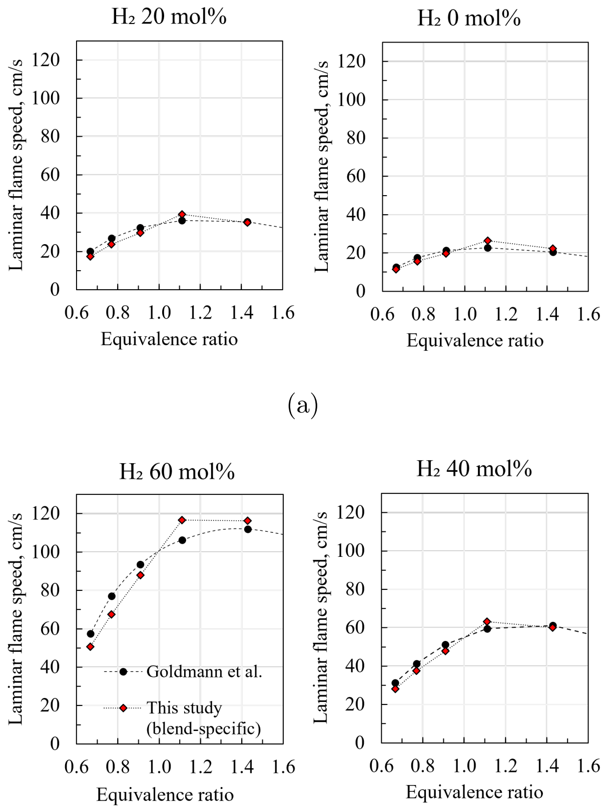

(a)

(b)

Figure 71: Laminar flame speed increment with the increase of $x_{\mathrm{H_2}}$: comparison of values obtained using the correlation by Goldmann and the blend-specific correlation developed in this study

In conclusion, correlations providing laminar flame speed values are derived using a dedicated fitting procedure over chemical kinetics simulation data (over 2500 total values, 360 for each blend). A data-set of values of freely propagating laminar flames was calculated from 1D chemical kinetics simulations for H_2/air (NH0), NH_3/air (NH100) and NH_3/H_2/air mixtures with an increasing H_2 content (10-20-40-60-80 mol%). The applied fitting procedure produces an average prediction error that is ∼2.5% or lower for each of the seven blends investigated in this study, whereas the maximum err%, which lies between 10% (NH100) and 16% (NH10 and NH40) is usually spotted for the higher values of pressure-temperature (e.g. 130 bar and 1208 K). The correlation validity range is suitable for full-load conditions in SI engines, i.e., for pressure ranging from 40 bar to 130 bar, unburnt temperatures from 720 K to 1208 K, and ultra-lean (from $\Phi = 0.4$) to rich mixtures (up to $\Phi = 1.5$). Thus, these correlations provide an alternative to the existing ones, whose application outside the validity range result in non-negligible errors. As for the fitting methodology, a simple polynomial correlation is employed for prediction within the range of $0.7 \leq \Phi \leq 1.5$, whereas a dedicated scaling procedure is employed to target the ultra-lean branch of the laminar flame speed. Finally, an attempt to derive a generalized correlation for high H_2 content (from 60mol% up to 90mol%) is presented for lean-to-rich mixtures ($0.7 \leq \Phi \leq 1.5$). Despite the percentage error is lower than 10%, the generalized correlation is less accurate than the dedicated fittings. The proposed correlations play a key role in flamelet combustion models, and they can be easily implemented in any CFD code. The laminar flame speed correlation is formulated via data-fit procedure, whose database consists of laminar flame speed values obtained from chemical kinetic simulations at several high pressure and temperature conditions.

3.3 Soot modelling

3.3.1 Chemistry-fidelity and tabulated approach for premixed combustion

Within the ICEs soot modelling, a test on the efficacy in catching the effect of differences in fuel chemical composition with the customized tabulated approach in conjunction with the Sectional Method is reported in this section. The main aim is to show that the use of tables, tailored on fuel chemistry, can lead to successful prediction of trends in fuel sooting tendency. For this purpose, full-engine cycle simulations are carried out for three fuels, characterized by stark differences in their chemical nature. The results of the study conducted by Hageman [22] are considered as an interesting experimental dataset for validation for because the soot produced is for the majority due to fuel combustion and partially to oil and engine-wear parts combustion (background soot), and this is accounted. Moreover, the gasoline employed in the study is a non-oxygenated gasoline (EEE) with 28 vol% of aromatic content and it is very similar to the reference gasoline of the surrogate [14] with 30 vol% of aromatics. For deriving tabulated coefficients for reckoning the soot source term in the Sectional Method implemented in the 3D-CFD code, it is mandatory to specify the fuel composition as an input in the chemical kinetics simulations. Unfortunately, gasolines are complex mixtures of several hydrocarbons and additives, thus the use of a surrogate fuel formulated to replicate the properties of interest of the reference fuel is essential. This way, first chemical kinetics simulations are carried out to derive the tabulated coefficients, then the chemistry information are read from the tables by the 3D-CFD code during engine cycle simulations. The experimental conditions [22] are reproduced in simulations of a simplified engine 3D geometry, then the soot produced is evaluated using the Sectional Method [31] [15] used with ECFM-3Z [102] [60], a flamelet model for the combustion of the Spark Ignition engine (SI). In the numerical analysis, three fuels are investigated at several equivalence ratio values (from 1.0 to 1.5): classical gasoline (TIER2[14]) similar to the EEE of the experiments, an oxygenated one (CHINA6[14]), and pure ethanol (C_2H_5OH) are qualitatively compared. The composition of the surrogates employed for the customization of the tables is shown in Table 26.

Table 25: Alcohol and aromatic content of the actual types of gasoline. For the numerical analysis, surrogates are employed with different contents of ethanol are considered: TIER2 (0 vol%) for comparison with experiments with EEE, CHINA6 (vol 10%), and finally pure ethanol.

Fuel	**Alcohol content**	**Aromatic content**	**Application for the results**
C_2H_5OH	100 vol%	0 vol%	Numerical
EEE [22]	0 vol%	28 vol%	Experimental
TIER 2 [14]	0 vol%	30 vol%	Numerical (substitute of EEE)
CHINA 6 [14]	10 vol%	35 vol%	Numerical

Table 26: Surrogate compositions employed with different contents of ethanol are considered: TIER2 (0 vol%) for comparison with experiments with EEE, CHINA6 (vol 10%), and finally pure ethanol.

Surrogate fuel ↓ | Composition →	C_2H_5OH	C_7H_8	C_7H_{16}	C_8H_{18}
surrogate - TIER2 [78]	0 mol%	45.15 mol%	13.91 mol%	49.94 mol%
surrogate - CHINA 6[78]	10.87 mol%	40.24 mol%	12.40 mol%	36.49 mol%

More specifically, the volumetric concentration of oxygenated compounds and aromatic content is varied to catch their impact on soot formation. The presence of OH-functional groups inhibits bigger particles proliferation [14] [143][22][17], and the aromatics promote PAHs and soot formation onset because a primary ring-structure of carbon atoms is already present [4][144]. For each fuel, whose composition is reported in Table 25, reaction rate tables are derived using DARSv4.30 licensed by Siemens PLM [105] by simulating a CP-reactor at several pressures, temperatures, and equivalence ratio values at engine-like conditions. The reaction mechanism employed for the chemical kinetics simulation is the one proposed by Cai et al. [17], derived from the [145] with the addition of specific pathways for PAHs in case of ethanol and oxygenated compounds. The reaction rates $\widetilde{RPAH}$, $\widetilde{k}_{\mathrm{d}}$, $\widetilde{k}_{\mathrm{rev}}$, $\widetilde{k}_{\mathrm{O_2}}$, and $\widetilde{k}_{\mathrm{OH}}$ are stored in the derived tables, and ready to be read by the 3D-CFD code and employed by Sectional Method for calculation of soot mass fraction [31]. This qualitative analysis has two main goals: identification of the threshold value of equivalence ratio Φ, and the confirmation that at least qualitatively the differences due to the chemical nature of fuels can be properly modelled with the tailored-table approach. Results of this analysis, as in Figure 72 show that the increase of ethanol content results in a higher threshold value of Φ in which the soot formation starkly increases in accordance with the experimental analysis conducted by Hageman [22]. More specifically, in Figure 72 the Particle Size Distribution Function (PSDF) is integrated (eq.(76)) to obtain a single value of sooting tendency for each equivalence ratio Φ_{i} (IPSDF). Since the numerical simulations provide only the soot due to fuel combustion, the background soot

(BGS) reported in the experimental data is added to the fuel-related quantities to get a fair comparison between simulation results and experiments. Finally, the IPSDF is normalized $\mathrm{IPSDF}^{\mathrm{Norm}}$ over the soot produce at stoichiometric conditions for each fuel (eq.(77)).

$$\mathrm{IPSDF}\left(\Phi_{\mathrm{i}}\right)=\sum_{i} \mathrm{PSDF}_{i} \cdot\left(\mathrm{d}_{\mathrm{i}+1}-\mathrm{d}_{\mathrm{i}}\right) \tag{76}$$

$$\mathrm{IPSDF}^{\mathrm{Norm}}\left(\Phi_{\mathrm{i}}\right)=\frac{\mathrm{IPSDF}\left(\Phi_{i}\right)+\mathrm{BGS}}{\mathrm{BGS}} \tag{77}$$

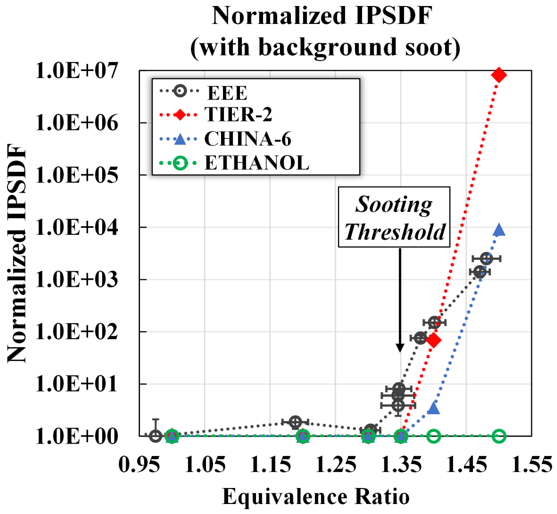

Figure 72: Comparison of normalized Particle Size Distribution Function for EEE [22] and TIER2, then with CHINA6 (ethanol 10 vol%) and pure ethanol.

In Figure 72 is shown that the sooting threshold of the EEE [22] (experimental) and TIER2 (numerical) are comparable and that the table tailored on the surrogate with similar aromatics content to the gasoline from experiments yields similar results (sooting threshold at $\Phi = 1.35$). As 10 vol% of ethanol is added (CHIAN6), the threshold shifts towards higher values of equivalence ratio ($\Phi \sim 1.4$). In light of these results, the tabulated approach is effective in catching different sooting tendencies of fuels.

3.3.2 Soot modelling for partially premixed combustion with table-switch

3.3.2.1 Diffusive and premixed table: comparison of the tabulated results In the default use of the Sectional Method, the two libraries are employed separately, and the decision of the input table is communicated to the 3D-CFD solver at the beginning of the simulation without any possibility of changing the setup. The current implementation is dictated by the idea that the predominant combustion mode can be selected and be fixed based on the engine technology (e.g. diffusive library for Diesel applications, premixed library for SI engines). However, it is not uncommon the case of predominantly premixed combustion devices that also exhibit secondary diffusive phenomena. For example, to meet this need, the Enhanced Coherent Flamelet Model (ECFM3Z) was developed for modelling the three combustion modes that can be found the modern combustion devices. An analogy for the Sectional Method has not yet been proposed. Since the input parameters for the two tabulation approaches present similarities, a switch between the libraries for reckoning the inputs to the soot mass fraction source terms can be an interesting possibility, especially if the switch can be performed only in computational cells in which the predominant diffusive combustion effect is detected, and not in the whole domain indistinctively. This is crucial to model localised changes in the predominant combustion mode. Before describing the test conditions for the switch, it is essential to thoroughly understand the differences between the two libraries in terms of outputs, thus in the tabulated coefficients (the reaction rates) stemming from the use of one or the other reactor in the chemical kinetic simulations. For this reason, within the same framework, single point simulations are carried out using the two reactors fed with C_7H_8 (100mol%) for the fuel, air as the oxidizer (N_2 79 mol% and O_2 21 mol%) without any type of dilution (EGR0%). The choice of toluene is based on the fact that it is the most sooting component of the surrogate mixture previously defined, thus it is the most relevant for the sensitivity analysis to the inputs for the tabulated rates. The chemical kinetic simulation inputs are summarised in Table 12. Since the equivalence ratio definition for the diffusive flame can be at best defined as a local quantity, instead of a (spatially) uniform value as for the cp-reactor (Φ), the mixture fraction Z is employed instead, which is linked to Φ via the expression in eq.(75) (α_{st} is the stoichiometric air-fuel ratio).

$$\Phi = \frac{Z}{1 - Z} \cdot \alpha_{\mathrm{st}} \tag{78}$$

Table 27: Test point for library comparison. Simulations are carried out using the reaction mechanism by Cai et al. [17]

Fuel (mol%)	**Oxidizer** (mol%)	T_u (K)	p (bar)	**Φ (or Z)** (-)
C_7H_8: 100%	N_2: 79%, O_2: 21%	500	10	1.0, 2.0, 3.0 (0.07, 0.13, 0.18)

Moreover, there are some user-independent simulation parameters with a fixed stepping (distancing between values), such as the combustion progress variable $c = 0.01 \div 101$ for the cp-reactor, or the grid axis for the reactant streams ($x = 0 \div 201$). The chemical kinetic simulations for the diffusive reactor are carried out by setting the scalar dissipation rate χ accordingly to Table 12. Although the reactant unburnt temperature is low, the chance for a comparison between the results obtained with the two reactors is still of relevance.

The following comparison investigates the eventual presence of trends or differences between the two libraries, in order to assess to which extent the reaction rates for the source terms of soot mass fraction of the sectional method are different depending on the type of reactor. The check is carried out by sampling the values of the reaction rates at three values of the the only different parameters: rvb and χ. Moreover, three representative values of local equivalence ratio (alternatively the mixture fraction) are considered for this analysis. This way, the sampling point of the test with the toluene tabulation at 500 K and 10 bar is carried out in nine points for each tabulation type (nine for the diffusive and nine for the premixed). In Figure 73-74-75-76-77 the tabulated reaction rate constants are compared for three sets of values: for the cp-reactor at values of c (or rvb) equivalent to 10%, 50%, 90%, whereas for the diffusive library the three selected values of χ are 1.0, 5.5, and 10; the rest of the parameters are equivalently set for both reactors (Table 27). As for the RPAH, the rates of PAH productions are comparable for very rich conditions ($\Phi = 3$), but still the premixed one yields a rate of $1 \times 10^{22}\,\mathrm{s}^{-1}\,\mathrm{m}^{-3}$, whereas the maximum of the diffusive is three orders of magnitude less. For stoichiometric mixture, a growing trend with the rvb value is exhibited for all the reaction rates for the premixed library, whereas for richer conditions it tends to flatten out (on the logarithmic plot). The premixed table exhibits a general trend of reaction rate increase with higher rvb, so as the combustion is goes towards completion as it can be intuitively guessed since the residence time and temperature increase with the progress of the combustion in the 0-D cp-reactor. As for the diffusive table, the oxidation rate constants $\widetilde{k}_{\mathrm{O_2}}$ and $\widetilde{k}_{\mathrm{OH}}$ exhibits a growing trend with the increase of the scalar dissipation χ coherently from stoichiometric to very rich mixture (Figure 76 and 77). For the surface growth, the variation of the $\widetilde{k}_{\mathrm{SG}}$ and $\widetilde{k}_{\mathrm{FR}}$with the scalar dissipation rate does not exhibit a common trend for all the equivalence ratio levels examined (Figure 74 and 75). However, for very rich mixture ($\Phi = 3$) the trend can be spotted as a monotonic increase of rate is observed with higher χ.

Finally, it is interesting to identify the sensitivity of the reaction rate constants to the unburnt fuel, which is a single value input for the library based on the diffusive flamelet reactor. As shown in Figure 78, the results of the simulations highlight that the fuel stream temperature has a limited impact on each set of reaction rate constants. For this reason, setting the fuel stream temperature (FST) equal to a target value that is expected in GDI engine before spark advance is a reasonable choice, and intense variations are not expected since the values shown in Figure 78 are related to a local value of Φ, which is close to an eventual sooting threshold for the investigated aromatic hydrocarbon. Thus, 650 K is the FST assigned in the library generation obtained with the diffusive flamelet reactor.

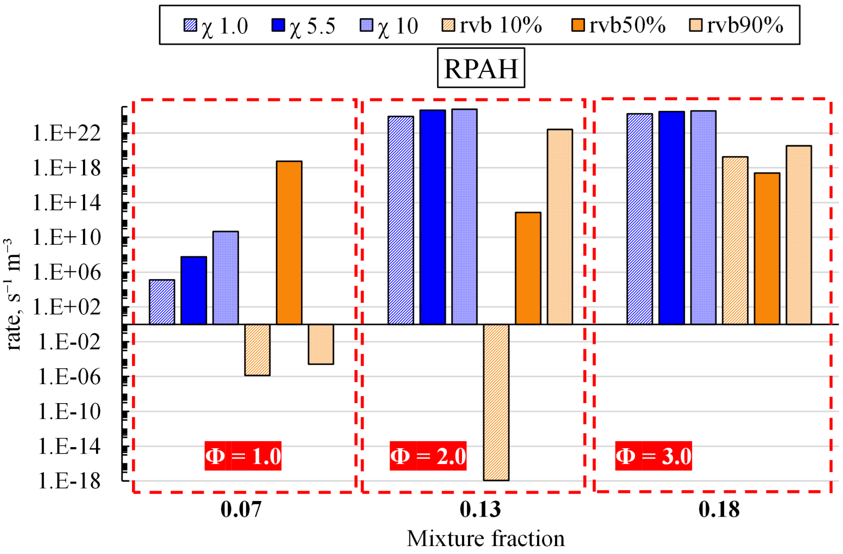

Figure 73: Comparison of RPAH (rate of PAH production) obtained with the premixed (orange) and with the diffusive (blue) libraries.

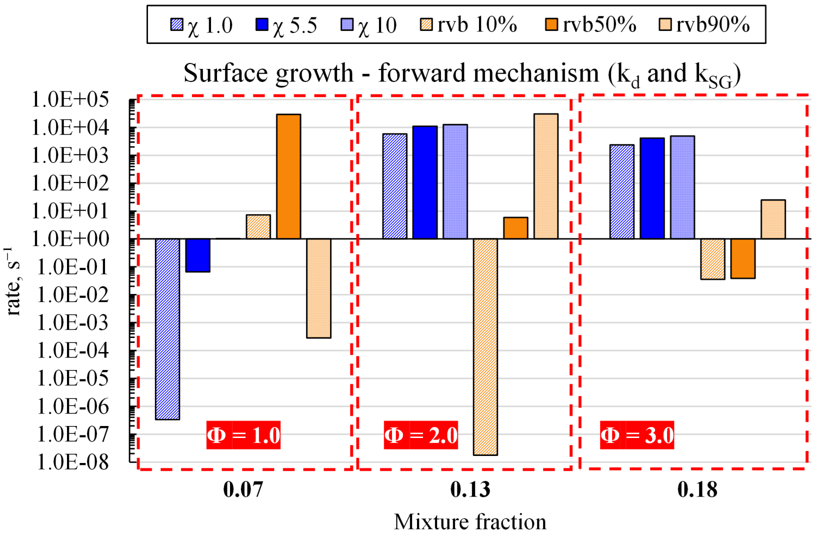

Figure 74: Comparison of rate constants for the forward surface growth mechanism obtained with the premixed (orange) and with the diffusive (blue) libraries.

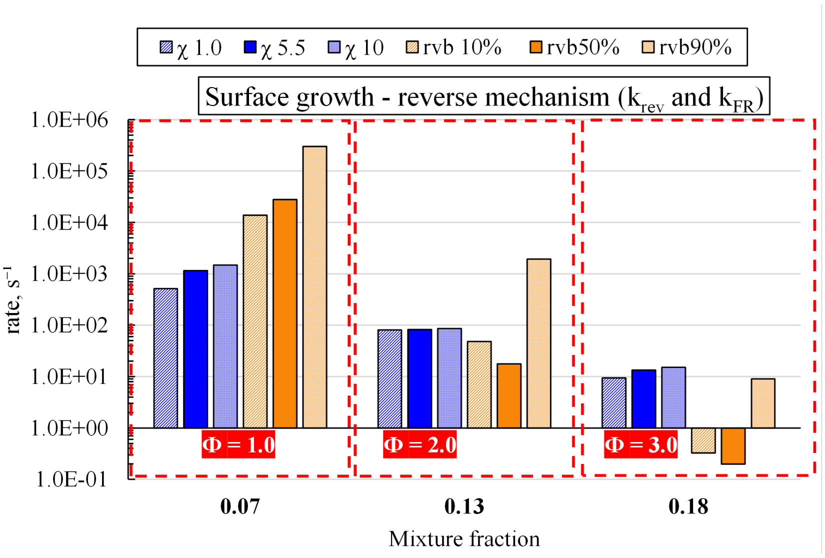

Figure 75: Comparison of rate constants for the reverse surface growth mechanism obtained with the premixed (orange) and with the diffusive (blue) libraries.

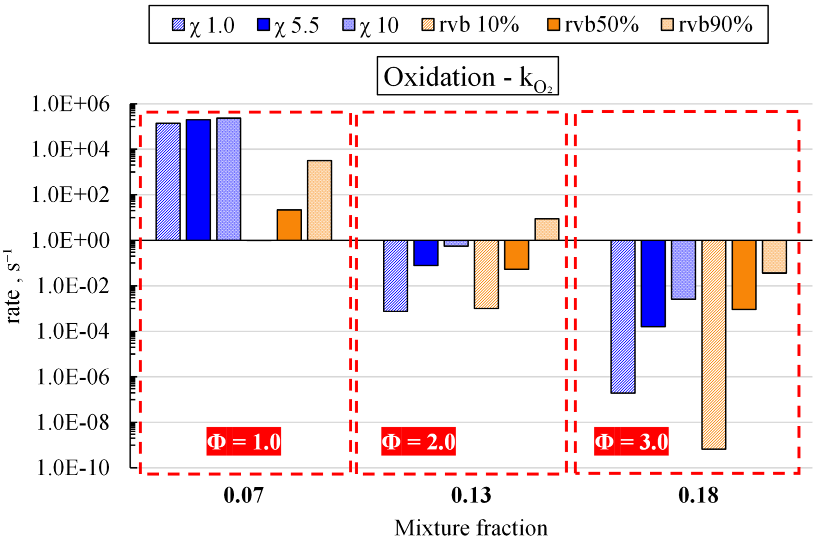

Figure 76: Comparison of rate constants for O_2 oxidation mechanism obtained with the premixed (orange) and with the diffusive (blue) libraries.

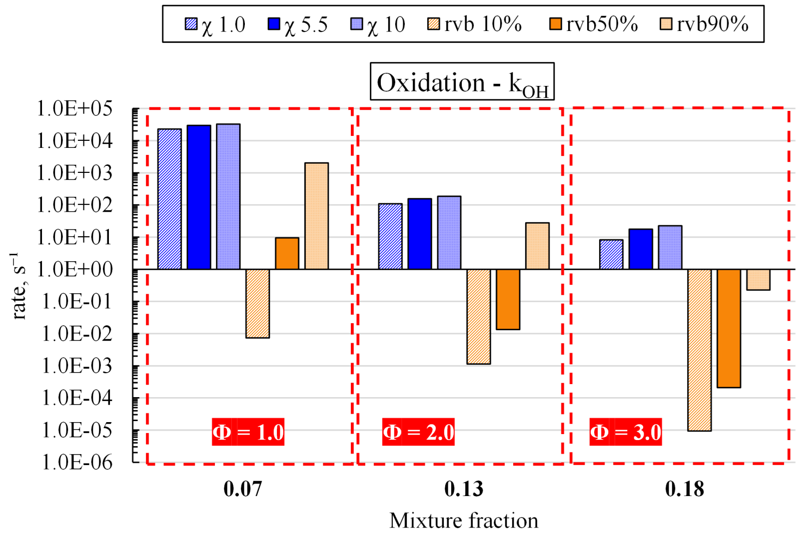

Figure 77: Comparison of rate constants for OH oxidation mechanism obtained with the premixed (orange) and with the diffusive (blue) libraries.

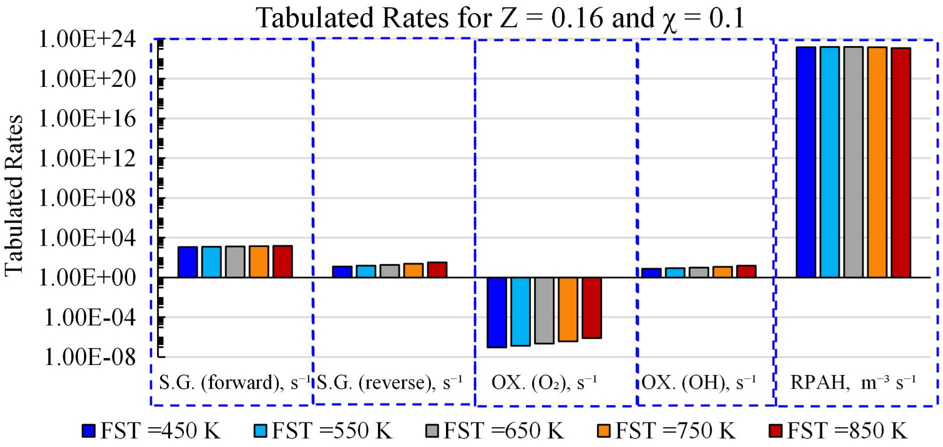

Figure 78: Comparison of reaction rate constant values at several fuel stream temperatures (FST) and for Z equal to 0.16; other parameters are set accordingly to Table 27.

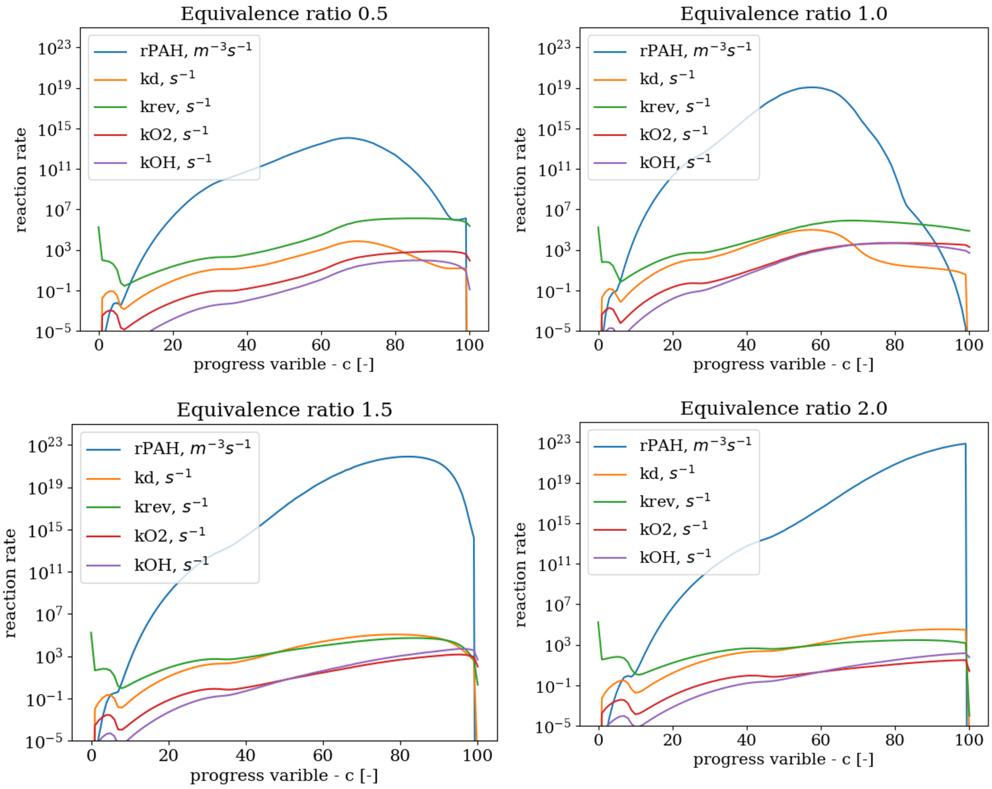

Equivalence ratio 0.5

Equivalence ratio 1.0

Equivalence ratio 1.5

Equivalence ratio 2.0

Figure 79: Plot of source tabulated reaction rate coefficients for cp-library; the y-axis is in a logarithmic scale. Results are related to unburnt temperatures of 700 K, 10 bar, and no dilution (EGR 0%), for lean, stoichiometric, and rich mixtures.

As for the premixed library, the variation of the tabulated reaction rate constant is plotted in Figure 79 for 10 bar, unburnt temperature of 700 K, and no dilution: the main feature observable is the shift of the peak, especially for rPAHs, towards the end of the combustion (values of c closer to 100%), and this behavior can be explained by the fact that the richer the mixture, the longer it takes for decomposing the molecule into PAHs, and the combustion temperatures generally tend to have a peak around $1.0 \div 1.1$, then it decreases with the increase of the equivalence ratio.

3.3.2.2 Switch testing The implemented modification is tested in three stages by answering these questions, one at a time:

1. Is the switch of the library occurring? (Effectiveness of the modification)
2. In what measure the modification of the code with the switch produces differences in the results.
3. Discussion on engine validation.

3.3.2.3 Results on engine sectors The answer to the first and second questions will be provided in this paragraph. As a first check, the correct functioning of the implemented code must be demonstrated. For this purpose, two test cases are employed: one-degree sector and the engine sector with the bowl-shaped piston. The main simulation setup is summarized in Figure 80. As for test case 1, the liquid film initialization is perfect for checking the value of rsOpt, which should be changing when the evaporation of the fuel creates locally rich fuel vapor in cells already interested by the combustion process. Thus a difference between GTF and Y_{TF} becomes relevant and the likelihood of it being higher than the 50% of the GTF is probable. The effective switch between libraries occurs in those cells where it is expected to, in which the liquid film was purposely initialized as 3 mm, as shown in Figure 81(a) and the RVB values Figure 81(b) are also plotted to highlight that test is carried out only in the cells where the combustion onset has already occurred, finally Figure 81(c) the logic results of the GFI-switch test condition is plotted and 0 corresponds to no switch, and 1 to the case in which the switch is carried out.

As for the diesel-engine sector, a similar test is carried out and the results are reported in Figure 82.

Once the switch between libraries is assessed, a first-order analysis of the results is conducted with focus on the soot that is produced. For all cases, the number of sections is set to 30 for the soot calculation with the Sectional method. To

Setup	Test case 1	Test case 2
Combustion model	ECFM-3Z spark	ECFM-compression
Soot model	Sectional - 30 sect.s	Sectional - 30 sect.s
Turbulence model	k-ε RNG	k-ε RNG
Liquid film initialization	3e-6 m	-
Fuel type	Gasoline, SA -30 deg bTDC	n-tetradecane, injection -43 deg bTDC
Geometry	one degree-engine sector with flat piston 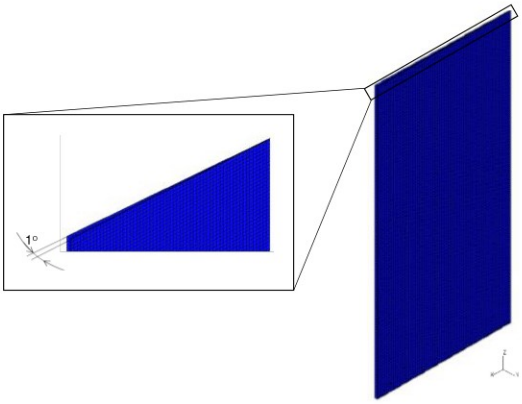	Diesel engine sector, bowl shaped piston 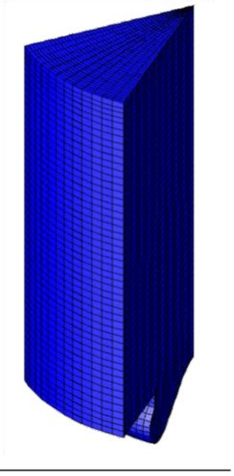

Figure 80: Summary of the test cases employed for checking the proper functioning of the implemented switch: one-degree SI-engine sector (96 mm Bore), and Diesel-engine sector.

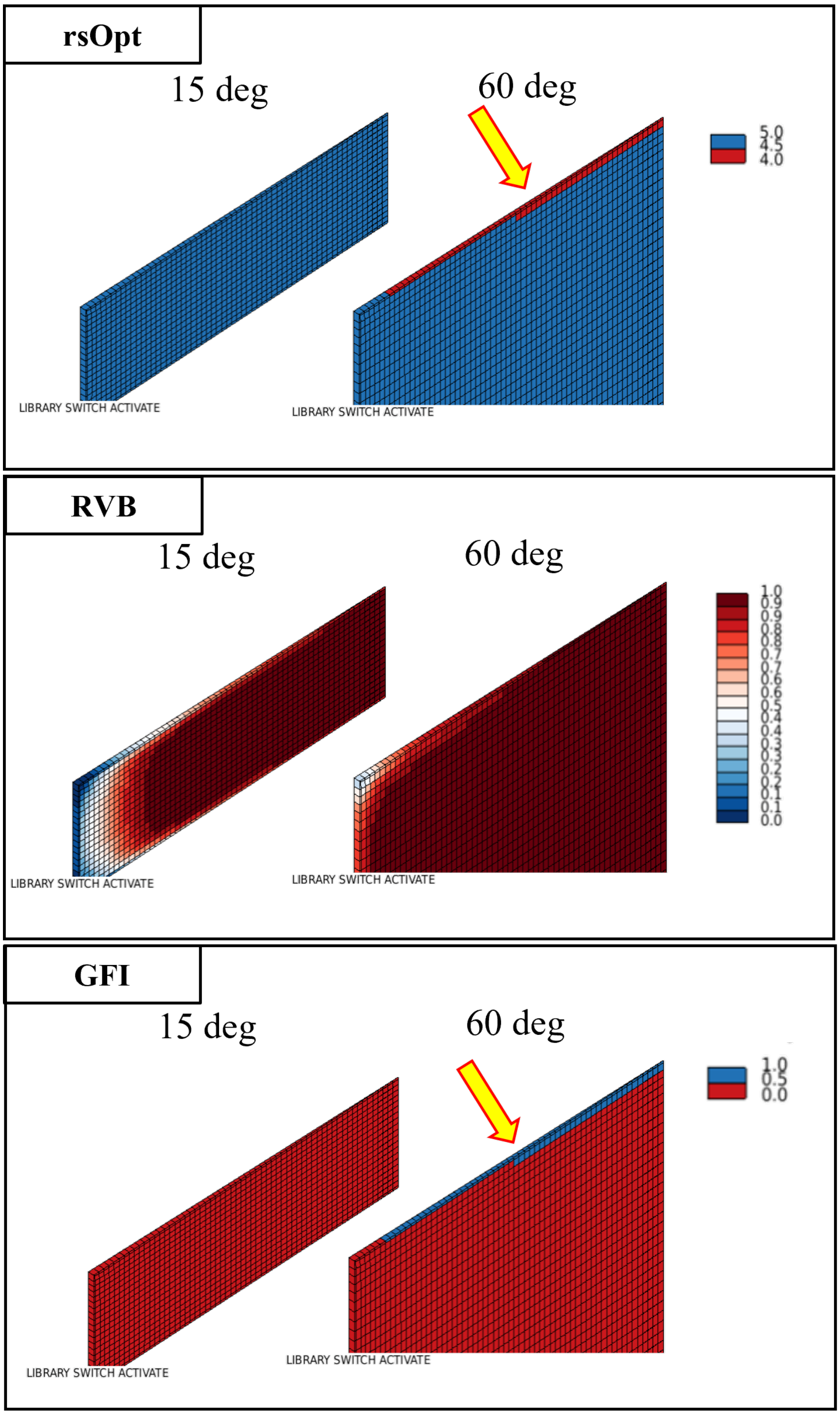

Figure 81: Results from test case 1: values of rsOpt (a), combustion progress variable (b), and GFI or test condition plot a logic value (c).

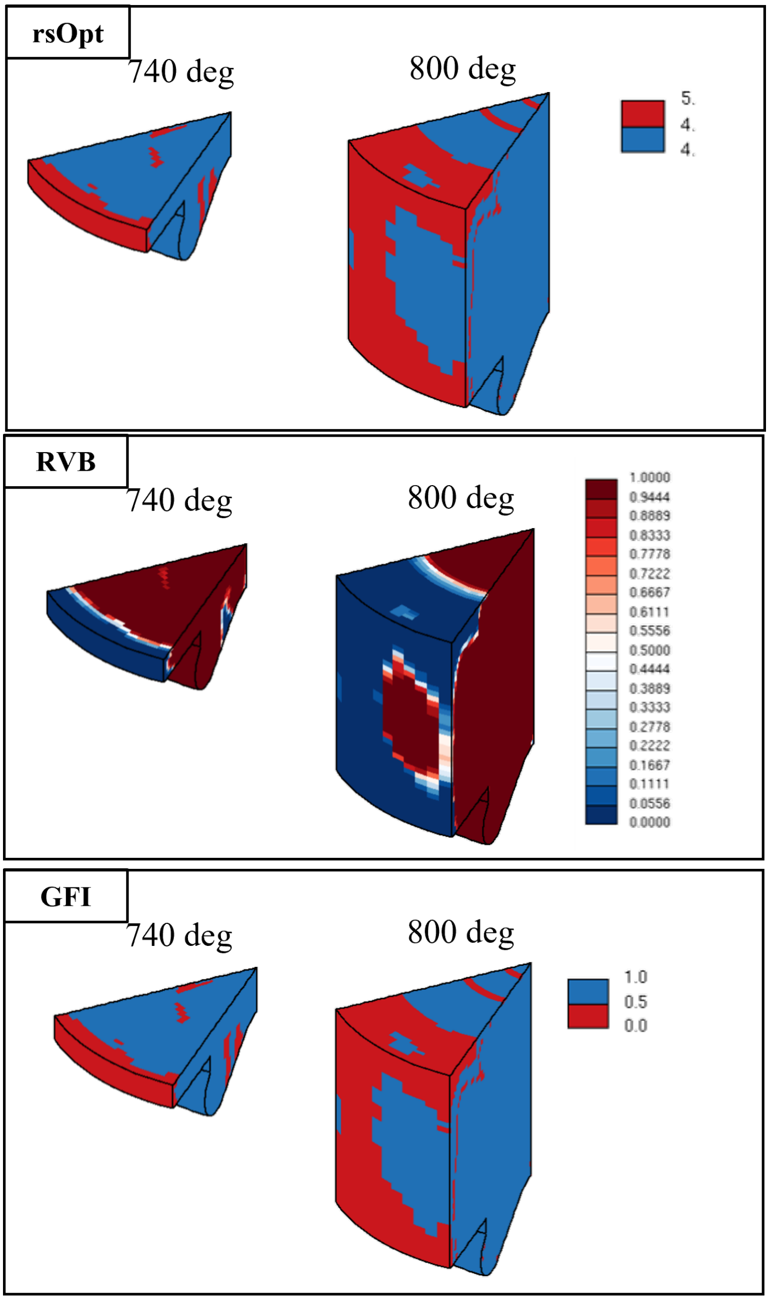

Figure 82: Results from test case 2: values of rsOpt (a), combustion progress variable (b), and GFI or test condition plot a logic value (c).

get a numerical measure of the impact of the library switch on the soot, first the libraries were tested alone, then with the switch. The use of the diffusive library derived in this study yields considerably fewer sooting results, thus an additional check is carried out with the default library available as default in the solver for a different fuel (n-heptane) to exclude any impact of the customized libraries on the soot results. Again, the diffusive library in the context of test case 1 yields fewer sooting results, and the possible explanation for this can be that the local values assumed by the mixture are not high enough to overcome the sooting threshold value (e.g. from literature: [22]).

On a final note, the impact of the library switch is still evident: the case 1 (Figure 83) with the library switch produces fewer sooting results accordingly to the restricted number of cell in which the switch occurs, in accordance with what is expected (Figure 81). For test case 2 (Figure 84), a similar result is obtained, but this time the predominant combustion mode is diffusive, thus the switch follows the diffusive library even more, since the switch occurs in a greater number of cells this time.

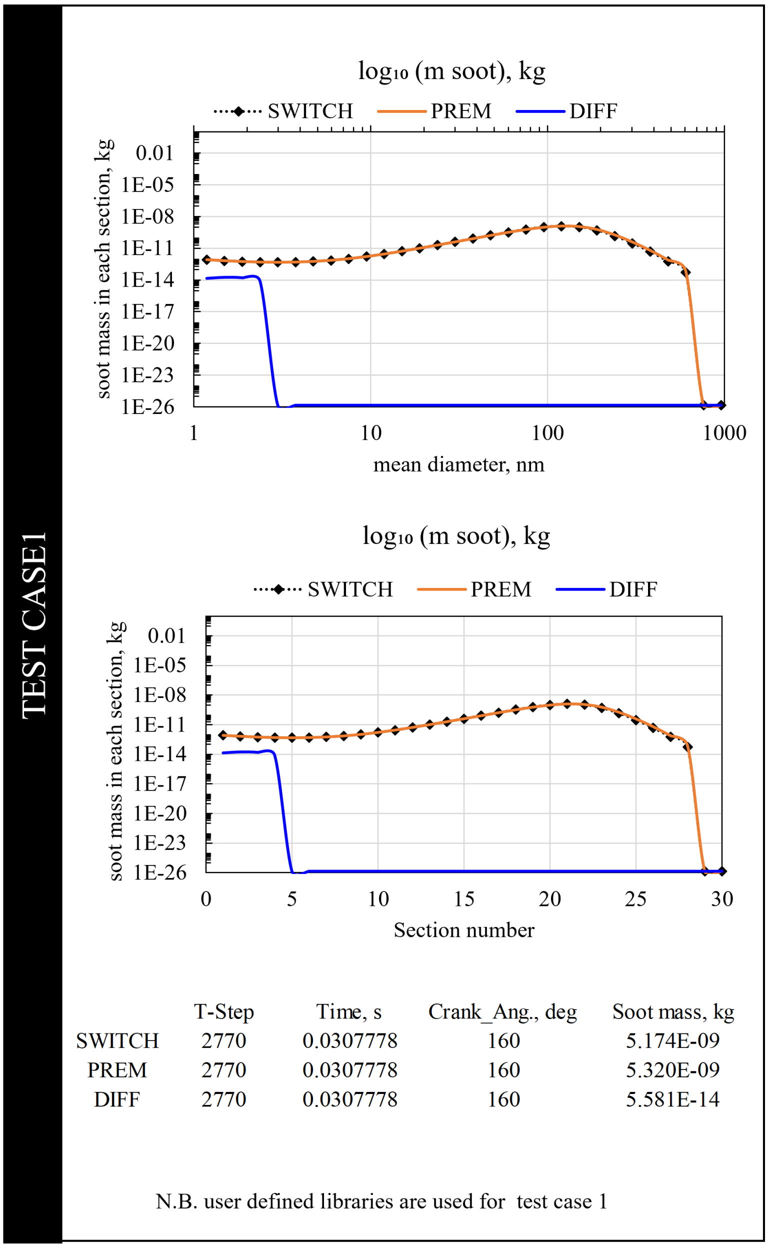

	T-Step	Time, s	Crank_Ang., deg	Soot mass, kg
SWITCH	2770	0.0307778	160	5.174E-09
PREM	2770	0.0307778	160	5.320E-09
DIFF	2770	0.0307778	160	5.581E-14

N.B. user defined libraries are used for test case 1

Figure 83: Results for test case 1. The aim is to test the switch condition and the effectiveness of the library reading after the switch for SI-engine. For the test, a one-degree sector of an engine of 96 mm bore.

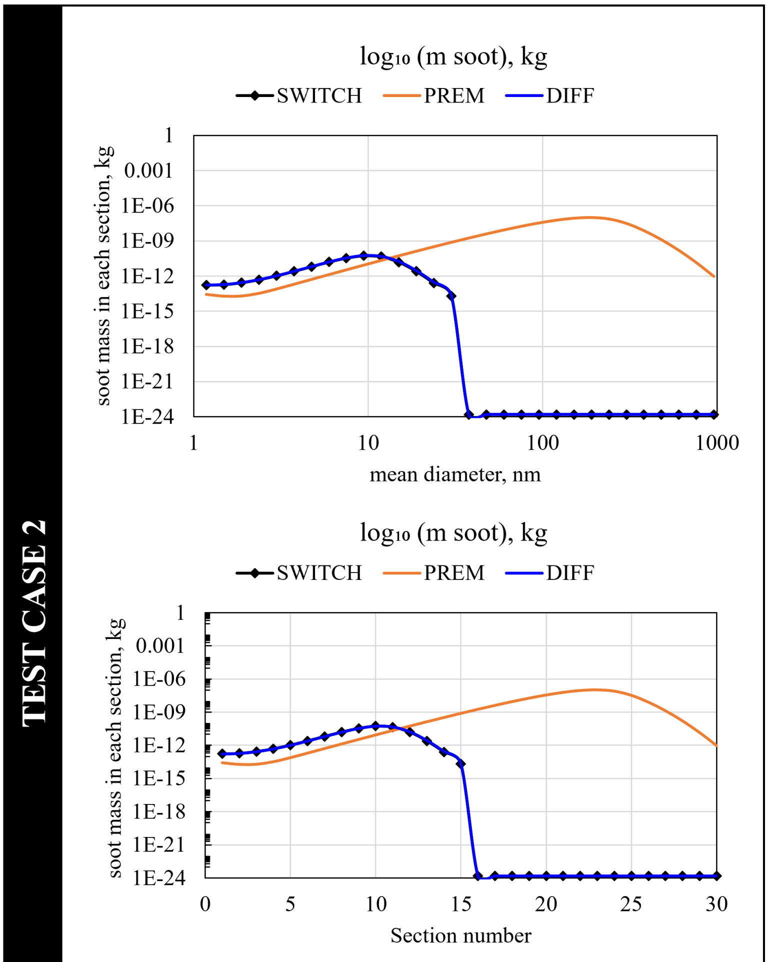

	T-Step	Time, s	Crank_Ang., deg	Soot mass, kg
SWITCH	2200	0.0152778	810	1.788E-10
PREM	2200	0.0152778	810	4.412E-07
DIFF	2200	0.0152778	810	1.854E-10

N.B. for test case 2:

- CP_LIB from STARDATA (single-component gasoline)
- FL_LIB from STARDATA (n-heptane)

Figure 84: Results for test case 1. The aim is to test the switch condition and the effectiveness of the library reading after the switch for predominantly diffusive combustion, with a five-degree Diesel engine sector.

3.3.2.4 Results on metal engine The results obtained for the test cases are still purely numerical, and their aim is to check if the switch has an effective implementation. Although they picture the two possible borderline cases, one very close to the purely premixed (test case 1) and the other one to the diffusive (test case 2). The aim of the test case is the evaluation of the correct implementation in the source code, and to check is if the switch between libraries works properly when integrated in the combustion and soot modelling framework. The test cases are purely numerical although relating to engine simulations, hence a validation on experimental data on a real engine are required. Experimental data are available for the engine discussed in the second chapter [15]. This is a single-cylinder equipped with optical access, and as discussed previously, the piston thermal drift is not negligible. During the expansion phase, the blow-by phenomenon may lead to leakage into the combustion chamber of vapors or liquid droplets escaping towards the carter during the compression stroke. Although this leads to secondary diffusive combustion sites, the numerical representation with high fidelity may be unpractical. Thus, a metal engine can be a better candidate for the task. The GDI metal engine adopted by Berni et al. [121] is employed in this study to investigate the impact of the library switch. Previously the soot model was achieved by the use of dedicated chemical simulations of a CP-reactor for the table generation of reaction rates for the soot mass fraction soot term. The fuel type is a surrogate of an oxygenated gasoline as reported in Table 11, whereas the library generation parameters are reported in Table 10 for the premixed library. In this work, a diffusive library is generated with the parameters described in Table 12 to test the switch. A quick overview on the engine simulation setup is summarised in Table 28 and extensively discussed in [121].

Table 28: Summary of the simulation setup for the metal engine test of the library switch. The setup is equivalent to [121] with the switch.

Engine model geometry	half chamber of a V8 engine
Combustion model	ECFM-3Z [103] [102]
Soot model	Sectional Method with 30 sections; SGR = 4, OX=0.01
Soot source terms tabulation	Customized tables for diffusive and premixed combustion
Library switch	implemented with GFI for test condition
Turbulence treatment	RANS $k-\varepsilon$ RNG
Grid cells	$\sim 3 \times 10^5$ at TDC,$\sim 7.5 \times 10^5$ at BDC
Numerics	2nd order scheme MARS for mass, momentum, energy, and turbulence equations
Time step	$\sim 2 \times 10^{-6}\,\mathrm{s} \div 2 \times 10^{-6}\,\mathrm{s}$
Investigated SOI	200, 245, and 300 bTDC

The multi-cycle engine simulation is carried out to get a consistent statistics on the soot particle number. This last is post processed using the same methodology described by [121] to account for the background soot and for the experimental instrument accuracy, which can play a relevant role as shown in section 3.3.1[1].

As discussed by Berni et al. [121], the experimental data are gathered with a particle counter that is characterized by a counting efficiency for particles between 13 and 40 µm, whereas particles below 13 µm are not measured. Moreover, the experimental apparatus is characterized by a dilution of 5000:1 of the sampling volume and for this reason, the particle number concentration is scaled on an equivalent volume as shown in eq.(79), where subscripts "CC" stands for quantities measured in the combustion chamber, "EXP" for the experimental ones, and "EVO" for exhaust valve opening. The engine simulation PN is collected and scaled over the equivalent volume at the Exhaust Valve Opening (EVO). The particle number concentration is the ratio of the sum of the particle number throughout the sections multiplied by the counting efficiency factor [121] and the

---

[1] Section 3.3.1: Chemistry-fidelity and tabulated approach for premixed combustion

equivalent volume.

$$\mathrm{V_{EQ}} = (1 + \mathrm{DR}) \cdot \left(\frac{p_{\mathrm{CC,EVO}}}{p_{\mathrm{in,EXP}}}\right) \cdot \left(\frac{T_{\mathrm{in,EXP}}}{T_{\mathrm{CC,EVO}}}\right) \cdot \mathrm{V_{cc,EVO}} \tag{79}$$

In this case, to be sure that the library switch occurs only after the primary premixed combustion has occurred, the check on the cell-wise value of RVB is set to 0.99 (99% of combustion completed), instead of the previously selected 0.01 (1%). Previously, this check on RVB was set as 1% arbitrarily because the tables have the combustion progress variable c stepping starting from 0.01. In the engine validation, instead, the reason for setting it as 99% is twofold:

1. first and foremost, we are interested in the cells in which the default predominant combustion mode is almost over, so that the onset of the secondary diffusive flame is more clear
2. secondly for computational cost, since the higher the number of the cells of the moving grid, the more number of cells in which the switch should be done.

The issue on point two can be solved with a future modification to the implementation: the current one enables the reading of one table at a time, and the tables are read anew anytime the switch changes from default premixed (rsOpt = 5) to diffusive (rsOpt = 4). After the new access, the storage of the corresponding values of tabulated coefficients is carried out. For this reason, this point of the code implementation can be further improved to speed up the calculation. However, it does not affect the qualitative result, so the result analysis is still valid for testing the efficacy of the switch in improving the numerical estimation with respect to the experiments.

Table 29: Concentration of particle number from 13 µm: experimental and numerical results.

SOI	**Experimental**	**With switch**	**Without switch**
300	17986	471000	726000

The results for three selected SOIs are reported in figure 85 and in Table 29 as the particle concentration. The results yielded by the purely premixed library are similar to the ones obtained with the switch for SOIs 200 and 245 because the liquid film persistence is not reaching the combustion angle, hence it all evaporates before the main front reaches the areas. The impact of the library switch is relevant when the liquid film is persistent after the combustion onset, as happens for SOI 300.

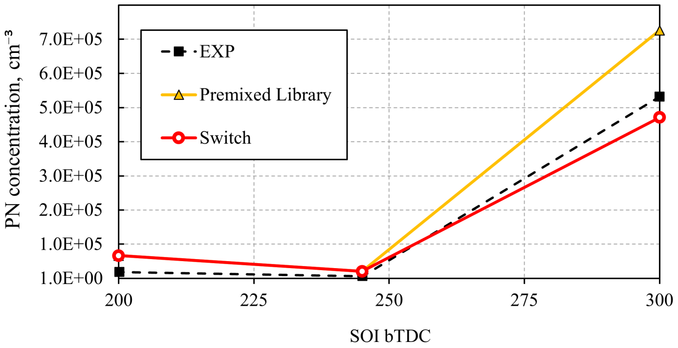

Figure 85: Particle number concentration: results with and without library switch compared to the experimental data.

For SOI 200 and SOI 245, the two strategies yield similar results, and this is due to the number of cells in which the switch is executed, due to the fewer locations in which the secondary diffusive flames triggered by sudden evaporation of the unwanted and persistent liquid film. occur. For SOI 300, as per experimental data, the number of cells in which the switch occurs increases so that the impact of the switch is more evident. The switch balances the soot formation in the cells with a rich mixture, as shown in the previous section 3.3.2.1[2]: for very rich mixtures, the reaction rates of the premixed tabulation are very high, yielding a peak of nucleation, hence the smallest diameters, which is not observed from experiments. Further validation is required for assessing the efficacy of these code modifications and of the library switch, for example, the extension of the dataset of the SOI can be considered. This data from PN concentration shows

---

[2] Section 3.3.2.1: Diffusive and premixed table: comparison of the tabulated results

a preliminary result, whereas future development should address also the mass concentration to draw further assessment.

Conclusions and Further Development

4. Conclusions and further development

In current times, the research combustion community is spending efforts in two main areas: strategies to curb emissions and investigation of carbon-neutral fuel combustion in current combustion devices, such as internal combustion engines. Besides experiments, computational tools can help in this area of research and development. Within this context, this thesis presents a methodology to enhance the current state of the art of CFD engine simulations with chemical kinetics simulation results, presenting applications and results for GDI engine application, with a ready-to-use set of correlations for ammonia-hydrogen laminar flame speed in all CFD codes and for different application.

The synergy between CFD solver and data from chemical kinetics is presented for several aspects of the full-cycle engine simulation:

- multi-phase modelling of gasoline surrogates: a methodology to model the TRF multi-phase is presented with a focus on the evaporation yielded by different Lagrangian multi-phase modelling strategies, and on the consequent **spatial distribution of the sooting tendency**
- flame propagation modelling with **customized correlations stemming from extensive chemical kinetics simulation results of laminar burning velocities**. The current state of the art is **applied to TRF components** and a flexible methodology is proposed to reckon TRF flame speed in case of any composition, via a user subroutine and a mixing rule. A **further step** is taken to provide correlations **for ammonia-hydrogen blends** adapting the current methodology for ultra-lean to the rich mixture, and finally, a novel approach is presented to account for hydrogen content

as an additional parameter in a new five-parameter correlation.

- finally, the emission modelling is focused on **soot modeling**. The state of art sectional model is applied first to the premixed case to show the successful approach with **customized tabulation of rates for the soot mass fraction source term**. Then, a step further is taken for the partially premixed combustion and a modification of the current source code is proposed. The aim is to switch dynamically the library during the simulation, depending on the local predominant combustion mode, which is not possible with the current version. The **dynamic switch** is tested on simple engine sectors, and then a validation against real metal engine data is presented.

The fundamental input that is in common with all the chemical kinetics tools employed in this work is fuel composition. Since gasoline is a complex mixture of several hydrocarbons, the formulation and use of surrogate fuels are mandatory for both the chemical kinetics and 3D-CFD engine simulations. For this reason, in the second chapter, a thorough discussion of the surrogate formulation is reported. Although the evaporation curve of a real gasoline requires heavier hydrocarbons to be matched, the TRF surrogate has been widely used to mimic the combustion behaviour and the sooting tendency. This last can be described by an index, TSI, that is calculated with a mixing rule for each blend, and the result is three TRFs with stark differences in TSI values and similar combustion properties (RON). The choice of such a simple surrogate is driven by the access to these hydrocarbons and their miscibility for experimental measurements. The TRFs employed can replicate the evaporation behaviour of a real gasoline at high loads, whereas it becomes more critical at part loads. However, the methodology employed for the surrogate formulation is flexible and leaves room for additional components, and the extensive target properties presented in the general part of the surrogate formulation methodology is integrated with ready-to-use mixing rules and indications for several properties, from combustion behaviour (RON, MON, LHV) up to liquid properties such as viscosity, and density. Hence, a ready-to-use toolkit is provided for more extensive applications, than the one presented in this work.

Spatial distribution of sooting tendency and multi-phase modelling strategy for TRF surrogates

Mixture formation and spatial characterization of the sooting tendency of the mixture are analyzed as well as their dependency on the Lagrangian multi-phase modelling approach. The gasoline with average properties [84] is modelled with three representative TRF surrogates with increasing toluene content (0mol%, 30 mol%, and 60mol%), with the aim to use an increased toluene content to characterize and show the impact of the Lagrangian multi-phase approach on the spatial distribution of the sooting tendency. Properties of both gas and liquid phase are characterized by either a single-component with averaged lumped properties based on mixing rules based on the composition or by a more sophisticated multi-component approach. In the multi-component approach, all the components are injected as a separate species and the liquid and gas phase properties are separately defined, whereas, in the single component, an equivalent fuel is defined. In this case, the gas and liquid phase properties, including the phase change, are derived as polynomial functions of the temperature for each one of the three surrogate blends. The novelty of this approach is in the implementation via Fortran user-subroutine of the cell-wise calculation of the TSI value: the combustion chamber is divided into four radial sectors to evaluate where the most sooting behaviour of the mixture tends to be located in the chamber (close to spark plug or in the end region). The TRF60 is, as expected, the most sooting out of the three surrogates (C_7H_8 60mol%). Although from the radial sectors volume average of the cell-wise TSI, the agreement between multi-component and single-component is acceptable, a thorough analysis provided by the local visualization of equivalence ratio, shows that the evaporation and charge stratification yielded by the two techniques have some differences. In particular, results shown that the TSI distribution in the combustion chamber is related to the equivalence ratio distribution, which is affected by the Lagrangian multi-phase modelling strategy. Specifically, lumping the properties of the TRF surrogate in a single-component yields results similar to the multi-component only for the case in which the composition is biased towards one component. The TRF30, blend with no stark differences in the composition, is not replicated properly by the lumped approach, whereas the multi-component is successfully depicting the trend. Acceptable agreement in results can be spotted for TRF60 and PRF, which are respectively biased towards toluene and iso-octane. The main difference lies in the evaporation process, which is dominated by the saturation pressure modelled by using the UNIFAC method, which accounts for the molecular interaction, whereas the lumped approach employs a simplified description with Raoult's law. The global trend of evaporation is respected for all the lumped components, whose evaporation is overall faster with respect to the multi-component counterparts. However, the plots of the equivalence ratio, show disagreement of charge stratification in the case of the absence of a predominant component, whereas the agreement in the case of a predominant component in the mixture is acceptable.

Laminar burning velocity correlations

In internal combustion engines, the turbulent combustion regime falls in the flamelet regime on the Borghi-Peters diagram [101], and for this reason, the turbulent combustion description can be achieved using the flamelet models. These models, such as G-equation (Level set) or ECFM-3Z, are based on the hypothesis that combustion is a one-step reaction and the reaction zone is described as a thickened laminar reaction region, known as the *flamelet brush*. The evolution of the turbulent flame front in the GDI engine combustion chamber is described with these models by using the laminar flame speed as an input. The *laminar burning velocity* depends on the local values of pressure, unburnt temperature, equivalence ratio, and eventual presence of dilution (e.g. EGR). Moreover, the laminar flame speed is also influenced by the chemical nature of the burning mixture, thus by the type of fuels. In this work, a methodology to produce input data based on a multi-parametric correlation is applied to different types of fuels and further developed and tested for describing the carbon-neutral fuel combustion. The multi-parametric correlations are based on values of laminar burning velocity derived from chemical kinetic simulations of a 1D flamelet that propagates freely. These simulations require as inputs the thermal and transport data of all the species involved as well as the reaction mechanism describing the fuel oxidation as a multi-step reaction scheme rather than a one-step reaction. In this case, the advantage of using a chemical kinetic solver is twofold:

- unlike the experiments, the chemical kinetic solver can reach the engine-relevant conditions, and the values can be calculated for the actual conditions of interest
- the fuel composition can be given as input, and it is possible to simulate fuels that are very different in nature

Ready-to-use correlations are derived and provided for two different applications:

- **TRF surrogates for gasoline**. The surrogate fuel laminar flame speed is derived. The methodology proposed is flexible and adaptable to all TRFs, since it is based on mixing rules. More in detail, a laminar flame speed correlation is derived from an extensive database of chemical kinetics simulations for a wide range of values of unburnt temperatures and pressures (up to 1010 K and 65 bar), for equivalence ratio values for very lean mixtures (0.4) to very rich (2.0) to cover all the potential conditions due to uneven charge stratification as well as ERG percentages from 0% up to 30 %. Then, starting from these three correlations, the value of the surrogate flame speed can be calculated for every condition using a mixing rule. Three mixing rules are compared to results obtained with the actual surrogate composition: linear-by-mass and linear-by-mole mixing rules and the one formulated by Le Chatelier, also based on the mole fractions. The three yielded fairly similar results and were in agreement with chemical kinetics simulations with the actual surrogate, and Le Chatelier's rule shown a slightly better fit, and for this it was employed. A user-subroutine with the laminar flame speed information is implemented to communicate with the combustion model the input and, since it is necessary within the framework of G-equation as implemented in the employed software (STARCD), also a turbulent flame speed should be provided as an input. The efficacy of this customized modelling of the multi-component surrogate is tested and a numerical comparison is done with the default implemented approach. The TRF30 with injection time 300 bTDC is selected as a case in the middle, both in terms of toluene content and injection timing. The results highlighted that the default implementation overestimates the pressure peak and the combustion velocity in the first part of the fuel oxidation, whereas the combination of the user-defined laminar and the turbulent flame speed is in better agreement with the experimental pressure trace.

- **ammonia and hydrogen blends**. These offer a valid tool for carbon-neutral fuel combustion modelling. First, the already existing methodology is applied to provide blend-specific correlations with four parameters, such as the one for the TRFs. Then, a novel correlation with five parameters is proposed. Several blends of ammonia/hydrogen are investigated to provide an answer to the input correlation for the laminar flame speed. To produce the laminar flame speed dataset, several chemical kinetics simulations are carried out at engine-relevant conditions (up to 130 bar and more than 1000 K), for ultra-lean mixtures ($\Phi = 0.4$) to the rich mixture ($\Phi = 1.5$). The blend-specific fit is derived for each blend with a hydrogen content from 0 mol% to 100mol%. Moreover, for a lean-to-rich mixture with hydrogen content between 60 mol% to 90mol%, a single correlation is formulated with hydrogen mole fraction as an additional parameter. The general correlation exhibits a slightly higher error than the blend-specific one, which is tailored to the chemical kinetics simulation results of that specific blend. Finally, the correlations formulated are compared to the others present in the literature. The derived correlations are compared with the other proposed in the literature by Verhelst [81] for pure hydrogen, and by Goldmann [83] for the ammonia pure and blended with hydrogen. The results are in good agreement with the ones from the literature in case of an overlapped range of validity. Furthermore, these correlations are extended to ultra-lean mixtures unlike the ones in the literature, and this range is relevant for the recent studies on ammonia-hydrogen engines fed with lean mixtures to reduce NOx. Moreover, in the literature, a correlation for pure hydrogen at very high loads is missing, and the one proposed in this study covers up to 130 bar, from ultra-lean to rich mixtures.

Soot modelling with sectional method and customized tabulated approach and proposal of model modification for a dynamic library switch for partially premixed combustion

Finally, the other subject undergoing intense study for the hydrocarbon-based fuels is investigated: the pollutant species known as particulate matter or soot. Unlike the other pollutant species, soot is a solid product of carbon-based fuel combustion and its origin in the gas-phase precursors is a complex interplay of physical and chemical processes. Since numerical modelling is the tool used in this thesis, soot formation is also discussed under the lens of one of the most articulate soot models: the Sectional Method. This method can be applied with customized tabulations of the reaction rates necessary for the calculation of the source term that appears in the transport equation of the soot mass fraction of each section. Every section can be considered as a bin of soot particles characterized by a size that falls in a specific range, in the same fashion as a particle counter employed in the experimental measurements. These tables can be assembled using chemical kinetic simulations, yet another example of a synergic application of CFD and chemical kinetics solvers. As a first case study, a premixed spark ignition engine from the literature is considered. The experimental versus numerical comparison is done with two types of fuel: American gasoline and pure ethanol. For each fuel, a table of the reaction rates for the soot source term is derived. Then, the efficacy in catching the sooting threshold value of the equivalence ratio of the mixture is assessed: the two experimental cases are in agreement with the numerical results. To further test the customized tabulated approach, another gasoline is tested, this time a Chinese gasoline with 10mol% of ethanol. As expected, the oxygenated gasoline exhibits a delayed sooting threshold compared to the one without any ethanol. After the test of this approach for the premixed engines, the case of GDI engine is considered. The use of CP-reactor-based tabulation has been validated previously, and in this work, the partially premixed combustion is examined.

Although the customized approach is successful, the current implementation of this model requires an a priori assignment of the table, which means that the predominant combustion mode must be assumed. In fact, these tables can be produced by using only one type of reactor, either premixed or diffusive. Modern combustion devices are not always characterized by such a sharp distinction. If in the case of PFI engines, it is easy to assign premixed tables, or for Diesel engines, it is diffusive, for DISI engines it may not be so clear, especially in the case of part loads, where unwanted sudden liquid film evaporation can lead to local secondary phenomena of diffusive combustion, which may yield different sooting tendencies.

To answer this necessity of partially premixed combustion, a modification of the current sectional model is presented and tested, including a preliminary analysis of experimental PN data of a metal engine. A dynamic switch between libraries is implemented in the Fortran source code. Assuming the predominant combustion mode is premixed, the default premixed library is switched to the diffusive one only in the cells in the switch condition is satisfied. In detail, the research question for this case is threefold:

1. is it possible to implement a *dynamic switch* between the two types of libraries?
2. how should the switch assess if the combustion is predominantly premixed or diffusive?

3. what is the impact of dynamically switching the libraries on the soot production?

The first question requires insight into the input and output parameters for table generation which are similar in some instances, yet differ in others. In order to have two libraries as equivalent as possible, the inputs should be equivalent between the two types. All these factors and differences between reactors are discussed and presented thoroughly to be sure of the equivalence of the two derived tables. The second question leads to the definition of a *flame index*, to assess which type of combustion is predominant. After a thorough literature review, the ones proposed were implemented and tested. Finally, two more new criteria based on the adopted combustion model (ECFM-3Z) are examined: one based on the distinction of the heat release types and the other one on the fuel tracer evolution. The chosen one is based on testing the amount of fuel tracer in a specific cell in which the main flame front has already passed (combustion progress variable $c \leq 0.01$). In this cell, if the value of fuel tracer is greater than 50% of the one stored right before combustion occurred in that cell, the combustion mode is switched from fully premixed to a local secondary diffusive one. The switch implementation and its interplay with the soot and combustion models are then described and tested for two extreme conditions: one-degree sector of a GDI engine with initialization of a liquid film (to test the evaporation of fuel which will increase the fuel tracer), and a Diesel engine sector, characterized by a predominant diffusive combustion. Results indicate that the library switch is effectively implemented in the source code and it successfully operates within the combustion and soot model framework. Finally, an answer to the third question is attempted with these test cases, which are enough to test the correct implementation of the switch and its interplay within the framework. Preliminary validation on the impact on the soot prediction is carried out on a metal engine for three SOIs, and the SOI 300 in which the liquid film persists after the combustion onset is the one closer to partially premixed combustion conditions. In this case, the PN concentration yielded by the switch is closer to experimental results than in the case run only with a premixed library. A possible explanation can be deduced by the sampling of the reaction rates: overall for very rich mixtures, the cp-reactor employed in the tabulation for the premixed case yields very high values of RPAH. This means that non-realistic nucleation is triggered in the CFD simulations in those cells where the sudden evaporation of the fuel produces a higher-than-average value of the equivalence ratio. As shown by the PN trend between, in fact, without the switch, the PN for the most sooting SOI is overestimated (more than twice), whereas a better prediction is offered by the switch. Although this work provides a preliminary analysis of the proposed structure of the modification of the current model, as a future development, the modification can be further tested with additional operative points, or by correlating the PN with the number of cells in which the switch is carried out. The relevance of this work for the soot modelling lies in the three levels of interactions:

- interactions between soot and combustion model quantities that are shared for the switch test
- the non-trivial implementation of changing the inputs to the sectional model for reckoning the soot source terms from the rates of the HACARC mechanism, which are previously tabulated with dedicated chemical kinetic simulations of predefined reactor type.
- a novel index is defined and compared to the ones from the literature, most of them also implemented in the CFD code used in this study. The flame index, GruMo Flame Index (GFI) is selected for reasons that can be summarised with the fact that the GFI allows to use the output from the combustion model, which is one of the most advanced model for the flamelet partially premixed combustion, hence perfect for the examined application.
- the library switch is dynamic, hence during the simulation, each cell is tested against the switch conditions, which is based on an arbitrary value of the increase of the fuel tracer with respect to the cell-wise value stored at the combustion onset. For the engine validation, the arbitrary difference is set

as 50%, which can be set differently. In this work, it is set as such since the test is executed in the cell in which the predominant premixed combustion (main combustion front) has already occurred, hence where the combustion progress variable is 99%, and since the global value of equivalence ratio is 1.0. In fact, from a cell-wise point of view, when the 99% of the main premixed combustion is done, and the switch test condition corresponds to 50% of the original value of unburnt fuel, it means that the newly evaporated fuel is locally 50% of the one right before the spark onset, thus globally speaking the value of the equivalence ration is 0.5. Of course, this is an approximation, and room for improvement can be fulfilled by comparing the newly evaporated fuel and oxidizer with the flammability limits to asses if the diffusive combustion can locally occur.

- the test condition on the progress variable rvb is switched from 1% for the test cases to 99% for the real engine case. The reason is that for the test a preliminary exploration is carried out to check is the implementation in the code works properly and if it produces an effect on the resulting PSDF. For the engine, this criterion is refined to 99% for the implication described for the switch test on the GFI to be 50%, and also because of the computational cost. Keeping it as 1% of the combustion progress variable requires a computational expense that is not justified by the results. In other words, the switch occurs only in cells with a consistent liquid film, which takes time and heat to evaporate, thus the 50% switch condition occurs after the at least more than cell-wise value of rvb 50% of the combustion. A systematic analysis can be also carried out to better quantify the impact of the threshold on the rvb on a general scale, although the consideration discussed here are valid for the three operative conditions explored in the results section.

- a further development can be achieved by speeding up the reading of the two libraries, but this requires to work on a deeper level of the source code and potentially on the input/output structure of the library, which is locked by the chemical kinetic solver.

- this work is conducted on engine simulations, but the concept can be extended to any combustion device characterized by partially premixed combustion to reduce soot emissions.

Appendix

Appendix A

Table 30: Coefficients for central branch for laminar flame speed calculation in cm/s for TRF surrogate components.

central	$\mathbf{C_7H_8}$	$\mathbf{C_7H_{16}}$	$\mathbf{C_8H_{18}}$
A0	8.916579E+01	1.102519E+02	98.68592961
A1	3.971166E+01	4.810823E+01	37.47414584
A2	-2.723256E+02	-3.039945E+02	-346.6691689
A3	-4.377247E+02	-3.986105E+02	-420.8625625
A4	3.170580E+02	2.541192E+02	401.8002489
A5	1.343573E+03	1.010038E+03	1309.562571
B0	2.416448263	2.395025558	2.473888405
B1	0.006835319	-0.354677038	-0.060369624
B2	3.952788423	5.785952047	4.310496157
B3	7.762184365	10.0748721	7.639216447
B4	-3.067127885	-18.19921265	-13.32922996
B5	-34.59011754	-63.33869201	-46.47158452
C0	-0.257818924	-0.297249074	-0.302657901
C1	-0.040662027	0.068011141	-0.021429371
C2	-0.84656154	-0.92276992	-0.729410895
C3	-0.960339298	-0.714991954	0.068614805
C4	3.564106724	5.614863916	4.433831876
C5	11.11909291	10.64500201	6.681582537
α_{st}	13.4	15.1	15.05
$\mathrm{k_{EGR}}$	2.42	2.17	2.43

Table 32: Reference values and weights for the PSF and TSF of laminar flame speed calculation in cm/s for TRF surrogate components.

$\mathrm{w_p}$	$\mathrm{w_T}$	$\mathrm{w_{tot}}$	$p_{\mathrm{ref,fit}}$	$T_{\mathrm{ref,fit}}$	$p_{0,\mathrm{fit}}$	$T_{0,\mathrm{fit}}$
1	5	6	35×10^5 Pa	450 K	35×10^5 Pa	810 K

Table 33: Coefficients for lean branch for laminar flame speed calculation in cm/s for TRF surrogate components.

lean		**C_7H_8**	**C_7H_{16}**	**C_8H_{18}**
PSF	l3	10.0432	2.293058	9.231581
	l_2	-3.029598	-0.7597261	-1.817887
	l_1	-2.559443	-2.844295	-3.213258
	l_0	1	1	1
	m_2	0.4177871	0.1188024	0.1174834
TSF	m_{low}^{lean}	-0.085568	-8.708034	-6.103044
		-0.4449878	8.830498	6.148129
		0.3496388	-2.069958	-1.421766
	q_{low}^{lean}	0.720738	14.95285	13.49401
		2.271651	-12.37183	-10.86653
		-1.074643	2.580132	2.209885
	m_{med}^{lean}	0.174053	-6.044307	-4.384941
		-0.9410217	6.214267	4.302956
		0.5343241	-1.479143	-0.9844504
	q_{med}^{lean}	2.657779	10.639	10.93258
		1.107895	-8.056716	-8.047802
		-0.94803	1.597846	1.533934
	m_{high}^{lean}	-0.3654135	-6.321898	-0.938151
		-0.3002211	6.475874	0.790407
		0.3377271	-1.538772	-0.1689103
	q_{high}^{lean}	2.399196	11.15932	4.867095
		1.228579	-8.51496	-1.80278
		-0.8991662	1.698403	0.0786771

Table 35: Coefficients for rich branch for laminar flame speed calculation in cm/s for TRF surrogate components.

rich		$\mathbf{C_7H_8}$	$\mathbf{C_7H_{16}}$	$\mathbf{C_8H_{18}}$
PSF	r_3	-1.124042	-0.5250177	-1.312003
	r_2	2.440559	1.826671	2.457822
	r_1	-2.056403	-1.799142	-2.00211
	r_0	1.000334	1.000482	0.9991761
	m_1	0.3171956	0.255619	0.2086679
TSF	$m_{low,1}^{rich}$	-10.53746	-12.67092	3.900521
	$m_{low,2}^{rich}$	76.09513	90.89796	-25.45374
	$m_{low,3}^{rich}$	-206.0419	-243.7674	60.81654
	$m_{low,4}^{rich}$	248.0104	289.9097	-62.5655
	$m_{low,5}^{rich}$	-111.7422	-128.8972	23.29049
	$q_{low,1}^{rich}$	15.87526	16.88232	-3.1943
	$q_{low,2}^{rich}$	-116.0196	-122.3828	18.47575
	$q_{low,3}^{rich}$	318.9845	332.7731	-35.65422
	$q_{low,4}^{rich}$	-391.7418	-403.2959	22.6675
	$q_{low,5}^{rich}$	181.6633	184.4211	0.6664611
	$m_{med,1}^{rich}$	-9.9075	-12.63629	3.835208
	$m_{med,2}^{rich}$	70.89694	90.35616	-25.49297
	$m_{med,3}^{rich}$	-190.3992	-241.4367	62.31862
	$m_{med,4}^{rich}$	227.6199	285.9781	-66.0066
	$m_{med,5}^{rich}$	-102.0058	-126.6057	25.51914
	$q_{med,1}^{rich}$	15.11268	17.79677	-2.577281
	$q_{med,2}^{rich}$	-109.806	-128.5588	14.78979
	$q_{med,3}^{rich}$	300.6171	348.2237	-27.70591
	$q_{med,4}^{rich}$	-368.3869	-420.2196	15.36669
	$q_{med,5}^{rich}$	170.8486	191.2651	3.060334
	$m_{high,1}^{rich}$	-8.003	-12.61599	5.442731
	$m_{high,2}^{rich}$	56.89711	90.1556	-36.49086
	$m_{high,3}^{rich}$	-151.9597	-240.727	90.35061
	$m_{high,4}^{rich}$	180.9391	284.876	-97.52491
	$m_{high,5}^{rich}$	-80.90062	-125.9998	38.68429
	$q_{high,1}^{rich}$	12.94087	19.88698	-7.182165
	$q_{high,2}^{rich}$	-93.41954	-143.3886	46.15127
	$q_{high,3}^{rich}$	254.638	387.4841	-107.1526
	$q_{high,4}^{rich}$	-311.6055	-466.1714	103.9772
	$q_{high,5}^{rich}$	144.8636	211.3563	-33.60438

Appendix B

Table 37: Coefficients for rich branch for laminar flame speed calculation in cm/s for ammonia/hydrogen.

NH_3 mol%	100	80	60	40	20	10	0
H_2 mol%	0	20	40	60	80	90	100
Blend Tag	NH100	NH80	NH60	NH40	NH20	NH10	NH0
A_0	40.0173	57.5226	87.4570	147.5105	291.8279	464.2770	858.1271
A_1	53.5770	72.4736	109.5226	186.1306	425.1703	724.4504	1455.0608
A_2	-35.9999	-50.3331	-67.7463	-117.4126	-143.9226	-134.0237	40.8495
A_3	-488.7584	-580.4957	-752.6518	-1025.5486	-1728.0115	-2116.3084	-2092.0141
A_4	-211.1658	-237.1176	-306.0228	-335.1146	-723.6756	-934.8126	-827.7233
A_6	1901.5215	2225.9609	2830.4634	3550.9174	5158.4112	5127.5189	3203.2466
B_0	3.5383	3.4569	3.4018	3.3137	3.3670	3.3968	3.4123
B_1	-1.1939	-1.2996	-1.1727	-1.4014	-1.6676	-1.9159	-2.5305
B_2	2.9636	1.9584	2.1754	1.0663	0.4914	0.5730	1.4067
B_3	11.0545	13.0351	8.2580	10.4294	9.7866	9.2392	5.3132
B_4	5.0055	7.6894	2.5042	8.9270	8.9911	6.5447	0.4891
B_5	-56.6582	-65.8449	-40.8437	-51.3569	-43.7961	-35.5784	-12.8829
C_0	-0.2473	-0.2830	-0.3442	-0.4445	-0.6020	-0.6608	-0.6735
C_1	-0.0382	0.0072	0.0089	0.0741	0.1836	0.3240	0.6853
C_2	-0.3076	-0.2229	-0.2794	0.0067	0.2292	0.1548	-0.1171
C_3	1.2897	0.3664	0.4506	-0.4645	-1.4771	-2.2759	-1.8766
C_4	0.9859	0.6060	1.1356	-0.8803	-1.9296	-1.7099	-0.4140
C_5	-4.7462	-0.3642	-0.8338	3.5740	8.0283	8.9987	4.6183
$T_{0,\mathrm{fit}}$	980 K						
$p_{0,\mathrm{fit}}$	90×10^5 Pa						

Table 39: Coefficients for rich branch for laminar flame speed calculation in cm/s for TRF surrogate components.

l_3	5.9723	8.2809	8.774	7.502	5.9246	4.4014	3.1024
l_2	-0.623	-1.2848	-1.6758	-1.4915	-0.7625	0.0038	1.2499
l_1	-2.5525	-2.4858	-2.4213	-2.4341	-2.6083	-2.7516	-3.1085
l_0	0.9091	0.9091	0.9091	0.9091	0.9091	0.9091	0.9091
m_2	0.5666	0.563	0.5538	0.5852	0.5839	0.4875	0.4712
$\mathrm{m}^{\mathrm{lean}}_{\mathrm{low},2}$	-5.1554	-7.0269	-9.5008	-6.5519	-5.7031	-4.4521	-3.155
$\mathrm{m}^{\mathrm{lean}}_{\mathrm{low},1}$	4.9635	6.2996	8.9249	5.9136	5.1414	3.9784	2.6993
$\mathrm{m}^{\mathrm{lean}}_{\mathrm{low},0}$	-0.8605	-0.9885	-1.6554	-0.9854	-0.861	-0.6324	-0.3578
$\mathrm{q}^{\mathrm{lean}}_{\mathrm{low},2}$	10.4246	13.2776	16.3903	13.025	11.2911	9.266	8.0918
$\mathrm{q}^{\mathrm{lean}}_{\mathrm{low},1}$	-7.992	-10.3278	-13.5988	-10.016	-8.218	-6.2419	-5.0685
$\mathrm{q}^{\mathrm{lean}}_{\mathrm{low},0}$	1.4118	1.7937	2.6174	1.7652	1.3419	0.9012	0.6233
$\mathrm{m}^{\mathrm{lean}}_{\mathrm{med},2}$	-11.5729	-5.8325	-9.4016	-6.6665	-2.3558	-3.2935	-2.2743
$\mathrm{m}^{\mathrm{lean}}_{\mathrm{med},1}$	10.8662	4.872	8.4787	5.6386	1.4303	2.6169	1.7408
$\mathrm{m}^{\mathrm{lean}}_{\mathrm{med},0}$	-2.0998	-0.6036	-1.4521	-0.7912	0.1507	-0.2498	-0.1107
$\mathrm{q}^{\mathrm{lean}}_{\mathrm{med},2}$	18.9268	12.0076	16.476	12.4014	6.2531	7.2005	6.398
$\mathrm{q}^{\mathrm{lean}}_{\mathrm{med},1}$	-15.7408	-8.5888	-13.0894	-8.7447	-2.6312	-3.8728	-3.2468
$\mathrm{q}^{\mathrm{lean}}_{\mathrm{med},0}$	3.0089	1.2574	2.3128	1.2472	-0.1765	0.2539	0.1649
$\mathrm{m}^{\mathrm{lean}}_{\mathrm{high},2}$	-7.6693	-3.6513	-2.9295	-9.2543	-4.2631	-0.5637	-1.7376
$\mathrm{m}^{\mathrm{lean}}_{\mathrm{high},1}$	7.0271	2.452	1.9859	8.2644	3.2553	-0.2842	1.1042
$\mathrm{m}^{\mathrm{lean}}_{\mathrm{high},0}$	-1.2386	-0.0353	-0.0013	-1.4197	-0.2805	0.4902	0.0391
$\mathrm{q}^{\mathrm{lean}}_{\mathrm{high},2}$	13.4326	8.5084	7.2937	14.9695	7.968	2.8459	5.1764
$\mathrm{q}^{\mathrm{lean}}_{\mathrm{high},1}$	-10.2424	-4.5996	-3.7127	-11.2472	-4.1883	0.7166	-1.8765

Table 41: Reference values and weights for the ammonia/hydrogen laminar flame speed calculation in cm/s.

w_p	w_T	w_tot	$p_{\mathrm{ref,fit}}$	$T_{\mathrm{ref,fit}}$
1	5	6	$90 \times 10^5\,\mathrm{Pa}$	$720\,\mathrm{K}$

Appendix C

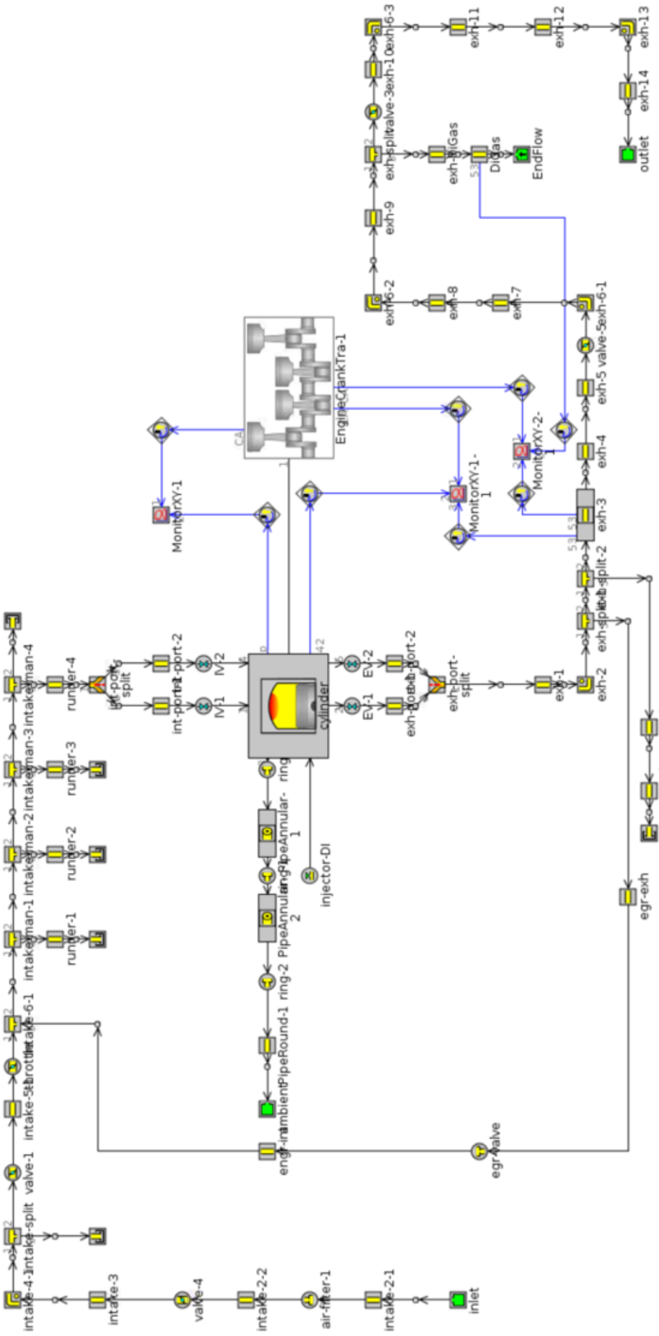

Figure 86: Block scheme of the whole engine 1D simulation.

References

[1] "International Energy Outlook 2016," p. 290, 2016.

[2] J. Slotnick, A. Khodadoust, J. Alonso, D. Darmofal, W. Gropp, E. Lurie, and D. Mavriplis, "CFD Vision 2030 Study: A Path to Revolutionary Computational Aerosciences," p. 58, 2014.

[3] S. Sarathy, A. Farooq, and G. T. Kalghatgi, "Recent progress in gasoline surrogate fuels," *Progress in Energy and Combustion Science*, vol. 65, pp. 67–108, Mar. 2018.

[4] M. L. Botero, S. Mosbach, and M. Kraft, "Sooting tendency of paraffin components of diesel and gasoline in diffusion flames," *Fuel*, vol. 126, pp. 8–15, Jun. 2014.

[5] P. Desgroux, X. Mercier, and K. A. Thomson, "Study of the formation of soot and its precursors in flames using optical diagnostics," *Proceedings of the Combustion Institute*, vol. 34, no. 1, pp. 1713–1738, 2013.

[6] S. Liang, Z. Li, J. Gao, X. Ma, H. Xu, and S. Shuai, "Pahs and soot formation in laminar partially premixed co-flow flames fuelled by prfs at elevated pressures," *Combustion and Flame*, vol. 206, pp. 363–378, 2019.

[7] S. Yan, E. G. Eddings, A. B. Palotas, R. J. Pugmire, and A. F. Sarofim, "Prediction of Sooting Tendency for Hydrocarbon Liquids in Diffusion Flames," *Energy & Fuels*, vol. 19, no. 6, pp. 2408–2415, Nov. 2005, Number: 6.

[8] W. Pejpichestakul, E. Ranzi, M. Pelucchi, A. Frassoldati, A. Cuoci, A. Parente, and T. Faravelli, "Examination of a soot model in premixed laminar flames at fuel-rich conditions," *Proceedings of the Combustion Institute*, vol. 37, no. 1, pp. 1013–1021, 2019.

[9] A. Nobili, L. Pratali Maffei, A. Baggioli, M. Pelucchi, A. Cuoci, C. Cavallotti, and T. Faravelli, "On the radical behavior of large polycyclic aromatic hydrocarbons in soot formation and oxidation," *Combustion and Flame*, vol. 235, p. 111 692, 2022.

[10] P. Borm, D. Robbins, S. Haubold, and et al., "The potential risks of nanomaterials: A review carried out for ecetoc.," *Part Fibre Toxicol*, vol. 3, 2006.

[11] L. V. Amaral, N. D. S. A. Santos, V. R. Roso, R. d. C. d. O. Sebastião, and F. J. P. Pujatti, "Effects of gasoline composition on engine performance, exhaust gases and operational costs," *Renewable and Sustainable Energy Reviews*, vol. 135, p. 110 196, Jan. 2021.

[12] Heywood, John, *Internal Combustion Engine Fundamentals*, 2nd Edition. McGraw Hill Book Co.,New York, NY.

[13] E. J. Barrientos, M. Lapuerta, and A. L. Boehman, "Group additivity in soot formation for the example of C-5 oxygenated hydrocarbon fuels," *Combustion and Flame*, vol. 160, no. 8, pp. 1484–1498, Aug. 2013, Number: 8.

[14] M. Del Pecchia, S. Fontanesi, J. Prager, C. Kralj, and H. Lehtiniemi, "A threshold soot index-based fuel surrogate formulation methodology to mimic sooting tendency of real fuels in 3D-CFD simulations," *Applied Energy*, vol. 280, p. 115 909, Dec. 2020.

[15] S. Fontanesi, M. Del Pecchia, V. Pessina, S. Sparacino, and S. Di Iorio, "Quantitative investigation on the impact of injection timing on soot formation in a gdi engine with a customized sectional method," *International Journal of Engine Research*, vol. 23, no. 4, pp. 624–637, 2022.

[16] P. Pepiotdesjardins, H. Pitsch, R. Malhotra, S. Kirby, and A. Boehman, "Structural group analysis for soot reduction tendency of oxygenated fuels," *Combustion and Flame*, vol. 154, no. 1-2, pp. 191–205, Jul. 2008, Number: 1-2.

[17] L. Cai and H. Pitsch, "Optimized chemical mechanism for combustion of gasoline surrogate fuels," *Combustion and Flame*, vol. 162, no. 5, pp. 1623–1637, May 2015, Number: 5.

[18] M. v. Smoluchowski, "Versuch einer mathematischen Theorie der Koagulationskinetik kolloider Lösungen," *Zeitschrift für Physikalische Chemie*, vol. 92U, no. 1, pp. 129–168, 1918, Number: 1.

[19] K. C. Hu and R. Mei, "Particle collision rate in fluid flows," *Physics of Fluids*, vol. 10, no. 4, pp. 1028–1030, 1998.

[20] H. Böhm, M. Bönig, C. Feldermann, H. Jander, G. Rudolph, and H. G. Wagner, "Pressure dependence of formation of soot and pah in premixed flames," in *Soot Formation in Combustion*, Springer, 1994, pp. 145–164.

[21] Z. A. Mansurov, "Soot Formation in Combustion Processes (Review)," *Combustion, Explosion, and Shock Waves*, vol. 41, no. 6, pp. 727–744, Nov. 2005, Number: 6.

[22] M. D. Hageman, S. S. Sakai, and D. A. Rothamer, "Determination of soot onset and background particulate levels in a spark-ignition engine," *Proceedings of the Combustion Institute*, vol. 35, no. 3, pp. 2949–2956, 2015, Number: 3.

[23] S. S. Merola, A. Irimescu, S. Di Iorio, and B. M. Vaglieco, "Effect of Fuel Injection Strategy on the Carbonaceous Structure Formation and Nanoparticle Emission in a DISI Engine Fuelled with Butanol," *Energies*, vol. 10, no. 7, p. 832, 2017.

[24] A. Irimescu, S. S. Merola, S. Di Iorio, and B. M. Vaglieco, "Investigation on the effects of butanol and ethanol fueling on combustion and PM emissions in an optically accessible DISI engine," *Fuel*, vol. 216, pp. 121–141, Mar. 2018.

[25] Glassman and P. Yaccarino, "The Effect of Oxygen Concentration on Sooting Diffusion Flames," *Combustion Science and Technology*, vol. 24, no. 3-4, pp. 107–114, Nov. 1980, Number: 3-4.

[26] A. Nobili, L. P. Maffei, A. Baggioli, M. Pelucchi, A. Cuoci, C. Cavallotti, and T. Faravelli, "On the radical behavior of large polycyclic aromatic hydrocarbons in soot formation and oxidation," *Combustion and Flame*, vol. 235, p. 111 692, 2022.

[27] G. W. Sidebotham and I. Glassman, "Flame temperature, fuel structure, and fuel concentration effects on soot formation in inverse diffusion flames," *Combustion and Flame*, vol. 90, no. 3, pp. 269–283, Sep. 1992, Number: 3.

[28] J. W. Martin, M. Salamanca, and M. Kraft, "Soot inception: Carbonaceous nanoparticle formation in flames," *Progress in Energy and Combustion Science*, vol. 88, p. 100 956, 2022.

[29] D. Stops, "The mean free path of gas molecules in the transition regime," *Journal of Physics D: Applied Physics*, vol. 3, no. 5, p. 685, 1970.

[30] R. Buckley and S. Loyalka, "Cunningham correction factor and accommodation coefficient: Interpretation of millikan's data," *Journal of aerosol science*, vol. 20, no. 3, pp. 347–349, 1989.

[31] C. Marchal, "Modelisation de la formation et de l'oxydation des suies dans un moteur automobile," Ph.D. dissertation, Université d'Orléans, 2008.

[32] C. Marchal, G. Moréac, C. Vovelle, C. Mounam-Rousselle, and F. Mauss, "Soot modelling in automotive engines," in *Proceedings of the European Combustion Meeting*, 2009.

[33] A. Khosousi and S. B. Dworkin, "Soot surface reactivity during surface growth and oxidation in laminar diffusion flames," *Combustion and Flame*, vol. 162, no. 12, pp. 4523–4532, Dec. 2015, Number: 12.

[34] M. Frenklach and S. J. Harris, "Aerosol dynamics modeling using the method of moments," *Journal of colloid and interface science*, vol. 118, no. 1, pp. 252–261, 1987.

[35] M. Frenklach, "Reaction mechanism of soot formation in flames," *Physical chemistry chemical Physics*, vol. 4, no. 11, pp. 2028–2037, 2002.

[36] K. Netzell, "Development and applications of detailed kinetic models for the soot particle size distribution function," Ph.D. dissertation, Lund University, 2006.

[37] F. Dawood, M. Anda, and G. Shafiullah, "Hydrogen production for energy: An overview," *International Journal of Hydrogen Energy*, vol. 45, no. 7, pp. 3847–3869, 2020.

[38] M. H. Hasan, T. M. I. Mahlia, M. Mofijur, I. Rizwanul Fattah, F. Handayani, H. C. Ong, and A. S. Silitonga, "A comprehensive review on the recent development of ammonia as a renewable energy carrier," *Energies*, vol. 14, no. 13, 2021.

[39] A. M. Elbaz, S. Wang, T. F. Guiberti, and W. L. Roberts, “Review on the recent advances on ammonia combustion from the fundamentals to the applications,” *Fuel Communications*, vol. 10, p. 100 053, 2022.

[40] D. Miura and T. Tezuka, “A comparative study of ammonia energy systems as a future energy carrier, with particular reference to vehicle use in japan,” *Energy*, vol. 68, pp. 428–436, 2014.

[41] A. Valera-Medina, H. Xiao, M. Owen-Jones, W. David, and P. Bowen, “Ammonia for power,” *Progress in Energy and Combustion Science*, vol. 69, pp. 63–102, 2018.

[42] A. Valera-Medina, F. Amer-Hatem, A. K. Azad, I. C. Dedoussi, M. de Joannon, R. X. Fernandes, P. Glarborg, H. Hashemi, X. He, S. Mashruk, J. McGowan, C. Mounaim-Rouselle, A. Ortiz-Prado, A. Ortiz-Valera, I. Rossetti, B. Shu, M. Yehia, H. Xiao, and M. Costa, “Review on ammonia as a potential fuel: From synthesis to economics,” *Energy & Fuels*, vol. 35, no. 9, pp. 6964–7029, 2021.

[43] J. S. Cardoso, V. Silva, R. C. Rocha, M. J. Hall, M. Costa, and D. Eusébio, “Ammonia as an energy vector: Current and future prospects for low-carbon fuel applications in internal combustion engines,” *Journal of Cleaner Production*, vol. 296, p. 126 562, 2021.

[44] X. Han, Z. Wang, Y. He, Y. Zhu, and K. Cen, “Experimental and kinetic modeling study of laminar burning velocities of nh3/syngas/air premixed flames,” *Combustion and Flame*, vol. 213, pp. 1–13, 2020.

[45] P. Kumar and T. R. Meyer, “Experimental and modeling study of chemical-kinetics mechanisms for h2–nh3–air mixtures in laminar premixed jet flames,” *Fuel*, vol. 108, pp. 166–176, 2013.

[46] Y. Bicer and I. Dincer, “Life cycle assessment of ammonia utilization in city transportation and power generation,” *Journal of Cleaner Production*, vol. 170, pp. 1594–1601, 2018.

[47] H. Xiao, A. Valera-Medina, and P. J. Bowen, “Modeling combustion of ammonia/hydrogen fuel blends under gas turbine conditions,” *Energy & Fuels*, vol. 31, no. 8, pp. 8631–8642, 2017.

[48] J. Lee, J. Kim, J. Park, and O. Kwon, “Studies on properties of laminar premixed hydrogen-added ammonia/air flames for hydrogen production,” *International Journal of Hydrogen Energy*, vol. 35, no. 3, pp. 1054–1064, 2010.

[49] A. Karan, G. Dayma, C. Chauveau, and F. Halter, “High-pressure and temperature ammonia flame speeds,” in *13th Asia-Pacific Conference on Combustion*, Abu Dhabi, United Arab Emirates, Dec. 2021.

[50] A. Hayakawa, Y. Arakawa, R. Mimoto, K. K. A. Somarathne, T. Kudo, and H. Kobayashi, "Experimental investigation of stabilization and emission characteristics of ammonia/air premixed flames in a swirl combustor," *International Journal of Hydrogen Energy*, vol. 42, no. 19, pp. 14 010–14 018, 2017.

[51] S. Mashruk, M. Kovaleva, C. Tung Chong, A. Hayakawa, E. C. Okafor, and A. Valera-Medina, "Nitrogen oxides as a by-product of ammonia/hydrogen combustion regimes," *Chemical Engineering Transactions*, vol. 89, pp. 613–618, 2021.

[52] E. C. Okafor, M. Tsukamoto, A. Hayakawa, K. K. A. Somarathne, T. Kudo, T. Tsujimura, and H. Kobayashi, "Influence of wall heat loss on the emission characteristics of premixed ammonia-air swirling flames interacting with the combustor wall," *Proceedings of the Combustion Institute*, vol. 38, no. 4, pp. 5139–5146, 2021.

[53] M.-C. Chiong, C. T. Chong, J.-H. Ng, S. Mashruk, W. W. F. Chong, N. A. Samiran, G. R. Mong, and A. Valera-Medina, "Advancements of combustion technologies in the ammonia-fuelled engines," *Energy Conversion and Management*, vol. 244, p. 114 460, 2021.

[54] K. P. Shrestha, C. Lhuillier, A. A. Barbosa, P. Brequigny, F. Contino, C. Mounaïm-Rousselle, L. Seidel, and F. Mauss, "An experimental and modeling study of ammonia with enriched oxygen content and ammonia/hydrogen laminar flame speed at elevated pressure and temperature," *Proceedings of the Combustion Institute*, vol. 38, no. 2, pp. 2163–2174, 2021.

[55] A. A. Khateeb, T. F. Guiberti, G. Wang, W. R. Boyette, M. Younes, A. Jamal, and W. L. Roberts, "Stability limits and no emissions of premixed swirl ammonia-air flames enriched with hydrogen or methane at elevated pressures," *International Journal of Hydrogen Energy*, vol. 46, no. 21, pp. 11 969–11 981, 2021.

[56] H. Xiao, M. Howard, A. Valera-Medina, S. Dooley, and P. Bowen, "Reduced chemical mechanisms for ammonia/methane co-firing for gas turbine applications," *Energy Procedia*, vol. 105, pp. 1483–1488, 2017, 8th International Conference on Applied Energy, ICAE2016, 8-11 October 2016, Beijing, China.

[57] C. Lhuillier, P. Brequigny, F. Contino, and C. Mounaïm-Rousselle, "Experimental study on ammonia/hydrogen/air combustion in spark ignition engine conditions," *Fuel*, vol. 269, p. 117 448, 2020.

[58] S. Verhelst and T. Wallner, "Hydrogen-fueled internal combustion engines," *Progress in energy and combustion science*, vol. 35, no. 6, pp. 490–527, 2009.

[59] S. B. Pope, *Turbulent Flows.* Cambridge University Press.

[60] N. Peters, *Turbulent Combustion.* Cambridge University Press, 2000.

[61] T. Poinsot and D. Veynante, *Theoretical and numerical combustion.* RT Edwards, Inc., 2005.

[62] E. Ranzi, A. Frassoldati, R. Grana, A. Cuoci, T. Faravelli, A. Kelley, and C. Law, “Hierarchical and comparative kinetic modeling of laminar flame speeds of hydrocarbon and oxygenated fuels,” *Progress in Energy and Combustion Science*, vol. 38, no. 4, pp. 468–501, 2012.

[63] J. M. Boyde, A. Fiolitakis, M. D. Domenico, and M. Aigner, “Correlations for the laminar flame speed, adiabatic flame temperature and ignition delay time for methane, ethanol and n-decane,” in *49th AIAA Aerospace Sciences Meeting including the New Horizons Forum and Aerospace Exposition.*

[64] M. Metghalchi and J. C. Keck, “Laminar burning velocity of propane-air mixtures at high temperature and pressure,” *Combustion and Flame*, vol. 38, pp. 143–154, 1980.

[65] R. Amirante, E. Distaso, P. Tamburrano, and R. D. Reitz, “Laminar flame speed correlations for methane, ethane, propane and their mixtures, and natural gas and gasoline for spark-ignition engine simulations,” *International Journal of Engine Research*, vol. 18, no. 9, pp. 951–970, 2017.

[66] N. Wang, S. Huang, Z. Zhang, T. Li, P. Yi, D. Wu, and G. Chen, “Laminar burning characteristics of ammonia/hydrogen/air mixtures with laser ignition,” *International Journal of Hydrogen Energy*, vol. 46, no. 62, pp. 31 879–31 893, 2021.

[67] S. Wang, A. El-Baz, Z. Wang, and W. L. Roberts, “The effect of oxygen content on the turbulent flame speed of ammonia/oxygen/nitrogen expanding flames under elevated pressures,” *Combustion and Flame*, vol. 232, p. 111 521, 2021.

[68] A. Ichikawa, A. Hayakawa, Y. Kitagawa, K. Kunkuma Amila Somarathne, T. Kudo, and H. Kobayashi, “Laminar burning velocity and markstein length of ammonia/hydrogen/air premixed flames at elevated pressures,” *International Journal of Hydrogen Energy*, vol. 40, no. 30, pp. 9570–9578, 2015.

[69] R. Kanoshima, A. Hayakawa, T. Kudo, E. C. Okafor, S. Colson, A. Ichikawa, T. Kudo, and H. Kobayashi, “Effects of initial mixture temperature and pressure on laminar burning velocity and markstein length of ammonia/air premixed laminar flames,” *Fuel*, vol. 310, p. 122 149, 2022.

[70] M. Mitu, D. Razus, and V. Schroeder, “Laminar burning velocities of hydrogen-blended methane–air and natural gas–air mixtures, calculated from the early stage of p(t) records in a spherical vessel,” *Energies*, vol. 14, no. 22, 2021.

[71] G. J. Gotama, A. Hayakawa, E. C. Okafor, R. Kanoshima, M. Hayashi, T. Kudo, and H. Kobayashi, “Measurement of the laminar burning velocity and kinetics study of the importance of the hydrogen recovery mechanism of ammonia/hydrogen/air premixed flames,” *Combustion and Flame*, vol. 236, p. 111 753, 2022.

[72] X. Han, Z. Wang, M. Costa, Z. Sun, Y. He, and K. Cen, “Experimental and kinetic modeling study of laminar burning velocities of nh3/air, nh3/h2/air, nh3/co/air and nh3/ch4/air premixed flames,” *Combustion and Flame*, vol. 206, pp. 214–226, 2019.

[73] E. C. Okafor, Y. Naito, S. Colson, A. Ichikawa, T. Kudo, A. Hayakawa, and H. Kobayashi, “Experimental and numerical study of the laminar burning velocity of ch4–nh3–air premixed flames,” *Combustion and Flame*, vol. 187, pp. 185–198, 2018.

[74] J. Otomo, M. Koshi, T. Mitsumori, H. Iwasaki, and K. Yamada, “Chemical kinetic modeling of ammonia oxidation with improved reaction mechanism for ammonia/air and ammonia/hydrogen/air combustion,” *International Journal of Hydrogen Energy*, vol. 43, no. 5, pp. 3004–3014, 2018.

[75] Y. Song, L. Marrodán, N. Vin, O. Herbinet, E. Assaf, C. Fittschen, A. Stagni, T. Faravelli, M. Alzueta, and F. Battin-Leclerc, “The sensitizing effects of no2 and no on methane low temperature oxidation in a jet stirred reactor,” *Proceedings of the Combustion Institute*, vol. 37, no. 1, pp. 667–675, 2019.

[76] A. Stagni, C. Cavallotti, S. Arunthanayothin, Y. Song, O. Herbinet, F. Battin-Leclerc, and T. Faravelli, “An experimental, theoretical and kinetic-modeling study of the gas-phase oxidation of ammonia,” *Reaction Chemistry & Engineering*, vol. 5, no. 4, pp. 696–711, 2020.

[77] M. Del Pecchia, S. Breda, A. d’Adamo, S. Fontanesi, A. Irimescu, and S. Merola, “Development of chemistry-based laminar flame speed correlation for part-load si conditions and validation in a gdi research engine,” *SAE International Journal of Engines*, vol. 11, no. 6, pp. 715–742, 2018.

[78] M. Del Pecchia, V. Pessina, F. Berni, A. d’Adamo, and S. Fontanesi, “Gasoline-ethanol blend formulation to mimic laminar flame speed and auto-ignition quality in automotive engines,” *Fuel*, vol. 264, p. 116 741, 2020.

[79] M. Di Lorenzo, P. Brequigny, F. Foucher, and C. Mounaïm-Rousselle, “Validation of trf-e as gasoline surrogate through an experimental laminar burning speed investigation,” *Fuel*, vol. 253, pp. 1578–1588, 2019.

[80] S. Verhelst, R. Woolley, M. Lawes, and R. Sierens, “Laminar and unstable burning velocities and markstein lengths of hydrogen–air mixtures at engine-like conditions,” *Proceedings of the Combustion Institute*, vol. 30, no. 1, pp. 209–216, 2005.

[81] S. Verhelst, J. Vancoillie, J. Demuynck, *et al.*, “A correlation for the laminar burning velocity for use in hydrogen spark ignition engine simulation,” *International Journal of Hydrogen Energy*, vol. 36, no. 1, pp. 957–974, 2011.

[82] G. D’Errico, A. Onorati, and S. Ellgas, “1d thermo-fluid dynamic modelling of an s.i. single-cylinder h2 engine with cryogenic port injection,” *International Journal of Hydrogen Energy*, vol. 33, pp. 5829–5841, 2008.

[83] A. Goldmann and F. Dinkelacker, "Approximation of laminar flame characteristics on premixed ammonia/hydrogen/nitrogen/air mixtures at elevated temperatures and pressures," *Fuel*, vol. 224, pp. 366–378, 2018.

[84] C. Pera and V. Knop, "Methodology to define gasoline surrogates dedicated to auto-ignition in engines," *Fuel*, vol. 96, pp. 59–69, Jun. 2012.

[85] D. Kim, J. Martz, and A. Violi, "A surrogate for emulating the physical and chemical properties of conventional jet fuel," *Combustion and Flame*, vol. 161, no. 6, pp. 1489–1498, Jun. 2014, Number: 6.

[86] D. Kim, J. Martz, A. Abdul-Nour, X. Yu, M. Jansons, and A. Violi, "A six-component surrogate for emulating the physical and chemical characteristics of conventional and alternative jet fuels and their blends," *Combustion and Flame*, vol. 179, pp. 86–94, May 2017.

[87] M. Mehl, J. Y. Chen, W. J. Pitz, S. M. Sarathy, and C. K. Westbrook, "An Approach for Formulating Surrogates for Gasoline with Application toward a Reduced Surrogate Mechanism for CFD Engine Modeling," *Energy & Fuels*, vol. 25, no. 11, pp. 5215–5223, Nov. 2011, Number: 11 Publisher: American Chemical Society.

[88] M. R. Riazi, *Characterization and properties of petroleum fractions.* ASTM International, 2005.

[89] A. G. A. Jameel, N. Naser, G. Issayev, J. Touitou, M. K. Ghosh, A.-H. Emwas, A. Farooq, S. Dooley, and S. M. Sarathy, "A minimalist functional group approach for surrogate fuel formulation," *Combustion and Flame*, vol. 192, pp. 250–271, 2018.

[90] A. S. Al Ramadan, S. M. Sarathy, M. Khurshid, and J. Badra, "A blending rule for octane numbers of prfs and tprfs with ethanol," *Fuel*, vol. 180, pp. 175–186, 2016.

[91] J. Badra, A. S. AlRamadan, and S. M. Sarathy, "Optimization of the octane response of gasoline/ethanol blends," *Applied Energy*, vol. 203, pp. 778–793, 2017.

[92] M. Smooke, M. Long, B. Connelly, M. Colket, and R. Hall, "Soot formation in laminar diffusion flames," *Combustion and Flame*, vol. 143, no. 4, pp. 613–628, Dec. 2005, Number: 4.

[93] A. Akare, "Investigating the links between smoke points, sooting thresholds, and particle number and size," *Department of Chemical Engineering*, 2009.

[94] D. B. Olson and J. C. Pickens, "The effects of molecular structure on soot formation, I. Soot thresholds in premixed flames," *Combustion and Flame*, vol. 57, no. 2, pp. 199–208, Aug. 1984, Number: 2.

[95] T. Kessler, P. C. St. John, J. Zhu, C. S. McEnally, L. D. Pfefferle, and J. H. Mack, "A comparison of computational models for predicting yield sooting index," *Proceedings of the Combustion Institute*, vol. 38, no. 1, pp. 1385–1393, Jan. 2021, Number: 1.

[96] M. J. Montgomery, D. D. Das, C. S. McEnally, and L. D. Pfefferle, "Analyzing the robustness of the yield sooting index as a measure of sooting tendency," *Proceedings of the Combustion Institute*, vol. 37, no. 1, pp. 911–918, 2019, Number: 1.

[97] R. Lemaire, D. Lapalme, and P. Seers, "Analysis of the sooting propensity of C-4 and C-5 oxygenates: Comparison of sooting indexes issued from laser-based experiments and group additivity approaches," *Combustion and Flame*, vol. 162, no. 9, pp. 3140–3155, Sep. 2015, Number: 9.

[98] K. Aikawa, T. Sakurai, and J. J. Jetter, "Development of a predictive model for gasoline vehicle particulate matter emissions," *SAE International Journal of Fuels and Lubricants*, vol. 3, no. 2, pp. 610–622, Oct. 2010.

[99] J. J. Batteh and E. W. Curtis, "Modeling transient fuel effects with alternative fuels," No. 2005-01-1127, 2005.

[100] R. C. Reid, J. M. Prausnitz, and B. E. Poling, *The properties of gases and liquids*. United States: McGraw Hill Book Co.,New York, NY, Jan. 1987.

[101] Peter Linstrom and William Mallard, *The NIST Chemistry WebBook: A Chemical Data Resource on the Internet*. 2001, Number: 46 Publisher: Journal of Chemical and Engineering Data.

[102] 2020 Siemens Digital Industries Software, *STAR-CD Version 2020.1, CFD/CCM User Guide*, version v.2020.1.2, 2020.

[103] O. Colin and A. Benkenida, "The 3-zones extended coherent flame model (ecfm3z) for computing premixed/diffusion combustion," *Oil & gas science and technology*, vol. 59, no. 6, pp. 593–609, 2004.

[104] M. D. Pecchia, V. Pessina, C. Iacovano, and G. Cantore, "Development of gasoline-ethanol blends laminar flame speed correlations at full-load Si engine conditions via 1D simulations," Erode, India, 2019, p. 020 063.

[105] S. D. I. Software, *Dars, user guide*, version v.2020, 2020.

[106] A. Stagni, A. Frassoldati, A. Cuoci, T. Faravelli, and E. Ranzi, "Skeletal mechanism reduction through species-targeted sensitivity analysis," *Combustion and Flame*, vol. 163, pp. 382–393, 2016.

[107] A. Stagni, A. Cuoci, A. Frassoldati, T. Faravelli, and E. Ranzi, "Lumping and Reduction of Detailed Kinetic Schemes: An Effective Coupling," *Industrial & Engineering Chemistry Research*, vol. 53, no. 22, pp. 9004–9016, Jun. 2014, Number: 22.

[108] E. Ranzi, A. Frassoldati, A. Stagni, M. Pelucchi, A. Cuoci, and T. Favarelli, "Reduced kinetic schemes of complex reaction systems: Fossil and biomass-derived transportation fuels," *International Journal of Chemical Kinetics*, vol. 46, no. 9, pp. 512–542, 2014.

[109] F. Bozza, F. Berni, F. Cicci, A. D'Adamo, V. D. Bellis, S. Fontanesi, E. E. Malfi, V. Pessina, and L. Teodosio, "Potentials of the Oversizing and H2-Supported Lean Combustion of a VVA SI Gasoline Engine Towards Efficiency Improvement," No. 2021-24-0007, SAE Internationa Congressl, 2021.

[110] V. Di Sarli and A. D. Benedetto, "Laminar burning velocity of hydrogen–methane/air premixed flames," *International Journal of Hydrogen Energy*, vol. 32, no. 5, pp. 637–646, 2007.

[111] S. Brusca, R. Lanzafame, A. M. C. Garrano, and M. Messina, "Effects of pressure, temperature and dilution on fuels/air mixture laminar flame burning velocity," *Energy Procedia*, vol. 82, pp. 125–132, 2015.

[112] A. Stagni, A. Cuoci, A. Frassoldati, T. Faravelli, and E. Ranzi, "Lumping and reduction of detailed kinetic schemes: An effective coupling," *Industrial & Engineering Chemistry Research*, vol. 53, no. 22, pp. 9004–9016, 2014.

[113] A. Stagni, A. Frassoldati, A. Cuoci, T. Faravelli, and E. Ranzi, "Skeletal mechanism reduction through species-targeted sensitivity analysis," *Combustion and Flame*, vol. 163, pp. 382–393, 2016.

[114] P. R. Lindstedt, "Simplified soot nucleation and surface growth steps for non-premixed flames," in *Soot formation in combustion*, Springer, 1994, pp. 417–441.

[115] R. P. Lindstedt and S. A. Louloudi, "Joint-scalar transported pdf modeling of soot formation and oxidation," *Proceedings of the Combustion Institute*, vol. 30, no. 1, pp. 775–783, 2005.

[116] M. B. Colket and R. J. Hall, "Successes and uncertainties in modeling soot formation in laminar, premixed flames," in *Soot formation in combustion*, Springer, 1994, pp. 442–470.

[117] M. Mueller, G. Blanquart, and H. Pitsch, "Hybrid method of moments for modeling soot formation and growth," *Combustion and Flame*, vol. 156, no. 6, pp. 1143–1155, 2009.

[118] S. Wu, D. Zhou, and W. Yang, "Implementation of an efficient method of moments for treatment of soot formation and oxidation processes in three-dimensional engine simulations," *Applied Energy*, vol. 254, p. 113 661, 2019.

[119] D. C. Quiros, S. Hu, S. Hu, E. S. Lee, S. Sardar, X. Wang, J. S. Olfert, H. S. Jung, Y. Zhu, and T. Huai, "Particle effective density and mass during steady-state operation of gdi, pfi, and diesel passenger cars," *Journal of Aerosol Science*, vol. 83, pp. 39–54, 2015.

[120] B. B. Mandelbrot, *The fractal geometry of nature.* San Francisco : W.H. Freeman, 1982.

[121] F. Berni, F. Mortellaro, V. Pessina, S. Paltrinieri, F. Pulvirenti, V. Rossi, M. Borghi, and S. Fontanesi, "Modeling of gaseous emissions and soot in 3d-cfd in-cylinder simulations of spark-ignition engines: A methodology to correlate numerical results and experimental data," *International Journal of Engine Research*, p. 14 680 874 221 112 564, 2022.

[122] D. Aubagnac-Karkar, "Modélisation des suies par méthode sectionnelle pour la simulation RANS des moteurs Diesel," Ph.D. dissertation, Ecole Centrale Paris, Dec. 2014.

[123] H. G. Wagner, "Soot Formation — An Overview," in *Particulate Carbon: Formation During Combustion*, D. C. Siegla and G. W. Smith, Eds., Springer US, 1981, pp. 1–29.

[124] R. J. Gill, D. B. Olson, and H. F. Calcote, "Correlations of Soot Formation in Turbojet Engines and in Laboratory Flames," in *Volume 3: Coal, Biomass and Alternative Fuels; Combustion and Fuels; Oil and Gas Applications; Cycle Innovations*, Amsterdam, The Netherlands: American Society of Mechanical Engineers, Jun. 1984, V003T06A018.

[125] M. Karalus, P. Thakre, G. Goldin, and D. Brandt, "Flamelet Versus Detailed Chemistry Large Eddy Simulation for a Liquid-Fueled Gas Turbine Combustor: A Comparison of Accuracy and Computational Cost," *Journal of Engineering for Gas Turbines and Power*, vol. 144, no. 1, p. 011 004, Jan. 2022, Number: 1.

[126] E. Van Kalmthout and D. Veynante, "Direct numerical simulations analysis of flame surface density models for nonpremixed turbulent combustion," *Physics of Fluids*, vol. 10, no. 9, pp. 2347–2368, 1998.

[127] T. Poinsot, D. Veynante, and S. Candel, "Diagrams of premixed turbulent combustion based on direct simulation," *Symposium (International) on Combustion*, vol. 23, no. 1, pp. 613–619, 1991, Number: 1.

[128] H. Yamashita, M. Shimada, and T. Takeno, "A numerical study on flame stability at the transition point of jet diffusion flames," *Symposium (International) on Combustion*, vol. 26, no. 1, pp. 27–34, 1996, Number: 1.

[129] D. A. Rosenberg, P. M. Allison, and J. F. Driscoll, "Flame index and its statistical properties measured to understand partially premixed turbulent combustion," *Combustion and Flame*, vol. 162, no. 7, pp. 2808–2822, Jul. 2015, Number: 7.

[130] P. Domingo, L. Vervisch, and J. Reveillon, "Dns analysis of partially premixed combustion in spray and gaseous turbulent flame-bases stabilized in hot air," *Combustion and Flame*, vol. 140, no. 3, pp. 172–195, 2005.

[131] S. Som, A. I. Ramirez, D. E. Longman, and S. K. Aggarwal, "Effect of nozzle orifice geometry on spray, combustion, and emission characteristics under diesel engine conditions," *Fuel*, vol. 90, no. 3, pp. 1267–1276, 2011.

[132] E. Knudsen and H. Pitsch, “A general flamelet transformation useful for distinguishing between premixed and non-premixed modes of combustion,” *Combustion and flame*, vol. 156, no. 3, pp. 678–696, 2009.

[133] C. D. Pierce and P. Moin, “Progress-variable approach for large-eddy simulation of non-premixed turbulent combustion,” *Journal of fluid Mechanics*, vol. 504, pp. 73–97, 2004.

[134] M. Ihme, C. M. Cha, and H. Pitsch, “Prediction of local extinction and re-ignition effects in non-premixed turbulent combustion using a flamelet/progress variable approach,” *Proceedings of the Combustion Institute*, vol. 30, no. 1, pp. 793–800, 2005.

[135] Sparacino, Berni, d’Adamo, Krastev, Cavicchi, and Postrioti, “Impact of the Primary Break-Up Strategy on the Morphology of GDI Sprays in 3D-CFD Simulations of Multi-Hole Injectors,” *Energies*, vol. 12, no. 15, p. 2890, Jul. 2019, Number: 15.

[136] S. Sparacino, F. Berni, M. Riccardi, A. Cavicchi, and L. Postrioti, “3D-CFD Simulation of a GDI Injector Under Standard and Flashing Conditions,” *E3S Web of Conferences*, vol. 197, p. 06 002, 2020.

[137] R. D. Reitz and R. Diwakar, “Effect of Drop Breakup on Fuel Sprays,” ISSN: 0148-7191, 1986.

[138] J. Senda, T. Kanda, M. Al-Roub, P. V. Farrell, T. Fukami, and H. Fujimoto, “Modeling Spray Impingement Considering Fuel Film Formation on the Wall,” *SAE Transactions*, vol. 106, pp. 98–112, 1997, Publisher: SAE International.

[139] F. Berni and S. Fontanesi, “A 3D-CFD methodology to investigate boundary layers and assess the applicability of wall functions in actual industrial problems: A focus on in-cylinder simulations,” *Applied Thermal Engineering*, vol. 174, p. 115 320, Jun. 2020.

[140] F. Berni, G. Cicalese, and S. Fontanesi, “A modified thermal wall function for the estimation of gas-to-wall heat fluxes in CFD in-cylinder simulations of high performance spark-ignition engines,” *Applied Thermal Engineering*, vol. 115, pp. 1045–1062, Mar. 2017.

[141] F. Berni, G. Cicalese, M. Borghi, and S. Fontanesi, “Towards grid-independent 3D-CFD wall-function-based heat transfer models for complex industrial flows with focus on in-cylinder simulations,” *Applied Thermal Engineering*, vol. 190, p. 116 838, May 2021.

[142] G. Technologies, *Gt-power v7.2, user guide*, version v.7.2.

[143] C.-S. Lim, J.-H. Lim, J.-S. Cha, and J.-Y. Lim, “Comparative effects of oxygenates-gasoline blended fuels on the exhaust emissions in gasoline-powered vehicles,” *Journal of Environmental Management*, vol. 239, pp. 103–113, 2019.

[144] D. D. Das, C. S. McEnally, T. A. Kwan, J. B. Zimmerman, W. J. Cannella, C. J. Mueller, and L. D. Pfefferle, “Sooting tendencies of diesel fuels, jet fuels, and their surrogates in diffusion flames,” *Fuel*, vol. 197, pp. 445–458, Jun. 2017.

[145] G. Blanquart, P. Pepiot-Desjardins, and H. Pitsch, “Chemical mechanism for high temperature combustion of engine relevant fuels with emphasis on soot precursors,” *Combustion and Flame*, vol. 156, no. 3, pp. 588–607, 2009.